UNIVERSITY OF NAIROBI

SCHOOL OF ENGINEERING

A MULTI-SCALE DISLOCATION MODEL APPLIED TO METAL PLASTICITY

Eng. KENNETH D. NJOROGE

F80/81641/2009

A thesis submitted in fulfilment of the requirements for the Degree of Doctor of Philosophy in the Department of Mechanical and Manufacturing Engineering at the University of Nairobi

APRIL 2015

DECLARATION

I declare that this thesis is my own original work. I also affirm that to the best of my knowledge this thesis has not been presented in this or any other university for examination, or for any other purpose.

Candidate: _____

Eng. KENNETH D. NJOROGE: Signature

1st Supervisor: _____

Eng. PROF. GEORGE O. RADING Signature

This thesis has been submitted for examination with my approval as one of the university's supervisors.

2nd Supervisor: _____

Eng. PROF. JOHN M. KIHIU Signature

This thesis has been submitted for examination with my approval as one of the university's supervisors.

3rd Supervisor: _____

PROF. M. J. WITCOMB Signature

This thesis has been submitted for examination with my approval as one of the university's supervisors.

4th Supervisor: _____

PROF. L. A. CORNISH Signature

This thesis has been submitted for examination with my approval as one of the university's supervisors.

ACKNOWLEDGEMENTS

I would like to thank my primary supervisor Professor George O. Rading for his continuous guidance throughout this study. I would also like to thank my secondary supervisors Professor John M. Kihiu, Professor Michael J. Witcomb and Professor Lesely A. Cornish for their comments and suggestions during the progress of this work.

I would like to thank Professors Cornish and Witcomb for my training in the use of Transmission Electron Microscopy conducted at the University of Witwatersrand. Special thanks to Dr. B. Odera who walked me through my stay at the University of Witwatersrand.

My gratitude goes to my family for their patience and their unwavering support throughout the period of my study.

This research has been supported by the African Materials Science and Engineering Network (AMSEN) funded by the Carnegie Corporation of New York. This research has also been supported by the Jomo Kenyatta University of Agriculture and Technology through their grant of study-leave to me. This support is greatly appreciated.

ABSTRACT

Multi-scale simulation techniques are increasingly being applied to the study of engineering problems, where characterizing phenomena occur at different length scales and where phenomena occurring at some length scale influences phenomena occurring at a different length scale. In material performance studies, it is understood that bonding at the atomic length scale, aggregation of grains, the existence and evolution of defects, all contribute to material behaviour.

The goal of this research was to develop models that enabled the simulation at various length scales intended to capture a metal's behaviour, and to link these models to enable data transfer up the length scales. The study was founded on the application of the embedded atom method (EAM) to the iron (Fe) and iron carbide (Fe-C) lattices, and on the understanding that plasticity is primarily driven by the motion of dislocations. The work involved the development of Fortran code for the implementation of the EAM, the simulation of the stress fields for both static and dynamic dislocation cores, the assembly of dislocation lines within slip planes, the assembly of slip planes within a material's lattice, and the implementation of grain evolution using finite element code. The models at the lower length scales were validated using empirical and Ab-initio Peierl's stress data. The work was carried out in five stages corresponding to the length scales considered.

The lowest level length scale (dislocation core-length scale) was used to study the evolution of the dislocation core. This was done by simulating the motion of dislocation core atoms in a lattice containing a single dislocation line, under an externally applied load, and tracking the resulting stress around the dislocation core. The principle result was the establishment of the link between the Peierl's stress and the smallest peak amplitude of the direct stress components for a dislocation line in the $[11\bar{1}]$ direction. This work gave rise to the path of least resistance (POLR) method used to predict the Peierls stress peak around the dislocation core. A mechanism for the motion of dislocation core atoms was established and the POLR stresses for different dislocation types were evaluated.

The line-length scale was used to characterize the effects of the dislocation core's distortion extended over a wider region than that possible within the capability of the EAM. This was done by the simulation of the stress profile resulting from a dislocation line, with the peak POLR stress as an input, and characterising of the stress profile and its corresponding characteristic distortion function.

This work gave rise to the misfit potential (MP) which enabled the determination of the longer range dislocation stress field through which, interactions with other lattice defects would take place. The results of the simulation of the behaviour of the interaction of dislocations dipoles are reported.

The plane-length scale accounted for the interaction of dislocation lines within the slip plane. The theory of generalized functions (distributions) was applied to profile the spatial position of interacting dislocations, and to relate them to the resulting stress amplitude profile. This work gave rise to the plane structure factor (PSF), which was used to determine the planar dislocation density which was used as an input at the next higher length scale. The model was used to determine the resulting stress field over a slip plane containing assemblies of planar dislocation structures, and the stress field was then used to predict the evolution of the dislocation assembly.

The structure-length scale accounted for the assembly of slip planes to construct 3-dimensional (3-D) dislocation structures. This stage accounted for the peak POLR stress and applied the misfit potential in the study of 2-dimensional (2-D) dislocation lines assembled into a 3-D dislocation structure. Simulations were carried out to determine the resulting stress field, which was used to characterize a 3-D dislocation structure factor. This work gave rise to the network structure factor (NSF), which was used to determine the network dislocation density which was used as an input at the next higher length scale. The model was used to determine the resulting stress field in a lattice containing dislocation structures.

The network structure factor was then used as an input into a finite element formulation that was used at the meso-length scale. This factor captured the mechanistic events at the underlying length scales and was used to drive the deformation of the finite elements as a result of evolution of the dislocation structure within the grain and its boundary. A variable discretization of the lattice was used to focus the dislocation effects in the areas of appreciable dislocation content. The method was evaluated by the generation of yield stresses, which were found to be in agreement with those proposed by the Hall-Petch relationship for the yield stress at various grain sizes.

The work presents a novel method capable of simulating material evolution under load, based on nano-scale to meso-scale events that contribute to the macro-scale material behaviour. The underlying goal in the use of a multi-scale formulation to study material behaviour was to

incorporate the physics of the material's behaviour in the prediction of its deformation. The outputs of this research are the POLR model, the MP model, the PSF model, the NSF model, the meso-scale model, the linkages between these models, the linking of these models with Peierls stress data and dislocation density data, and the link to grain size driven yield stresses of materials. These results are expected to complement current and future work in materials characterization and alloy development, and enhance the value of simulation in engineering design.

NOMENCLATURE

$A(x, z, \varphi)$	Distortion variation in the plane normal to the dislocation line direction
$B(\theta_s)$	Distortion variation due to curvature of the dislocation line
B_V	Strain displacement matrix for the bulk of the grain containing the mobile dislocations
C_{ij}	Coefficients of the co-factor matrix
$C_k,\ B_l\ \&\ A_p$	Fitting constants
D	Function of the distortion variation
D_g	Diameter of grain (m)
$\overline{D}_{e-max}$	Maximum distortion in the direction of the edge dislocation Burger's vector
$\overline{D}_{s-max}$	Maximum distortion in the direction of the screw dislocation Burger's vector
E_c	Cohesive energy of the block of atoms forming the perfect lattice (J)
$E_{elastic}$	Elastic energy in the two half-spaces (J)
E_k	Energy of motion of each atom contributing to the dislocation core (J)
E_{misfit}	Misfit energy (J)
E_m	Energy required to move the dislocation through the lattice (J)
F	Embedding energy (eV/atom)
$F[\varrho]$	Embedding potential
F_k	Force at radius r_k from the dislocation core (N)
$\mathcal{F}: \mathcal{F}_\mu$	Distribution of dislocations within the slip system – PSF
G	Shear modulus (GPa)
H_i	Heaviside function
L_i	Area of the i^{th} slip system (Å^2)
L_τ	Area of the slip system containing the dislocations (Å^2)
L_p	Area between the dislocations within the slip system (Å^2)
L'_p	Sum of spacing within a single slip system comprising one slip plane (Å^2)
$\mathcal{M}$	Distribution of slip planes within the network system – NSF
N_i	Shape function
NSF_1	Reference Network structure factor
NSF_2	Final Network structure factor
R	Relative inter-atomic distance between the atom species (Å)

S	Length of dislocation line segment given by $n.\boldsymbol{b}_s$ (Å)
$\boldsymbol{T}_k$	Force vector acting on each atom (N)
U	Internal energy (J)
V	Pairing energy (eV/atom)
$V[r_{ij}]$	Pair potential
X	Potential energy of the system due to dislocation interaction (J)
Z	Initial separation (m)
$Z_1,\ Z_2$	Atomic numbers of interacting atoms in an alloy
Z_A, Z_B	Atomic numbers of atom species “A” and “B”
a, b	Nodes of segment
a_k	Polynomial coefficients
a_{ij}	Coefficient set for the particular dislocation’s equation
$\boldsymbol{b}_1$	Burger’s vector corresponding to distortion vector in the x direction (Å)
$\boldsymbol{b}_e$	Burger’s vector corresponding to distortion vector in the y direction (Å)
$\boldsymbol{b}_n$	Burger’s vector corresponding to distortion vector in the z direction (Å)
b_{ij}	Coefficient set for the reference dislocation’s equation
$\bar{e}$	Unit vector in the direction of the pure edge dislocation (Å)
g	Piecewise function representing the path of motion
$g(x_i, c)_\xi$	Curve of motion of the atoms around the dislocation core
$j{:}\,k$	Number of pairs formed by adjacent dislocations within slip system
l	Normalized position of the dislocation between the start and end points
l_1	Normalized end point for the dislocation spacing
l_0	Normalized start point for the dislocation spacing
l_k	Spacing between dislocation cores measured along a normal from the reference dislocation line (Å)
ls_0	Normalized start point on the reference slip plane
ls_1	Normalized start point on the referred slip plane
m	Number of finite elements of the slip systems
m_p	Number of planar structures involved in each network structure
n	Number of terms in the test function

n_c	Number of dislocation core sites considered
n_k	Number of atoms contributing to the dislocation core
n_P	Number of network structures involved in the material matrix
n_z	Factor used to increase load from 0 to 100% of target maximum load
$\mathrm{n_s}, \mathrm{n_d}$	Number of outer orbital s and d electrons
np	Number of slip planes
$\bar{n}$	Slip plane normal
p	Index identifying the dislocation line
q	Number of elements in the segment
r_1	Inner cut-off radius (Å)
r_{ij}	Inter-atomic distance (Å)
r_{kj}	Position vector of the lattice point from some reference point
r_k	Outer cut-off radius (Å)
r_m	Intermediate cut-off radius (Å)
r_o	Distance to the lattice site in a perfect lattice (Å)
r_p	Order of the polynomial
r_t	Translation tensor for the slip system, with respect to some origin
$\bar{s}$	Unit vector in the direction of the pure screw dislocation
s	Normalized spacing between two adjacent slip planes
s_1, s_0	Locations of the first and reference dislocations
w	Index number of the slip system
x	Distance measured from the dislocation core site along the edge component Burger's vector to the lattice point under consideration (Å)
x_i	Independent variables
x_o	Reference point on the *x* axis
x, z	Displacement from the reference core site to the point of analysis (Å)
z_s	Distance measured from the dislocation core site along the normal to the slip plane, to the lattice point under consideration (Å)
z_o	Reference point on the *z* axis
α_{Fe}	Constant of proportionality (0.3 for Fe)

α_p, β_p	Fitting parameters
α_r	Cycle amplitude factor
α_n , β_n & b_n	Fitting constants
α_i, β_i	Polynomial coefficients
γ	Inclination of segment directions to Burger's vector (deg)
δ_r	Displacement of the lattice point in a defined direction (Å)
δ_{x3}	Distortion about the slip plane in 3 dimensional space
$\delta_1, \delta_2, \delta_3$	Unit distortion vectors in the x, z and dislocation line directions
$\delta_{\boldsymbol{n}}, \delta_{\boldsymbol{e}}$, $\delta_{\boldsymbol{s}}$	Unit normal, edge and screw distortions along the respective Burger's vectors
ε	Factor to set the profile over the slip plane
ϵ_i	Factor to set the profile of the stress humps across the slip planes
ζ_r	Atom ring number
ξ, η, ρ	Independent variables
η_x	Orientation tensor of the slip system with respect to the crystal/grain boundaries
θ	Angle of curvature of the dislocation segment at the point on the dislocation line considered (deg)
θ_s	Angular coordinate of the dislocation core site measured from the line normal to the dislocation line direction, to the lattice point under consideration (deg)
λ	Number of Burger's vector intervals to the location where dislocation core's stress field is negligible
$\boldsymbol{\nu}_k$	Displacement vector of each atom, not necessarily in the same direction as the Burger's vector (Å)
ϕ	Dependent variable
ρ^a	Atomic density of the multi-component system
ρ_s, ρ_d	Respective densities of the wave functions (electrons/m^3)
ρ_b	Density of grain boundary dislocations (m/m^3)
ρ_m	Density of mobile dislocations (m/m^3)
ϱ	Electron density (electrons/m^3)
$\hat{\varrho}$	Dislocation planar density (m/m^2)
σ_{ij}	Dislocation driving stress (Pa)
$\hat{\sigma}_{ij}$	Dislocation core atom driving stress.

σ_{mi}	Principle stress in the lattice (Pa)
τ_y	Yield stress (Pa)
v	Velocity space coordinate (m/s)
φ	Angle representing the location between lattice sites in a perfect material (deg)
$\emptyset_d$	Dislocation network density (m/m^2)
ω	Inclination of net force on segment
Λ	Equation of the path traced by the dislocation line
Λ_p	Polynomial characterizing the dislocations spatial organization
Θ_j	Offset of the slip planes along the length of the slip plane (Å)
Θ_k	Offset of the slip planes along the depth of the slip plane (Å)
Π_ρ	Polynomial relating the root of the grain's dislocation density and the NSF
Π_b	Polynomial relating the grain boundary dislocation density and the NSF
Π_x	Polynomial relating the POLR peak stress and the NSF
Y_j	Gradient of change of the separation along the length of the slip plane
Y_k	Gradient of change of the separation along the depth of the slip plane
Υ	Fitting constant
X_s, Ω_s, Ω_e	Coefficients determined from boundary conditions
Ψ	Distortion energy forming the dislocation (J)
$\Psi[\delta]$	Misfit potential energy (J)
Ψ_s and Γ_e	Screw and edge dislocation factors
$\Omega(\emptyset_x)$	Frenkel sinusoidal inter-planar potential
$\langle xxx \rangle$	Refers to a family of directions
$[xxx]$	Refers to a specific direction
$\{xxx\}$	Refers to a family of planes
(xxx)	Refers to a specific plane

ABBREVIATIONS

BCC	Body Centered Cubic
DD	Dislocation dynamics
EAM	Embedded atom method
FCC	Face Centered Cubic
FEAt	Finite element atomic model
FEM	Finite element method
FMDCA	Free Motion of Dislocation Core Atoms
GND	Geometrically necessary dislocations
HCP	Hexagonal Close Packed
MAAD	Material Analysis using Atomistic Dynamics
MEAM	Modified embedded atom method
NSF	Network structure factor
PA	Planar arrays
PBC	Periodic boundary conditions
POLR	Path of Least Resistance
P-N	Peierl's-Nabarro
PSB	Persistent slip bands
PSF	Plane structure factor
QC	Quasi Continuum
QM	Quantum Mechanical
RBM	Rigid Body Movement
SND	Statistically necessary dislocations
TEM	Transmission electron microscopy

CONTENTS

LIST OF TABLES

LIST OF FIGURES

CHAPTER 1: INTRODUCTION

Market needs and increased demand for efficiency in industry have continued to place stringent demands on engineering design. The need for techniques that provide more precise engineering solutions has been driven by the demand for greater efficiency in the use of resources employed. In addition, the demand for higher performance products has given rise to the desire for high performing materials. Both the strategy to provide more precise engineering solutions and the need for high performing materials would benefit from a better understanding of material degradation phenomena under loading conditions. Beneficiaries of such techniques would include the manufacturing industry's efforts in weight reduction of machine components and the metals industry's efforts in probing studies for alloy development. The former would benefit from a more precise evaluation of component strength under loading, which would enable designers identify more precisely, areas of weight saving. The latter would benefit from low cost simulation of the performance of futuristic alloys postulated on the basis of known degradation behaviour of the materials formed from their constituent elements.

Body centered cubic (BCC) materials include iron (Fe) which is the most widely used material by volume. Dislocation studies of BCC crystal structures are not as extensive as those of face centered cubic (FCC) crystal structures. Specifically, the study of dislocation evolution in plain carbon steel (Fe-C) and its alloys would provide engineers and industry with methods that could aid efficiency in design, and possibly open new horizons in the use of these materials.

It has been demonstrated that dislocation evolution is the principle mechanism giving rise to material flow in plastically deforming metals [1]. Dislocation motion studies have demonstrated real promise in the area of material degradation studies and subsequent microstructural evaluation at the nano-scale (10^{-8} to 10^{-10} m) and micro-scale (10^{-6} to 10^{-7} m) structural levels. The fundamental benefit is that it enables mechanistic structural evaluation thereby eliminating the need to assume a particular physical mechanism for plastic flow [1].

The characterization of dislocation evolution remains an area requiring much definitive work. The behaviour of groups of dislocations has been widely investigated [2-8] with emphasis on crystal geometry. The treatment of ensemble dislocations with an emphasis on the concentrations

of dislocations may provide a vehicle in the treatment of mechanistic material behaviour. The challenge has been to document the behaviour of families of dislocations, and develop a unified theory applicable at the meso–scale (10^{-4} to 10^{-5} m) and the macro-scale ($>10^{-3}$ m). In addition, the opportunity to employ models based on an improved physical description of dislocation core structures at the smallest length scale exists.

Early multi-scale mechanistic formulations used the discrete dislocation framework [9] to generate nano-scale structure behaviour, which was in turn used to generate input data for higher length scale simulations. The complexity of the nano-scale behaviour leads to high degrees of freedom in these simulation methods and thus the techniques are limited in their application to nano-scale structures and phenomena. The development of multi-scale techniques for macro-structural analysis that would greatly enhance engineering design would require novel techniques to integrate the nano-structural computation into the macro-scale.

1.1. PROBLEM STATEMENT

Current plasticity models presume some set of phenomenological events. This approach is therefore limited to the relevance of the presumed material degradation phenomenon and reliability is achieved by the use of sensible safety factors. Engineering design and material development activities would benefit from analysis tools that are based on the physical mechanisms giving rise to material degradation, and this would lead to a greater level of confidence in design analysis, performance and failure prediction.

Current industry trends include forecasting material performance on the basis of the performance of the constituent elements. This enables researchers narrow down possible solutions to industry needs prior to undertaking empirical work. However, existing techniques have focused on the simulation of degradation phenomena dependent on point defects, excluding the deformation due to line defects due to the higher level of computational capacity required. Opportunity exists to incorporate material degradation due to line defects, and utilize the results to predict material performance. Specific focus on BCC materials are guided by the understanding that iron is the most widely used material by volume, and a good number of its alloys are of BCC structure.

Such an undertaking would require the capacity to account for actual nano-structural and microstructural evolution events in establishing critical material performance at the macro-scale level. This naturally demands the development of multi-scale techniques that up-scale events at lower length scales and transfer pertinent information to guide material evolution events at higher length scales. This study seeks to develop such a technique that systematically up-scales dislocation evolution phenomena and that leads to a macro-scale predictive model of metal plasticity.

1.2. OBJECTIVES

The overall objective of this work is to develop a multi-scale simulation technique that is founded on the dislocation core structure and its evolution and to enable a more precise simulation of plastically deforming BCC structures. The specific objectives are:

1. Develop dislocation core model based on dislocation type
2. Formulate dislocation line model founded on the dislocation core model
3. Formulate dislocation structure model founded on the dislocation line model
4. Integrate dislocation structure model into a meso scale dislocation energy model
5. Integrate meso scale model into a macro scale model
6. Correlate dislocation density with standard material testing data such as Young's Modulus (E), Yield Stress (YS) and Ultimate Tensile Strength (UTS).

1.3. OUTLINE OF WORK DONE

The principle goal of this work was to develop dislocation evolution models at several length scales, link these models and predict plasticity events at the macro length-scale. For each length-scale considered, models of the physical lattice containing dislocations were developed, and computational techniques applied to evaluate the stress field around the dislocation structures. The stress fields and the associated distortion resulting from the dislocation structures were studied and correlations established. In addition, the data generated was used as an input at the next higher length-scale resulting in a coupled simulation technique.

At the dislocation core length-scale, different types of dislocation cores were studied and variations of the stress field as the dislocation moved through the lattice were recorded and

analysed. At the dislocation line length-scale, different types of straight dislocations were introduced into the lattice and the resulting distortion and stress field was studied. At the dislocation plane length-scale, dislocation dipoles formed from the different dislocation types were introduced into the lattice and the resulting stress field analysed. At the dislocation structure length-scale, pairs of slip planes containing dislocation dipoles were introduced into the lattice and the resulting stress field analysed. At the meso-scale level of resolution, a finite element discretization was introduced with elements formed to replicate grains within the lattice. The evolution of these grains under load was accounted for by allowing for dislocation structures within the grain and at its boundary using dislocation data generated at the lower length-scales. The meso-scale model therefore formed the building block for macro-scale material simulation. The individual models were implemented in computer codes and used to simulate material behaviour at the various length scales. The proposed interaction of the models is illustrated in Figure 1.1.

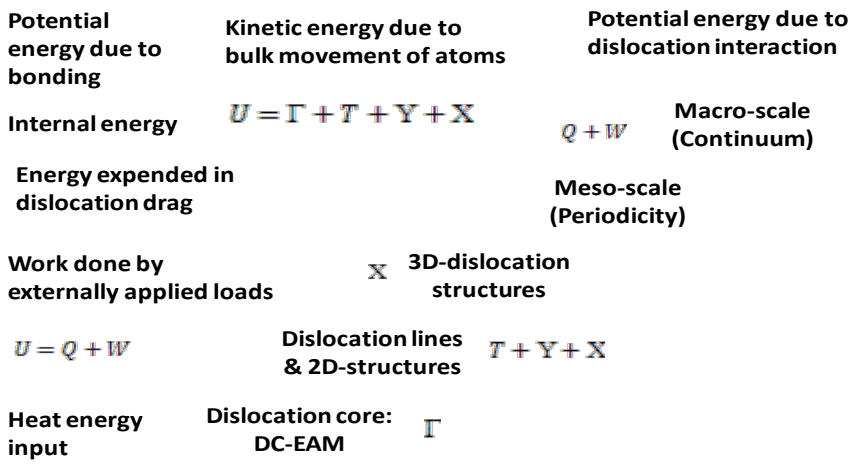

Figure 1.1: Hierarchical model

This thesis is divided into the following chapters. Chapter one outlines an outline of the problem to be addressed, the research objectives and a summary of the work done, while chapter two reviews the existing body of knowledge. Chapter three describes the method, chapter four

presents the results and discussion, and chapter five the conclusions and recommendations. Each chapter is divided into sections that relate to the five length scales illustrated in Figure 1.1.

CHAPTER 2: LITERATURE REVIEW

2.1. MULTI -SCALE MODELLING

Multi-scale material modelling is a modern technique in the field of structural mechanics that is capable of analyzing structures in at least two different length scales [10]. This method has evolved from the field of materials modelling, where it was understood that a material's response is profoundly influenced by its microstructure. The need to understand the mechanisms responsible for material behaviour, and the development of microstructure-composition-property correlations, has driven the development of theory and simulation of material behaviour. Several techniques have emerged differentiated by their treatment of the micro-scale of the problem [11-16].

Several hybrid models linking atomistic regions to continuum finite element regions have been developed. These include the "Finite Element Atomic" (FEAt) model [12], the "Material Analysis using Atomistic Dynamics" (MAAD) approach [14,16] and the "Quasi Continuum" (QC) method [15]. All these methods allow regions of fully atomistic resolution to be coupled to continuum regions. The FEAt and MAAD models require that the atomistic region be specified at the start of the computation, thereby limiting any non-linear deformation (including dislocations) to a predefined region. The QC method has the advantage of being able to adapt the atomistic region during simulation, but treats a dislocation as a fully atomistic phenomenon. Every dislocation in a QC problem requires the definition of all the atomistic degrees of freedom around the core and along the dislocation slip plane, so that the computational effort in the QC method approaches that of a fully atomistic model such as the EAM [11], once a relatively small number of dislocations has developed in the microstructure.

Opportunity exists in the advancement of current multi-scale techniques into methodologies for application in material degradation studies, structural design and manufacturing where the structure is highly heterogeneous, and where classical finite element codes with meaningful discretization can lead to very large degrees of freedom that render their use computationally prohibitive. There also exist related developments that focus on material analysis [17-23].

2.1.1. DISCRETE DISLOCATION TECHNIQUES

Several researchers contributed to the development of the discrete dislocation techniques, where a continuum finite element model was extended to include individual dislocations [3, 13]. Only their Burger's vectors, and their core locations through stress and displacement fields that they induced, were used to represent these dislocations. The discrete dislocation approach accurately described the long-range interactions between dislocations, but could not be described as a truly atomic scale method.

2.1.2. STANDARD DISCRETE DISLOCATION FORMULATION

The standard discrete dislocation formulation for the inhomogeneous problem of an elastic-plastic body containing an elastic metallurgical inclusion was derived by Van der Gissen and Needleman [24]. The inclusion was a discrete elastic particle containing a distribution of dislocations, within the overall elastic material that did not contain dislocations. This method modelled edge dislocations as line defects in an isotropic elastic material constrained to glide on a fixed slip plane. Long-range dislocation interactions occurred through their continuum elastic fields, while short-range interactions were governed by constitutive rules for dislocation nucleation, motion and annihilation. The polarization stress that corrects for the inclusion was computed at each inclusion's integration point, which required the stress field of each dislocation be evaluated at these points. This was a major limitation when applying the discrete dislocation method to elastically inhomogeneous structures. As the number of dislocations became large and/or the number of inclusions increased, the evaluation of the polarization stress dominated the finite element calculation.

2.1.3. DISCRETE DISLOCATION SUPER-POSITION FORMULATION

The superposition technique of the discrete dislocation method, developed by O'day et al. [25], resolved the problem associated with the polarization stress in the standard discrete dislocation method. In this approach, the regions of elastic inhomogeneity and the area of the metallurgical inclusion were excluded from the discrete dislocation sub-problem, which in turn was modelled with generic boundary conditions, in this case, set to zero. The only information used in this stage was the geometry of the plastic region and the displacement or traction boundary conditions applied to the boundaries between the discrete dislocation sub-problem and the full problem. The

discrete dislocation sub-problem was solved in the same manner as that used in standard discrete dislocation problems. The complementary problem modelled the entire structure and was subject to all the true boundary conditions. The regions covered by the discrete dislocation sub-problem were modelled as isotropic elastic materials. In the absence of non linear regions such as cohesive zone surfaces, the complementary problem was fully linear and the finite element equations could be solved very quickly, since the inversion or decomposition of the entire elastic stiffness matrix could be accomplished only once at the start of the calculation. Superposition was permitted since in the regions where it was used, both problems were linearly elastic as all information on plasticity was completely contained in the motion and position of the dislocations in the underlying elastic material. The discrete dislocation sub-problem contained no polarization stresses (described in Section 2.12), as it was elastically homogeneous. The technique was therefore advantageous as it could be used in elastically inhomogeneous problems with large numbers of dislocations treated as inclusions containing dislocations.

2.1.4. 3D DISCRETE DISLOCATION FORMULATION

The use of the 3-D discrete dislocation method in the study of small scale plastic phenomena was reported by Zbib et al. [26]. This 3-D continuum based finite element formulation for elastic-viscous-plasticity incorporated discrete dislocation simulation replacing the usual plasticity constitutive relations. The superposition principle was utilized in order to find the effects of boundaries on the dislocation movement, and the multi-scale frame merged the two scales of micro-scale where plasticity was determined, to the continuum scale where the energy transport was based. The method was, however, limited by the existing computational capacity and the time required for generating sufficient strain to account for plasticity. As a result, application was limited to nano-technology [26]. Opportunities exist for researchers to overcome these drawbacks and extend the technique to larger sized structures.

The 3-D discrete dislocation approach required the evaluation of the stress field due to the presence of dislocations and applied tractions, which in turn was used to evaluate the forces acting on each dislocation segment. This was then used in a backward integration scheme to evaluate the dislocation velocity, and subsequently to compute the macro-strains. The evaluation of the dislocation forces required a very fine mesh, particularly when dealing with dislocation-defect

interactions [26]. As a result, to capture the effects of small defects, it was necessary that the dislocation segment size be comparable to the size of the defect. This requirement added a further computational load to the simulation process by making it necessary to make several simulations before an appreciable macro-strain was achieved. To achieve a 0.3% strain, over one million iterations were required [26].

There exists potential for researchers to reduce the number of steps in evaluating microstructural evolution by eliminating the need to evaluate the forces on the dislocation structure and instead use the stress field in the micro/macro-structural evaluation. This would necessitate a different formulation for the governing equation for dislocation motion. In addition, a direct computation of the macro-structural variables without computing the dislocation velocity would also reduce the computational load of the simulation.

2.1.5. COUPLED APPROACHES

Coupled approaches involve the matching of boundary conditions at multiple length scales. The QC approach [15] is one such method where concurrent solution of the governing equations at multi-scales was employed. 'Handshake' algorithms were used to bridge neighbouring regions of different resolutions. Other such methods include the Three-scale Bridging technique of Broughton et al. [27] and the Dynamic Bridging Scale method of Park et al. [28]. These methods have been applied successfully in the solution of problems where the bulk material remains relatively homogeneous, and where the micro-scale is confined to a relatively small volume.

2.1.1. DECOUPLED APPROACHES

Decoupled methods do not involve direct matching of boundary conditions at multiple length scales. Instead, lower length scale simulations generate information that is used as input data in higher length scales. Atomistic simulations of motion have been used by Hao et al. [29] to generate bulk elastic and plastic properties, while Spearot et al. [30] generated interfacial properties. These methods were used where a small group of defect types were considered under periodic conditions, which enabled the micro-scale simulation to remain as small as possible.

2.1.2. INTRINSIC DISLOCATION DENSITY–FINITE ELEMENT METHOD

In previous work, a framework that incorporated the dislocation information in a continuum finite element model, under quasi-static conditions was proposed [31]. The work done in the evolution of the microstructure was modelled as the sum of the contributions of dislocation motion, dislocation formation and annihilation, dislocation interactions and work done against obstacles to dislocation motion. Integrating the microstructural evolving energy contribution over an elemental volume gave rise to the elastic and plastic dissipation at the macro-scale level. The energy balance equations were formulated in terms of the dislocation density and gave rise to a governing equation that superposed the effects of the dislocation structure by a black box technique (user need not know the internal workings of the system) onto an elastic matrix.

The dislocation information was contained in the dislocation density integral function whose value was defined on the slip plane discretized by a slip plane shape function [31]. The elastic matrix was discretized using periodic cells incorporating micro-finite elements suitable for capturing the crystal geometry of the metal. The principle of superposition implicitly used in the development was acceptable as the development of the relations governing the dislocation behaviour was based on the theory of elasticity. This method demonstrated the ability to simulate plastic yielding, but failed to demonstrate post yield strain hardening (that represents dislocation accumulation in the material) – a failure attributed to the selection of the dislocation evolution algorithm.

2.1.3. SIMULATION CELL SIZE

Dislocations form space structures, which may traverse nano-scale to meso-scale length scales. Consequently, the selection of simulation cells should ensure that effects of image dislocations generated by the boundaries do not introduce errors in the simulation results. When space is discretized, it may seem intuitive that the discrete dislocation simulation results converge towards the theoretical values when the discretization length is refined down to vanishingly small values. Not only is this untrue, but in addition, the numerical errors can be quite severe in such conditions. Gomez et al. [32] provided the following explanation for this :- the smaller the value of the reference scale for the discretization of the dislocation, the larger the number of straight segments required to describe a curved dislocation, and also the larger the number of

‘corners’ between adjacent segments. Point singularities of the stress field were associated with these ‘corners’. As a consequence, an increased number of ‘corners’ introduced spurious stress fields, that were responsible for errors in the numerical results. At the other end of the spectrum, if the discretization length was too large, the shape of a curved dislocation segment was approximated in too rough a manner, by an insufficient number of segments, and the accuracy was poor.

For the mass simulations, periodic boundary conditions (PBCs) were needed in order to ensure that dislocation fluxes were balanced at the boundaries of the primary simulation cell in order to avoid undesirable size effects due to finite dimensions and artificial dislocation losses due to image forces. Every time a portion of dislocation line crossed a boundary between 2 cells, its images emerged in all the cells at the equivalent position on the opposite boundary. A balance of fluxes was then established through all the internal interfaces of the simulated volume. However, the application of PBCs to linear objects has been known to lead to spurious self-interactions [33]. In the case of dislocations, a given portion of line could self-annihilate with one of its images after a certain number of boundary crossings. Self-annihilation could therefore reduce the mean free-path of dislocations, and this could have drastic consequences. A too short effective mean free-path affected the density of mobile dislocations and their storage rate, and hence, both the arrangement of the microstructure and the strain hardening properties [33].

Simulation cell size and its effects on dislocation density driven simulations has not been previously examined. The concept of image [34] effects does not apply in dislocation density based simulations and thus the method has its advantages. Intuitive thinking guiding this work was that modelling of dislocations as spatial scalar or vector densities could overcome the effects of prescribed boundaries and enable refined discretization, which could result in convergence of results as in typical finite element techniques.

2.2. DISLOCATION CORE LENGTH SCALE

The dislocation core length scale is suitable for tracking the interaction of atoms around the dislocation core. Deformation processes in materials involve the translation of many atoms and the simulation of this process requires statistical averaging over many atomic events. Computer

modelling of such processes [35-37] has been realized with the application of inter-atomic potentials. These enable the rapid computation of the total energies and inter-atomic forces of the atom assemblies, thus enabling the simulation of the behaviour of systems containing millions of atoms within a reasonable time frame. Examples of such applications are given by Mason, Foulkes and Sutton [38] and Malreba et al. [39]. The challenge has been in the development of potentials capturing the essential features of inter-atomic bonding and bond evolution, while maintaining computational efficiency and accuracy.

Early atomistic simulations employed pair potentials of the Morse or the Leonard Morse type [40, 41]. However, these potentials were not suited for use in the simulation of materials based on metallic bonding as they did not account for the many-body interaction between atoms. A more advanced potential developed within the EAM was proposed by Daw and Baskes [11]. This potential incorporated the many-body interactions between atoms, which are significant in atomic bonding in metals. Daw and Baskes [11] applied the density functional theory from first principles to develop a functional form for the many-body cohesive term referred to as the embedding function. Finnis and Sinclair [42] developed a similar functional form for the many-body term as a generalization of the effective medium theory [43] and the second moment approximation to the tight-binding theory [42, 44]. Ercolessi, Parrinello and Tosatti [45] proposed the glue model, which incorporated the standard two-body pair potential alongside the many-body term. This work linked the local atom coordination with the many-body term and suggested improved techniques in the fitting of the potential's coefficients. A review of the differences of these methods and their variants is given in Sections 2.2.1 and 2.2.2.

As a result of the large number of approximations involved in the development of EAM, connections with first principles are of little help in determining optimal functions for a given material. Consequently, nowadays, it is treated as a working expression with adjustable parameters fitted to empirical results and to data generated from first principle calculations [46].

EAM has been successively used in the study of the structure and resulting properties of bulk materials and materials with defects. Examples of applications of EAM in defect analysis are given in Section 2.2.3. However, the simulation of the varied dynamic-spatial atomic structure of

dislocation cores and its contribution to the behaviour of dislocations viewed on an atomic scale has not been comprehensively addressed. A potential-based method that enables the simulation of atomic scale behaviour, the modelling of dislocation evolution and the resulting contribution to material behaviour over a longer length scale than is typical of the EAM is proposed in this research.

In the development of the EAM from the density functional theory [5], two simplifications were introduced. The first was that the kinetic, exchange and correlation energies were expressed as functional terms dependent on the local electron density and its derivatives. The second was that the electron density was in turn expressed as a linear superposition of the atomic density. These assumptions presumed a nearly uniform electron cloud density, which in many metals was closely associated by the superposition of atomic densities. In an extremely defective material matrix such as one containing dislocations, these assumptions may not hold. As a result of this approximation, the energy depended only on the limited environment immediately around the embedded atom [11]. An atom therefore experienced a locally uniform electron density and with further simplification, the atom experienced the electron density sampled only at the site of the atom. However, it was noted that extreme local electron density, completely uniform electron density or uniform positive background could result in unrealistic solid properties [11]. Corrections applied involved gradients to the density, equivalent to sampling the density in a finite region around the target lattice site [47]. Wu et al. [48] attributed problems of potential transferability to the uniform background density approximation in the derivation of EAM. The authors then proposed a density correction to the EAM formalism based on earlier work by Scot and Zaremba [47] to attend to this anomaly. The simplification that the host electron density be approximated by the sum of the atomic densities [11] may have been reasonably applied to a perfect single element lattice. However, doubts arose on its applicability to imperfect lattices and those formed by more than one element. This concern was further heightened by the results from Puska et al. [49], who established that while inert elements have energies that are linear in density, chemically active elements have linear regions only at high densities with a single minimum at lower densities. The depth of this minimum was related to the strength of the bonds formed by that element.

The characterization of dislocation properties frequently go beyond the simple continuum model and involve the lattice structure at the core of the dislocation. It has been established that the effects of the dislocation core are significant in low-temperature behaviour of BCC metals [50], in the plastic anisotropic behaviour of ionic crystals [51, 52] and hexagonal close packed (HCP) metals [53], and in the dislocation climb behaviour in oxide crystals [54].

The Peierl's-Nabarro (P-N) model was the first successful model to account for the structure at the core of the dislocation [55]. A more accurate representation of the dislocation core configuration was later accomplished through lattice static and atomic models [56, 57]. Lattice static models are limited to the harmonic approximation, which is not strictly valid in the core region of the dislocation [56]. Atomic models are more suited to dealing with highly distorted lattice configurations [57]. In atomic models, the volume surrounding the core of the dislocation (region I) is modelled as consisting of atoms interacting via a given non-linear potential, while the volume surrounding region I (region II) is treated using the theory of elasticity. The power of the atomic models lies in their ability to accurately describe the dislocation core, which is dependent on the physical validity of the potentials used to describe the interaction among the atoms. A rigorous determination of the minimum energy with respect to the configuration of the dislocation core requires the use of quantum mechanical (QM) models. However, the highly distorted nature of the core severely limits the detail to which these interactions could be evaluated. The aim has been to find tractable, approximate treatments that are physically accurate over the range of distortions anticipated. The description of the core has been used to predict the physical behaviour of the dislocation in terms of motion and evolution, and to determine the strain energy and the Peierl's stress at which these physical actions take place.

Peierl's stress calculations have concentrated on the BCC metals because it was realized that their dislocation core contributed to high Peierl's stresses. It was reported that in FCC metals, Peierl's stresses were small and the dissociated dislocations widely separated, making core effects less important [58, 59]. This was not the case in BCC metals, where dissociation was localized to the dislocation core region and, in the case of the $[111]$ screw dislocation, it was non-planar [37, 60]. The BCC screw dislocation core is rather compact and this gives rise to a large Peierl's stress [60]. The extended FCC dislocation core resulted in less movement by atoms

in the core relative to their neighbours for the dislocation to move. In addition, while more atoms moved for this wider core, the highly non-linear inter-atomic interactions in the core resulted in a lower Peierl's barrier.

2.2.1. FORMS OF PAIR POTENTIALS AND EMBEDDING POTENTIALS

The inter-atomic bonding strength has been characterized using many-body potentials of the form [11, 61]:

$$E = \sum F_i[\varrho_{ij}] + \sum V_{ij}(r_{ij}) \quad \ldots\ldots (2.1)$$

where:

E is the bonding strength per atom

$F[\varrho]$ is the embedding potential

$V[r]$ is the pair potential

ϱ is the electron density

r_{ij} is the inter-atomic distance.

The functions forming the pair potential functions, the embedding potential functions and the density relations have been modelled according to analytical functions containing fitting parameters [46, 62]. The pair potential in the Columbic form, $F_{12} = k_e \frac{Z_1 Z_2}{r}$ (where Z_1, Z_2 are atomic numbers of interacting atoms in an alloy, k_e the Coulomb's constant, F_{12} is the interacting force between the two atom species), and variants that incorporate products with basis functions have mostly been adopted [46]. On the other hand, the form of the embedding function was varied dependent on the characterization of the atomic density for the application desired.

Finnis and Sinclair [42] identified the shortcomings in the use of the pair potential function on its own in the modelling of metals as the discrepancy in the calculation of the Cauchy pressure and the equity in the vacancy formation energy and the cohesive energy. These computations were in contradiction with empirical observations. To incorporate the essential band character of metallic cohesion, the authors adopted the second moment approximation to the tight binding model,

where the cohesive energy per atom varied as $\sqrt{c}$, where "c" was the atomic coordination number varying from one in a diatomic molecule to twelve in close packed crystals. Consequently, the cohesive term in the EAM, $\sum F_i$, was of the form $\sqrt{\varrho}$ so as to mimic the result of the tight binding theory [63], where the density functional ϱ was interpreted as a sum of the squares of overlapping integrals. The authors then developed relations of the bulk modulus, elastic constants, the Cauchy relation, force constants, and the surface and vacancy formation energies in terms of the pair potential and cohesive functions of the embedding potential. Adopting a parabolic form for the cohesive function and quadratic polynomial for the pair potential, and by adopting constraints to the effects of lattice coordination, the authors generated relations from which the coefficients of the potential components could be determined. This model applied well to the BCC lattice for single elements, but not for alloys.

Daw and Baskes [11] used cubic splines selected for generality to fit the embedding function and the effective charge function. The authors took reference atomic densities from the calculations of Clementi et al. [64], which were based on single determinant Hartree-Fock theory [65], that did not allow proper mixing of different electronic configurations.

Foiles, Baskes and Daw [66] noted that the pair potential, which was purely repulsive, was reasonably approximated by the geometric mean of the pair potentials of the individual species. This observation suggested that the pair interaction term for two species may be written as:

$$\emptyset_{AB} = {}^{Z_A(R).Z_B(R)}\!/_{R} \quad \ldots\ldots\ldots\ldots\ldots\ldots\ldots\ldots\ldots\ldots (2.2)$$

where:

Z_A, Z_B are the atomic numbers of atom species “A” and “B”

R is the relative interatomic distance between the atom species

In addition, the authors noted that while the optimum electronic configuration for the free atom was known, the configuration best suited for a solid was unclear [66]. This was not a serious problem for pure metals as the main effect of changing the relative ‘s’ and ‘d’ electrons was to change the electron density at the distances that are used in these calculations by a multiplicative

factor. This did not change the properties computed for a single element. For a multi-component system, changing the atomic density of one of the components strongly affected the mixing energies of the alloy. Foiles, Baskes and Daw [66] used the Hartree-Fock [65] wave function giving:

$$\rho^a(r) = n_s\rho_s(r) + n_d\rho_d(r) \quad \ldots\ldots (2.3)$$

where:

n_s, n_d	are the number of outer orbital s and d electrons
ρ_s, ρ_d	are the respective densities of the wave functions
ρ^a	is the atomic density of the multi-component system

Ercolessi, Parrinello and Tosatti [45] used sixth order polynomial forms for the pair potential, fourth order polynomial forms for the cohesive term and a cubic spline function for the atomic density to give rise to the glue Hamiltonian of the same form as the EAM functional. The potential was suitable for noble or near noble metals and was applied to the simulation of gold.

Johnson and Oh [67] used a cubic spline for the effective pair potential, which enabled matching of four equations for the physical relations involving only this potential. These were the un-relaxed vacancy formation energy, the lattice equilibrium requirement, a relation between the Voigt average shear modulus and the second order derivative of the pair potential, and a relation between the anisotropy ratio and the first and second derivatives of the pair potential. The authors also used a two-term polynomial for the embedding function and obtained relations between the embedding function, the gradient of the embedding function, and the second derivative of the embedding function in terms of physical properties. Additionally, the authors applied a power function for the atom density, which was selected for analytic convenience. This model applied to iron was stable at close packing, but could not be fitted to chromium due to the negative curvature required in the embedding energy.

Pasianot, Farkas and Savino [68] proposed a many-body inter-atomic potential applied to BCC metals, which comprised the EAM potential plus a many-body shear related term related to bond

angles. This extension of the EAM was motivated by the need to account for covalent-like bonding in transition metals. The authors applied a polynomial form of the pair interaction term and a density function based on a Thomas-Fermi screening function [69] of the exponential form.

Baskes [70] applied the modified embedded atom method (MEAM) to cubic materials and impurities. A logarithmic form [71] of the embedding energy as a function of atomic density was used as it had been previously shown to give correct coordination dependence between bond length and energy. The atomic density function took the exponential form, which was set to unity at equilibrium. This form also represented the electron density quite well for the bulk material, near vacancies and free surfaces [72].

Ackland et al. [73] developed many-body potentials for iron-iron (Fe-Fe) and copper-copper (Cu-Cu) of the same form to enable the development of a Fe-Cu cross potential from the individual element potentials. The authors took the cubic spline form for computational convenience. These potentials were applied to investigate atomic collisions in radiation damage where atom-atom interactions were described by pair-wise interactions between charged nuclei. For small separations, the pair functions for Fe-Fe, Cu-Cu and Fe-Cu were matched to the universal screened Coulomb function of Biersack and Ziegler [74].

Mendelev et al. [46] used a pair potential segmented over the interaction radius comprising a universal screened Coulomb function, an exponential function, and a cubic spline of the form proposed by Ackland et al. [73]. The density function was written as a cubic spline function and the embedding energy as a two-term polynomial. This work focused on the application of different sets of fitting target data in potential generation and the resulting potential capability.

Caro, Crowson and Caro [75] prepared potentials for the pure elements by defining a normalized density, which minimized the contribution of the embedding term to the alloy formation energy. This allowed the combination of potentials from different sources [46, 76] based on unrelated magnitudes of densities to form the cross potential. The concern arose as the embedding term always introduced a heat of formation, which was non-linear when expressed as a function of

composition. This was in contrast to ideal solutions, which presented null excess quantities and their energies were linear interpolations between the constituents. The alloy's potential terms were then adjusted, focusing on the non-linearity built upon the pair potential cross term alone. This treatment enabled the development of a potential that correctly reproduced the alloy formation energy, lattice parameter and bulk modulus for a complex alloy of any composition.

Hepburn and Ackland [77] proposed a iron-carbon (Fe-C) many-body potential comprising Fe-Fe, Fe-C and carbon-carbon (C-C) terms. The pure iron (Fe) terms were taken from an earlier developed potential [62] fitted to a wide range of defect configurations. The elemental environment for carbon in steels was irrelevant [77], hence no effort was made in modelling pure carbon. Instead, Fe-C and C-C interactions in iron were modelled. Fe-C and C-C pair potentials took the form of the universal screened Coulomb function of Biersack and Ziegler [74] connected to an empirically fitted quadratic polynomial function with a cut-off radius. The embedding function for carbon adopted a cubic spline form in between plateau regions as did the iron carbon density function. The cubic spline function was employed to ensure continuity of these piecewise functions and their derivatives.

The above review demonstrates the varied experiences of different researchers and leads to the conclusion that no definitive theory has been developed in the optimization of potential functions. Nevertheless, these complimenting observations by different researchers provide a valuable foundation for future development of potentials for multi-scale simulation work. A preference to cubic spline functions was driven largely by the continuity of functions and their derivatives between determined data points. An extensive review of potential forms has been carried out by Erkoc [78].

2.2.2. Fe-C POTENTIAL

The key motivation for the study of Fe-C systems was the need to understand metastable phases and defect interactions in this lattice. It was understood that carbon binds strongly to crystal defects such as vacancies. A number of studies [79, 80] are available on the interaction and evolution of defect structures in a Fe-C matrix. Forst et al. [81] determined the concentration of point defects and defect clusters in Fe-C alloys using first principle calculations of the formation

energies of specific defects, and a free energy formulation allowing either the carbon or iron to be out of equilibrium. The authors showed that the presence of carbon in the iron matrix could cause the vacancy concentration to increase rapidly over intrinsic vacancy concentration in iron. Lau et al. [82] developed a many-body potential that described the properties and the structure of carbon-vacancy point defects in BCC alpha-iron (α-Fe) alloyed with carbon. Of interest to the current work was their hypothesis that the dominant carbon-vacancy relation over a range of concentrations, of both the carbon and vacancies, was at most three carbon atoms associated with each vacancy. Hence, up to the point of formation of Fe_3C, non-planar structures requiring angular bonds were not expected.

One of the challenges reported in a majority of studies of Fe-C potentials was that carbon has high solvation energy, around 6 eV [81, 83], which was above the Fermi energy of iron. A second challenge was that existing potentials do not account for covalent bonding. Carbon in iron exhibits covalent type bonding to vacancies [84]. Additionally, carbon in iron is located at octahedral sites, which have much lower energy than tetrahedral sites [85]. The carbon atoms do not bond directly with one another, but prefer covalent bonding directly to two iron nearest neighbours with a bond length of 1.77 Å and no significant bonding to second nearest neighbours [77].

The potential of Becquart et al. [83] was developed by fitting to data generated by *ab initio* calculations where the six 3*d* electrons and the two 4*s* electrons for Fe are taken as valence electrons, in addition to the 2*p* and 2*s* electrons for carbon (C). The potential by Hepburn and Ackland [77] was specifically tailored to account for the large carbon solvation energy arising from unfilled *p*-like electron state in carbon and the absence of covalent bonding between octahedral-sited carbon and the two nearest neighbour iron atoms. The pair potentials Fe-C and C-C were of the same form as those given by Ackland et al. [62] fitted to spline points using polynomial interpolation functions. Additionally, Hepburn and Ackland [77] and Becquart et al. [83] ignored the C-C interactions as the concentration of C atoms was low.

Ackland et al. [62] proposed a pair potential and an embedding potential for iron to be used with phosphorous impurities. In an earlier development of this potential, Ackland et al. [73] did not

tailor the potential for defect properties, which was remedied in the later work [62]. Ackland (ibid) developed an energy potential for Fe-P comprising three pairwise potentials $\sum V_{FeFe}(r)$, $\sum V_{PP}(r)$ and $\sum V_{FeP}(r)$, three density functions $\sum \emptyset_{FeFe}(r)$, $\sum \emptyset_{PP}(r)$ and $\sum \emptyset_{FeP}(r)$, and two embedding functions $\sum F_{Fe}[\varrho]$ and $\sum F_{P}[\varrho]$. A similar approach was adopted by Becquart et al. [83] and Hepburn and Ackland [77] for a dilute Fe-C system. It was noted that the trend for modelling low concentrations of non-metallic interstitial impurities was to account for impurity-lattice interaction while treating the impurity - impurity interactions as negligible.

2.2.3. APPLICATION OF POTENTIALS IN MATERIAL DEFECT ANALYSIS

The EAM has been applied to a wide variety of problems related to material properties [11, 61]. Information on structure, dynamics, phase transitions, vibrations, diffusion and segregation has been obtained [61]. EAM was typically implemented in one of four types of calculations. These were: energy minimization, molecular dynamics (MD), Monte Carlo, and vibration-normal-mode analysis [61]. A comprehensive review of EAM application was carried out by Daw, Foiles and Baskes [61]. Analytical expressions and their derivatives used to define EAM functions were coded directly into simulation programs. However, an alternative practice was to compute each function at a large number of points and store these values in tabular form. During simulation, these values were read into the program and used to generate the coefficients of cubic spline functions, which then characterized the EAM functions. The latter method is computationally more efficient.

Initial work largely focused on development and validation of potentials. Most applications were therefore focused on demonstrating the competency of the approach. Applications to determine the surface energy, hydrogen migration, vacancy migration and fracture in metals were developed by Daw and Baskes [11], Ercolessi, Parrinello and Tosatti [45], Foiles, Daw and Baskes [66]. Daw, Foiles and Baskes [61] presented a comprehensive review for work undertaken up to 1993, in which work on bulk properties, grain boundaries, surfaces, alloy development and mechanical properties was discussed.

A greater use of *ab initio* studies as a fitting and validation tool in the development of potentials [46, 62, 83, 84, 86] was further strengthened by the fitting to material properties, some which were determined for fictitious forms of metal alloys [62]. Coupled with transmission electron microscopy, this technique enabled the establishment of a better reference plane with which many-body potentials could be developed.

Further work delved into the subject of material defect structures. Applications were developed for the study of the structure of tilt boundaries [87, 88], phonon dispersion [73, 89], linear thermal expansion [89], point defects [73, 84, 82] and lattice dynamics [73, 90]. More recent work has modelled potentials for application to industry-specific problems. Potentials for studies on the effect of phosphorous on the embrittlement of nuclear reactor pressure vessels [62], reactor pressure vessel steel thermal annealing [91], generation of phase diagrams [50, 92], and the dissolution and diffusion of hydrogen in bulk α-Fe, as well as binding of hydrogen to surfaces, vacancies and dislocations [93] were derived. There exists the opportunity to advance the development and application of potentials to model dislocation cores and dislocation families.

2.2.4. DISLOCATION CORE POLARIZATION

In contrast to the FCC-like planar splitting of dislocations used to explain observed slip phenomena [58, 59, 94], it was reported that BCC screw dislocations dissociated into more than one plane that contributed to the high Peierl's barrier and the strong temperature dependence of the yield stress [95]. Studies [35, 95, 96] revealed that this dissociation was a three-way polarization phenomenon, resulting from a symmetry-breaking dislocation core reconstruction into three equivalent $\{110\}$ planes. This polarization could occur even when no plane in the $[111]$ zone contained a stable stacking fault [35, 96]. On the other hand, non-screw dislocations in BCC lattice showed moderate spreading in the glide plane, although no planar dissociation was observed.

Polarization of the screw dislocation in BCC metals was a special case of dislocation core reconstruction, in which two segments each with a different reconstructed dislocation core appeared. The two types of dislocation cores in a reconstructed $\frac{1}{2}[111]$ screw dislocation in a

BCC lattice were denoted as AxB and BxA flips [95, 97]. The dislocation core reconstruction involved the movement of three central rows of atoms in the same direction with respect to their neighbour rows in the direction of the Burger's vector, $\boldsymbol{b}$ [95]. One variant produced a shift in one direction, while the other produced an identical shift in the opposite direction. When adjacent dislocation core segments shifted towards each other, they produced a compressive region (BxA flip), whilst when they shifted away from each other, they produced an extended region (AxB flip). If the displacement of the rows was equal to **b**/6, the maximum possible value, then the BxA flip was an interstitial-like defect, while the other gave rise to a vacancy-like defect [97].

2.3. DISLOCATION LINE LENGTH SCALE

The dislocation line length scale provides a window of resolution where the evolution of the dislocation line can be studied. Of interest are the onset of dislocation motion and the long range effects of dislocation lines on other lattice features.

The P-N model [98, 99] considered a solid divided by a slip plane into two half space linear elastic continua. The slip plane had a misfit between adjacent rows of atoms next to the partition between the half-spaces, which were connected by a non-linear potential force. The model applied linear elasticity in the two half-space elastic continua and an inter-planar potential in the region around the dislocation core. The inter-planar potential was approximated by the Frenkel sinusoidal potential.

The distorting displacements were accompanied by restoration forces due to the distorted bonds across the slip plane, $z = 0$, which resulted in local values of stress σ_{xz} at the slip plane. Any shearing of the solid at the slip plane was resisted by a periodic energy barrier corresponding to energy peaks as atoms across the slip plane by-passed each other, and energy troughs as atoms by-passed the mid-span location between consecutive atoms across the slip plane. The period of this energy barrier equalled the spacing between atoms, which equalled the Burger's vector $\boldsymbol{b}$**.** Thus, the total energy in the P-N model was summed as [100]:

$$E = E_{elastic} + E_{misfit} \quad \ldots\ldots\ldots\ldots\ldots\ldots\ldots\ldots\ldots\ldots\ldots\ldots\ldots\ldots\ldots\ldots\ldots\ldots\ldots\ldots \; (2.4)$$

where:

$E_{elastic} = \int_{R^3} \sum_{i,j=1}^{3} \frac{1}{2} \sigma_{ij} \varepsilon_{ij} \, dxdydz$: is the elastic energy in the two half-spaces

$E_{misfit} = \int_{-\infty}^{\infty} \Omega(\emptyset_x) \, dx$: is the misfit energy

$\Omega(\emptyset_x) = \frac{G\boldsymbol{b^2}}{4\pi^2 r_o}(1 - \cos\left(\frac{2\pi\emptyset_x}{\boldsymbol{b}}\right))$: is the Frenkel sinusoidal inter-planar potential

$\boldsymbol{b}$ is the Burgers vector

x is the displacement from the reference lattice point along the direction of the Burgers vector.

Peierl's and Nabarro [101] assumed that the elastic strain energy over the elastic continua did not vary as the dislocation moved and therefore the variation in the lattice potential was responsible for the changes in the misfit energy. To correctly account for the periodic variation in the misfit energy, it was necessary to account for the lattice discreteness. Peierl's and Nabarro summed the misfit energy at discrete lattice points. The initial summation was carried out per row of atoms on one side of the glide plane, and over all the rows of atoms on both surfaces resulting in what is known as the double counting scheme [100]. An alternative scheme involved the summation, as a function of de-registry between pairs of atoms, known as the bond pair summation, because the change in bond spacing was the cause in the energy variation. The elastic displacements and dislocation translations were both captured by the variable de-registry. The bond pair method did not give analytical results, except in the limiting case, while the double counting scheme resulted in incorrect maxima and minima energy barriers offset by a value of $\frac{\boldsymbol{b}}{2}$.

The P-N model received criticism in several areas as outlined below [100]. The model allowed for a blend of continuum elasticity with a potential defined at discrete points. In addition, the treatment also assumed linear elasticity at the dislocation core. The use of a sinusoidal potential resulted in the overshooting of the point of inflection in the energy displacement curve, due to the relatively short range of inter-atomic repulsive forces. The model also assumed that the dislocation core profile did not vary as the dislocation moved. Additionally, the model neglected thermal effects. Consequently, it was found that the use of the P-N model was more qualitative than quantitative.

Variants to the P-N model have since been implemented by various researchers. Forman et al. [102] used phenomenological force laws to approximate more realistic lattice potentials, which gave greater dislocation widths and lower Peierl's energies. Huntington [103] considered the role of displacements normal to the glide plane and introduced nonlinear elastic corrections for the near core region. Kuhlmann-Wilsdorf [104] considered the role of temperature. Haasen [105] incorporated non-conservative rearrangements, thus drastically departing from the P-N basic assumption that only conservative displacements occurred. Wei et al. [106] utilized the discrete Fourier transform in a generalized P-N model applied to curved dislocations in a simple cubic crystal lattice. Using the double counting scheme and the Fast Fourier Transform, Wei et al. [106] implemented a two-dimensional (2-D) potential and generalized stacking fault energy. The solution was obtained by the minimization of the potential energy that included the elastic energy, the misfit energy and a corrective term that accounted for the effects of the applied stress. Lu et al. [100] reported on the relative merits of the sampling schemes – the double counting scheme and the single counting scheme. The authors argued that the double counting scheme, which previously was seen to result in an incorrect periodicity in the energy barrier, did so due to an error in the specification of the position of the lattice points. With this corrected, the double counting scheme resulted in the correct periodicity for both the facing and alternating lattices. Butalov and Kaxiras [107] proposed a semi-discrete variational method to calculate the misfit energy, resulting in improved results in the description of narrow dislocation cores. Joos et al. [99] studied the properties of kinks using the P-N model, adapted with a generalized stacking fault potential comprising two terms of the Fourier expansion of the restoration stresses. The authors made a significant departure from the P-N formulation by determining the amplitude of the sinusoidal restoration force from the maximum value of the product of the derivative of the generalized stacking fault energy, and the Burger's vector. This provided a more physically sound criterion and the Burger's vector used was that of a perfect or partial dislocation. The Peierl's energy was modified by the addition of the dislocation line energy, which was dominantly elastic in origin. However, the contribution of the core to the dislocation line energy was not established, and the screening factor was determined rather arbitrarily.

The generalized stacking fault theory [108] postulated that the restoring stress along a stacking fault surface equalled the gradient of the surface energy resulting from the displacement causing the stacking fault surface. This stress was zero where the fault vector was zero or a whole number multiple of the lattice vector. An energy maximum existed between these two zero values. Bulatov and Kaxiras [107] in the semi-discrete variational model incorporated a discrete misfit energy term alongside the elastic energy term in the dislocation energy functional. The amplitude of the periodic variations represented the Peierl's energy, and its maximum derivative with respect to the translation represented the Peierl's stress. This model drew from the relationship between physical distortion and the energy and strain values. Additionally, it retained lattice discreteness by sampling of the misfit energy at discrete lattice points, assembled together by piecewise smooth curves whose 1^{st} and 2^{nd} order gradients with respect to the de-registry yielded the Peierl's stress and force respectively. Illustrations of basic dislocation types are shown in Figure A2.1 in appendix A.2.

2.4. PLANE LENGTH SCALE

The plane length scale provides a window of resolution for the behaviour of interacting dislocations within a slip plane. The slip plane is one of the dominant structures through which dislocation evolution takes place [34]. Even when dislocations run out of an existing slip plane, they do so through an intersecting slip plane. Consequently, the study of dislocation evolution within the slip plane provides information on the basic building block for multi-scale simulation of materials containing dislocations. Illustrations of 2 dimensional dislocation structures are shown in Figure A2.2 in appendix A.2.

Slip trace analysis has been used in many instances to directly trace the existence of slip planes. Imaging of traces may be done using optical microscopy, backscattered scanning electron microscopy, transmission electron microscopy, Laue X-ray diffraction analysis, and atomic force microscopy [109]. Work by Calliard [110, 111] on Fe at temperatures from 100K to 300K showed that while the edge dislocations may glide on {110} or {112} slip planes, screw dislocations slip on {110} planes. Generally, slip plane analysis shows that slip in BCC materials at low temperatures occurs on {110} planes transitioning at about 100K to slip on {112} planes [112].

2.4.1. DIPOLES

Early work in the study of dislocation dipoles by Neumann [113] established that the dislocation dipoles tended to be unstable under applied stress and this was used to explain evidence of slip instability such as coarse slip steps and strain bursts. Formation of bands of dislocation dipoles in Stage I deformation has been reported to be associated with forest dislocations [114] while the transition to Stage II deformation has been related to the interaction of secondary dislocations from sources near the dipoles and the dipoles [114]. Kroupa [115] proposed two key mechanisms for the formation of dislocation dipoles. In the first, dislocation dipoles form by the reorientation of sections of bypassing dislocation loops to form stable segments with oppositely oriented Burger's vectors. Kroupa also suggested that this mechanism was likely to apply to edge dislocation segments as screw dislocation segments were likely to annihilate by cross-slip [115]. Dislocation dipoles could also form in the wake of moving screw dislocations with large jogs [115]. Dislocations forming dipoles exert forces on each other, with components in their slip plane and normal to their slip plane. At low temperatures, the dipole possesses high stability as the interacting forces cancel each other at large distances [115]. In the neighbourhood of the dipole, the stress fields may combine to result in stress in the order of $\frac{G}{20}$ [115]. The relative dominance and/or interaction of dislocation dipoles and dislocation kinks need to be established.

2.4.2. KINKS

Historically, various models have been used to model kinks in screw dislocations in BCC metals [37, 110, 116]. Direct atomistic calculations of kinks were too expensive and/or inaccurate, and they produced relatively few data points for kink energy calculations. The continuum models, although approximate, provided an inexpensive alternative to atomistic calculations for general studies of the variation of kink-pair energy with stress. By matching the continuum models to suitable atomistic counterparts at selected data points, valid results could be achieved over a wider range of temperature and stress conditions.

When a straight dislocation moves in its slip plane, its energy level changes periodically indicating that an energy barrier is overcome. This energy barrier is known as the Peierl's barrier and the minimum stress required to drive the dislocation over this barrier is the Peierl's stress. In reality, a dislocation line lies in different Peierl's valleys connected by kinks, and the motion of

the dislocation is controlled by kink nucleation and migration. The energy barrier and the minimum stress necessary to move an individual kink are the second Peierl's barrier and the second Peierl's stress. Only a few attempts have been made to calculate the 2nd Peierl's stress and the 2nd Peierl's energy, within the frameworks of the P-N model. Examples are exhibited in the works of Joos et al. [99] and Sanders [117].

Early calculations by Duesbery [95] showed that nucleated kinks in BCC metals experienced very low resistance to their motion along the screw dislocation line. This was consistent with the observation of very long and geometrically straight screw dislocations [118]. Hence, the overall rate of dislocation motion seemed to be controlled by kink-pair nucleation events. Later calculations [119] confirmed that the kink motion barrier was indeed low relative to the kink-pair nucleation barrier, and the energy of a stand-alone kink [37].

Edagawa et al. [120] proposed a continuum model of kink pairs in screw dislocations, where the dislocation lattice coupling was specified as a 2-D surface perpendicular to the direction of the Burger's vector. The dislocation containing a kink pair was represented by a continuously curved line in 3-D space whose shape was obtained by the variation of the total energy consisting of the line tension energy, the Peierl's energy per unit length integrated over the entire dislocation length and the mechanical work due to the external stress causing the bowing of the dislocation line. This model correctly accounted for the non-planar core structure of screw dislocations and the kink-pair nucleation barrier in BCC metals. The linking of this continuum model with a core-based model resulted in the enhancement of the quality of results of kink simulation.

In the investigation of the motion of screw dislocations, a series of molecular dynamics simulations of a 100 **b** long screw dislocation moving in α-Fe (using the Finnis-Sinclair model [42]) was performed [121]. The simulations carried out at 400 MPa applied stress and at 300K revealed that an almost equal number of kinks nucleated on the {110} planes as on the cross-slip {110} plane inclined at 60^{o}. The dislocations were at rest for most of the time, while the kinks moved rapidly along the dislocation line. The high mobility of the kink was expected as the 2nd Peierl's stress for kinks was 20 MPa, while the Peierl's stress for the dislocation was 900 MPa [121]. The kink motion was therefore limited only by the phonon drag mechanism. For screw

dislocations, the ease of cross-slip introduced a new mechanism, the formation of a cross kink and debris loops, which significantly limited the dislocation velocity, even above the Peierl's stress. The observation of debris formation confirmed the hypothesis [121] that given the ease of cross-slip, a moving screw dislocation could contain both "glide" kink-pairs and "cross-slip" kink pairs whose collision produced non-planar defects, which have been called "cross-kinks" [122].

2.4.3. JUNCTIONS IN BCC METALS

Before two interacting dislocation segments intersect, they experience both an attractive force along their common perpendicular direction and torque forces in their slip planes [123, 124]. The torque tends to align the segments along the direction of the incipient junction and, at any stage, the actual shape of the junction is locally governed by the competing torque forces and the resisting line tension forces [125]. Some attractive dislocation states do not favour the zipping of dislocations to form junctions. If the interactive forces are weak, then they cannot overcome the line tension forces and instead the dislocations form a quadruple node at the point of crossing to form what is known as a crossed state [73]. Puschl [126] studied the energy gain from junction reactions in BCC metals using virtual displacements of triple nodes. All possible combinations of slip systems containing $\langle 111 \rangle$ Burger's vectors on $\{110\}$ and $\{112\}$ slip planes were considered, with the reaction product of the $\langle 100 \rangle$ type. Puschl established that the reaction product possessed a higher energy in BCC metals, and this resulted in smaller junction lobes and dislocation loops elongated in the screw direction.

Junctions have also been described as obstacles by which grain boundaries are pinned [127]. Junction immobility acts as a barrier to further dislocation motion until a critical local stress value is attained, which destroys the junction and enables dislocation crossing. Early investigations on the configurations of dislocation junctions were performed using elastic theory with strong simplifications [128]. More recent studies on a few junction configurations using atomistic [129, 130] and mesoscopic [131, 132] simulations confirmed that the contribution of the dislocation core regions to junction stability was negligible compared to regions outside the core.

Dislocation junction nodes have been observed to influence kink behaviour in BCC metals. Matsui and Kimura [133] suggested that the triple nodes were sources of dislocation kinks. Garratt-Reed and Taylor [134] suggested that attractive dislocations exerted torques on each other, inducing kinks, even without crossing. Both hypotheses supported the notion that dislocation junction inception contributed to enhanced dislocation mobility. Recent direct atomistic simulations [10] of the motion of a screw dislocation network have been performed for BCC metals, where 2 sets of $\frac{1}{2}<111>$ screw dislocations "zipped" to form a $<001>$ junction and a dislocation network was formed in the $\{110\}$ plane. The network was able to move conservatively in any direction in this plane, dependant on the applied stress direction and magnitude.

Kink nucleation at the nodes appeared to be the mechanism for enhanced dislocation mobility [10] with kink nucleation taking place at the trailing node of the moving junction, followed by kink motion towards the leading nodes. For such nodal enhancement of dislocation mobility to occur, a high barrier to kink-pair nucleation on a straight screw dislocation and a low kink migration barrier were required [135]. However, the formation of junctions between mixed dislocations and their contribution to dislocation motion needs investigation.

2.4.4. DISTRIBUTIONS

The theory of distributions [136] has provided mathematicians and engineers with a calculus that applies to improper functions. Examples are the Heavyside step function $H(x)$, the Dirac delta function $\delta(x)$ and their derivatives. Within the domain of distributions, these functions can be infinitely differentiated [137]. The use of distributions also enables the extension of the limits of integration of functions, normally defined within finite limits. This technique is suitable where the integration of discontinuous functions is desired [136].

There are examples of the application of the theory of distributions to the study of dislocations [138, 139]. Vinogradov and Wills [138] used the theory of distributions to characterize the spatial locations of the dislocations and hence the resulting dislocation density. The dislocation creation and annihilation were achieved by adding a source term to the distribution equation. Deng and El-Azab [139] used the theory of distributions to correlate the dynamics of dislocations

as evolving densities. The technique's suitability in the modelling of material features only characterized by discrete functions was illustrated.

2.5. NETWORK LENGTH SCALE

2.5.1. DISLOCATION STRUCTURES

There are relationships between the mechanical behaviour of metals and dislocation structures. Such structures may be highly heterogeneous and include dislocation cells, slip bands, shear bands and dislocation tangles [140, 141]. The quantitative analysis of the formation and evolution of these structures, and the contribution to work hardening remains a challenge due to the large number of dislocations encountered. Over the years, several models have been proposed dealing with dislocation patterning. The general trend has been the shift from equilibrium dynamics based models to more physically founded approaches involving non-linear dynamics [140]. Transmission electron microscopy studies of metals confirmed the existence of these 3-D patterns [142] and during deformation, two key dislocation cells were observed. The first were cell walls which were low angle boundaries that formed from statistical trapping of glide dislocations with forest dislocations [131]. The second were cell blocks which were high angle boundaries that formed from the collection of geometrically necessary dislocations arising from glide induced lattice rotations [142].

Dislocation structures may or may not exhibit a spontaneous tendency to self-organize. Patterning has been observed when the dislocation–dislocation interactions govern the average dislocation mobility, and where the average intrinsic mobility is high [127, 140]. In such cases, strain hardening and dislocation patterning depends on dislocation storage, which in turn is dependent on cross-slip [125, 140]. Consequently, dislocation pattern evolution and related strain hardening models need to incorporate the cross-slip mechanism.

Non-uniform microstructures have been observed where dislocation contact occurs [127, 140]. However, in the analysis of non-uniform microstructures, accounting for dislocation mobility and its dependence on the core structure is required. In such cases, gliding dislocations are blocked by forest dislocations and kink pairs are produced simultaneously between pinning

points. Consequently, hardening is not associated with storage, which is very small, but with the interaction of gliding dislocations on different slip systems.

Slip lines and bands form when generated dislocations migrate to and accumulate on the surface of a crystal. However, not all dislocations formed are involved in these surface structures, and some are trapped within the crystal. Some dislocations are trapped by the random interactions within the crystal and are known as statistically necessary dislocations (SND), while others result in lattice rotations and are known as geometrically necessary dislocations (GND) [7]. GND have been related to macro-scale hardening using continuum models [143, 144].

The foregoing illustrates the need for a well grounded understanding of dislocation structures and their contribution to dislocation mobility in the study of plastic deformation mechanisms. The capacity to translate these micro-structural events to the meso-scale and the macro-scale has remained a challenge worth addressing if mechanistic plasticity is to emerge at the macro-scale as a reliable technique.

2.5.2. CROSS-SLIP

Cross-slip has been reported to play a pivotal role in the organization of dislocations [125]. In addition, this mechanism has been shown to aid emergence of secondary slip systems coupled by increases in dislocation density, and counteracted by annihilation of dislocations resident on different slip planes [145]. These counteracting events are reported to cause initial softening followed by subsequent hardening [145]. Cross-slip has also been observed to stabilize dislocation tangles and govern self organization kinetics in addition to aiding 3-D dissemination of slip [127].

2.5.3. DISLOCATION JOGS

Jogs are formed when dislocations encounter dislocations in other slip planes during cross-slip. The intersection induces a step in the pair of intersecting dislocations that spans adjacent slip planes. The formation of jogs is dependent on the nature of the dislocation, the dislocation Burger's vectors, the direction of motion, and the relative orientation of the slip planes [146]. The formation of jogs is a consequence of the interaction of a dislocation with forest dislocations

and is responsible largely for strain hardening [146]. Specific properties of screw dislocations that favour the formation and motion of jogs and their interaction with kinks needs further study.

2.5.4. GRAIN BOUNDARY MIGRATION

Grain boundary migration is a pivotal mechanism in the plastic evolution of metal structures. Early models presented by Mott [147] proposed that parts of the crystal melted from one grain and solidified on the adjacent grain. The rationale behind this model – the removal of atoms from one grain to another, was adopted in similar models by Babcock and Balluffi [148], Jhan and Bristowe [149], and Schonfelder et al. [150], Zhang and Srolovitz [151]. The migration of grain boundary by dislocation glide has been applied to grain boundaries of small angles [152]. However, these studies are largely unsupported by simulation work as dynamical constraints limit the application of empirical studies at the atomic level.

Simulation studies on BCC tungsten by Zhou et al. [153] revealed that the grain boundary migration remained planar, with the softer grain advancing using collective motion of atoms, as they migrated from one grain to the adjacent, in a back-and-forth motion. This motion resulted in the migration of dislocation cores, and was consistent with the “peeling action” described in POLR model in this work. Additionally, Zhou et al. [153] established that six to nine atoms near each dislocation core, with three atoms in each of the two or three atomic planes perpendicular to the dislocation, were responsible for glide motion of a dislocation kink. Consequently, Zhou et al. [153] were able to correlate these two models.

2.6. MESO-SCALE

The design of suitable finite elements is guided by the need to maintain the highest level of accuracy in the computation. In addition, the computation must in itself be stable to consistently provide acceptable solutions. The fundamental guiding principle is the minimizing of the effects of all sources of errors.

2.6.1. MESH GENERATION TECHNIQUES

Mesh generation is a critical activity in any finite element analysis. The location of the nodes determines the shape and the types of the finite elements, and as such, the criterion for locating

the nodes is important. When the placement of the nodes is carried out manually, the process is susceptible to errors. Consequently, automatic mesh generation techniques have been developed and are reviewed by Ho-Le [155] and Lo [156]. The Delaunay triangulation [157], which maximizes the sum of the smallest angles of the triangles, has been considered as the most suitable by finite element researchers [155].

Ho-Le [155] proposed four basic classes of mesh generation techniques. These are the “Mesh topology first”, the “Nodes first”, the “Adapted mesh template” and “Mesh generation” where nodes and elements are created simultaneously. Of these methods, the “Adapted mesh template” has proven to be the most popular in existing commercial mesh generators [155]. Where the problem involves predefined internal boundaries, the “Adapted mesh template” using the “Grid based approach” [155] is suitable.

Mesh generated by automatic processes may contain elements that are not well shaped. There are several methods available to enable generation of a quality mesh [158], such as controlling the degree of discretization, the distortion of individual element shapes and the edge valence of mesh nodes. Adaptive meshing is employed to control the discretization error by increasing the number of degrees of freedom in regions with a steeper gradient in the solution variable [156]. A process of smoothing is required to improve on the mesh. Mesh smoothing [159] improves the quality by adjusting the location of nodes, and may be classified into local and global techniques [160]. The most popular technique applied is the Laplacian [161, 162] smoothing method. This method seeks to reposition the elements such that the central node is located at the centroid of the polygon forming it.

Mesh generation will often result in changes in element sizes across a region. Additionally, techniques to improve the mesh will often result in subdivision of elements. However, these processes are limited when mesh conformity is maintained [155]. When mesh non-conformity is allowed, mesh refinement, as well as transitioning from coarse to fine-mesh regions becomes easier [155]. However, techniques are required to enable handling of the mid-side nodes.

2.6.2. SERENDIPITY FINITE ELEMENTS

Serendipity elements contain additional nodes along the boundary of an element. This serves to increase the accuracy of the discretization, without increasing the number of elements defining the structure. This increase is accompanied with a penalty, the increase in the size of system matrices to be solved. Considerable work has been undertaken on the 2-D serendipity finite elements, but only limited work exists for 3-D serendipity finite elements [163].

Serendipity elements provide a subspace with C^0 continuity, which has a significantly smaller dimension than the Lagrange element family [163]. The basic approximation function is a quadratic polynomial in each axis. Higher order polynomials require the definition of the derivatives of the nodal parameters at each node. For nodal values already defined as derivatives of the principle variable, restrictions will therefore exist in the application of such Cauchy boundary conditions.

Jagota and Sethi [164] presented a systematic technique for the evaluation of the performance of a 2-D eight node finite element. Such distortion sensitivity would give poor performance where the meshing technique did not suitably compensate for structure limitations to the meshing process. The specific distortion modes considered were aspect ratio distortion, taper distortion, unevenly spaced nodes distortion and curved edge distortion. The findings were that there was no effect due to the aspect ratio, but effects were evident due to the taper distortion, unevenly spaced nodes distortion and curved edge distortion. Consequently, the authors recommended that mesh generation routines should incorporate checks for these distortions. It is expected that the 3-D finite elements are likely to exhibit the same performance.

2.6.3. SOURCES OF ERRORS IN FEM

Finite element errors occur from three sources. These are rounding or truncating errors, discretization errors and trial function/shape function errors. Rounding or truncating errors are associated with the computational procedure where the values are rounded off to chosen significant figures. This type of error may be minimized by the selection of a greater level of precision in the representation of the values in the computational framework [154]. This precision is largely hardware dependant, although software implementation may present a greater

reduction of precision. The number of significant figures in the resulting output of the computation must guide the number of significant figures of the underlying values used in the computation of the result.

Discretization errors result from geometrical differences between the boundaries of the region and its finite element approximation adopted by in the implemented mesh. Two methods are available to enhance the accuracy of the mesh. The first is to increase the degree of discretization, resulting in the improvement of the approximation of the boundaries of the structure to be modelled. The second method is to provide elements with a greater capacity to approximate the shape of the boundary of the structure to be modelled [154]. The popularity of the triangle element in 2-D finite elements is an example of this technique. The alternative is to use finite elements with boundaries capable of curvature to better model structure boundaries. This may be achieved by the use of serendipity finite elements.

Trial function/shape function errors arise from the difference between the true solution and its trial function representation. This type of error is minimized by adopting a higher order polynomial approximating function, but this in turn places additional burden in the resulting size of element [154]. The application of Cauchy boundary conditions may be used to limit this.

2.6.4. THE HALL-PETCH MODEL

The Hall-Petch relationship [165, 166] has been applied over the years in the study of the relationship between dislocation-grain boundary interaction and the yield strength. Meyers and Ashworth [167] proposed a three stage characterization of the boundary that corresponds to the three stage deformation curve of metals. This model better accounts for the contribution of the grain boundary to the associated stress strain curve. Masumura et al. [168] exposed the limitations for the Hall-Petch relationship in the area of fine grained materials and proposed a model that is a combination of the Hall-Petch relationship [165, 166] for large grains, and room temperature Coble creep [169] for fine grains.

Fu et al. [170] developed a model that was an improvement on that of Hall and Petch. In this model, a better accounting of the variation of the yield stress with grain size relation, and the

deviation of this relationship from the Hall-Petch line was explained over the nm to mm range. This relationship [170] is consistent with the empirical work of Meyers and Ainsworth [167], Mallow and Koch [171] and Abrahamson [172].

2.6.5. SUMMARY

The review above presents developments that are distinct, though whose contribution in the studies in material performance is well established. However, technological developments that impact industry are multi-faceted, and the need to link distinct research findings and generate viable industrial innovation continues to be a crucial and definitive need. This work is an effort in this direction and seeks to determine a technique that couples several material performance levels, each capable of application on its own, and provide a method based on the behaviour of the nano-scale to meso-scale material structures to predict a materials performance. This method will therefore enable a simulation of plasticity events that are based on actual nano to meso-structural degradation phenomena rather than on some presumed phenomenological mechanism. It is proposed that simulations of dislocation core evolution will be used to predict dislocation line evolution, which in turn will be used to simulate the evolution of families' of dislocation lines, which in turn will be used to predict meso-scale plasticity events. The technique is expected to complement current and future efforts in materials characterization, enhance the quality of outputs in simulation for engineering design, and provide a platform for exploratory evaluation in alloy development.

CHAPTER 3: METHODOLOGY

3.1. OVERALL APPROACH

This research set out to develop a multi-scale hierarchical model that spanned the atomic scale to the meso-scale applied to metal behaviour. The model comprises of a dislocation core model, a dislocation line model, 2-D and 3-D dislocation structure models, and a meso-scale model. The development of each sub-model is outlined below. The method employed was to use results from simulations from each length scale as an input to the simulations carried out in the immediate higher length, and therefore transfer mechanistic information all the way to the meso-scale.

3.1.1. HIERARCHICAL MODEL

The material space was discretized along five length scales, namely:

- the nano-scale accounting for short range dislocation core atomic interaction,
- the "dislocation line" length scale accounting for dislocation dynamics,
- the "dislocation plane" length scale accounting for interaction of dislocation lines within a slip plane,
- the micro-scale accounting for the interaction of slip planes containing dislocations, and
- the meso-scale applied as an assembly of dislocation structures.

The length scales were selected to take advantage of existing body of knowledge on material structure evolution, and to explore the interaction of material species at different levels of assembly. These included features of dislocation core structures in BCC materials such as the formation of dislocation flips [95, 97], compact dislocation [135, 173], dislocation line motion which occurs predominantly by kink motion [60], the high Peierl's stress opposing dislocation [174] and grain boundary [175] motions.

3.1.2. ENERGY EVOLUTION FORMULATION

Consider a phase space Ω containing a network of dislocations of mixed type. The internal energy of this system represented by the relation:

$$U = E_c + \Psi + E_m + \mathrm{X} \quad (3.1)$$

where:

U is the internal energy

E_c is the cohesive energy of the block of atoms forming the perfect lattice

Ψ is the distortional energy forming the dislocation

E_m is the kinetic energy required to move the dislocation through the lattice

X is the potential energy of the system due to dislocation interaction.

The contribution of the various energy components may be determined in its most basic form at different length scales. This is suitably illustrated by the use of the EAM to determine the cohesive energy [11], while the kinetic energy due to dislocation interaction was suitably handled using DD methods [26]. These two methods have been applied at different length scales and, as such, a hierarchical model needed to be employed.

3.1.3. DISLOCATION CORE LENGTH SCALE SUB-MODEL

At the "dislocation core" length scale, the metastable dislocation core structure was taken as the reference state and an atomic bonding energy functional was used to define the critical stress (that represented the critical bonding energy) for dislocation motion. In this research, the EAM energy functional was applied. Ultimately, the dislocation core motion was related to the bonding energy in excess of the critical bonding energy. The critical bonding energy was taken as that representing the dislocation core, at the state prior to the application of an external stress. Figure 3.1 illustrates the interacting elements of the nano-scale analysis contained in the dislocation core length scale sub-model.

The displacement profile was separately modelled as the POLR. The hypothesis postulated in this model was that the path traced by the atoms forming an evolving dislocation core was primarily along the local minimum principle stress acting on the atom. This local stress minimum was found to interchange between the two least direct stresses as postulated in the POLR hypothesis explained in Section 4.1.

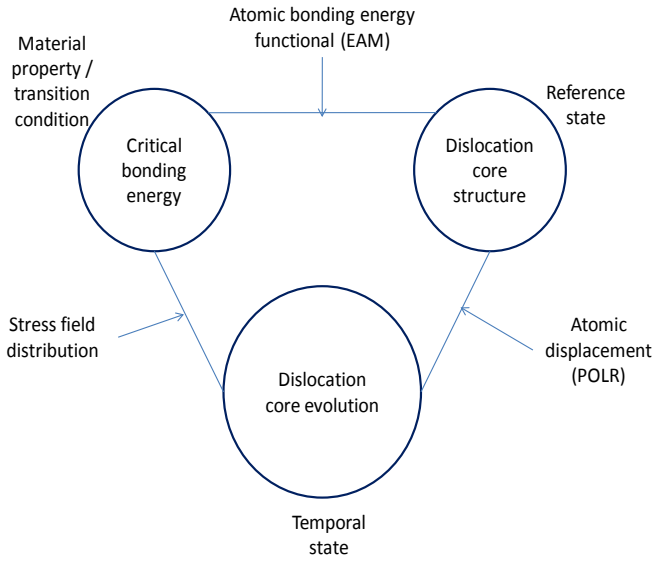

Figure 3.1: State evolution property triad for the dislocation core length scale

3.1.4. DISLOCATION LINE LENGTH SCALE SUB-MODEL

The "dislocation line" length scale was characterized by the assembly of dislocation cores to form a quasi-equilibrium line structure and was taken as the reference state. An energy functional was used to translate the effects of the dislocation core to the material remote from the dislocation core. This functional was modelled as a parametric curve based on a distortion profile, and fitted to the POLR stress and known stress values at points remote from the dislocation core. The stress field was used to relate the effects of the core on other dislocations in its vicinity, and the POLR hypothesis used to predict the initiation of dislocation motion. Figure 3.2 illustrates the interacting elements of this formulation, and embodied in the dislocation line length scale of Section 4.2.

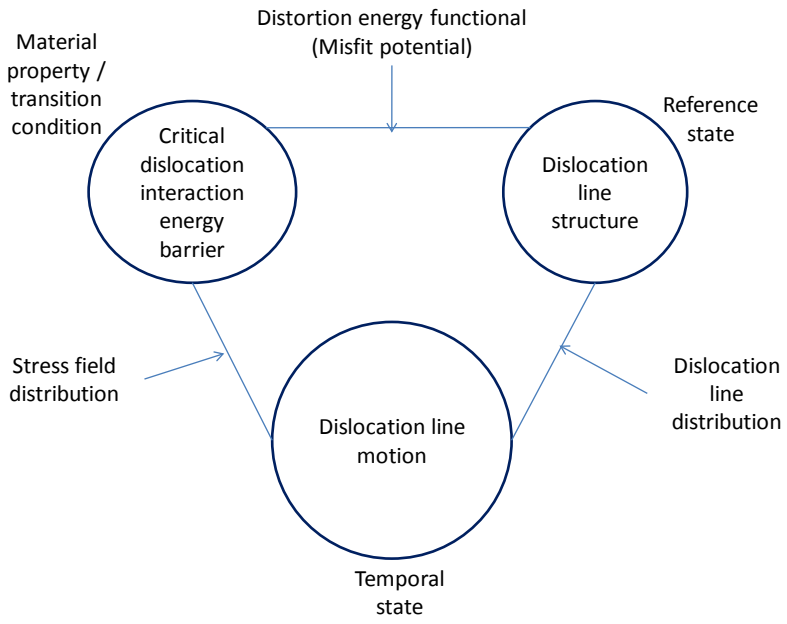

Figure 3.2: State evolution property triad for the dislocation line length scale

3.1.5. SLIP PLANE LENGTH SCALE SUB-MODEL

The 2-D dislocation structure length scale was established to account for the formation and interaction of fundamental dislocation structures. Of specific interest were dislocation kinks and junctions. The consideration of these basic forms enabled the simulation of conservative and non-conservative dislocation motion, and structures from quasi-equilibrium dislocation core forms. The 2-D numerical integration of the misfit energy functional was used to determine the stress profile of the lattice that would affect the evolution of the interacting 2-D dislocation structures. A structure factor was proposed and related to critical 2-D structures at which planar dislocation reconstruction would occur. The planar reconstruction was related to the structure factor by the stress field. This model enabled a longer range dislocation interaction, which was vital in the assessment of dislocation motion. Figure 3.3 illustrates the interacting elements of the dislocation slip plane model of Section 4.3.

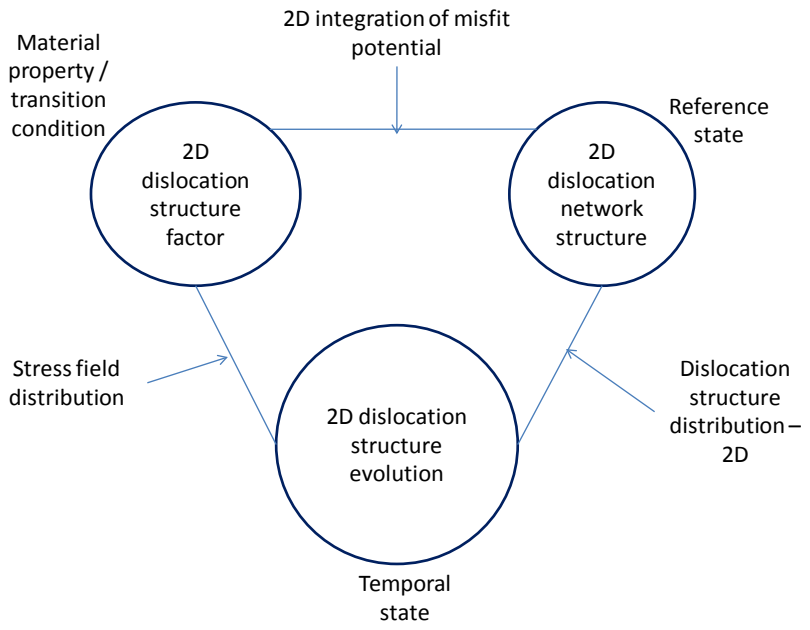

Figure 3.3: State evolution property triad for the 2-D dislocation structure length scale

3.1.6. MICRO-SCALE SUB-MODEL

The 3-D dislocation network length scale was adopted to account for the evolution of 3-D dislocation networks. The reference state was taken as an idealized network formed by a combination of slip planes containing 2-D dislocation structures and plain dislocation lines. The 3-D dislocation networks of interest were dense and sparse dislocation accumulation features. The former were likened to grain and sub-grain boundaries, while the latter were likened to geometrically and statistically necessary dislocations [143, 176] responsible for the small distortions between slip planes within a material matrix. The 3-D numerical integration of the misfit energy functional was used to determine the stress profile of the lattice that would affect the evolution of the interacting 3-D dislocation structures. A structure factor was proposed and used to define critical 3-D dislocation structures at which network reconstruction would occur. The network reconstruction was related to the structure factor by the stress field. Figure 3.4 illustrates the interacting elements in the 3-D dislocation network model.

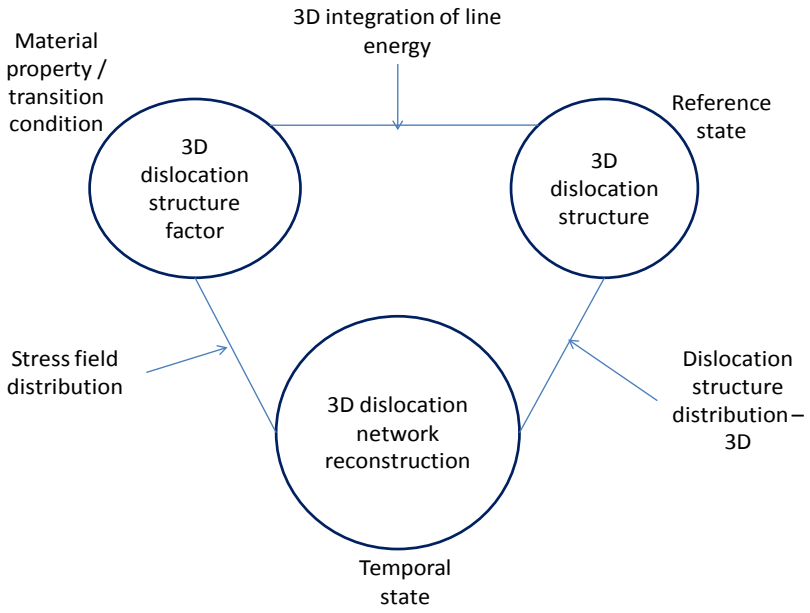

Figure 3.4: State evolution property triad for the 3-D dislocation network length scale

3.1.7. MESO-SCALE MODEL

The meso-scale model comprised an assemblage of cells containing 3-D dislocation structures. The cell size was set equal to typical grain sizes that span the range of 50μm to 200μm [168]. A variety of cells differentiated by the different systems of dislocation structures contained was employed.

The meso-scale was employed to account for the ensemble of distinct dislocation networks in a material structure element that could be incorporated in macro-scale analysis. The critical output from this length scale was a dislocation density, a material characteristic function dependent on the underlying material structure and its properties, and a stress-based energy functional that could be applied in a finite element formulation. These separate inputs were selected as they could be determined from a combination of material confirmation tests and fundamental simulation work. The dislocation density could be separately determined from transmission electron microscopy (TEM) [177] or X-ray diffraction work [178, 179], while the material characteristic function could be determined by material simulation dependant on basic inputs from TEM work.

3.1.8. GENERATING THE BCC LATTICE

In the simulation code, the BCC perfect lattice was generated by the regular arrangement of atomic base planes related to each other by a displacement vector equal to a Burger's vector between corresponding lattice sites on successive planes. The atomic base plane was in turn generated by atomic displacement between lattice points using multiples of two lattice vectors from the $\langle 111 \rangle$ family of directions within the plane. The plane lattice points were generated about a central lattice point considered as the origin to enable EAM computation of energies to the required coordination level. The resulting symmetrical lattice was altered by a variation of the lattice parameter to cater for different single element lattice arrays.

The dislocated structure was generated by the application of a set of displacement vectors to the points of a perfect lattice about the prescribed dislocation core. This was achieved by the movement of atomic half planes by a displacement equal to half a Burger's vector, generating the maximum misfit possible. In all cases, the dislocation line was retained in the direction of displacement of the base plane in the generation of the solid, which is the $\frac{1}{2}[1\bar{1}1]a_o$ direction. The displacement vectors were set to the magnitude of the Burger's vector in the prescribed direction for the defined dislocation type in the slip plane. This direction was defined as that direction that defined the Burger's vector with respect to the dislocation line, and such that this direction resulted in a whole number of lattice displacements for the defined dislocation type. This definition resulted in two pure and two mixed dislocations for the BCC lattice. These were the pure screw, the 35.26^o screw, the 70.53^o screw and the pure edge dislocations. Dislocation core flips were generated by the implementation of a set of displacement vectors to lattice points in the neighbourhood of the dislocation core using the displacement scheme provided by Duesbery and Vitek [35].

Alloy structures were generated by inserting interstitial carbon atoms or substitution metallic elements at given locations across the lattice. To achieve this, an interstitial lattice was generated and superposed over the regular BCC lattice. Additionally, a suitable algorithm enabled the specification of the element type at defined lattice point to enable substitution element specification within the Fe lattice.

Lattice defects were handled in their un-relaxed conditions as it was expected that the long range summations averaged out errors resulting from the un-relaxed state. In addition, it was noted that real lattices are not always equilibrium structures. Examples of such treatment are given by Wang et al. [180].

3.1.9. DEVELOPMENT AND TESTING OF THE SIMULATION CODE

The code was developed in the form of modules containing sub-routines that were called by several main programs. The modules were set up for a single core processor, but in a form that would enable easy migration to a multi-processor environment in the future. A Fortran PowerStation Version 4.0 compiler was used. The initial coding was carried out on a 64bit, 4Gb RAM, Intel core i5, 2.27 GHz central processing unit to complete testing. The program was then mounted on a 64bit, 16Gb RAM, 4 processor Quad core, 2.2 GHz CPU for full scale implementation. Testing of the code was carried out by selective data input for each model to verify the output.

The code functioned as a down-up multi-scale simulation where lower length scale data output was used as an input in higher length scale simulations. A compact disc containing the compiled code is attached to this thesis. Current efforts are focused on the development of a “user friendly” screen based data input to enable use by people other than the developer.

3.2. PATH OF LEAST RESISTANCE

3.2.1. COMPUTATIONAL PLATFORM

The work involved the development of simulation code based on the EAM and implemented the Fe potential developed by Mendelev et al. [46]. This potential was tested and found to stabilize the non-degenerate dislocation core sliding on {110} glide planes in agreement with experimental data for dislocation motion at low temperatures [181]. The pair potential comprised the universal screening Coulomb function of Biersack and Ziegler [74] for the nearest neighbour spacing, a series of cubic spline functions for the outer spectrum of pair-wise interactions, and an interpolation function between the nearest neighbour and outer spectrum ranges that ensured that the pair function and its first and second derivatives were continuous at the knot points bounding

this range. The cut-off radii were selected to make the second derivative of $V[r_{ij}]$ as smooth as possible. A detailed explanation of the functional form of the pair potential as shown in Equation 3.2 was developed by Ackland et al. [73]:

$$\sum_{i,j} V[r_{ij}] = \left\{\sum_{k}^{4} C_k (r_{ij} - r_k)^3\right\}_{r_k \geq r_{ij} \geq r_m} + exp\left\{\sum_{l=0}^{3} B_l {r_{ij}}^l\right\}_{r_m \geq r_{ij} \geq r_1} + \frac{Z_1 Z_2}{r_{ij}}\left\{\sum_{p=1}^{4} A_p e^{-\alpha_p r_{ij}}\right\}_{r_1 \geq r} \quad \ldots\ldots\ldots\ldots\ldots\ldots\ldots\ldots\ldots\ldots\ldots\ldots\ldots\ldots\ldots\ldots\ldots\ldots (3.2)$$

where:

$V[r_{ij}]$ is the pair potential

r_{ij} is the inter-atomic distance

$C_k,\ B_l\ \&\ A_p$ are the fitting constants

$Z_1,\ Z_2$ are the atomic number of interacting atoms

r_k is the outer cut-off radius

r_m is the intermediate cut-off radius

r_1 is the inner cut-off radius

α_p is the fitting parameter.

The embedding energy function comprised a polynomial basis function with a cubic spline basis function for the density function adopted from Mendelev et al. [46], and given as:

$$\sum_{j} F[\varrho(r_{ij})] = \sum_{n=1}^{4} a_n . \varrho^{\beta_n} \quad \ldots\ldots\ldots\ldots\ldots\ldots\ldots\ldots\ldots\ldots\ldots\ldots\ldots\ldots\ldots\ldots\ldots\ldots\ldots\ldots (3.3)$$

$$\varrho(r_{ij}) = \sum_{j} \left\{\sum_{m=1}^{3} b_m (r_m - r_{ij})\right\}_{r_m \geq r_{ij}} \quad \ldots\ldots\ldots\ldots\ldots\ldots\ldots\ldots\ldots\ldots\ldots\ldots\ldots\ldots\ldots\ldots\ldots\ldots (3.4)$$

where:

$F[\varrho]$ is the embedding potential

ϱ is the electron density

a_n , β_n & b_n are the fitting constants.

The cubic spline knots spanned the spectrum of interacting atomic radii with near regular inter-atomic distance ranges that sensibly accommodated points of interest within the range such as distances to neighbours, interstitials and defect structure elements. The popularity of the cubic spline stems from the relative ease in its computational implementation. When used, all the properties modelled are linear functions of the coefficients of the basis functions. The coefficients of the embedding function had been fitted to the lattice parameter, cohesive energy, un-relaxed vacancy formation energy and elastic constants for α-Fe at $T = 0K$. The extra terms in this function (the first term was so chosen to mimic the second-moment tight-binding bond behaviour) incorporated the kinetic energy term, accounting for smooth change between the hopping and free-electron dominated regimes [62].

The Fe-C potential adopted the Fe-Fe potential as described above and the potential by Becquart et al. [83]. This latter had been found to be suitable for modelling of a single element lattice with interstitial impurity and had been applied to the study of Fe-C solid solutions for low carbon concentrations.

3.2.2. IMPLEMENTATION OF THE EAM

The lattice was generated by the application of a set of displacement vectors to define lattice points in 3-D space. The vectors used to generate the lattice were $a_o[111]$, $a_o[\bar{1}\bar{1}1]$ and $a_o[\bar{1}1\bar{1}]$, where a_o was the magnitude of the lattice vector.

Each dislocation line was inserted at a predetermined location within the block of atoms along a predetermined dislocation line vector. The introduction of each dislocation was achieved by applying displacement vectors to specific lattice points related to the dislocation's slip plane to generate the lattice distortion.

This study sought to investigate the properties of dislocation cores in BCC Fe lattice and the effects of interstitial carbon content. The analysis involved the evaluation of the dislocation core

stress generated by atomic scale displacements. In this technique, no effort was made to attain equilibrium conditions, as these were considered unlikely in actual loading conditions. Uniform and stress driven dislocation line displacements were separately adopted. This method sought to evaluate dynamic stresses and compare them to the Peierl's stress. The evaluation of the effect of the dislocation core was achieved by the analysis of a specific point (chosen as the centre of the block of atoms). The dislocation was inserted off-set from the centre of the block of atoms and then moved across the slip plane through the centre of the block of atoms. The motion of the dislocations was achieved by the extension of the slip plane by extending the lattice distortion in a prescribed direction.

The EAM computation was conducted at the end of each displacement to determine the lattice stress tensor and the cohesive strength at a predetermined lattice point within the slip plane. No computations were conducted at points occupied by interstitial atoms though their contribution to the bonding energy was considered. However, no allowance was made for the energy contribution from vacancies. Graphs for stress tensor components using Cartesian coordinates aligned to the edges of the BCC lattice cell, versus normalized displacement with reference to the centre of the block of atoms were plotted.

The computation utilized a single scale atomic model with an extended "region I" of 1331 atoms in an "11 x 11 x 11" block of atoms to carry out the simulations. This was a variation to the traditional atomic model which used two scale atomic model [57] and the simplification adopted enhanced computational efficiency.

3.2.3. DEVELOPMENT OF THE DISLOCATION CORE EVOLUTION EQUATIONS

The total energy of a system of atoms encapsulating an isolated mobile dislocation was obtained from Equation 3.1, excluding dislocation interaction effects as:

$$U = E_c + \Psi + E_m \dots\dots\dots\dots\dots\dots (3.5)$$

where:

$$E_m = \sum_{k=1}^{n_k} E_k \ldots\ldots\ldots\ldots\ldots\ldots\ldots\ldots\ldots\ldots\ldots\ldots\ldots\ldots\ldots\ldots\ldots\ldots\ldots\ldots (3.6)$$

E_k	is the energy of motion of each atom contributing to the dislocation core
n_k	is the number of atoms contributing to the dislocation core.

The driving stress generating the dislocation's motion was defined as the 2nd order gradient of the total energy of the system. However, the cohesive energy of the perfect lattice was constant, while the distortional energy forming the dislocation varied as the dislocation core atoms moved. Consequently, under this model, the driving stress generating the dislocation's motion was defined as the 2nd order gradient of the distortional energy of the dislocation core. This energy 2nd order gradient was due to an externally applied stress and was given by the expression:

$$\sigma_{ij} = \sum_{k=1}^{n_k} \frac{\partial^2 E_k}{\partial x_i \partial x_j} \ldots\ldots\ldots\ldots\ldots\ldots\ldots\ldots\ldots\ldots\ldots\ldots\ldots\ldots\ldots\ldots\ldots\ldots (3.7)$$

where:

σ_{ij}	is the dislocation driving stress.

The work done in generating the motion of individual atoms may be given as:

$$E_k = \int_{\mathcal{g}} \boldsymbol{T_k} . \boldsymbol{\nu_k} \ldots\ldots\ldots\ldots\ldots\ldots\ldots\ldots\ldots\ldots\ldots\ldots\ldots\ldots\ldots\ldots\ldots\ldots\ldots (3.8)$$

where:

$\boldsymbol{T}_k$	is the force vector acting on each atom
$\boldsymbol{\nu}_k$	is the displacement vector of each atom, not necessarily in the same direction as the corresponding force
$\mathcal{g}$	is the piecewise function representing the path of motion.

The motion of atoms along the minimum energy path may be defined by the expression:

$$E_m = \sum_{k=1}^{n_k} \int_{\mathscr{g}} \boldsymbol{T}_k . \boldsymbol{\nu}_k \tag{3.9}$$

Defining atomic displacements dependant on the atomic ring around the dislocation core by:

$$\boldsymbol{\nu}_k = \Delta \mathscr{g}(\zeta_r, \delta_r)_k \tag{3.10}$$

where:

ζ_r is the atom ring number,

δ_r is the displacement of the lattice point in a defined direction,

and in the limit where the displacements were small:

$$E_m = \sum_{k=1}^{n_k} \int_{\mathscr{g}} \boldsymbol{T}_k . d\mathscr{g} \tag{3.11}$$

Equation 3.11 represents the sum of the energies of the moving atoms and illustrates that is possible to define a continuous function representing the minimum energy path of the atoms for each atom ring. The first order derivative of Equation 3.9 gave:

$$\frac{\partial E_m}{\partial x_i} = \sum_{k=1}^{n_k} \int_{\mathscr{g}} \left(\boldsymbol{T}_k . \frac{\partial(\boldsymbol{\nu}_k)}{\partial x_i} + \frac{\partial \boldsymbol{T}_k}{\partial x_i} . (\boldsymbol{\nu}_k) \right) \tag{3.12}$$

hence:

$$\frac{\partial E_k}{\partial x_i} = \int_{\mathscr{g}} \left(\boldsymbol{T}_k . \frac{\partial(\boldsymbol{\nu}_k)}{\partial x_i} + \frac{\partial \boldsymbol{T}_k}{\partial x_i} . (\boldsymbol{\nu}_k) \right) \tag{3.13}$$

Additionally, the stress field driving the dislocation core atom was given by:

$$\frac{\partial^2 E_k}{\partial x_i \partial x_j} = \hat{\sigma}_{ij} \ldots\ldots\ldots\ldots\ldots\ldots\ldots\ldots\ldots\ldots\ldots\ldots\ldots\ldots\ldots\ldots (3.14)$$

where:

$\hat{\sigma}_{ij}$	is the dislocation core atom driving stress.

hence:

$$\hat{\sigma}_{ij} = \int_g \boldsymbol{T}_k . \frac{\partial^2(\boldsymbol{\nu}_k)}{\partial x_i \partial x_j} + \frac{\partial \boldsymbol{T}_k}{\partial x_j} . \frac{\partial(\boldsymbol{\nu}_k)}{\partial x_i} + \frac{\partial \boldsymbol{T}_k}{\partial x_i} . \frac{\partial(\boldsymbol{\nu}_k)}{\partial x_j} + \frac{\partial^2 \boldsymbol{T}_k}{\partial x_i \partial x_j} . \boldsymbol{\nu}_k \ldots\ldots\ldots\ldots (3.15)$$

The force acting on a particular atom k was given by the expression [183]:

$$\boldsymbol{T}_k = \sum_{j \neq k} f_{kj}\left(r_{kj}\right) \frac{r_{kj}{}^{x_i}}{r_{kj}} \ldots\ldots\ldots\ldots\ldots\ldots\ldots\ldots\ldots\ldots\ldots\ldots\ldots\ldots (3.16)$$

where:

r_{kj}	is the position vector of the lattice point from some reference point,

and:

$$f_{kj}\left(r_{kj}\right) = V'_{k,j}\left(r_{kj}\right) + F'_k(\bar{\rho}).\rho'_j\left(r_{kj}\right) + F'_j(\bar{\rho}).\rho'_k\left(r_{kj}\right) \ldots\ldots\ldots\ldots\ldots\ldots\ldots (3.17)$$

where:

$V'_{k,j}\left(r_{kj}\right)$	is the first derivative of the pair potential with respect to r_{kj}
$F'_k(\bar{\rho})$	is the first derivative of the embedding function with respect to $\bar{\rho}$
$\rho'_j\left(r_{kj}\right)$	is the first derivative of the density function with respect to r_{kj}.

Expressions for the gradient and divergence of the force vector $\boldsymbol{T}_k$ were derived as [183]:

$$\frac{\partial \boldsymbol{T}_k}{\partial x_i} = \sum_{j \neq k} \left[f_{kj}\left(r_{kj}\right). \frac{\partial \left(\frac{r_{kj}{}^{x_i}}{r_{kj}}\right)}{\partial x_i} + f_{kj}{}'\left(r_{kj}\right). \frac{r_{kj}{}^{x_i}}{r_{kj}} \right] \ldots\ldots\ldots\ldots\ldots\ldots\ldots\ldots\ldots\ldots (3.18)$$

$$\frac{\partial^2 \boldsymbol{T}_k}{\partial x_i \partial x_j} = \sum_{j \neq k} \left[2.f_{kj}{}'\left(r_{kj}\right). \frac{\partial \left(\frac{r_{kj}{}^{x_i}}{r_{kj}}\right)}{\partial x_i} + f_{kj}\left(r_{kj}\right). \frac{\partial^2 \left(\frac{r_{kj}{}^{x_i}}{r_{kj}}\right)}{\partial x_i \partial x_j} + f_{kj}{}''\left(r_{kj}\right). \frac{r_{kj}{}^{x_i}}{r_{kj}} \right] \ldots\ldots\ldots (3.19)$$

where:

$$f_{kj}{}'\left(r_{kj}\right) = V''{}_{k,j}\left(r_{kj}\right) + F''{}_k(\bar{\rho}).\rho'{}_j\left(r_{kj}\right) + F'{}_k(\bar{\rho}).\rho''{}_j\left(r_{kj}\right) + F''{}_j(\bar{\rho}).\rho'{}_k\left(r_{kj}\right) + F'{}_j(\bar{\rho}).\rho''{}_k\left(r_{kj}\right) \ldots\ldots\ldots\ldots\ldots\ldots\ldots\ldots (3.20)$$

$$f_{kj}{}''\left(r_{kj}\right) = V'''{}_{k,j}\left(r_{kj}\right) + F'''{}_k(\bar{\rho}).\rho'{}_j\left(r_{kj}\right) + 2.F''{}_k(\bar{\rho}).\rho''{}_j\left(r_{kj}\right) + F'{}_k(\bar{\rho}).\rho'''{}_j\left(r_{kj}\right) + F'''{}_j(\bar{\rho}).\rho'{}_k\left(r_{kj}\right) + 2.F''{}_j(\bar{\rho}).\rho''{}_k\left(r_{kj}\right) + F'{}_j(\bar{\rho}).\rho'''{}_k\left(r_{kj}\right) \ldots\ldots\ldots (3.21)$$

Since r_{kj} and $r_{kj}{}^{x_i}$ are defined at discrete points, the partial derivatives did not exist, and Equations 3.18 and 3.19 reduced to:

$$\frac{\partial \boldsymbol{T}_k}{\partial x_i} = \sum_{j \neq k} \left[f_{kj}{}'\left(r_{kj}\right). \frac{r_{kj}{}^{x_i}}{r_{kj}} \right] \ldots\ldots\ldots\ldots\ldots\ldots\ldots\ldots\ldots\ldots\ldots\ldots (3.22)$$

$$\frac{\partial^2 \boldsymbol{T}_k}{\partial x_i \partial x_j} = \sum_{j \neq k} \left[f_{kj}{}''\left(r_{kj}\right). \frac{r_{kj}{}^{x_i}}{r_{kj}} \right] \ldots\ldots\ldots\ldots\ldots\ldots\ldots\ldots\ldots\ldots\ldots\ldots (3.23)$$

The dislocation line was visualized as a series of dislocation cores assembled together so that the atom positions with respect to the dislocation line were replicas of atom positions of a source dislocation core. Consequently, the characterization of the dislocation line and its evolution required the accounting for the location and evolution of each representative set of dislocation core atoms.

The representative set of atoms adopted in this model was defined as that set of atoms that when replicated and assembled would be sufficient to define the dislocation line. Additionally, this set would be able to capture the basic spatial structure forming around the dislocation line and enable application of the proposed simulation method. The method of choice for the simulations was simulation code based on the EAM and hence the representative set was required to include up to the 3rd nearest neighbour.

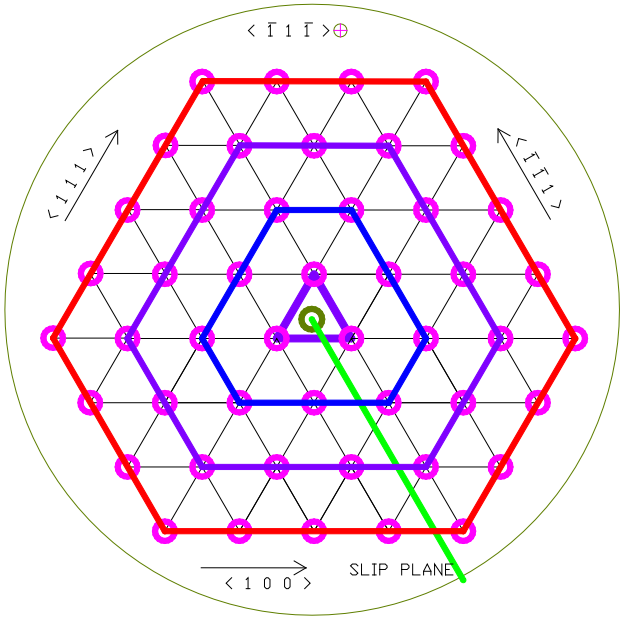

Figure 3.5: Representative set of atoms about the dislocation core

Figure 3.5 shows the lattice viewed along the $[\bar{1}1\bar{1}]$ (vector into the page) dislocation line, where the representative set of atoms was divided into four rings of atoms around the dislocation core. In addition, taking into consideration that the distortion could be modelled as affecting only one side of the slip plane, a reduced number of atoms contributing to the representative set was defined. The summary of atoms contributing to the representative set is given in Table 3.1.

The motion of the "displaced ring of atoms" was considered to be identical, differing only in the atom's position within the distortion cycle. The equations proposed are of the form given in Equation 3.24. A cubic spline function was adopted to mimic an asymptotic growth in the distortion as the dislocation moved. This motion characterized the movement of columns of

atoms in planes parallel to the slip plane, and as such was considered as the motion of the specific plane.

Table 3.1: **Atoms forming a representative set in the BCC lattice**.

Ring Number (ζ_r)	Ring Atoms	Displaced Ring Atoms
R1	3	2
R2	9	5
R3	15	8
R4	21	11
Ring Equation	$3 + 6(\zeta_r - 1)$	$3\zeta_r - 1$

$$g(x_i, c)_{\zeta_r} = \sum_{i=1}^{3} \sum_{\zeta_r=1}^{5} \left[c_{ij} . (x_i - x_o)^3 . H_i \right]_{\zeta_r} \dots \tag{3.24}$$

where:

x_o	is the reference point on the x axis
$g(x_i, c)_{\zeta_r}$	is the curve of motion of the atoms around the dislocation core
x_i	are the independent variables
H_i	is the Heaviside function, $H_i = H_i(x_i - x_o)$

The model accounted for distortions only between planes adjacent to the slip plane and resulted in $2n$ coefficients in Equation 3.24.

Applying the 1st order Taylor series expansion [184] to Equation 3.24 gave:

$$g(x_{i+1}, c)_{\zeta_r} = g(x_i, c)_{\zeta_r} + \frac{\partial g(x_i, c)_{\zeta_r}}{\partial x_1} . \Delta x_1 \dots \tag{3.25}$$

Therefore:

$$\boldsymbol{\nu}_k = \frac{\partial(\mathscr{g})}{\partial x_i}.\Delta x_i = \sum_{i,j=1}^{n} 3c_{ij}.(x_i - x_o)^2.H_i.\Delta x_i \tag{3.26}$$

$$\frac{\partial \boldsymbol{\nu}_k}{\partial x_i} = \frac{\partial^2(\mathscr{g})}{\partial {x_i}^2}.\Delta x_i = \sum_{i,j=1}^{n} 6c_{ij}.(x_i - x_o).H_i.\Delta x_i \tag{3.27}$$

$$\frac{\partial^2 \boldsymbol{\nu}_k}{\partial {x_i}^2} = \frac{\partial^3(\mathscr{g})}{\partial {x_i}^3}.\Delta x_i = 6c_{ij}.H_i.\Delta x_i \tag{3.28}$$

The mixed derivatives were simplified as:

$$\frac{\partial^2(\mathscr{g})}{\partial x_i \partial x_j} = \frac{\partial^2(\mathscr{g})}{\partial {x_i}^2};\ i = j \tag{3.29}$$

$$\frac{\partial^2(\mathscr{g})}{\partial x_i \partial x_j} = 0;\ i \neq j \tag{3.30}$$

The direction of motion was considered to take place along the valleys of the stress field curves. This coincided with the least of the principle stresses within the lattice, and was therefore consistent with the concept of the POLR.

The development of Equations 3.24 to 3.30 was limited to materials under direct forces, where the rotational forces on an atom were considered small in comparison to the direct forces acting on it. Consequently, only the direct force components and derivatives of the force tensor $\boldsymbol{T}_k$ were non-zero. Applying this constraint to terms in Equation 3.15 gave the following:

$$\frac{\partial \boldsymbol{T}_k}{\partial x_j}.\frac{\partial(\boldsymbol{\nu}_k)}{\partial x_i} = \frac{\partial \boldsymbol{T}_k}{\partial x_i}.\frac{\partial(\boldsymbol{\nu}_k)}{\partial x_j} \tag{3.31}$$

for $i = j$,

$$\frac{\partial \boldsymbol{T}_k}{\partial x_j} . \frac{\partial(\boldsymbol{\nu}_k)}{\partial x_i} = 0 \ldots\ldots\ldots\ldots\ldots\ldots\ldots\ldots\ldots\ldots\ldots\ldots (3.32)$$

for $i \neq j$,

$$\frac{\partial^2 \boldsymbol{T}_k}{\partial x_i \partial x_j} = \frac{\partial^2 \boldsymbol{T}_k}{\partial {x_i}^2} \ldots\ldots\ldots\ldots\ldots\ldots\ldots\ldots\ldots\ldots\ldots\ldots (3.33)$$

for $i = j$,

$$\frac{\partial^2 \boldsymbol{T}_k}{\partial x_i \partial x_j} = 0 \ldots\ldots\ldots\ldots\ldots\ldots\ldots\ldots\ldots\ldots\ldots\ldots (3.34)$$

for $i \neq j$.

Substituting Equation 3.34 into Equation 3.14 gave:

$$\sigma_{ij} = 0 \ldots\ldots\ldots\ldots\ldots\ldots\ldots\ldots\ldots\ldots\ldots\ldots (3.35)$$

for $i \neq j$.

$$\sigma_{ij} = \sigma_{ii} = \int_g \boldsymbol{T}_k . \frac{\partial^2(\boldsymbol{\nu}_k)}{\partial {x_i}^2} + 2. \frac{\partial \boldsymbol{T}_k}{\partial x_i} . \frac{\partial(\boldsymbol{\nu}_k)}{\partial x_i} + \frac{\partial^2 \boldsymbol{T}_k}{\partial {x_i}^2} . \boldsymbol{\nu}_k \ldots\ldots\ldots\ldots\ldots\ldots (3.36)$$

The greatest contribution to the energy evolution occurs when the direction of motion coincides with that of the lowest of the principle stresses.

The POLR was based on the hypothesis that dislocation evolution occurred along the path of least dissipation of energy. Under quasi-equilibrium conditions of loading, it was reasonable to summarize this motion in the relation:

$$\boldsymbol{T}_k.\frac{\partial(\boldsymbol{\nu}_k)}{\partial x_i} + \frac{\partial \boldsymbol{T}_k}{\partial x_i}.(\boldsymbol{\nu}_k) \approx 0 \ldots \ldots \ldots \ldots \ldots \ldots (3.37)$$

Additionally, the displacement was zero at some point ahead of the dislocation. This point was taken as the tip of the dislocation core and inscribed the value "0" on the coordinate axis.

$$\boldsymbol{\nu}_\xi = 0 \ldots \ldots \ldots \ldots \ldots \ldots (3.38)$$

for $x_i = 0$.

Finally, excluding small perturbations arising from the "peeling action" – (out of plane motion enabling the atoms to move past other atom rows) of the atoms, the displacement was parallel to the slip plane, that is:

$$\int_{n_k} \boldsymbol{\nu}_i \pm \int_{n_k} \boldsymbol{\nu}_j = 0 \ldots \ldots \ldots \ldots \ldots \ldots (3.39)$$

where:
$i \neq j$ for the $\{110\}$ slip plane over n_k consecutive cycles.

Having established the relevant stress component correlated to the motion of the dislocation core, the equation of this stress field with respect to the distance from the dislocation core was sought. The stress component values were fitted to a parametric equation with the distance to the lattice as the dependant variable. The parametric curve was partitioned into n regions with nodes at sites x_j, selected so as to optimally group sampling points along the curve. Fitting was employed to determine the coefficients c_{i*} to the curve of the stress field of a representative core atom site. The solution for c_{i*} for the $i = 1,2,3$ was obtained using a least squares minimization of the total energy.

3.2.4. IMPLEMENTATION OF SIMULATIONS

The first sets of simulations were carried out to illustrate the correlation of the POLR to the Peierl's stress. Two approaches were used to simulate the motion of the dislocation. The first method involved the "rigid body movement" (RBM) of the dislocation through the lattice. This method did not require the definition of an applied load and the results were used to reveal the behaviour to be expected when the dislocation moved independently of the cause of motion. The second method involved the movement of atoms according to the force vector acting on each atom at each simulation cycle. This method required the definition of an applied load and the results were useful in determining the effects of external loading on the "free motion of dislocation core atoms" (FMDCA). Stress cycles were calculated in each case to illustrate the profile of the POLR.

The next sets of simulations were carried out to characterize a minimal energy path of atoms as the dislocation moved through the lattice. This involved the fitting of coefficients to Equation 3.26. This visualization of the POLR was carried out to characterize the energy evolution of the moving core as a part of the total energy dissipated in the deforming lattice. The simulations were carried out under an externally applied load. The sequence of cycles was carried out as follows:

a. The node points contributing to the energy evolution of the lattice were determined.
b. The forces acting at these lattice sites along the $[100]$, $[010]$, $[001]$ directions were calculated using Equation 3.16.
c. The stress field of the resulting lattice was established using Equation 3.36. The principal stresses at the lattice sites were then calculated.
d. Using least squares minimization, coefficients of a parametric curve that characterized the principal stresses as a function of the displacement from the dislocation core, were determined. The fitting process applied the following constraints:
    - The node points were selected to ensure non-zero coefficients.
    - The maximum amplitude occurred where the first maximum resolved amplitude was attained.

- The fitting process was carried out at an external load of 0.2kN. This load was selected to adequately discretize the displacement path to reveal the pertinent behaviour.

e. The parametric curve was used to generate the principal stresses and the resulting peak displacement for the POLR for each scenario, and these were used as inputs for simulations at the next length scale.

The following parameters were varied to determine their effects on the behaviour of the dislocation.

i. Type of dislocation. Four types of dislocations were considered. These were the pure screw dislocation, the pure edge dislocation, and two types of mixed dislocations defined in Section 3.1.8.

ii. Symmetry in the screw dislocation.

iii. Effects of the presence of interstitial carbon.

3.3. MISFIT POTENTIAL

3.3.1. DISLOCATION LINE MOTION CHARACTERIZATION

A dislocation line of mixed character of length l_o is shown in Figure 3.6.

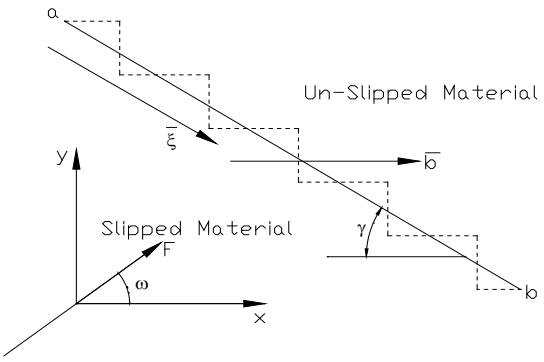

Figure 3.6: Representation of a dislocation line

In Figure 3.6, $\boldsymbol{\gamma}$ is the inclination of dislocation line direction to Burger's vector, $\boldsymbol{\xi_l}$ is the direction of dislocation line, $\boldsymbol{a, b}$ are the nodes of dislocation line, $\boldsymbol{\omega}$ is the inclination of net force on dislocation line, and $\boldsymbol{q}$ is the number of elements in the dislocation line.

The dislocation line was modelled as an alternating series of edge-screw segments, as shown by the dotted line in Figure. 3.6. Providing for q segments on this dislocation, the length of a segment may be given by:

$$\Delta l = \frac{l_o}{q} \quad \ldots\ldots (3.40)$$

Taking limits:

$$dl = \lim_{q \to \infty} \frac{l_o}{q} \quad \ldots\ldots (3.41)$$

where $l_o = sqrt[(x_b - x_a)^2 + (y_b - y_a)^2]$.

The effective screw and edge components of each segment are given by $dl.sin(\gamma)$ and $dl.cos(\gamma)$ respectively. Also:

$$\frac{\boldsymbol{b}x\bar{n}}{|\boldsymbol{b}|}.\xi = \sin\gamma \quad \ldots\ldots (3.42)$$

$$\frac{\boldsymbol{b}.\xi}{|\boldsymbol{b}|} = \cos\gamma \quad \ldots\ldots (3.43)$$

where

$\bar{n}$ Slip plane normal.

The geometry considered was generalized by allowing the dislocation line to bow out under the action of external forces, to give an arbitrary curved dislocation loop. In this case, the angle γ varied along the loop and with time, hence $\gamma = \gamma(x, t)$. Taking an arbitrary initial position, the initial length of the k^{th} segment was given by:

$$dl^o{}_k = \frac{dl}{|\boldsymbol{b}|}\{(\boldsymbol{b}.\xi).\bar{e} + (\boldsymbol{b}x\bar{n}).\xi.\bar{s}\} \quad (3.44)$$

where:

$\bar{e}$ Unit vector in the direction of the pure edge dislocation

$\bar{s}$ Unit vector in the direction of the pure screw dislocation.

If this dislocation segment moves at a velocity v_k, the length of the dislocation segment after m time steps is:

$$dl^m{}_k = dl^o{}_k + v_k.m.\Delta t \quad (3.45)$$

Taking limits and writing the dislocation velocity as a gradient of the displacement gives:

$$dl^m{}_k = dl^o{}_k + \lim_{\Delta t \to 0} \sum_{1}^{m} \left(\frac{\partial x}{\partial t}\right) \Delta t \quad (3.46)$$

hence:

$$dl^m{}_k = dl^o{}_k + \int_0^{t_m} \left(\frac{\partial x}{\partial t}\right) dt \quad (3.47)$$

The kink motion contributes to growth of the dislocation as follows: the growth of the screw component occurs due to motion of the edge component and vice versa. Hence, the length of the k^{th} segment after t_m is given by:

$$dl^m{}_k = \frac{dl}{|\boldsymbol{b}|}\{(\boldsymbol{b}.\xi).\bar{e} + (\boldsymbol{b}x\bar{n}).\xi.\bar{s}\} + \int_0^{t_m} \left(\frac{\partial x}{\partial t}.\bar{e} + \frac{\partial x}{\partial t}.\bar{s}\right) dt \quad (3.48)$$

where:

$$\frac{\partial x}{\partial t}.\bar{e} = \frac{\partial}{\partial t}\left\{\frac{dl}{|\boldsymbol{b}|}.\boldsymbol{b}\right\} \quad (3.49)$$

$$\frac{\partial x}{\partial t}.\bar{s} = -\frac{\partial}{\partial t}\left\{\frac{dl}{|\boldsymbol{b}|}.(\boldsymbol{b}x\bar{n})\right\} \quad \ldots (3.50)$$

This characterization of the dislocation segment provides a vectorial representation of an arbitrary curved dislocation segment of mixed type, and its temporal variation.

3.3.2. DEVELOPMENT OF THE MISFIT POTENTIAL

In the proposed model, a misfit potential was introduced to account for lattice distortion. This characterization of the distortion differed from that presented by Peierl's and Nabarro [98, 99] as it sought to model the distortion over a longer length scale independent of the distortion across the slip plane. The distortion was modelled as a decaying function with maximum distortion at lattice points adjacent to the dislocation core. Additionally, the distortional effects of different core sites, summed at a lattice point resulted in the net distortion at that lattice site. The proposed model characterized this distortion (for an arbitrarily curved dislocation as illustrated in Figure 3.7), using a function dependant on in-plane coordinates r and θ_s and an out-of-plane coordinate z_s, of the form:

$$\delta = D(x, \theta_s, z_s, \varphi) \quad \ldots (3.51)$$

where:

D is the function of the distortion variation

x is the distance measured from the dislocation core site along the edge component Burger's vector of the dislocation line, in the slip plane, to the lattice point under consideration

θ_s is the angular coordinate of the dislocation core site measured from the line normal to the dislocation line direction, to the lattice point under consideration

φ is the angle representing the location between lattice sites in a perfect material

z_s is the distance measured from the dislocation core site along the normal to the slip plane, to the lattice point under consideration.

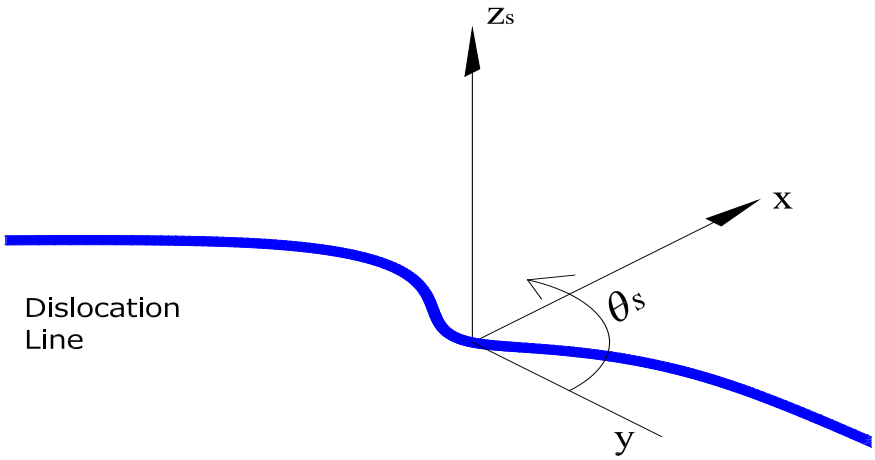

Figure 3.7: **Coordinate set for spatial mapping of the dislocation line**

In the proposed model, the distortional effect of each dislocation core site was similarly characterized using a partition function of the form:

$$D(x, \theta_s, z_s, \varphi) = A(x, z_s, \varphi). B(\theta_s) \quad \ldots \ldots \ldots \ldots (3.52)$$

where:

$A(x, z, \varphi)$	is the distortion variation in the plane normal to the dislocation line direction. This accounts for both in-plane and out-of-plane distances
$B(\theta_s)$	is the distortion variation due to curvature of the dislocation line.

The forms in Equations 3.51 and 3.52 were selected to allow for the characterization of a family of possible slip planes defined by the dislocation line and a possible set of Burger's vectors.

An exponential distortion function with distance from the dislocation core site as the independent variable was adopted. Additionally, the in-plane radial variation of the distortion amplitude was postulated as a sinusoidal function (to mimic the sinusoidal de-registry as postulated in the P-N model [101], with maximum distortion amplitude directly ahead of the dislocation core site, and minimum along the dislocation line. The functions of the amplitudes were of the following forms:

$$A(x,z,\varphi) = \delta_1 . e^{-\alpha_p x} . sin(\varphi/\boldsymbol{b}_1) + \delta_{\boldsymbol{2}} . e^{-\beta_p z} \quad (3.53)$$

$$B(\theta) = \delta_{\boldsymbol{3}} . cos(\theta) \quad (3.54)$$

where:

α_p, β_p	are the fitting parameters
δ_p	is the unit distortion vectors (subscript 1,2,3) in the x, z and y directions
$\boldsymbol{b}_1$	is the Burger's vector corresponding to distortion vector in the x direction
θ	is the angle of curvature of the dislocation segment at the point on the dislocation line considered.

Amalgamating these equations into one yielded a partition function for the distortion due to each core site of the form:

$$D(x,z,\theta,\varphi) = \delta_{\boldsymbol{1}} . e^{-\alpha_p x} . sin(\varphi/\boldsymbol{b}_1) + \delta_{\boldsymbol{2}} . \left(e^{-\beta_1 z} - e^{-\beta_2 z}\right) + \delta_{\boldsymbol{3}} . cos(\theta) \quad (3.55)$$

On translation of the coordinate axes, δ_1 represented the distortion along the edge dislocation Burger's vector, $\delta_{\boldsymbol{3}}$ represented the distortion along the screw dislocation Burger's vector, while $\delta_{\boldsymbol{2}}$ represented the distortion along the out-of-plane Burger's vector**.** Equation 3.55 can be re-written as:

$$D(x,z,\theta,\varphi) = \delta_{\boldsymbol{e}} . e^{-\alpha_p x} . sin(\varphi/\boldsymbol{b}_e) + \delta_{\boldsymbol{n}} . \left(e^{-\beta_1 z} - e^{-\beta_2 z}\right) + \delta_{\boldsymbol{s}} . cos(\theta) \quad (3.56)$$

where:

β_p	is the fitting parameter
$\delta_{\boldsymbol{n}}, \delta_{\boldsymbol{e}}, \delta_{\boldsymbol{s}}$	are the unit normal, edge and screw distortions along the Burger's vector
$\boldsymbol{b}_e$	is the Burger's vector corresponding to distortion vector in the *x* direction.

Equation 3.56 can be modified to account for distortion effects behind the moving dislocation and to provide for symmetrical distortion about the slip plane (in the ± z direction) as follows:

$$D(x,z,\theta,\varphi) = \left(\delta_{\boldsymbol{e}}.\, e^{-\alpha_p x}.\, sin(\varphi/\boldsymbol{b}_e).\, \mathrm{H}(x - x_o)\right) + \left(\delta_{\boldsymbol{n}}.\left(e^{-\beta_1 z} - e^{-\beta_2 z}\right).\, \mathrm{H}(z - 0)\right)$$
$$+\, \delta_{\boldsymbol{s}}.\, cos(\theta) \ldots\ldots (3.57)$$

The interaction effects arising from a family of dislocation sites on a lattice point (x, z) gave:

$$\overline{D}(x,z,\theta,\varphi) = \sum_{i}^{n_c} \left(\delta_{\boldsymbol{e}}.\, e^{-\alpha_p x}.\, sin(\varphi/\boldsymbol{b}_e).\, \mathrm{H}(x - x_o)\right) + \left(\delta_{\boldsymbol{n}}.\left(e^{-\beta_1 z} - e^{-\beta_2 z}\right).\, \mathrm{H}(z - z_o)\right)$$
$$+\, \delta_{\boldsymbol{s}}.\, cos(\theta) \ldots\ldots (3.58)$$

where:

n_c	is the number of dislocation core sites considered
x_o	is the reference point on the *x* axis
z_o	is the reference point on the *z* axis.

The following boundary conditions were applied:

For the pure screw dislocation,

$$\delta_{\boldsymbol{e}} = \boldsymbol{0} \ldots\ldots (3.59a)$$

For the pure edge dislocation,

$$\delta_{\boldsymbol{s}} = \boldsymbol{0} \ldots\ldots (3.59b)$$

$$\text{at } x = \lambda \boldsymbol{b}_e, \overline{D} = 0 \ldots\ldots (3.59c)$$
$$\text{at } z = \lambda \boldsymbol{b}_n, \overline{D} = 0 \ldots\ldots (3.59d)$$
$$\text{at } x = 0.5 * \boldsymbol{b}_e, \overline{D} = \overline{D}(x)_{max} \ldots\ldots (3.59e)$$
$$\text{at } z = -0.5 * \boldsymbol{b}_n, \overline{D} = \overline{D}(z)_{max} \ldots\ldots (3.59f)$$
$$\overline{D}(x)_{max} = F(POLR) \ldots\ldots (3.59g)$$
$$\overline{D}(z)_{max} = G(POLR) \ldots\ldots (3.59h)$$

where:

λ is the no. of Burger's vector intervals to the location where dislocation core's stress field is negligible,

$\boldsymbol{b_n}$ is the Burger's vector corresponding to distortion vector in the z direction.

The model defined in Equation 3.58 evaluated the distortion in a set of 2-D spaces comprising the normal planes to the dislocation direction, defined by the set of Burger's vectors $\boldsymbol{b_e}$ *and* $\boldsymbol{b_n}$**.** Together, these 2-D spaces defined the active components of the 3-D lattice space, and as such, were sufficient to characterize the slip behaviour of the lattice. The distortion was used to determine the coordinates of the lattice site at a distance r from the dislocation core using Equation 3.60:

$$r_k = r_o + \delta \quad (3.60)$$

where:

r_k is $(x^2 + z^2)^{1/2}$

r_o is the distance to the lattice site in a perfect lattice.

Equation 3.60 relates the lattice distortion and the position of a lattice site. The cohesive energy at a lattice site has traditionally been calculated using the EAM and the position of the lattice site. Consequently, in the proposed model, the energy change due to the distortion with respect to the cohesive energy of the perfect lattice is given by the functional:

$$\Psi[\delta] = E_c - \mathrm{F}[\rho(\delta)] + V(\delta) \quad (3.61)$$

where:

$\Psi[\delta]$ is the misfit potential energy

F is the embedding energy

V is the pair potential energy.

The misfit core potential pre-supposes that dislocation core effects are variable in 3-D spaces. Some observations can be made about this functional form. The first is that the distortion due to a dislocation core along the dislocation line varies only due to line curvature. The significance of this is that dislocation tension becomes a function of the screw Burger's vector and the line curvature. The second is that the loss in cohesive strength is intrinsically accounted for by the increased inter-atomic separation resulting from the distortion.

$\Psi[\delta]$ is a discrete function with a physical sense only at discrete lattice positions. In this form, the unknowns are the fitting parameters α_i and β_i (Equation 3.57) for each dislocation core. The fitting of the model therefore focused on the definition of these coefficients. Applying physical boundary conditions for each dislocation line type, the coefficients were determined. The development for each type of dislocation line is detailed in Sections 3.3 to 3.6. The resulting misfit energy is required to model the Peierl's stress and the dislocation interaction in the neighbourhood of the dislocation core.

The first derivative of the misfit potential energy with respect to distortion yielded the force associated with the dislocation configuration and is given in Equation 3.62:

$$\mathrm{F_k} = \frac{\mathrm{d}\Psi}{\mathrm{d}\delta} = \frac{\partial\Psi}{\partial \mathrm{x}} + \frac{\partial\Psi}{\partial z} \quad (3.62)$$

where:

$\mathrm{F_k}$ is the force at radius r_k from the dislocation core.

The second derivative of the misfit potential energy yielded the stress due to the dislocation core and was given by:

$$\sigma_\mathrm{k} = \frac{\partial^2\Psi}{\partial x^2} + \frac{\partial^2\Psi}{\partial z^2} \quad (3.63)$$

The Peierl's stress was extracted from Equation 3.63 as the maximum stress configuration in the neighbourhood of the dislocation core as provided in Equation 3.64:

$$\sigma_{k_{max}} = 0 \ldots\ldots\ldots\ldots\ldots\ldots\ldots\ldots\ldots\ldots (3.64)$$

where $\frac{d\sigma_k}{d\delta}_{r\to 0} = 0.$

Dislocation generated stresses give rise to imbalanced forces on any cell boundary. To balance these forces, imaginary dislocations located outside the cell boundaries may be introduced. Image forces present an implementation challenge in the simulation scheme, as a parallel computation path is required for each cell analysed, to compute image forces and place them into adjacent cells. In this work, the choice of boundary conditions provided for an alternative scheme where the simulation cell selected was large enough so that boundary stresses were negligible compared with the other stresses in the lattice. This therefore negated the need to compute the image forces.

3.3.3. FITTING TO A STRAIGHT DISLOCATION LINE

To demonstrate the application of this model, an infinitely long single dislocation line was considered. For a straight dislocation, $cos(\gamma) = 1$, and this reduced Equation 3.58 to:

$$\bar{D}(x,z,\varphi) = \sum_{i}^{n_c} \left(\delta_{\boldsymbol{e}}.\, e^{-\alpha_p x}.\, sin(\varphi/\boldsymbol{b}_e).\, \mathrm{H}(0-x)\right) + \left(\delta_{\boldsymbol{n}}.\left(e^{-\beta_1 z} - e^{-\beta_2 z}\right).\, \mathrm{H}(x-0)\right) + \delta_{\boldsymbol{s}} \ldots\ldots\ldots\ldots\ldots\ldots\ldots (3.65)$$

where:
$\varphi = \pi x.$

The constraints set out in Equations 3.59a to 3.59g were applied to Equation 3.65 for a straight screw dislocation, and yielded:

$$\delta_{\boldsymbol{s}} = -\delta_{\boldsymbol{n}}.\left(e^{-\beta_1.\lambda \boldsymbol{b}_n} - e^{-\beta_2.\lambda \boldsymbol{b}_n}\right) \ldots\ldots\ldots\ldots\ldots\ldots\ldots\ldots (3.66)$$

$$\bar{D}(z,\lambda) = \delta_{\boldsymbol{n}} \sum_{i}^{n_c} \left(e^{-\beta_1 z} - e^{-\beta_2 z}\right) - \left(e^{-\beta_1.\lambda \boldsymbol{b}_n} - e^{-\beta_2.\lambda \boldsymbol{b}_n}\right) \ldots\ldots\ldots\ldots\ldots\ldots (3.67)$$

$$\overline{D}_{s-max} = \delta_{\boldsymbol{n}} \sum\nolimits_{i}^{n_c} \left(e^{0.5\beta_1 \boldsymbol{b}_n} - e^{0.5\beta_2 \boldsymbol{b}_n}\right) - \left(e^{-\beta_1.\lambda \boldsymbol{b}_n} - e^{-\beta_2.\lambda \boldsymbol{b}_n}\right) \ldots\ldots\ldots\ldots\ldots (3.68)$$

$$\overline{D}(z,\lambda) = \overline{D}_{s-max} \cdot \sum\nolimits_{i}^{n_c} \frac{\left[\left(e^{-\beta_1 z} - e^{-\beta_2 z}\right) - \left(e^{-\beta_1.\lambda \boldsymbol{b}_n} - e^{-\beta_2.\lambda \boldsymbol{b}_n}\right)\right]}{B} \ldots\ldots\ldots\ldots (3.69)$$

where:

$B = \left[\left(e^{0.5\beta_1 \boldsymbol{b}_n} - e^{0.5\beta_2 \boldsymbol{b}_n}\right) - \left(e^{-\beta_1.\lambda \boldsymbol{b}_n} - e^{-\beta_2.\lambda \boldsymbol{b}_n}\right)\right]$

λ	is the number of Burger’s vector intervals to location where dislocation core’s stress field is negligible
$\overline{D}_{s-max}$	is the maximum distortion in the direction of the screw dislocation Burger’s vector.

Equation 3.69 was reorganized to give:

$$\overline{D}(z, \mathrm{X_s}, \Omega) = \mathrm{X_s} + \Omega_{\mathrm{s}}. \sum\nolimits_{i}^{n_c} \left(e^{-\beta_1 z} - e^{-\beta_2 z}\right) \ldots\ldots\ldots\ldots\ldots\ldots (3.70)$$

where:

$$\Omega_{\mathrm{s}} = \frac{\overline{D}_{s-max}}{B} \ldots\ldots\ldots\ldots\ldots\ldots\ldots\ldots (3.71)$$

and:

$$\mathrm{X_s} = -\Omega_{\mathrm{s}}. n. \left(e^{-\beta_1.\lambda \boldsymbol{b}_n} - e^{-\beta_2.\lambda \boldsymbol{b}_n}\right) \ldots\ldots\ldots\ldots\ldots\ldots (3.72)$$

Equation 3.70 is composed of a sum of simple decaying functions from a preset maximum at the core. As a first approximation, the distances between the core sites contributing to the dislocation line were taken as diminishingly small and the summation was replaced as an integral over the length of the dislocation segment. Consequently,

$$\overline{D}(z, \mathrm{X_s}, \Omega) = \mathrm{X_s} + \Omega_{\mathrm{s}}. \int_0^S \left(e^{-\beta_1 z} - e^{-\beta_2 z}\right) ds \ldots\ldots\ldots\ldots\ldots\ldots (3.73)$$

where

S is the length of dislocation line segment given by $n_c.\boldsymbol{b}_s$.

Integration of Equation 3.73 yielded:

$$\overline{D}(z, \mathrm{X_s}, \Omega) = \mathrm{X_s} + \Omega_\mathrm{s}.S.\left(e^{-\beta_1 z} - e^{-\beta_2 z}\right) \ldots\ldots(3.74)$$

It is observed that the screw dislocation processes a single degree of symmetry about a plane intersecting the dislocation line and containing a plane of close coupled atoms. Consequently, lattice points at distances measured from this plane parallel to the dislocation line experience the same distortion both in magnitude and direction.

Defining X, Y and Z as vectors along close coupled directions used to generate the lattice points for the BCC structure analyzed, the lattice sites may then be defined by the relation:

$$L_{i,j,k}(a,b,c) = \mathrm{a.X} + b.Y + c.Z \ldots\ldots(3.75)$$

For Equation 3.75 to hold:

$$L_{i,j,k}(a,b,c) = L_{i,j,k}(a,b,-c) \ldots\ldots(3.76)$$

Consequently:

$$c = 0 \ldots\ldots(3.77)$$

This constraint effectively limited the contribution of the dislocation core to lattice sites with the plane containing the dislocation core and $n_c = 1$.

By determining the value of the maximum distortion, $\overline{D}_{s-max}$, the distortion at some selected set of displacements from the core, $\overline{D}_i$, and selecting an appropriate value of "n_c", the distortion at any point within the lattice resulting from the screw dislocation core was determined. It was presumed that the material that had not received any distortion was not appreciably influenced by the dislocation core and hence the misfit potential was not applied to this region.

Applying the same set of constraints for a straight edge dislocation, and replicating the development in Equations 3.66 to 3.76 yielded the following:

$$\overline{D}(x,z,\varphi) = \sum_i^{n_c} \left(\delta_{\boldsymbol{e}}.\, e^{-\alpha_p x} sin(\varphi/\boldsymbol{b}_e)\mathrm{H}(0-x)\right) + \left(\delta_{\boldsymbol{n}}\left(e^{-\beta_1 z} - e^{-\beta_2 z}\right)\mathrm{H}(x-0)\right) \ldots (3.78)$$

$$-\delta_{\boldsymbol{n}} = \frac{\delta_{\boldsymbol{e}}.\, sin(\varphi/\boldsymbol{b}_e).\, e^{-\lambda.\alpha_p.\boldsymbol{b}_e}}{\left(e^{-\lambda\beta_1 \boldsymbol{b}_n} - e^{-\lambda\beta_2 \boldsymbol{b}_n}\right)} \ldots\ldots\ldots\ldots\ldots\ldots\ldots\ldots\ldots\ldots\ldots\ldots\ldots\ldots\ldots\ldots\ldots\ldots\ldots\ldots\ldots\ldots\ldots\ldots (3.79)$$

Substituting for $\delta_{\boldsymbol{n}}$ using Equation 3.79 yielded:

$$\overline{D}(x,z,\varphi) = \sum_i^{n_c} \delta_{\boldsymbol{e}}.\, sin(\pi x/\boldsymbol{b}_e).\, \frac{\left(e^{-\alpha_p x} - e^{-\lambda.\alpha_p.\boldsymbol{b}_e}.\left(e^{-\beta_1 z} - e^{-\beta_2 z}\right)\right)}{\left(e^{-\lambda\beta_1 \boldsymbol{b}_n} - e^{-\lambda\beta_2 \boldsymbol{b}_n}\right)} \ldots\ldots\ldots\ldots\ldots (3.80)$$

$$\overline{D}_{e-max} = \sum_i^{n_c} \delta_{\boldsymbol{e}}.\, sin(0.5\pi).\, \frac{\left(e^{-0.5\alpha_p \boldsymbol{b}_e} - e^{-\lambda\alpha_p \boldsymbol{b}_e}.FC\right)}{\left(e^{-\lambda\beta_1 \boldsymbol{b}_n} - e^{-\lambda\beta_2 \boldsymbol{b}_n}\right)} \ldots\ldots\ldots\ldots\ldots\ldots\ldots\ldots\ldots\ldots\ldots\ldots (3.81)$$

$$\overline{D}(x,z) = \overline{D}_{e-max} \cdot \frac{sin(\pi x/\boldsymbol{b}_e)}{sin(0.5\pi)} \sum_i^{n_c} \frac{\left[e^{-\alpha_p x} - e^{-\lambda\alpha_p \boldsymbol{b}_e}.\left(e^{-\beta_1 z} - e^{-\beta_2 z}\right)\right]}{DC} \ldots\ldots\ldots\ldots\ldots\ldots (3.82)$$

where:

$DC = e^{-0.5\alpha_p \boldsymbol{b}_e} - e^{-\lambda.\alpha_p \boldsymbol{b}_e}.FC$

$FC = e^{0.5\beta_1 \boldsymbol{b}_n} - e^{0.5\beta_2 \boldsymbol{b}_n}$

$\overline{D}_{e-max}$ is the maximum distortion in the direction of the edge dislocation Burger's vector.

Equation 3.82 may be re-written as:

$$\overline{D}(x,z,\Omega) = \Omega_{\mathrm{e}}.\, sin(\pi x/\boldsymbol{b}_e) \sum_i^{n_c} \left[e^{-\alpha_p x} - e^{-\lambda\alpha_p \boldsymbol{b}_e}.\left(e^{-\beta_1 z} - e^{-\beta_2 z}\right)\right] \ldots\ldots\ldots\ldots\ldots\ldots\ldots (3.83)$$

where:

$\Omega_{\mathrm{e}} = \overline{D}_{e-max} \Big/ DC.\, sin(0.5\pi)$

Writing Equation 3.83 as an integral and solving it yields:

$$\bar{D}(x,z,\Omega) = \Omega_e . S . sin(\pi x/\boldsymbol{b}_e)\left[e^{-\alpha_p x} - e^{-\alpha_p \boldsymbol{b}_e}.\left(e^{-\beta_1 z} - e^{-\beta_2 z}\right)\right] \ldots\ldots\ldots\ldots\ldots\ldots\ldots\ldots (3.84)$$

where:

x, z is the displacement from the reference core site to the point of analysis.

The distortion due to the screw dislocation was used to solve for one decay coefficient, β, while that of the edge dislocation was used to solve for the second decay coefficient, α. It was presumed that the material behind the dislocation core received negligible distortion as the material had not encountered the distortion.

3.3.4. ASSEMBLY OF OTHER DISLOCATIONS

The distortion as a result of other types of dislocations was obtained by the super-positioning of pure screw and pure edge dislocation segments to form the other type of dislocation. For mixed dislocations, this was achieved by super-positioning edge and screw dislocation distortions to the proportions contained in the dislocation type. This assembly was at the same spatial location, that is the effects were computed for the same location. On the other hand, the assembly to form a dislocation dipole, kink, junction or jog was achieved by the computation of dislocations at different spatial locations.

The distortion was assembled and then the stress field calculated for the resulting lattice. This method was applied to determine the effects of the mixed dislocations as the partitioning into separate edge and screw components was hypothetical, and they were one structure. Consequently, it was considered a more physical solution to assemble the distortion and then compute their resulting effect. The resulting distortion is given by:

$$\bar{D}(z,\varphi) = \Psi_s.\left(X_s + \Omega_s . S.\left(e^{-\beta_1 z} - e^{-\beta_2 z}\right)\right) + \Gamma_e . \Omega_e . S . sin(\pi x/\boldsymbol{b}_e)\left[e^{-\alpha_p x} - e^{-\lambda\alpha_p \boldsymbol{b}_e}.\left(e^{-\beta_1 z} - e^{-\beta_2 z}\right)\right] \ldots\ldots\ldots\ldots (3.85)$$

where:

Ψ_s, Γ_e are the screw and edge dislocation factors.

3.3.5. DISLOCATION LINE MOBILITY

The application of the proposed model in the characterization of dislocation line mobility is considered. As a dislocation moves, the lattice distortion profile moves with it. The dislocation mobility may therefore be measured by the time rate at which the distortion changes at a given location. Applying time gradients to Equation 3.85 yields:

$$\left.\frac{\partial(D[x,z])}{\partial t}\right|_{r=r_c} = -\Psi.\Omega_s.S.\left(\frac{1}{\beta}.\frac{\partial z}{\partial t}.e^{-\beta z}\right) - \Gamma.\Omega_e.S.\left(\frac{1}{\alpha}.\frac{\partial x}{\partial t}+\frac{1}{\beta}.\frac{\partial z}{\partial t}\right).\Phi \ldots\ldots\ldots\ldots (3.86)$$

where:

$$\Phi\left(e^{-\alpha_p x} - e^{\lambda.(\beta.\boldsymbol{b}_n - \alpha_p \boldsymbol{b}_e)-\beta z}\right) \ldots\ldots\ldots\ldots\ldots\ldots\ldots\ldots\ldots\ldots\ldots\ldots\ldots\ldots\ldots\ldots\ldots\ldots\ldots\ldots\ldots\ldots\ldots\ldots (3.87)$$

Equation 3.86 defines the dislocation velocity and is fully specified once the time rates of change of x and z are specified. Results of dislocation mobility may be qualitatively verified using the relative mobility of edge and screw dislocations [118, 119].

3.3.6. GENERATION OF SIMULATIONS

A block of 25 x 25 x 25 (15,625) lattice points was used to analyse the Fe lattice using the misfit potential. The resulting misfit and stress profile for consecutive atoms passing through the dislocation core was plotted. Sampling points were selected along the dislocation line and normal to the dislocation line. Additional simulations were undertaken along the path normal to the dislocation line with misfit effects. The block size was increased to 101 x 101 x 101 (1,030,301) lattice points and the stress curve was plotted.

The sampling points were selected to present the stress patterns of both the un-slipped and slipped regions of the lattice. The misfit distortion profile was sampled along the front plane, which contained lattice sites number 313 to 625, the mid-plane, which contained lattice sites number 7813 to 8125, and the rear plane, which contained lattice sites number 15313 to 15625. The stress values were calculated using the EAM formulation.

3.4. PLANE STRUCTURE FACTOR

3.4.1. DEVELOPMENT OF THE 2-D STRUCTURE MODEL

The dislocation plane model presented a functional that linked the spatial position of dislocation arrays to the dislocation density. Additionally, it linked the spatial position of dislocation arrays to the planar stress profile. As a result, the planar dislocation density was linked to the planar stress profile. The implementation enabled the tracking of the phase length of the dislocation line and subsequent assembly of these lengths to form 2-D dislocation structures. This analysis focused on the assembly of straight line dipoles that captured interaction phenomena, kinks that captured dislocation mobility and junctions that captured contact interaction in dislocations.

The computation utilized the applied stress, which modified the internal stress to give the net stress field. The net stress field was used to compute the resulting dislocation line response. The computation was therefore able to capture the dislocation's spatial contribution, 2-D interaction, and provided a mechanism for forecasting possible motion. The resulting computations were used to characterize the behaviour of the slip plane and 2-D dislocation structures formed by collections of dislocations, using the dislocation structure factor. This factor incorporated the following data:

- Planar dislocation density, which related to the number of contributing dislocations and their spatial locations
- Internal stress field resulting from the interaction of multiple dislocations
- Dislocation type, which defined the specific Peierl's stress.

For a set of slip systems designated μ_i and a phase space Ω such that:

$\mu_i \subset \Omega$ and $\mu_i = \mu_i(x, \theta, v)$

where:

x is the linear space coordinate

θ is the angular space coordinate

v is the velocity space coordinate.

The distribution of the dislocation segments in slip system $\mu_p : \left\{\{l_k\} \subset \Omega\right\}$ was modelled using the spacing between them as:

$$L'_p = \sum_{k=1}^{n} l_k \quad \ldots\ldots\ldots\ldots\ldots\ldots\ldots\ldots\ldots\ldots\ldots\ldots\ldots\ldots\ldots\ldots (3.88)$$

where:

L'_p is the sum of spacing within a single slip system comprising one slip plane

n is the number of dislocation cores in reference dislocation line

l_k is the spacing between dislocation cores measured along a normal from the reference dislocation line.

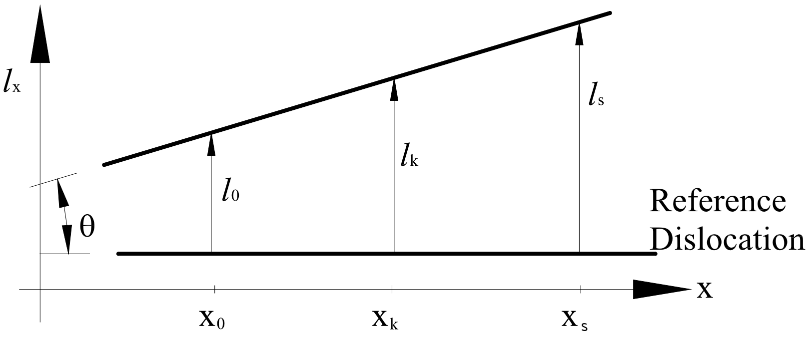

Figure 3.8: Dislocation dipole in a slip system

Considering two dislocation lines inclined at an angle θ as illustrated in Figure 3.8, the sum in Equation 3.88 can be written as:

$$L_p = l_0 + \cdots + l_s \quad \ldots\ldots\ldots\ldots\ldots\ldots\ldots\ldots\ldots\ldots\ldots\ldots\ldots\ldots\ldots\ldots (3.89)$$

In the extreme case, as $s \rightarrow \infty$, the spacing between sampling core points becomes negligibly small and the sum tends to the area of the space between the two dislocations. Consequently, Equation 3.89 can be written as:

$$L_p = \int_{x_s} l.dl \dots\dots\dots\dots\dots\dots\dots\dots\dots\dots\dots\dots\dots\dots\dots\dots\dots\dots\dots\dots\dots\dots\dots\dots\dots\dots\dots \text{(3.90)}$$

where:

L_p	is the area between the dislocations within the slip system containing the dislocations
x_s	is the length of the reference dislocation.

This integral was also interpreted as the area bounded by the second dislocation line and the x-axis, minus the area bounded by the reference dislocation line and the *x*-axis. Hence, Equation 3.90 can be written as:

$$L_p = \left| \int_l \Lambda_{\mathrm{p+1}}.\mathrm{dx} - \int_l \Lambda_{\mathrm{p}}.\mathrm{dx} \right| \dots\dots\dots\dots\dots\dots\dots\dots\dots\dots\dots\dots\dots\dots\dots\dots\dots\dots\dots \text{(3.91)}$$

where:

Λ	is the equation of the path traced by the dislocation line
p	is the index identifying the dislocation line.

The total area spanned by the dislocations in a single slip system μ_i in phase space Ω may then be given by:

$$L_\tau = \sum_{\mu_w} L_{p-jj} \dots\dots\dots\dots\dots\dots\dots\dots\dots\dots\dots\dots\dots\dots\dots\dots\dots\dots\dots\dots\dots\dots\dots\dots\dots\dots\dots\dots\dots\dots\dots\dots\dots\dots \text{(3.92)}$$

where:

w	is the index number of the slip system
$j{:}k$	is the number of pairs formed by adjacent dislocations within slip system μ_w.

and:

$$\sum_{\mu_w} L_{p-j:k} = L_{p-1:2} + L_{p-2:3} + L_{p-3:4} + L_{p-4:5} + \cdots \dots\dots\dots\dots\dots\dots\dots\dots\dots\dots\dots\dots\dots\dots\dots\dots\dots \text{(3.93)}$$

where:

L_τ is the area of the slip system containing the dislocations.

In the limit as $w \to \infty$

$$L_\tau = \int_\mu L_p . d\mu \ldots\ldots\ldots\ldots\ldots\ldots\ldots\ldots\ldots\ldots\ldots\ldots\ldots\ldots\ldots\ldots\ldots\ldots\ldots\ldots\ldots\ldots\ldots\ldots\ldots\ldots\ldots\ldots\ldots (3.94)$$

where:

$$d\mu = dxd\theta dv \ldots\ldots\ldots\ldots\ldots\ldots\ldots\ldots\ldots\ldots\ldots\ldots\ldots\ldots\ldots\ldots\ldots\ldots\ldots\ldots\ldots\ldots\ldots\ldots\ldots\ldots\ldots\ldots\ldots\ldots\ldots\ldots (3.95)$$

The function L_τ was represented as a distribution to enable the evaluation of L_τ and its integrals. An arbitrary functional $\mathcal{F}(x, \theta, v, t)$, corresponding to the phase length L_p and operating over an interval $\{[a, b]: a < \mu < b\}$ was selected. Therefore:

$$\langle \mathcal{F}', \psi \rangle = \int_a^b L_\tau . d\mu \equiv \int_{-\infty}^{\infty} L_\tau . \psi . d\mu \ldots\ldots\ldots\ldots\ldots\ldots\ldots\ldots\ldots\ldots\ldots\ldots\ldots\ldots\ldots\ldots\ldots\ldots\ldots\ldots\ldots (3.96)$$

or

$$\langle \mathcal{F}', \psi \rangle = \int_{-\infty}^{\infty} \left(L_{p-1:2} . \psi_1 + L_{p-2:3} . \psi_2 + L_{p-3:4} . \psi_3 + \cdots \right) d\mu \ldots\ldots\ldots\ldots\ldots\ldots\ldots\ldots\ldots (3.97)$$

The change in the function L_p in the direction of the reference dislocation line was contained in the equation of the dislocation line. However, the change in the function L_p in the direction joining the adjacent dislocation lines along dislocation rows was undefined. From Equation 3.97, the test function ψ was defined by the relation:

$$\psi = \begin{cases} 0 \; if \; \mu \geq b_i \\ 1 \; if \; a_i < \mu < b_i \\ 0 \; if \; \mu \leq a_i \end{cases} \ldots\ldots\ldots\ldots\ldots\ldots\ldots\ldots\ldots\ldots\ldots\ldots\ldots\ldots\ldots\ldots\ldots\ldots\ldots\ldots\ldots\ldots\ldots\ldots (3.98)$$

The above corresponded to a Heaviside function with compact support on $[a, b]$. This test function was selected to provide the cut-off of each contributing distribution function between pairs of dislocation lines and was defined by the relation:

$$\int_{-\infty}^{\infty} \psi . d\mu = 1 \tag{3.99}$$

In addition, it was necessary to capture the character of the interacting dislocations. This was achieved by the distribution:

$$\langle \mathcal{F}_{\mu}{}' , \varphi \rangle = \int_{-\infty}^{\infty} L_{\tau} . \varphi . dl \tag{3.100}$$

where:

$$\varphi_i = \begin{cases} 0 \ if \ l \geq l_1 \\ \dfrac{e^{a} . (e^{b} + \varepsilon)}{\varepsilon (e^{-1} - 1)} \ \ if \ l_0 < l < l_1 \\ 0 \ if \ \mathrm{l} \leq l_0 \end{cases} \tag{3.101}$$

where:

$$a_i = \begin{cases} 0 \ if \ l \geq l_1 \\ -\dfrac{(l_i - l_0)}{(l - l_0)} if \ l_0 < l < l_1 \\ 0 \ if \ \mathrm{l} \leq l_0 \end{cases} \tag{3.102}$$

$$b_i = \begin{cases} 0 \ if \ l \geq l_1 \\ -\dfrac{(l_i - l_0)}{(l_1 - l)} if \ l_0 < l < l_1 \\ 0 \ if \ \mathrm{l} \leq l_0 \end{cases} \tag{3.103}$$

and:

l_o	is the start point for the dislocation spacing
l_i	is the end point for the dislocation spacing
ε	is the factor to set the profile over the slip plane
e	is Eulers number, 2.7182.

The above corresponded to a pulse function with compact support on $[l_1, l_0]$. This test function was selected to mimic the stress profile generated by a pair of interacting dislocation line types and was defined by the relation:

$$\int_{-\infty}^{\infty} \varphi_i . dl = 1 \quad \text{(3.104)}$$

Next, a dislocation structure was defined as an array of slip systems containing dislocations by the tensor $\mathcal{T}\colon\mathcal{T}(r_t, \mathcal{F}\colon\mathcal{F}_{\mu})$:

where:

r_t is the translation tensor for the slip system, with respect to some origin

$\mathcal{F}\colon\mathcal{F}_{\mu}$ is the distribution of dislocations within the slip system – PSF.

The dislocation structure functional took the form:

$$\mathcal{T}\left(r_t, \mathcal{F}\colon\mathcal{F}_{\mu}\right)_{ij} = \{r_t\}\left[\mathcal{F}\colon\mathcal{F}_{\mu}\right]_{ij} \quad \text{(3.105)}$$

A relationship between the dislocation planar density and the plane structure factor was sought in the form given in Equation 3.106. The coefficient,ϒ, was obtained for each dislocation type as:

$$\hat{\varrho} = \frac{\Upsilon}{\langle \mathcal{F}, \psi \rangle} \quad \text{(3.106)}$$

where:

$\hat{\varrho}$ is the dislocation planar density.

3.4.2. DISLOCATION SETS

A polynomial form was selected for the dislocation line equation. For a dislocation dipole:

$$\Lambda_p = \int \sum_{j=1}^{r} \sum_{i=1}^{3} a_{ij} x_i^{j} . dx \quad \text{(3.107)}$$

where:

Λ_p is the polynomial characterizing the dislocations spatial organization

r is the order of the polynomial

a_{ij} is the coefficient set for the particular dislocation's equation.

Consequently:

$$L_p = \left| \int_l \sum_{j=1}^{r} \sum_{i=1}^{3} \left(a_{ij} x_i^{\,j} - b_{ij} x_i^{\,j} \right) . dx \right| \ldots\ldots\ldots\ldots\ldots\ldots\ldots\ldots\ldots\ldots\ldots\ldots\ldots\ldots\ldots (3.108)$$

where:

b_{ij} is the coefficient set for the reference dislocation's equation.

Absolute values were adopted to ensure non-negative areas, hence:

$$L_\tau = \left| \int_\mu \int_l \sum_{j=1}^{r} \sum_{i=1}^{3} \left(a_{ij} x_i^{\,j} - b_{ij} x_i^{\,j} \right) . dx . d\mu \right| \ldots\ldots\ldots\ldots\ldots\ldots\ldots\ldots\ldots\ldots\ldots\ldots (3.109)$$

where:

$d\mu$ is the change in phase space variables distance, rotation and velocity.

$$\langle \mathcal{F}', \psi \rangle = \left| \int_{-\infty}^{\infty} \left\{ \int_l \sum_{j=1}^{r} \sum_{i=1}^{3} \left(a_{ij} x_i^{\,j} - b_{ij} x_i^{\,j} \right) . dx . \psi \right\} . d\mu \right| \ldots\ldots\ldots\ldots\ldots\ldots\ldots\ldots (3.110)$$

and:

$$\langle \mathcal{F}_\mu{}', \varphi \rangle = \left| \int_{-\infty}^{\infty} \left\{ \int_l \sum_{j=1}^{r} \sum_{i=1}^{3} \left(a_{ij} x_i^{\,j} - b_{ij} x_i^{\,j} \right) . dx . \varphi \right\} . dl \right| \ldots\ldots\ldots\ldots\ldots\ldots\ldots\ldots\ldots (3.111)$$

Equation 3.108 was generalized to account for a set of m dislocations, where b_{ij} is the set of coefficients for the $(m^{th} - 1)$ dislocation equation, and a_{ij} is the set of coefficients for the m^{th} dislocation equation.

$$L_p = \left| \int_l \sum_{\mathrm{k}=2}^{\mathrm{m}} \sum_{\mathrm{j}=1}^{r} \sum_{\mathrm{i}=1}^{3} \left(\mathrm{a_{ij}} \mathrm{x_i}^{\mathrm{j}} - \mathrm{b_{ij}} \mathrm{x_i}^{\mathrm{j}} \right) . \mathrm{dx} \right| \dots\dots\dots\dots (3.112)$$

3.4.3. DISLOCATION DIPOLES

Applying Equations 3.107 to 3.111 for straight dislocations to the dislocation dipole oriented such that the reference dislocation was along the local x-axis provided the following results:

$$L_p = |0.5(\mathrm{a_1} - \mathrm{b_1})(\mathrm{x_1}^2 - \mathrm{x_0}^2) + (\mathrm{a_2} - \mathrm{b_2})(\mathrm{x_1} - \mathrm{x_0})| \dots\dots\dots\dots (3.113)$$

For a single pair of straight dislocations, θ was constant, $L_p = L_\tau$ and $\psi = 1$, hence:

$$\langle \mathcal{F}', \psi \rangle = \left| \int_{-\infty}^{\infty} [0.5(\mathrm{a_1} - \mathrm{b_1})(\mathrm{x_1}^2 - \mathrm{x_0}^2) + (\mathrm{a_2} - \mathrm{b_2})(\mathrm{x_1} - \mathrm{x_0})] . dx \right| \dots\dots\dots\dots (3.114)$$

and:

$$\langle \mathcal{F}_\mu{}', \varphi \rangle = \left| \int_{-\infty}^{\infty} [0.5(\mathrm{a_1} - \mathrm{b_1})(\mathrm{x_1}^2 - \mathrm{x_0}^2) + (\mathrm{a_2} - \mathrm{b_2})(\mathrm{x_1} - \mathrm{x_0})] . \varphi . dl \right| \dots\dots\dots\dots (3.115)$$

where φ was given by Equation 3.101.

Evaluating Equations 3.114 and 3.115 gave:

$$\langle \mathcal{F}, \psi' \rangle = |[0.5(\mathrm{a_1} - \mathrm{b_1})(\mathrm{x_1}^2 - \mathrm{x_0}^2) + (\mathrm{a_2} - \mathrm{b_2})(\mathrm{x_1} - \mathrm{x_0})](\mathrm{x_1} - \mathrm{x_0})| \dots\dots\dots\dots (3.116)$$

$$\langle \mathcal{F}_\mu, \varphi' \rangle = |[0.5(\mathrm{a_1} - \mathrm{b_1})(\mathrm{x_1}^2 - \mathrm{x_0}^2) + (\mathrm{a_2} - \mathrm{b_2})(\mathrm{x_1} - \mathrm{x_0})] . \Theta| \dots\dots\dots\dots (3.117)$$

where:

$$\Theta = \frac{e^a}{(l_1 - l_0) . \varepsilon (e^{-1} - 1)} \left[\frac{(l_1 - l)^2 (l - l_0)^2 e^b}{(l - l_0)^2 - (l_1 - l)^2} - (l - l_0)^2 . \varepsilon \right]_{l_0}^{l_1} \dots\dots\dots\dots (3.118)$$

Allowing the reference dislocation dipole to be located at the origin of the coordinate system, and the reference dislocation to be aligned with the crystal/grain boundaries provided “identity” translation and orientation tensors. The dislocation structure functional took the form:

$$\Phi = \{r_{1-2}\}\left[\left[\mathcal{F}:\mathcal{F}_{\mu}\right]_{1-2}\right] \dots\dots\dots\dots\dots\dots\dots\dots\dots\dots\dots\dots\dots\dots\dots\dots\dots\dots\dots\dots\dots\dots\dots\dots\dots\dots\dots\dots\dots\dots\dots (3.119)$$

3.4.4. DISLOCATION TRIPOLES

Applying Equations 3.107 to 3.111 for straight dislocations to the dislocation tripole oriented such that the reference dislocation was along the local x-axis provided the following relationships:

$$L_{p-1:2} = |0.5(\mathrm{a}_1 - \mathrm{b}_1)(\mathrm{x}_1{}^2 - \mathrm{x}_0{}^2) + (\mathrm{a}_2 - \mathrm{b}_2)(\mathrm{x}_1 - \mathrm{x}_0)| \dots\dots\dots\dots\dots\dots\dots\dots\dots\dots\dots\dots (3.120)$$

$$L_{p-2:3} = |0.5(\mathrm{b}_1 - \mathrm{c}_1)(\mathrm{x}_3{}^2 - \mathrm{x}_2{}^2) + (\mathrm{b}_2 - \mathrm{c}_2)(\mathrm{x}_3 - \mathrm{x}_2)| \dots\dots\dots\dots\dots\dots\dots\dots\dots\dots\dots\dots\dots (3.121)$$

For straight dislocations, θ was constant and $\psi = 1$, hence:

$$\langle \mathcal{F}, \psi \rangle = \int_{-\infty}^{\infty} \left(L_{p-1:2} + L_{p-2:3}\right).\, dx \dots\dots\dots\dots\dots\dots\dots\dots\dots\dots\dots\dots\dots\dots\dots\dots\dots\dots\dots\dots\dots\dots (3.122)$$

and

$$\langle \mathcal{F}_{\mu}, \varphi \rangle = \int_{-\infty}^{\infty} \left(L_{p-1:2}.\, \varphi_1 + L_{p-2:3}.\, \varphi_2\right).\, dl \dots\dots\dots\dots\dots\dots\dots\dots\dots\dots\dots\dots\dots\dots\dots\dots\dots (3.123)$$

where φ was given by Equation 3.101.

Evaluating Equations 3.122 and 3.123 gave:

$$\begin{aligned}\langle \mathcal{F}, \psi \rangle = |&[0.5(\mathrm{a}_1 - \mathrm{b}_1)(\mathrm{x}_1{}^2 - \mathrm{x}_0{}^2) + (\mathrm{a}_2 - \mathrm{b}_2)(\mathrm{x}_1 - \mathrm{x}_0)](\mathrm{x}_1 - \mathrm{x}_0) \\ &+ [0.5(\mathrm{b}_1 - \mathrm{c}_1)(\mathrm{x}_3{}^2 - \mathrm{x}_2{}^2) + (\mathrm{b}_2 - \mathrm{c}_2)(\mathrm{x}_3 - \mathrm{x}_2)](\mathrm{x}_3 - \mathrm{x}_2)| \dots\dots\dots\dots (3.124)\end{aligned}$$

$$2 * \langle \mathcal{F}_{\mu}, \varphi \rangle = |[(a_1 - b_1)(x_1{}^2 - x_0{}^2) + (a_2 - b_2)(x_1 - x_0)].\Theta_1 + [(b_1 - c_1)(x_3{}^2 - x_2{}^2) + (b_2 - c_2)(x_3 - x_2)].\Theta_2| \ldots\ldots\ldots\ldots\ldots\ldots\ldots (3.125)$$

$$\Theta_1 = \frac{e^a}{(l_1 - l_0).\varepsilon(e^{-1} - 1)}\left[\frac{(l_1 - l)^2(l - l_0)^2 e^b}{(l - l_0)^2 - (l_1 - l)^2} - l^2.\varepsilon\right]_{l_0}^{l_1} \ldots\ldots\ldots\ldots\ldots\ldots\ldots\ldots\ldots\ldots\ldots (3.126)$$

$$\Theta_2 = \frac{e^c}{(l_3 - l_2).\varepsilon(e^{-1} - 1)}\left[\frac{(l_3 - l)^2(l - l_2)^2 e^d}{(l - l_2)^2 - (l_3 - l)^2} - l^2.\varepsilon\right]_{l_2}^{l_3} \ldots\ldots\ldots\ldots\ldots\ldots\ldots\ldots\ldots\ldots\ldots (3.127)$$

Allowing the reference dislocation of the first pair to be located at the origin of the coordinate system, and the reference dislocation to be aligned with the crystal/grain boundaries provided "identity" translation and orientation tensors. The dislocation structure functional took the vector form:

$$\Phi = \{r_{1-2} \quad r_{2-3} \quad r_{1-3}\}\begin{bmatrix}[\mathcal{F}:\mathcal{F}_{\mu}]_{1-2}\\ [\mathcal{F}:\mathcal{F}_{\mu}]_{2-3}\\ [\mathcal{F}:\mathcal{F}_{\mu}]_{1-3}\end{bmatrix} \ldots\ldots\ldots\ldots\ldots\ldots\ldots\ldots\ldots\ldots\ldots\ldots\ldots\ldots\ldots\ldots\ldots\ldots\ldots\ldots (3.128)$$

3.4.5. CONSTRUCTION OF 2-D DISLOCATION STRUCTURES

The construction of 2-D dislocation structures was achieved by the tessellation of dislocation lines within the slip planes. Initial simulations were carried out on dislocation dipoles to demonstrate the method. It was noted that this approach could be expanded to account for a greater number of dislocation structures at varying orientations. Consequently, the creation of a variety of planar structures, including dislocation kinks, Frank-Reed sources, dislocation junctions, and other 2-D dislocation features was possible.

3.4.6. SAMPLE CALCULATIONS

Below is a sample calculation for the edge dislocation dipole set at three and four lattice steps from the sampling line. Using the boundary condition given in Equation 3.102:

$a_1 = 0$ and $b_1 = 0$.

Additionally, for the given configuration:

$a_2 = 3 * 2.465 * 10^{-9}$ and $b_2 = 4 * 2.465 * 10^{-9}$.

where 3 and 4 are steps of the sampling point from the dislocation. Additionally, x_0 and x_1 are the start and finish of the pulse function representing the stress profile spanning the space between the dislocation lines. Hence:

$x_0 = -1 * 2.465 * 10^{-9}$ and $x_1 = 1 * 2.465 * 10^{-9}$.

Substituting in Equations 3.113 and 3.116 gave:

$L_p = 1.215 * 10^{-17}$ and $\langle \mathcal{F}, \psi \rangle = 5.991 * 10^{-26}$.

For the same configuration and selecting a point along the line midway between the two dislocation lines gave:

$l_1 = 1 * 2.465 * 10^{-9}$, $l_0 = -1 * 2.465 * 10^{-9}$ and $l = 3.5 * 2.465 * 10^{-9}$,

where l_0 and l_1 were the start and end points of the pulse function. The coefficient ϵ was obtained by fitting of the leading end of the hump of the trial function to the value of the front end of the hump of the POLR stress amplitude profile.

Hence, evaluating Equation 3.117 and 3.118 gave:

$\langle \mathcal{F}_{\mu}, \varphi \rangle = 3.317 * 10^{-25}$ and $\hat{\varrho} = 4.06 * 10^{8}$.

3.4.7. GENERATION OF RESULTS

Several 2-D structures were set up and their dislocation planar density generated using Equations 3.99 and 3.101. The structures were then loaded onto simulation software and the resulting stress

field correlated with the dislocation planar density. The stress components were calculated using the EAM potential with the longer range effects of the dislocation core accounted for by the misfit potential. The stress profile was plotted against the number of lattice steps from the core for each arrangement of dislocations and the curves analysed.

3.5. NETWORK STRUCTURE FACTOR

The computation utilized the net stress field to compute the resulting dislocation core response, taking into account dislocation motion constraints, dislocation annihilation and the source mechanisms. The computation was thus able to capture the dislocation's evolution, 3-D interaction and motion.

The resulting computations were used to characterize the structure formed by a collection of dislocations, using the dislocation structure factor. The dislocation structure factor was used to model known types of dislocation structures and grain boundary formations. The dislocation structure factor incorporated the following data:

i. Dislocation density, which relates to the number of contributing dislocations
ii. Internal stress field resulting from the interaction of multiple dislocations and the interaction of slip planes
iii. Dislocation orientation, which relates to the net stress on the dislocation
iv. Dislocation type, which defines the specific Peierl's stress.

Considering a set of slip systems designated μ_s and a phase space Ω such that $\mu_s \subset \Omega$ and $\mu_s = \mu_s(\hat{\varrho}, s, \mathcal{M})$,

where:

s is the separation of slip planes

$\mathcal{M}$ is the distribution of slip planes within the network system.

The set of slip systems is illustrated in Figure 3.9.

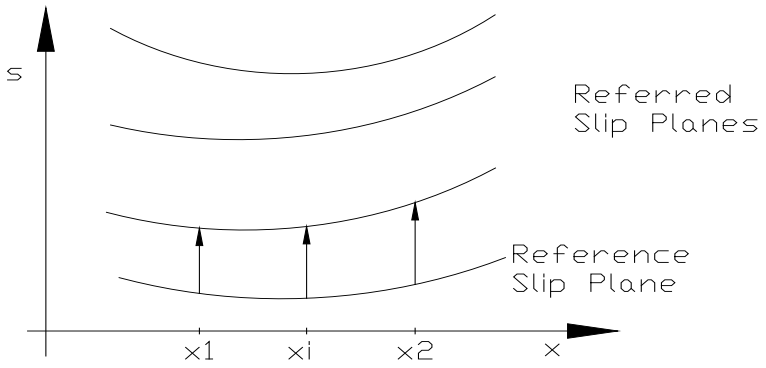

Figure 3.9: Set of slip systems

For a distance s between interacting slip systems $\mu_s : \{\{s^m\} \subset \Omega\}$, the total space over which the slip systems μ_s acted was given by:

$$s_\tau = \frac{1}{m}\sum_{k=1}^{m} s^m \dots\dots(3.129)$$

where:

m is the number of finite elements of the slip systems.

In the limit as the element size tended to zero, Equation 3.129 was written as:

$$s_\tau = \int s^m \, d\mu_s \dots\dots(3.130)$$

The density of the network was given by:

$$\emptyset_d = \frac{1}{\int s_i . d\mu_s}\sum_i \hat{\varrho}_i . L_i \dots\dots(3.131)$$

where:

L_i is the area of the i^{th} slip system

$\emptyset_d$ is the dislocation network density.

The density $\hat{\varrho}_i$ was obtained from Equation 3.106, while the area L_i was obtained from Equation 3.90.

This part of the work sought to represent the function s_i as a distribution to enable evaluation of s_τ and its derivatives. An interval $\{[a,b]: a < \mathrm{\mu_s} < b\}$ was selected and an arbitrary distribution $\mathcal{M}\left(r_t, r, \mathcal{F}\colon \mathcal{F}_{\mathrm{\mu}}\right)$ constructed to correspond to the phase length s_i. Therefore:

$$\langle \mathcal{M}, \chi \rangle = \int_a^b s_{\tau i} \,.\, d\mathrm{\mu_s} \equiv \int_{-\infty}^{\infty} s_{\tau i} \,.\, \chi_i \,.\, ds \ldots\ldots\ldots\ldots\ldots\ldots\ldots\ldots (3.132)$$

or

$$\langle \mathcal{M}, \chi \rangle = \{r_{t:a-b}\} \left[\left[\mathcal{F}\colon \mathcal{F}_{\mathrm{\mu}}\right]_{1-2}\right]^T \{r_{1-2}\}^T \ldots\ldots\ldots\ldots\ldots\ldots\ldots\ldots (3.133)$$

where:

From Equation 3.132, a test function χ was defined by the relation:

$$\chi_i = \begin{cases} 0 \; if \; s \leq ls_0 \\ \dfrac{e^b.(e^a + \epsilon_1)}{\epsilon_1.(e^{-1} - 1) + \epsilon_2.(e^{-1} - 1)} \,.\, \mathrm{H}(s - ls_0).\, \mathrm{H}(c - s) if \; ls_0 < s < c \\ \dfrac{e^e.(e^f + \epsilon_2)}{\epsilon_1.(e^{-1} - 1) + \epsilon_2.(e^{-1} - 1)} .\, \mathrm{H}(s - c).\, \mathrm{H}(ls_1 - s) \;\; if \; c < s < ls_1 \\ 0 \; if \; ls_1 \leq s \end{cases} \ldots\ldots\ldots\ldots (3.134)$$

where:

$$a = \begin{matrix} 0 \; if \; s \leq ls_0 \\ -\dfrac{0.5d}{(s - ls_0)} if \; ls_0 < s < c. \\ 0 \; if \; c \leq s \end{matrix} \ldots\ldots\ldots\ldots\ldots\ldots\ldots\ldots (3.135)$$

$$b = \begin{matrix} 0 \; if \; s \leq ls_0 \\ -\dfrac{0.5d}{(c - s)} if \; ls_0 < s < c \\ 0 \; if \; c \leq s \end{matrix} \ldots\ldots\ldots\ldots\ldots\ldots\ldots\ldots (3.136)$$

$$c = \frac{(ls_1 + ls_0)}{2} \ldots\ldots\ldots\ldots\ldots\ldots\ldots\ldots (3.137)$$

$$d = ls_1 - ls_0 \ldots\ldots\ldots\ldots\ldots\ldots\ldots\ldots\ldots\ldots\ldots\ldots\ldots\ldots\ldots\ldots\ldots\ldots (3.138)$$

$$\begin{aligned} &\qquad if\ s < c \\ e = &-\frac{0.5d}{(s-c)} if\ c < s < ls_1 \ldots\ldots\ldots\ldots\ldots\ldots\ldots\ldots\ldots\ldots\ldots\ldots\ldots\ldots (3.139) \\ &\quad 0\ if\ ls_1 \le s \end{aligned}$$

$$\begin{aligned} &\qquad if\ s < c \\ f = &-\frac{0.5d}{(ls_1 - s)} if\ c < s < ls_1 \ldots\ldots\ldots\ldots\ldots\ldots\ldots\ldots\ldots\ldots\ldots\ldots\ldots\ldots (3.140) \\ &\quad 0\ if\ ls_1 \le s \end{aligned}$$

where:

ls_0	is the start point on the reference slip plane
ls_1	is the start point on the referred slip plane
ϵ_i	is the factor to set the profile of the stress humps across the slip planes.

The above corresponds to a pulse function with compact support on $[ls_1, ls_0]$. This test function was selected to mimic the stress profile generated by a pair of interacting slip planes and was defined by the relation:

$$\int_{-\infty}^{\infty} \chi_i . ds = 1 \ldots\ldots\ldots\ldots\ldots\ldots\ldots\ldots\ldots\ldots\ldots\ldots\ldots\ldots\ldots\ldots\ldots\ldots\ldots (3.141)$$

Next, a slip plane structure was defined as an array of slip systems containing dislocations by the tensor $\Re : \Re(r^*, \mathcal{M})$.

Applying expressions for dislocation density obtained from Equation 3.106, the dislocation network density was defined as:

$$\emptyset_d = \frac{1}{\langle \mathcal{M}, \chi \rangle} \sum_i \hat{\varrho}_i . L_i \ldots\ldots\ldots\ldots\ldots\ldots\ldots\ldots\ldots\ldots\ldots\ldots\ldots\ldots\ldots\ldots (3.142a)$$

In the limit as the plane area tended to a small value, Equation 3.142 is re-written as:

$$\emptyset_d = \frac{1}{\langle \mathcal{M}, \chi \rangle} \int_{\mu_s} \hat{\varrho}_i . dL_i \ldots\ldots\ldots\ldots\ldots\ldots\ldots\ldots (3.142b)$$

where the expression under the integral sign was obtained from Equation 3.106 for the density within the slip plane.

The dislocation density was alternatively calculated by the relationship:

$$\emptyset_d = 2 * \frac{(ls_1 - ls_0)}{\left(Z * (s_1 - s_0)(ls_1 - ls_0)\right)} \ldots\ldots\ldots\ldots\ldots\ldots\ldots\ldots (3.143)$$

where:

s_1, s_0	are the locations of the first and reference dislocations.

3.5.1. SLIP PLANE SETS

Considering a pair of slip planes separated by a distance $s_1(x_j, x_k)$ where x_j represented the length and x_k the depth of the reference plane, for non-parallel slip planes a bi-linear expression of the separation was obtained as:

$$s_1 = \Upsilon_{\mathrm{j}}(x_j + \Theta_{\mathrm{j}}) + \Upsilon_{\mathrm{k}}(x_k + \Theta_{\mathrm{k}}) + \mathrm{Z} \ldots\ldots\ldots\ldots\ldots\ldots\ldots\ldots (3.144)$$

where:

Z	is the initial separation at $x_j, x_k = 0$
Υ_{j}	is the gradient of change of the separation along the length of the slip plane
Θ_{j}	is the offset of the slip planes along the length of the slip plane
Υ_{k}	is the gradient of change of the separation along the depth of the slip plane
Θ_{k}	is the offset of the slip planes along the depth of the slip plane.

Substituting for $\mathcal{M}$ and χ in Equation 3.132 gives:

$$\langle \mathcal{M}, \chi \rangle = \left[\frac{1}{\sum \epsilon_i . (e^{-1} - 1)}\right] \int_{-\infty}^{\infty} \left[\Upsilon_{\mathrm{j}}(x_j + \Theta_{\mathrm{j}}) + \Upsilon_{\mathrm{k}}(x_k + \Theta_{\mathrm{k}}) + \mathrm{Z}\right] . \mathrm{X} . ds \ldots\ldots\ldots\ldots\ldots\ldots (3.145)$$

where:

$$\mathrm{X} = \{e^b . (e^a + \epsilon_1)\mathrm{H}_1(s - ls_0)\mathrm{H}_2(c - s)\} + \{e^e . (e^f + \epsilon_2)\mathrm{H}_3(s - c)\mathrm{H}_4(ls_1 - s)\} \ldots (3.146)$$

3.5.2. PLANE SETS CONTAINING DISLOCATION DIPOLES

Considering a BCC unit cell, geometric analysis of combinations of pairs of slip planes reveals that only two combinations are possible. The first consists of slip planes that will intersect along a line and may contain dislocation junctions, sections of dislocation jogs, and dislocation dipoles formed from dislocation loops each on a different slip plane (Type 1 dipoles). The second consists of slip planes that are parallel and may contain dislocation dipoles formed from dislocation loops (Type 2 dipoles), segments of dislocation jogs and dislocation kinks. The analysis of intersecting slip planes is therefore suited for dislocation motion studies where dislocation contact is important, while the study of parallel slip planes would be more suited for the study of long range dislocation interaction and the resulting stress field. The network structure factor model is concerned with the evaluation of long range stress fields resulting from dislocations found within the metal and of particular interest are dislocation dipoles formed by dislocation loops generated by dislocation point sources. Consequently, this work focused on the analysis of parallel slip planes.

Considering a pair of parallel slip planes containing dislocation dipoles, for parallel planes, Equation 3.145 reduced to:

$$\langle \mathcal{M}, \chi \rangle = \left[\frac{\mathrm{Z}}{\sum \epsilon_i . 0.5d . (e^{-1} - 1)}\right] \int_{-\infty}^{\infty} \{e^b . (e^a + \epsilon_1) . \mathrm{H}_1(s - ls_0) . \mathrm{H}_2(c - s)\} + \{e^e . (e^f + \epsilon_2) . \mathrm{H}_3(s - c) . \mathrm{H}_4(ls_1 - s)\} . ds \ldots\ldots\ldots\ldots\ldots\ldots\ldots\ldots\ldots\ldots (3.147)$$

Rearranging gives:

$$\langle \mathcal{M}, \chi \rangle = \left[\frac{\mathrm{Z}}{0.5d.(e^{-1}-1)}\right] \int_{ls_0}^{c} \frac{1}{\epsilon_1}\{e^{a+b} + \epsilon_1 . e^{b}\}.ds + \int_{c}^{ls_1} \frac{1}{\epsilon_2}\{e^{e+f} + \epsilon_2 . e^{e}\}.ds \ldots . (3.148)$$

Hence:

$$\langle \mathcal{M}, \chi \rangle = \left[\frac{\mathrm{Z}}{0.5d.(e^{-1}-1)}\right] \left[\frac{1}{\epsilon_1}\left\{-\frac{(s-ls_0)(c-s).e^{a+b}}{(s-ls_0)^2-(c-s)^2} - \epsilon_1(c-s)^2 e^{b}\right\}_{ls_0}^{c} + \frac{1}{\epsilon_2}\left\{-\frac{(s-c)(ls_1-s).e^{e+f}}{(ls_1-s)^2-(s-c)^2} + \epsilon_2(s-c)^2 e^{e}\right\}_{c}^{ls_1}\right] \ldots\ldots\ldots\ldots\ldots\ldots\ldots (3.149)$$

where:

Z is the initial separation at $x_j, x_k = 0$

a, b, c, d are given in Equations 3.135, 3.136, 3.137, 3.138, and the density was obtained using Equation 3.143.

3.5.3. CONSTRUCTION OF 3-D DISLOCATION STRUCTURES

The construction of 3-D dislocation structures was achieved by the tessellation of slip planes containing dislocations. Initial simulations were carried out on two parallel slip planes to demonstrate the method. It was noticed that this approach could be expanded to account for a greater number of slip planes at varying spacing. In addition, the orientation of the slip planes could be varied, allowing slip planes to intersect. Consequently, the creation of a variety of network structures, including slip bands, dislocation cells, shear bands and dislocation tangles, geometrically and statistically necessary dislocations, grain and sub-grain boundaries, and other dislocation features was possible.

3.5.4. SAMPLE CALCULATIONS

Below is a sample calculation for twin slip planes at a separation of seven lattice spaces, containing the edge dislocation dipole set at five and three lattice steps from the sampling line. For the given configuration:

$ls_0 = 5 * 2.465 * 10^{-9}$

$ls_1 = -5 * 2.465 * 10^{-9}$

$c = 0$

$a = -1$

$b = -1$

$d = 10 * 2.465 * 10^{-9}$

$Z = 7 * 2.465 * 10^{-9}$.

The coefficient ϵ_1 in Equation 3.149 was obtained by fitting of the leading end of the first hump of the trial function to the value of the front end of the hump of the POLR stress amplitude profile. Additionally, the coefficient ϵ_2 in Equation 3.149 was obtained by fitting of the trailing end of the second hump of the trial function to the value of the rear end of the hump of the POLR stress amplitude profile.

Applying Equations 3.143 and 3.149 gives:

$\langle \mathcal{M}, \chi \rangle = 1.7255 * 10^{-8}$

$\emptyset_d = 2.351 * 10^{16}$.

3.5.5. GENERATION OF RESULTS

Several twin planes containing dislocation structures were set up and their network shape functions generated using Equation 3.149. The structures were loaded onto simulation software and the resulting stress field used to fit the unknown coefficients. The stress components were calculated using the EAM potential with the longer range effects of the dislocation core accounted for using the misfit potential. The stress profile was plotted against the number of lattice steps from the core for each network structure factor and the curves analysed. The plane structure factor intrinsically contained in the planar dislocation density was used to account for dislocations in each slip plane, and together with the network structure factor, was used to determine the network dislocation density.

3.6. MESO-SCALE

3.6.1. THE SELECTION OF THE FINITE ELEMENTS

The first principle requirement is that the finite elements, as closely as possible, model the shape of the grains within the matrix. Typical grains may be visualized as spheres, elongated in one direction, and the extent of the elongation is dependant on the amount of cold working the material has undergone. The second requirement is to provide as much flexibility as possible to the mesh generation module, by the use of finite elements with curved boundaries.

To accommodate these requirements, 24 node serendipity finite elements and four node tetrahedral finite elements were selected for use. The development of the shape functions was as follows.

Consider a four node, one-dimensional, isoparametric finite element as shown in Figure 3.10:

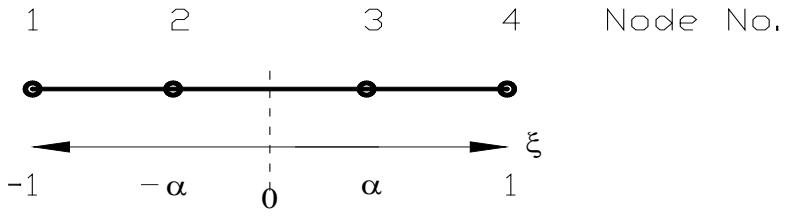

Figure 3.10: Four node, linear isoparametric finite element

A trial function was selected as follows:

$$\phi = a_0 + a_1\xi + a_2\xi^2 + a_3\xi^3 \ldots\ldots\ldots\ldots\ldots\ldots\ldots\ldots\ldots\ldots\ldots\ldots\ldots\ldots\ldots\ldots\ldots\ldots\ldots (3.150)$$

where:

a_k	Polynomial coefficients
ϕ	Dependent variable
ξ	Independent variable.

On applying the relevant nodal coordinate values, Equation 3.150 was written as:

$$\{\phi_i\} = [A]\{a_k\} \ldots\ldots\ldots\ldots\ldots\ldots\ldots\ldots\ldots\ldots\ldots\ldots (3.151)$$

where:

$$\{\phi_i\}_{i=1}^{4} = \begin{Bmatrix} \phi_1 \\ \phi_2 \\ \phi_3 \\ \phi_4 \end{Bmatrix} \ldots\ldots\ldots\ldots\ldots\ldots\ldots\ldots\ldots\ldots (3.152)$$

$$[A] = \begin{bmatrix} 1 & -1 & 1 & -1 \\ 1 & -\alpha & \alpha^2 & -\alpha^3 \\ 1 & \alpha & \alpha^2 & \alpha^3 \\ 1 & 1 & 1 & 1 \end{bmatrix} \ldots\ldots\ldots\ldots\ldots\ldots\ldots\ldots\ldots\ldots (3.153)$$

$$0 \le \alpha \quad \le 1 \ldots\ldots\ldots\ldots\ldots\ldots\ldots\ldots\ldots\ldots\ldots\ldots\ldots (3.154)$$

$$\{a_k\} = \begin{Bmatrix} a_0 \\ a_1 \\ a_2 \\ a_3 \end{Bmatrix} \ldots\ldots\ldots\ldots\ldots\ldots\ldots\ldots\ldots\ldots\ldots (3.155)$$

By a process of matrix inversion, the values of the polynomial coefficients were obtained as:

$$\{a_k\} = [A]^{-1}\{\phi_i\} \ldots\ldots\ldots\ldots\ldots\ldots\ldots\ldots\ldots\ldots\ldots (3.156)$$

where:

$$[A]^{-1} = \begin{bmatrix} N_{11} & N_{21} & N_{31} & N_{41} \\ N_{12} & N_{22} & N_{32} & N_{42} \\ N_{13} & N_{24} & N_{33} & N_{43} \\ N_{14} & N_{24} & N_{34} & N_{44} \end{bmatrix} \ldots\ldots\ldots\ldots\ldots\ldots\ldots\ldots\ldots (3.157)$$

and:

$$N_i = N_{i1} + N_{i2}\xi + N_{i3}\xi^2 + N_{i4}\xi^3 \ldots\ldots\ldots\ldots\ldots\ldots\ldots\ldots (3.158)$$

where:

N_i is the shape function

Consequently, the shape functions were obtained as follows:

$$N_1 = \frac{-0.5(1-\xi)(\alpha-\xi)(\alpha+\xi)}{(1-\alpha)(1+\alpha)} \quad (3.159)$$

$$N_2 = \frac{0.5(1-\xi)(1+\xi)(\alpha-\xi)}{\alpha(1-\alpha)(1+\alpha)} \quad (3.160)$$

$$N_3 = \frac{0.5(1-\xi)(1+\xi)(\alpha+\xi)}{\alpha(1-\alpha)(1+\alpha)} \quad (3.161)$$

$$N_4 = \frac{-0.5(1+\xi)(\alpha-\xi)(\alpha+\xi)}{(1-\alpha)(1+\alpha)} \quad (3.162)$$

The use of the variable α to determine the intermediate nodes along a boundary was adopted to enable the optimization of the node locations with regard to the shape of the physical unit being modelled. It was noticed that the concept could be applied to all the three coordinate axes. The technique used to determine the shape functions for the four node linear finite element in Figure 3.10 was then used to construct a 24 node, 3-D finite element as shown in Figure 3.11. The variables β and γ were used to characterize the intermediate nodes in the remaining two coordinate axes. The node numbers and the respective coordinates are shown in Table 3.2.

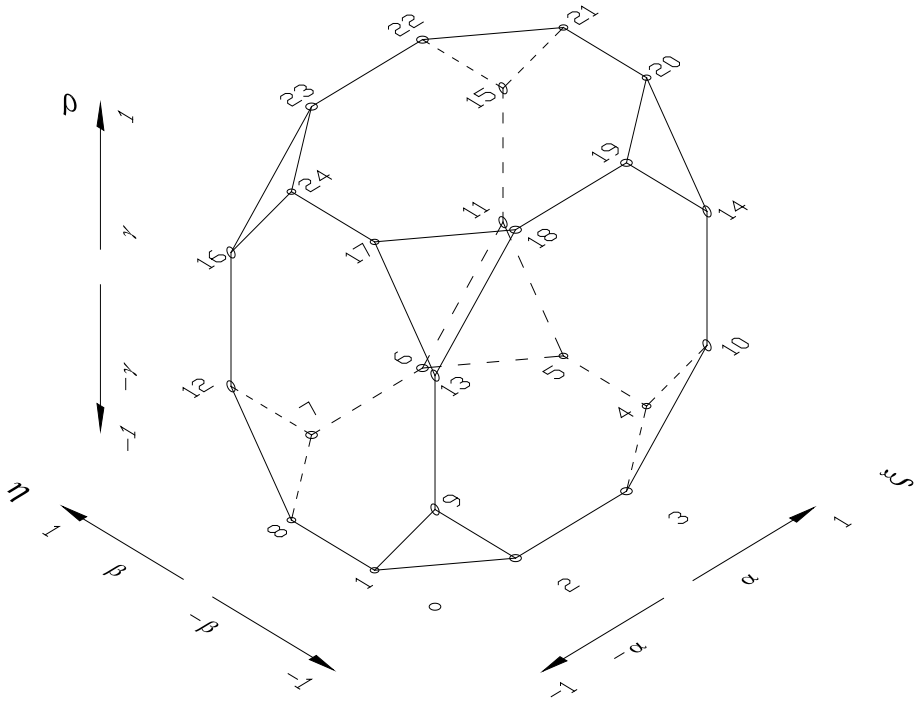

Figure 3.11: 24 node isoparametric serendipity finite element

The 24 node serendipity finite element was employed as it met the criteria set out in the selection of elements. It was necessary to account for the curvature found on grain surfaces and as a result this element had nodes along the edges of the element. This enabled curvature of the element to fit the shape of the grains. It was also possible to couple this element with tetrahedral elements, and together it was possible to account for regions with large curvature of grains. It was important to keep the system matrix as small as possible and this was achieved by reducing the number of nodes on this element. This was achieved by using an element without facial nodes and without internal nodes. The internal nodes were not required as the dominant deformation surface was at the grain boundary and the deformation on the inside of the grain was accounted for by equal distribution of these effects to the boundary nodes.

Table 3.2: Coordinates of the 24 node isoparametric serendipity finite element.

Node number	ξ	η	ρ
1	-1	$-\beta$	-1
2	$-\alpha$	-1	-1
3	α	-1	-1
4	1	$-\beta$	-1
5	1	β	-1
6	α	1	-1
7	$-\alpha$	1	-1
8	-1	β	-1
9	-1	-1	$-\gamma$
10	1	-1	$-\gamma$
11	1	1	$-\gamma$
12	-1	1	$-\gamma$
13	-1	-1	γ
14	1	-1	γ
15	1	1	γ
16	-1	1	γ
17	-1	$-\beta$	1
18	$-\alpha$	-1	1
19	α	-1	1
20	1	$-\beta$	1
21	1	β	1
22	α	1	1
23	$-\alpha$	1	1
24	-1	β	1

where:

ξ, η, ρ are the independent local variables corresponding to the Cartesian coordinate system

α, β, γ are the variable factors.

The resulting shape functions were as follows:

$$N_1 = N_{\alpha 1} N_{\beta 2} N_{\gamma 1} \quad (3.163)$$

$$N_2 = N_{\alpha 2} N_{\beta 1} N_{\gamma 1} \quad (3.164)$$

$$N_3 = N_{\alpha 3} N_{\beta 1} N_{\gamma 1} \quad (3.165)$$

$$N_4 = N_{\alpha 4} N_{\beta 2} N_{\gamma 1} \quad (3.166)$$

$$N_5 = N_{\alpha 4} N_{\beta 3} N_{\gamma 1} \quad (3.167)$$

$$N_6 = N_{\alpha 3} N_{\beta 4} N_{\gamma 1} \quad (3.168)$$

$$N_7 = N_{\alpha 2} N_{\beta 4} N_{\gamma 1} \quad (3.169)$$

$$N_8 = N_{\alpha 1} N_{\beta 3} N_{\gamma 1} \quad (3.170)$$

$$N_9 = N_{\alpha 1} N_{\beta 1} N_{\gamma 2} \quad (3.171)$$

$$N_{10} = N_{\alpha 4} N_{\beta 1} N_{\gamma 2} \quad (3.172)$$

$$N_{11} = N_{\alpha 4} N_{\beta 4} N_{\gamma 2} \quad (3.173)$$

$$N_{12} = N_{\alpha 1} N_{\beta 4} N_{\gamma 2} \quad (3.174)$$

$$N_{13} = N_{\alpha 1} N_{\beta 1} N_{\gamma 3} \quad (3.175)$$

$$N_{14} = N_{\alpha 4}N_{\beta 1}N_{\gamma 3} \tag{3.176}$$

$$N_{15} = N_{\alpha 4}N_{\beta 4}N_{\gamma 3} \tag{3.177}$$

$$N_{16} = N_{\alpha 1}N_{\beta 4}N_{\gamma 3} \tag{3.178}$$

$$N_{17} = N_{\alpha 1}N_{\beta 2}N_{\gamma 1} \tag{3.179}$$

$$N_{18} = N_{\alpha 2}N_{\beta 1}N_{\gamma 4} \tag{3.180}$$

$$N_{19} = N_{\alpha 3}N_{\beta 1}N_{\gamma 4} \tag{3.181}$$

$$N_{20} = N_{\alpha 4}N_{\beta 2}N_{\gamma 4} \tag{3.182}$$

$$N_{21} = N_{\alpha 4}N_{\beta 3}N_{\gamma 4} \tag{3.183}$$

$$N_{22} = N_{\alpha 3}N_{\beta 4}N_{\gamma 4} \tag{3.184}$$

$$N_{23} = N_{\alpha 2}N_{\beta 4}N_{\gamma 4} \tag{3.185}$$

$$N_{24} = N_{\alpha 1}N_{\beta 3}N_{\gamma 4} \tag{3.186}$$

where:

$$N_{\alpha 1} = \frac{-1}{2 * (1-\alpha)(1+\alpha)}(1-\xi)(\alpha-\xi)(\alpha+\xi) \tag{3.187}$$

$$N_{\alpha 2} = \frac{1}{2 * \alpha(1-\alpha)(1+\alpha)}(1-\xi)(1+\xi)(\alpha-\xi) \tag{3.188}$$

$$N_{\alpha 3} = \frac{1}{2 * \alpha(1-\alpha)(1+\alpha)}(1-\xi)(1+\xi)(\alpha+\xi) \tag{3.189}$$

$$N_{\alpha 4} = \frac{-1}{2 * (1-\alpha)(1+\alpha)}(1+\xi)(\alpha-\xi)(\alpha+\xi) \ldots\ldots\ldots\ldots\ldots\ldots\ldots\ldots\ldots\ldots\ldots\ldots\ldots (3.190)$$

where $0 \leq \alpha \leq 1$.

$$N_{\beta 1} = \frac{-1}{2 * \beta(1-\beta)(1+\beta)}(1-\eta)(\beta-\eta)(\beta+\eta) \ldots\ldots\ldots\ldots\ldots\ldots\ldots\ldots\ldots\ldots\ldots\ldots\ldots (3.191)$$

$$N_{\beta 2} = \frac{1}{2 * (1-\beta)(1+\beta)}(1-\eta)(1+\eta)(\beta-\eta) \ldots\ldots\ldots\ldots\ldots\ldots\ldots\ldots\ldots\ldots\ldots\ldots\ldots (3.192)$$

$$N_{\beta 3} = \frac{1}{2 * (1-\beta)(1+\beta)}(1-\eta)(1+\eta)(\beta+\eta) \ldots\ldots\ldots\ldots\ldots\ldots\ldots\ldots\ldots\ldots\ldots\ldots\ldots (3.193)$$

$$N_{\beta 4} = \frac{-1}{2 * \beta(1-\beta)(1+\beta)}(1+\eta)(\beta-\eta)(\beta+\eta) \ldots\ldots\ldots\ldots\ldots\ldots\ldots\ldots\ldots\ldots\ldots\ldots\ldots (3.194)$$

where $0 \leq \beta \leq 1$.

$$N_{\gamma 1} = \frac{-1}{2 * \gamma(1-\gamma)(1+\gamma)}(1-\rho)(\gamma-\rho)(\gamma+\rho) \ldots\ldots\ldots\ldots\ldots\ldots\ldots\ldots\ldots\ldots\ldots\ldots\ldots (3.195)$$

$$N_{\gamma 2} = \frac{1}{2 * (1-\gamma)(1+\gamma)}(1-\rho)(1+\rho)(\gamma-\rho) \ldots\ldots\ldots\ldots\ldots\ldots\ldots\ldots\ldots\ldots\ldots\ldots\ldots (3.196)$$

$$N_{\gamma 3} = \frac{1}{2 * (1-\gamma)(1+\gamma)}(1-\rho)(1+\rho)(\gamma+\rho) \ldots\ldots\ldots\ldots\ldots\ldots\ldots\ldots\ldots\ldots\ldots\ldots\ldots (3.197)$$

$$N_{\gamma 4} = \frac{-1}{2 * \gamma(1-\gamma)(1+\gamma)}(1+\rho)(\gamma-\rho)(\gamma+\rho) \ldots\ldots\ldots\ldots\ldots\ldots\ldots\ldots\ldots\ldots\ldots\ldots\ldots (3.198)$$

where $0 \leq \gamma \leq 1$.

The integrations were carried out over 24 sampling points, as shown in Table 3.3:

Table 3.3: Sampling points for the 24 node isoparametric serendipity finite element.

$\alpha = \beta = \gamma = 0.8, 0.85, 0.9$			
Node No.	ξ	η	ρ
1	-0.8611	-0.33998* β	-0.8611
2	-0.3399* α	-0.8611	-0.8611
3	0.3399* α	-0.8611	-0.8611
4	0.8611	-0.3399* β	-0.8611
5	0.8611	0.3399* β	-0.8611
6	0.3399* α	0.8611	-0.8611
7	-0.3399* α	0.8611	-0.8611
8	-0.8611	0.33998* β	-0.8611
9	-0.8611	-0.3399	-0.3399* γ
10	0.8611	-0.3399	-0.3399* γ
11	0.8611	0.3399	-0.3399* γ
12	-0.8611	0.3399	-0.3399* γ
13	-0.8611	-0.3399	0.3399* γ
14	0.8611	-0.3399	0.3399* γ
15	0.8611	0.3399	0.3399* γ
16	-0.8611	0.3399	0.3399* γ
17	-0.8611	-0.33998* β	0.8611
18	-0.3399* α	-0.3399	0.8611
19	0.3399* α	-0.3399	0.8611
20	0.8611	-0.3399* β	0.8611
21	0.8611	0.3399* β	0.8611
22	0.3399* α	0.3399	0.8611
23	-0.3399* α	0.3399	0.8611
24	e=-0.8611	0.3399* β	0.8611

The corresponding weighting functions were as given in Table 3.4.

Table 3.4: Weighting for the 24 node isoparametric serendipity finite element.

Node No.	Weighting
1	0.34785 * 0.65214 * 0.34785
2	0.34785 * 0.65214 * 0.34785
3	-0.34785 * 0.65214 * 0.34785
4	-0.34785 * 0.65214 * 0.34785
5	0.34785 * 0.65214 * 0.34785
6	0.34785 * 0.65214 * 0.34785
7	-0.34785 * 0.65214 * 0.34785
8	-0.34785 * 0.65214 * 0.34785
9	0.34785 * 0.65214 * 0.65214
10	-0.34785 * 0.65214 * 0.65214
11	0.34785 * 0.65214 * 0.65214
12	-0.34785 * 0.65214 * 0.65214
13	-0.34785 * 0.65214 * 0.65214
14	0.34785 * 0.65214 * 0.65214
15	-0.34785 * 0.65214 * 0.65214
16	0.34785 * 0.65214 * 0.65214
17	-0.34785 * 0.65214 * 0.34785
18	-0.34785 * 0.65214 * 0.65214
19	0.34785 * 0.65214 * 0.65214
20	0.34785 * 0.65214 * 0.34785
21	-0.34785 * 0.65214 * 0.34785
22	-0.34785 * 0.65214 * 0.65214
23	0.34785 * 0.65214 * 0.65214
24	0.34785 * 0.65214 * 0.34785

The four node isoparametric tetrahedral finite element was developed from a four node tetrahedron shown in Figure 3.12. The coordinates of the nodes of the element are summarized in Table 3.5.

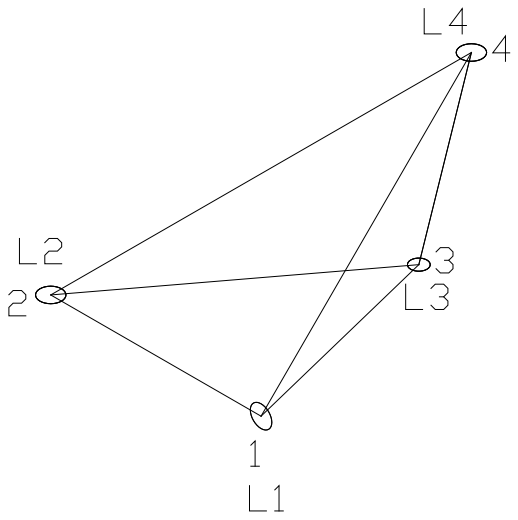

Figure 3.12: Four node isoparametric tetrahedral finite element

Table 3.5: Volume coordinates of the four node isoparametric tetrahedral finite element.

Node number	L_1	L_2	L_3	L_4
1	1	0	0	0
2	0	1	0	0
3	0	0	1	0
4	0	0	0	1

A trial function was selected as follows:

$$\phi = a_I + a_{II}\xi_i + a_{III}\eta_i + a_{IV}\rho_i \dots\dots\dots\dots\dots\dots\dots\dots\dots\dots\dots\dots\dots\dots\dots\dots\dots\dots\dots\dots. (3.199)$$

where:

a_t are the polynomial coefficients, $t = I \ to \ IV$

On applying the relevant nodal coordinate values, Equation 3.199 was written as:

$$\{\phi_i\} = [A]\{a_t\} \quad (3.200)$$

where:

$$\{\phi_s\}_{s=1}^{4} = \begin{Bmatrix} \phi_1 \\ \phi_2 \\ \phi_3 \\ \phi_4 \end{Bmatrix} \quad (3.201)$$

and:

$$[A] = \begin{bmatrix} 1 & \xi_1 & \eta_1 & \rho_1 \\ 1 & \xi_2 & \eta_2 & \rho_2 \\ 1 & \xi_3 & \eta_3 & \rho_3 \\ 1 & \xi_4 & \eta_4 & \rho_4 \end{bmatrix} \quad (3.202)$$

$$\{a_t\} = \begin{Bmatrix} a_I \\ a_{II} \\ a_{III} \\ a_{IV} \end{Bmatrix} \quad (3.203)$$

By a process of matrix inversion, the values of the polynomial coefficients were obtained as follows:

$$\{a_t\} = [A]^{-1}\{\phi_s\} \quad (3.204)$$

$[A]^{-1}$ was obtained by Crammers rule [185] in Equation 3.205

$$[A]^{-1} = \frac{1}{|A|}\left[C_{ij}\right] \quad (3.205)$$

hence:

$$[A]^{-1} = \frac{1}{C_{11} + C_{21} + C_{31} + C_{41}} \begin{bmatrix} C_{11} & C_{21} & C_{31} & C_{41} \\ C_{12} & C_{22} & C_{32} & C_{42} \\ C_{13} & C_{23} & C_{33} & C_{43} \\ C_{14} & C_{24} & C_{34} & C_{44} \end{bmatrix} \quad (3.206)$$

where:

C_{ij} are the co-factors of $[A]$ matrix

Substituting for the coefficients a_t in Equation 3.199 yields Equation 3.207:

$$\phi = \sum_{i=1}^{4}\left(A_{1i}{}^{-1}.\phi_i\right) + \sum_{i=1}^{4}\left(A_{2i}{}^{-1}.\phi_i\right)\xi + \sum_{i=1}^{4}\left(A_{3i}{}^{-1}.\phi_i\right)\eta + \sum_{i=1}^{4}\left(A_{4i}{}^{-1}.\phi_i\right)\rho \ldots\ldots (3.207)$$

Rearranging gives:

$$\phi = \sum_{i=1}^{4}\left(A_{1i}{}^{-1} + A_{2i}{}^{-1}\xi + A_{3i}{}^{-1}\eta + A_{4i}{}^{-1}\rho\right)\phi_i \ldots\ldots\ldots\ldots\ldots\ldots\ldots\ldots\ldots\ldots\ldots\ldots\ldots (3.208)$$

The resulting shape functions were determined as follows:

$$L_1 = \frac{C_{11} + C_{12}\xi + C_{13}\eta + C_{14}\rho}{C_{11} + C_{21} + C_{31} + C_{41}} \ldots\ldots\ldots\ldots\ldots\ldots\ldots\ldots\ldots\ldots\ldots\ldots\ldots\ldots\ldots\ldots (3.209)$$

$$L_2 = \frac{C_{21} + C_{22}\xi + C_{23}\eta + C_{24}\rho}{C_{11} + C_{21} + C_{31} + C_{41}} \ldots\ldots\ldots\ldots\ldots\ldots\ldots\ldots\ldots\ldots\ldots\ldots\ldots\ldots\ldots\ldots (3.210)$$

$$L_3 = \frac{C_{31} + C_{32}\xi + C_{33}\eta + C_{34}\rho}{C_{11} + C_{21} + C_{31} + C_{41}} \ldots\ldots\ldots\ldots\ldots\ldots\ldots\ldots\ldots\ldots\ldots\ldots\ldots\ldots\ldots\ldots (3.211)$$

$$L_4 = \frac{C_{41} + C_{42}\xi + C_{43}\eta + C_{44}\rho}{C_{11} + C_{21} + C_{31} + C_{41}} \ldots\ldots\ldots\ldots\ldots\ldots\ldots\ldots\ldots\ldots\ldots\ldots\ldots\ldots\ldots\ldots (3.212)$$

3.6.2. CONVERGENCE OF THE ELEMENT EQUATIONS

The convergence of finite elements is traditionally established by ensuring that all the terms in the trial function polynomial are present to the highest order of the polynomial. For a four node linear element, the trial function takes the form of Equation 3.150. Consequently, the shape

functions must contain the independent variable up to the third power in the shape functions. On inspection of Equations 3.150 and 3.199, it is evident that the all powers of the polynomial are present, as the equations are of the form:

$$N = k(1 + s\xi)(1 + t\xi)(1 + r\xi) \ldots \ldots \ldots \ldots \ldots \ldots \ldots \ldots \ldots \ldots \ldots \ldots \ldots \ldots \ldots \ldots \ldots \ldots \ldots \ldots \ldots \ldots \ldots \ldots (3.213)$$

which can be re-written as:

$$N = k[1 + (s + t + r)\xi + (st + sr + tr)\xi^2 + (str)\xi^3] \ldots . \ldots \ldots \ldots \ldots \ldots \ldots \ldots \ldots \ldots \ldots \ldots (3.214)$$

Consequently, the 24 node finite element is complete and conforming. The four node finite element is based on a linear variation in all three independent variables. Consequently, the trail functions for the ξ and η independent variables are of the form:

$$\emptyset = b_0 + b_1\xi \ldots \ldots \ldots \ldots \ldots \ldots \ldots \ldots \ldots \ldots \ldots \ldots \ldots \ldots .. \ldots \ldots \ldots \ldots \ldots \ldots \ldots \ldots .. \ldots \ldots \ldots \ldots \ldots \ldots \ldots (3.215)$$

On inspection of the shape functions, it is evident that all the powers of the polynomial are present and the element was complete and conforming. With the elements confirmed as complete and conforming, convergence was established.

3.6.3. COUPLING OF DIFFERENT TYPES OF FINITE ELEMENTS

The assembly of the two types of finite elements required the development of the system matrix from two types of finite elements. Equation 3.216 is the governing equation for equilibrium structural analysis.

$$\int_V [B]^T[C][B]\{d\}.\,dV = \int_V [B]^T\{X\}\{d\}.\,dV + \int_S [B]^T\{P\}\{d\}.\,ds \ldots . \ldots \ldots \ldots \ldots . \ldots (3.216)$$

The development of the constitutive, strain displacement, displacement matrices was based on a 3-D coordinate system for isotropic stress conditions. The application of this formulation to the

two types of finite elements was compatible, with the difference being the manner in which the assembly of the elemental stiffness matrices was achieved.

The assembly of a large number of meso-scale finite elements generates a system matrix of considerable size. Coupling the output at this length scale to the macro-scale required the matching of the meso-scale assembly to a macro-scale element of much lower order in a non-conforming meshing process [155]. This involved the elimination of some nodal points on the outer surface of the assembly of meso-scale finite elements. Several schemes to achieve this are available [156]. Two schemes were implemented as follows. In the first approach, the nodal values at the corresponding nodes of the two length scales were correlated with all other nodal values approximated by the interpolating function along the boundary. In the second approach, a curve of best fit through the nodal values along a boundary was obtained and nodal values from this curve were adopted. Results of the two approaches are provided.

3.6.4. LINKING OF THE STRUCTURE FACTORS TO THE GOVERNING EQUILIBRIUM EQUATION

The fundamental requirement is that the elements incorporate the intrinsic stress profile generated at lower length scales. This was achieved by the application of the network shape factor and the plane shape factors to generate the associated stress profile. These scalar factors were defined along the boundary of the meso-scale, which corresponded to PSB and PA forming cell structures and sub-grain boundaries [2, 141]. These dislocation structures alongside mobile dislocations within the body of the grain were the principal contributors to plastic flow and were therefore the focus of the implementation.

Considering the network structure factor of a section of the cell structure boundary as defined in Equation 3.133 in the development of the NSF, the structure of the overall cell structure boundary may be obtained from the assembly represented by:

$$\mathrm{NSF} = \sum_{i=1}^{n_P} NSF_i \left(\sum_{j=1}^{m_p} PSF_i\left(r, \eta_x, L_p\right) \right) \quad (3.217)$$

where:

m_p	is the number of planar structures involved in each network structure
n_P	is the number of network structures involved in the material matrix
η_x	is the orientation tensor of the slip system with respect to the crystal/grain boundaries.

However, the representation in Equation 3.217 does not readily apply to the finite element discretization provided. Instead, values of the network structure factor were evaluated at the boundaries of a unit finite element where the boundaries were taken as concentrations of dislocation networks. To cater for dislocations dispersed within the material matrix, statistically necessary dislocations SND [186] were introduced in the body of the finite element, while geometrically necessary dislocations GND [143, 176] were used to characterize the grain boundaries. Network structure factor were defined within the finite element to represent each of these dislocation populations. The contribution of these scalar quantities at the finite element nodes were evaluated using the relation:

$$NSF_{2i} = \sum_{i=1}^{t} NSF_{gnd}\,.\,N_i + NSF_{snd}\,.\,N_i \ldots\ldots\ldots\ldots\ldots\ldots\ldots\ldots\ldots\ldots\ldots\ldots\ldots\ldots\ldots . \ldots . \ldots\ldots\ldots . (3.218)$$

where:

NSF_{gnd}	is the network structure factor accounting for geometrically necessary dislocations
NSF_{snd}	is the network structure factor accounting for statistically necessary dislocations
NSF_{Si}	is the network structure factor at finite element node *i* due to dislocations dispersed over the material matrix.

It was also necessary to specify the network structure factor in tensor form corresponding to the Cartesian coordinate system. The notation adopted was to define the network structure factor vector as the product of the scalar network structure factor multiplied by the stress tensor at the peak point along the POLR, and normalized such that the peak component corresponded to the network structure factor value.

The equilibrium energy equation was therefore obtained as:

$$\int_V [B]^T[C][B]\{d\}dV = \int_V [B]^T\{X\}\{d\}dV + \int_S [B]^T\{P\}\{d\}ds + W_{NSF} \dots\dots\dots\dots\dots (3.219)$$

The work done on the dislocation structures was developed as follows:

$$W_{NSF} = \int_V [\sigma]\{\varepsilon\}^T dV + \int_S [\sigma]\{\varepsilon\}^T dS \dots\dots\dots\dots\dots\dots\dots\dots\dots\dots\dots\dots\dots\dots\dots\dots\dots\dots (3.220)$$

The first term provided for dislocation driven energy dissipation within the bulk of the element, while the second provided for energy dissipation at the grain boundary. The former comprised the dissipation due to mobile dislocations within the bulk of the grain, while the latter comprised dislocation structure rearrangements which included dislocation emission and trapping activities within the grain boundary that resulted in the increase in the boundary's inclination angle.

To account for the evolution within the bulk of the element, Argon's relation for the stress σ_m driving the mobile dislocations [187] was applied:

$$\rho_m = \left(\frac{\sigma_m}{\alpha_{Fe} G \boldsymbol{b}}\right)^2 \dots\dots\dots\dots\dots\dots\dots\dots\dots\dots\dots\dots\dots\dots\dots\dots\dots\dots\dots\dots\dots\dots\dots\dots\dots\dots\dots\dots (3.221)$$

where:

ρ_m	is the density of mobile dislocations
G	is the shear modulus
α_{Fe}	is the constant of proportionality (0.3 for Fe).

The mobile dislocations were considered a component within the statistically necessary dislocations. A plot of the square root of the dislocation density versus the network structure factor for each dislocation type, for the various dipole configurations was obtained. A line of best fit was obtained through these points and used to relate the network structure factor and the root

of the dislocation density. This result was a key characteristic of the meso-scale model, and is summarised in Equation 3.222:

$$\sqrt{\rho_m} = \Pi_\rho(NSF) \quad (3.222)$$

where:

Π_ρ is the polynomial relating the root of the grain's dislocation density and the NSF.

Hence:

$$\sigma_m = \alpha_{Fe} G\boldsymbol{b}.\Pi_\rho[NSF] \quad (3.223)$$

In this form, the network structure factor matrix is a 6x6 vector whose components are proportional to the 6 independent stress tensor components in the Cartesian coordinate axes. In addition:

$$[\varepsilon]^T = [B_V]^T\{d\} \quad (3.224)$$

where:

B_V is the strain displacement matrix for the bulk of the grain containing the mobile dislocations.

Consequently:

$$\int_V [\sigma]\{\varepsilon\}^T dV = \alpha_{Fe} G\boldsymbol{b} \int_V \Pi_\rho[NSF][B_V]^T\{d\}dV \quad (3.225)$$

The density of dislocations in the grain boundary was obtained from Equation 3.222 and the resulting work done in moving the dislocations in the bulk of the grain was derived from Equation 3.225. A plot of the dislocation density versus the network structure factor for each dislocation type, for the various dipole configurations was obtained. Again, a line of best fit was obtained through these points and was used to relate the network structure factor and the

dislocation density. This relation defined a key characteristic of the meso-scale model, and is given in Equation 3.226 as:

$$\rho_b = \Pi_b(NSF) \quad (3.226)$$

where:

Π_b is the polynomial relating the grain boundary dislocation density and the NSF

ρ_b is the density of grain boundary dislocations.

In addition, a plot of the first POLR peak stress versus the corresponding network structure factor was obtained for each dislocation type, for the various dislocation dipole configurations. A line of best fit was obtained from this plot and was used to relate the network structure factor and the Peierl's stress in the grain boundary. This relation, obtained in this work, is given in Equation 3.227.

$$\sigma = \Pi_x(NSF) \quad (3.227)$$

where:

Π_x is the polynomial relating the POLR peak stress and the NSF

Stress from Equation 3.227 was used as an input in the second term of Equation 3.220 with the strain obtained from Equation 3.224 to obtain the net force acting in the grain boundary:

$$\int_S [\sigma]\{\varepsilon\}^T dS = \int_S \Pi_x(NSF)[B_S]^T\{d\}dS \quad (3.228)$$

The final relation for the work done in the movement and reconstruction of dislocation structures is given by:

$$W_{NSF} = \alpha_{Fe} G\boldsymbol{b} \int_V \Pi_\rho[NSF][B_V]^T\{d\}dV + \int_S \Pi_x(NSF)[B_S]^T\{d\}dS \quad (3.229)$$

Equation 3.229 captures the contribution of the dislocation network structure within the lattice. These terms account for the contribution of the dislocations to the elastic strain energy, and therefore represent the inherent material in-homogeneity and the spatial plasticity of the material.

3.6.5. MESH GENERATION

A mesh was developed to represent the shape of the grains within the material as accurately as possible. In addition, the mesh generation had to capture the assembly of grains into the matrix as accurately as possible. The combination of the 24 node finite elements and the four node finite elements was chosen for this purpose. The tetrahedral finite elements were selected to account for those zones of adjacent grains that were severely distorted and therefore not suited for modelling with the 24 node finite element. Where extensive work hardening had taken place, the grains would be considerably elongated and these elements would shrink considerably.

The mesh for the meso-scale element was developed manually using the "Adapted mesh template" and the "Grid based approach" [155]. A 2-D rectangular grid was prepared using the typical grain length and width obtained from "grain size estimate and distribution". A micrograph was obtained using a Universal Microscope (Optika B-353 MET) at 256X magnification, with microstructural analysis carried out using "Microstructural Characterizer 3.0" software developed by TCR Advanced Engineering, India. A grain size of 200 μm was obtained [188], and the grid was superposed onto the micrograph and adjusted to better match the distribution of the grains. Nodal data was then obtained and used to characterize the meso-scale discretization for the FEM computation.

Nodal points were obtained in a two step process. The first step was to discretize the whole space into macro-scale elements using the eight node cubic element. The second step was to identify the zone undergoing plastic deformation, and this region was discretized into meso-scale finite elements. This second stage was achieved in three steps. The first step determined a full scale discretization using average length, width and height dimensions based on the dimensions obtained from the 2-D "Adapted mesh template" described above. The width and height of each element were taken as the width of the element from the 2-D mesh generation exercise, while the length of the element was taken as the length of the 2-D mesh generation exercise. The second

step used a suitable algorithm to define the finite elements over this space in a process that eliminated surplus node points. A rectangular specimen was used in the macro-scale simulations with dimensions to mimic the dimensions of the proposed experimental work piece. The third step defined the element identification number.

3.6.6. CONNECTION OF THE MESO-SCALE TO THE MACRO-SCALE

The meso-scale finite elements were evaluated and the resulting stiffness and strain gradient matrix defined. A coupling of the meso-scale finite elements to the respective macro-scale finite element containing them was achieved by elimination of internal node points in a process known as static condensation proposed by Yang and Hsieh [189]. The condensation process involved determining the contributions of the forces and displacements at the nodes of the meso-scale finite elements to the nodes of the macro-scale finite elements containing them. With this relationship established, the nodes of the meso-scale finite elements were then deleted from the mesh to leave the nodes of the macro scale finite elements, together with the effective forces and displacements at the remaining nodes. The result was a mesh with fewer degrees of freedom that represented the macro length-scale and a reduced computational load. The effects of the grain boundary contribution were contained in a surface force that was condensed to the macro-scale finite element nodes and used in the computation of the quasi-static response of the structure.

CHAPTER 4: RESULTS AND DISCUSSION

4.1. PATH OF LEAST RESISTANCE

Sections 4.1.1 and 4.1.2 give results for dislocation cores in BCC Fe lattice loaded using the rigid body movement (RBM) method, while Sections 4.1.3 and 4.1.4 give results for dislocation cores in BCC Fe-C lattice loaded using the same method. Sections 4.1.5 and 4.1.6 summarize the characteristic peak stress components for the Fe and the Fe-C lattices respectively, also loaded using the same method.

Sections 4.1.7 and 4.1.8 give results for dislocation cores in BCC Fe lattice loaded using the free motion of dislocation core atoms (FMDCA) method. Sections 4.1.10 and 4.1.11 give results for dislocation cores in BCC Fe-C lattice loaded using the same method. Sections 4.1.9 and 4.1.12 summarize the characteristic peak stress components for the Fe and Fe-C lattices respectively, also loaded using the same method.

4.1.1. MOTION OF DISLOCATION CORES – RBM METHOD

Figures 4.1 to 4.8 show stress tensor components for dislocations moving in specific directions. These results provide insight into the stresses required to move the dislocation core atoms in Fe and Fe-C lattices, while maintaining lattice cohesion.

4.1.1.1. Mechanism of Motion of the Dislocation Core Atom

Simulations were carried out on the lattice to evaluate the stress components acting on four different types of dislocation cores in the quasi equilibrium state. The results are shown in Table 4.1. These stress values represent the retained stress components due to lattice distortion, which need to be overcome by an externally applied stress to enable motion of the atoms about the dislocation core.

The simulated results reveal that the lowest stress for the screw and the mixed dislocations is the σ_{11} tensor component which corresponds to the $[100]$ direction, while the lowest stress for the edge dislocation is the σ_{22} tensor component which corresponds to the $[010]$ direction. The $\langle 100 \rangle$ directions are of interest as dislocations in these directions contribute substantially to the flow stress [190] and may be formed by the interaction of two $\frac{1}{2}[111]$ dislocations.

Table 4.1: Stress tensor components for four types of dislocations.

Dislocation type	Stress (GPa)					
	σ_{11}	σ_{12}	σ_{13}	σ_{22}	σ_{23}	σ_{33}
Pure screw	1.48	-6.28	-5.16	4.13	-5.61	3.78
70.53^{o} screw	-2.16	-7.64	-5.56	4.63	-5.75	2.68
35.26^{o} screw	1.50	-6.22	-5.10	4.35	-5.41	4.00
Pure edge	2.24	-7.17	-5.07	1.93	-5.84	3.80

The dissociation of screw dislocation cores has been known to occur across adjacent $\{110\}$ planes [58, 59, 94]. In addition, the spreading of the edge dislocation core to adjacent $\{112\}$ planes has been reported [35]. The combination of pairs of $\langle 100 \rangle$ motion suggests that pairs of $\langle 100 \rangle$ stresses are responsible for the [110] type motion necessary for dislocation core reconstruction across the [110] zone axis. Additionally, the intersection of non-coplanar dislocations and their interaction may be enhanced by the presence of the [110] zone axis. It is recommended that analysis of combinations of dislocation core stress components be used to explain dislocation core spreading and core-core interaction.

The precise motion of the individual atoms forming the dislocation core has not been established, but the values of the stress tensor components suggest that motion in the [100], [010] and [001] directions are to be expected. This motion corresponds to atomic movement in different $\{110\}$ and $\{112\}$ planes belonging to the given $\langle 110 \rangle$ zone and two possible mechanisms for this motion are suggested. The first is an "out-of-plane motion" in which atoms ahead of the dislocation move out of the slip plane with corresponding motion of atoms into the slip plane behind the dislocation line. This results in a "peeling" of atoms around the dislocation line, resulting in dislocation motion. The second is an "in-plane" motion where atoms shuffle along the slip plane resulting in dislocation motion. The very nature of a 3-D lattice suggests that the "out-of-plane" motion is necessary for the cleavage of the lattice to enable dislocation motion. Additionally, the presence of the [110] zone axis intersecting in the $[\bar{1}1\bar{1}]$ direction, enables the "out-of-plane" motion to occur at the lower stress levels corresponding to the [100], [010] and [001] directions. Consequently, it is concluded that the "peeling" of atoms is the most probable mechanism for dislocation motion in BCC dislocation cores. Additionally, this visualization is

consistent with observations of moderate non-planar spreading of dislocation cores in BCC lattices [35, 96]. It is also noteworthy that the difference between the values of direct stress components for the edge dislocation is smaller than for the other dislocation types. This further reinforces the thinking that the "peeling action" is active when considered alongside empirical evidence of the higher mobility of the edge dislocation [118]. However, these results are a snapshot of the equilibrium lattice condition, and a more comprehensive understanding may be obtained from studying the stress profiles resulting from the motion of dislocations.

The "peeling action" is illustrated in Figure 4.1. These results were obtained from the application of a $[2, \bar{2}, 2]$ kN load on the moving atoms on one side of the slip plane, while allowing for normalized displacements proportional to the driving force. The displacements were recorded in directions corresponding to the Cartesian coordinate system over 70 displacement increments in the Fe lattice. For an in-plane motion to occur, a linear X-Y curve was expected. Instead, both graphs demonstrate that reversal in direction of motion occurred and therefore the "peeling" mechanism was verified.

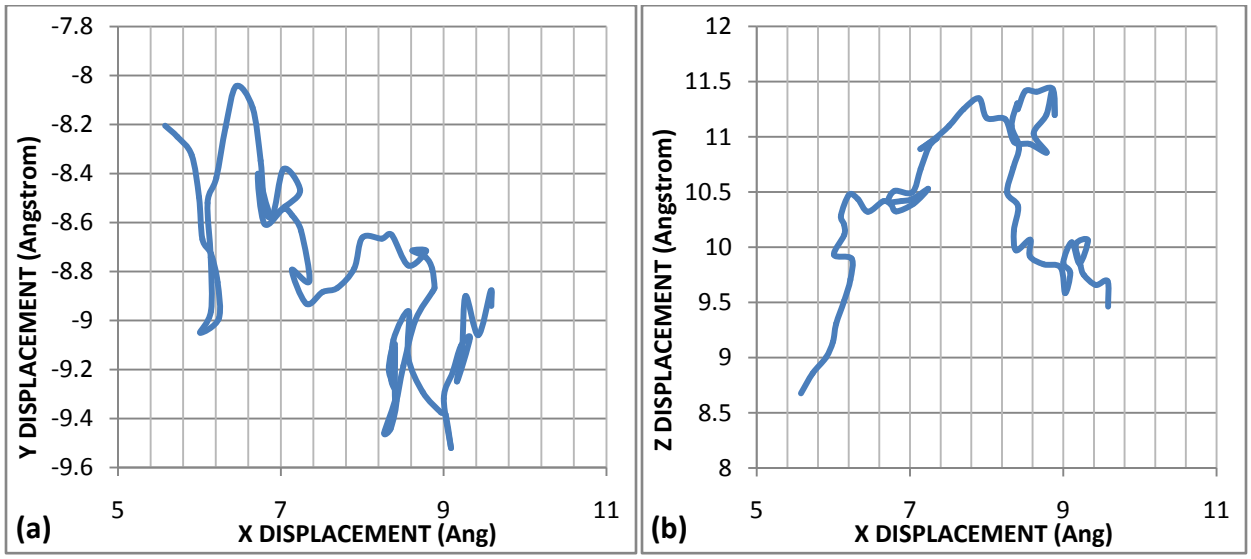

Figure 4.1: (a) X versus Y, (b) X versus Z, displacement of core atoms as a dislocation moves in Fe in the $[1\bar{1}1]$ direction –magnitude of displacement - X1.

These simulations were then repeated on the same lattice, with an increase in the magnitude of the atomic displacements by a factor of 100. The resulting path is illustrated in Figure 4.2, and

reveals that reversals of direction of atom motion continues to occur independent of the magnitude of the applied load. These results provide additional evidence that the "peeling action" in dislocation core atoms does occur.

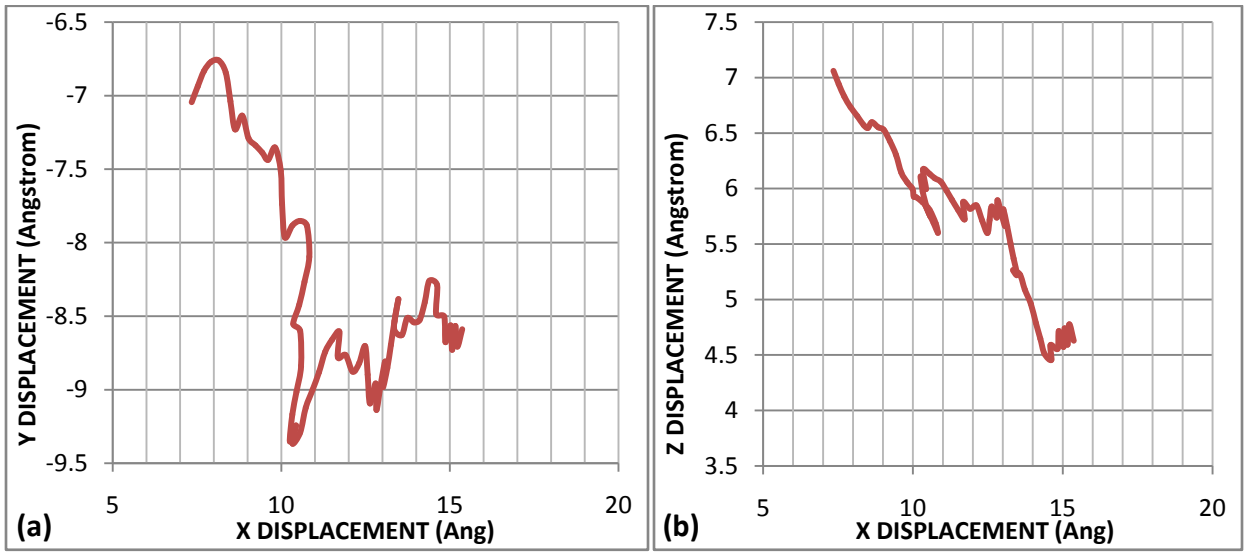

Figure 4.2: (a) X versus Y, (b) X versus Z, displacement of core atoms as a dislocation moves in Fe in the $[1\bar{1}1]$ direction –magnitude of displacement - x100.

Comparison between Figures 4.1a and 4.2a, and Figures 4.1b and 4.2b, reveals that a smaller displacement provides a much finer tracking of an atom's motion. In addition, the overall atom displacement in the X-Y direction is similar, while that in the X-Z direction is reversed. This difference is attributed to the displacement direction obtained from the net driving force. A smaller displacement is expected to provide a more realistic path of the atom's motion.

4.1.1.2. Stress Analysis of the Dynamic Dislocation

The stress components σ_{11} and σ_{22} correspond to motion on the (011) and (101) planes respectively, and involves the displacement of atoms away from the (110) glide plane ahead of the dislocation core. The stress component σ_{33} corresponds to motion along the (110) plane, and involves displacement of atoms along the (110) glide plane ahead of the dislocation core. The Cartesian coordinate notation adopted in this work is illustrated in Figure 4.3.

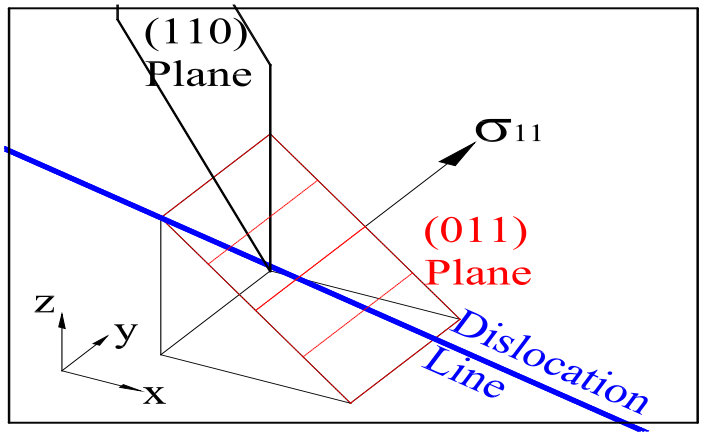

Figure 4.3: Relationship between the σ_{11} stress component and the (011) and (110) planes

Figures 4.4 and 4.5 show the curves of the lattice stress about the dislocation core as the dislocation moves along the direction of its Burger's vector. These results were obtained from the application of a $[2, \bar{2}, 2]$ kN load. All the dislocations generated cyclic stress curves for all stress components, differing in the pattern formed, magnitude of values, and the amplitudes of individual curves. The cyclic behaviour suggests that the movement of rows of atoms past adjacent rows is synchronised, enabling the simulation to detect the cyclic variation. The positive and negative values are interpreted as tensile and compressive stresses respectively, with the direct stresses positive (except for σ_{11} component where the troughs dipped below zero) and the shear stresses negative. It is expected that dislocation motion would follow the POLR, which involves changes in displacement of atoms along the path provided by the minimum direct stress component.

The stress cycle for the screw dislocation is given in Figure 4.4a. The POLR is in the σ_{11} direction over most of the path. At some point, the curve for σ_{11} intersects that of σ_{33} and exceeds it for a short potion of the cycle. Over this period, σ_{33} is at its lowest value and its curve provides the POLR, after which σ_{11} curve resumes as the POLR. This path oscillates between 1.26 GPa and 2.27 GPa with saddle points at 1.65 GPa and at 2.27 GPa. The POLR values compare well with published values of the Peierl's stress of 1.2 - 1.8 GPa by Chaussidon et al. [181] and 1.3 - 1.9 GPa by Ventelon [191] for BCC Fe.

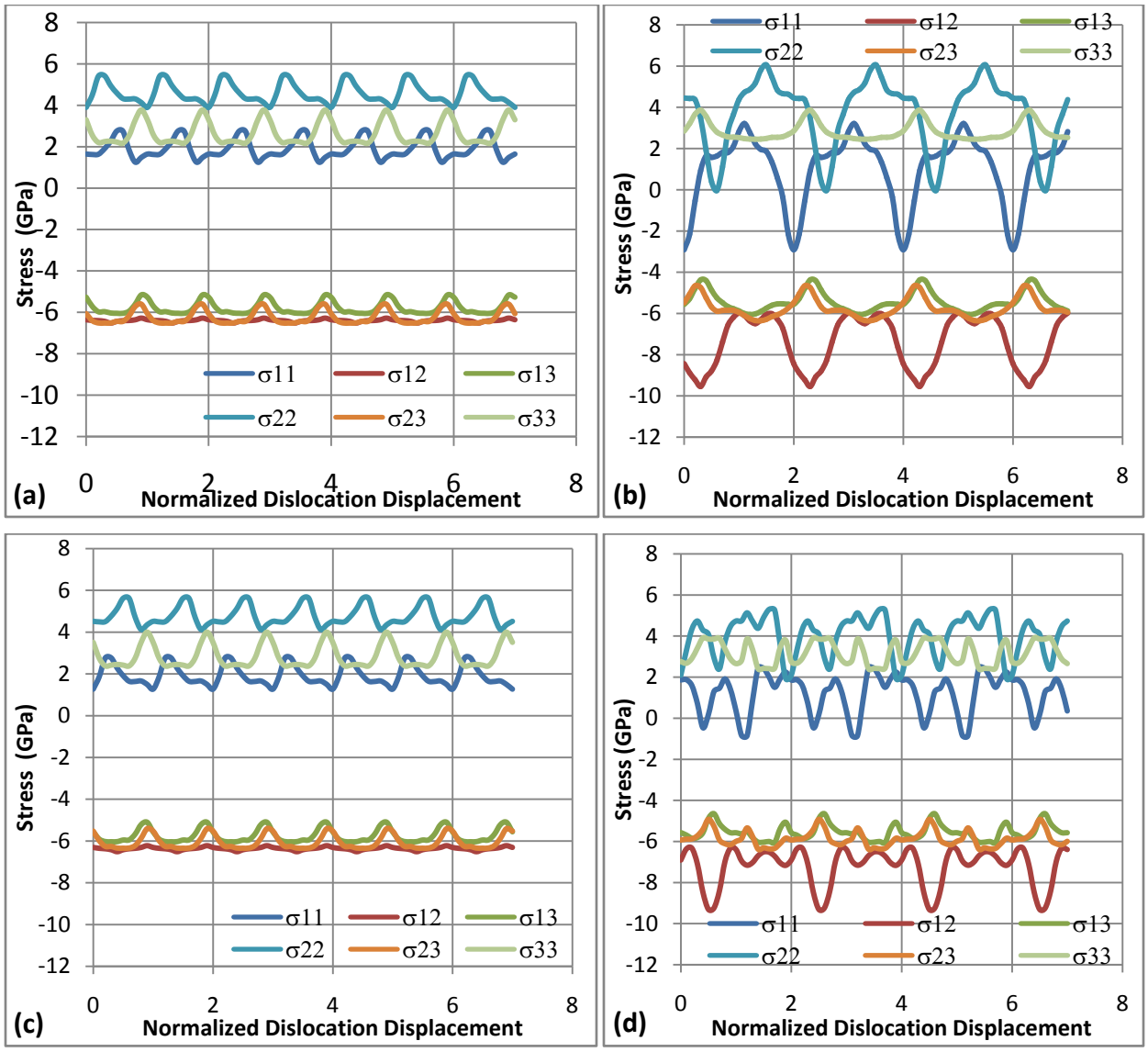

Figure 4.4: Stress variation as (a) screw, (b) 70.53° screw, (c) 35.26° screw, (d) edge, dislocations in Fe move in the (a) $[1\bar{1}1]$, (b) $[\bar{1}10]$, (c) $[\bar{1}11]$, (d) $[\bar{1}12]$, directions.

The observed sequence where different stress components provide the minimum value stress path supports the hypothesis that dislocation motion occurs predominantly by the "peeling" of atoms around the dislocation core, as a stress-enabled mechanism. This mechanism is consistent with empirical observations that have confirmed that dislocation motion is jerky at low temperatures [111]. It is suggested that the jerks may occur when atom motion along the lowest stress path encounters direction changes that are accompanied with a reduction in the resisting

stress. The shear stresses obtained are of a higher order of magnitude (-6.41 GPa) than the direct stresses. Additionally, the magnitude of the shear stresses is of the same order of magnitude as the peak direct stress of 5.41 GPa. These higher stress values are an indication of the value of the stress components required to generate catastrophic fracture of the lattice. It is reasonable to infer that the ultimate tensile stress should be in the order of 2.8 times the yield stress. This result is obtained by comparing the maximum stress values related to catastrophic failure and those related to dislocation motion, and hence material yielding.

The stress component cycles for the 70.53^o screw dislocation are presented in Figure 4.4b. The POLR is along the direction corresponding to the σ_{11} stress component. It is noteworthy that this stress component traverses the zero stress value, with a maximum positive value of 3.21 GPa and a maximum negative value of -2.91 GPa. This curve intersects that of σ_{22} at 1.91 GPa and σ_{33} at 2.54 GPa at different periods of the cycle. The intersection occurs over small intervals, and the resulting POLR for the atoms around the dislocation core traverses three directions. The larger maximum value of σ_{11} (although negative in sign) implies that a 70.53^o screw dislocation is harder to move than a pure screw dislocation. In comparison with results for the pure screw dislocation, the maximum direct stress value increases to 6.06 GPa, with a corresponding increase of the maximum shear stress to -9.55 GPa. The larger value of the maximum shear stress and the divergence in shear stress curves implies that a narrow band catastrophic ultimate stress would not result from the presence of 70.53^o screw dislocations. The larger amplitude of the stress cycles implies an increase in the degree of difficulty for motion of this dislocation. These results are supported by empirical findings of exceptionally high Peierl's stress experienced by the 70.53^o screw dislocation [60].

The stress component curves for the 35.26^o screw dislocation are given in Figure 4.4c. The POLR is again along the direction corresponding to the σ_{11} stress component. This stress component oscillates between a maximum value of 2.76 GPa and a minimum value of 1.27 GPa. The POLR changes direction when the σ_{33} stress component curve intersects the σ_{11} stress component curve at about 2.42 GPa. A maximum magnitude shear stress of -6.51 GPa is recorded, with a spread of the shear stress components similar to that of the pure screw

dislocation. This implies that a narrow band catastrophic ultimate stress is possible for the 35.26^{o} screw dislocation.

Results on simulations for the edge dislocation shown in Figure 4.4d show the largest number of peaks and troughs of the four types of dislocations considered. For the other dislocations, stress component curves exhibit a single crest and a single trough with possible single saddle point. For the edge dislocation, three crests are recorded for σ_{11}, σ_{22} and σ_{33}. Similar curves are obtained for the shear stress components. The POLR is again provided by σ_{11} which spans the range -0.848 to 2.45 GPa. Along this curve, intersection with σ_{22} at 1.93 GPa and σ_{33} at 2.4 GPa occurs, suggesting that a change in direction into adjacent zone $\langle 110 \rangle$ axis is possible. The availability of a larger number of atom motion directions, only replicated by the 70.53^{o} screw dislocation, is envisaged as a possible mechanism for the greater mobility of the edge dislocation. This is despite a larger maximum stress value of 2.4 GPa for the POLR, higher than that of the screw dislocation. Additionally, this dislocation has the lowest magnitude stress of -0.848 GPa, which may enhance edge dislocation motion over other types of dislocations. The spreading of the shear stress curves also suggests that a narrow band catastrophic ultimate stress would not result from this type of dislocation.

Figure 4.5 reveals that the edge dislocation provides the least resolved stress curve (the resolved stress is the stress resultant in the direction of the Burger's vector), while the pure screw dislocation has a similar curve at an elevated mean. It is therefore inferred that the edge dislocation possesses the greatest mobility consistent with empirical findings [118]. The 70.53^{o} screw dislocation has a curve with a much higher amplitude and peak stress. This is again consistent with empirical findings which report its high Peierl's stress [192]. Also noteworthy is that the magnitude of the resolved stress is much higher than both experimental and calculated Peierl's stresses [35, 181]. Therefore, it is concluded that the Peierl's stress is related to the active stress components, and not to the overall resolved shear stress, while dislocation mobility is related to the resolved stress amplitude.

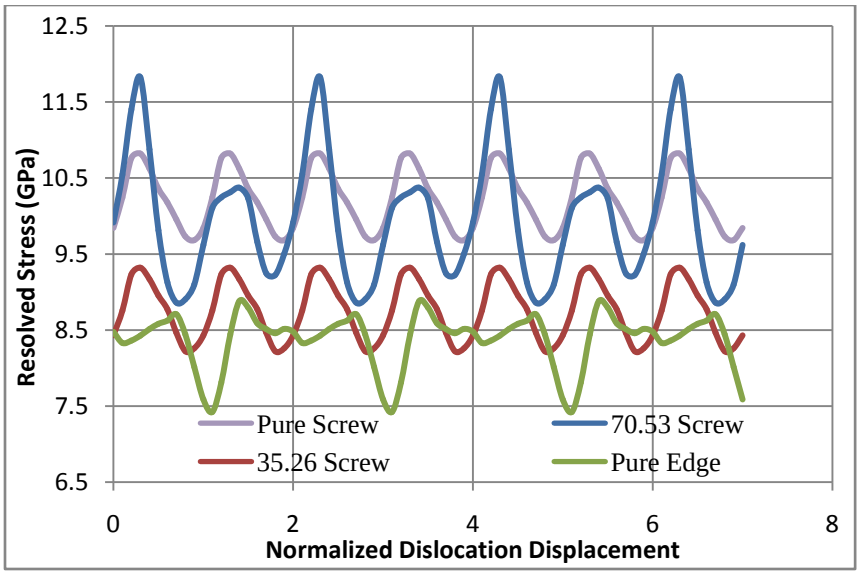

Figure 4.5: Resolved stress variation as dislocations in Fe move in the direction of their Burger's vector.

The curves in Figures 4.4 and 4.5 demonstrate that the EAM formulation implemented has the required sensitivity to differentiate between dislocation types. This supports the earlier assertion that dislocation dynamics based upon the EAM model is a viable tool in material defect analysis. Specifically, it is suggested that the combinations of stress component curves result in the POLR, and therefore determine the Peierl's stress profile. The lack of symmetry of the stress curves result from the effects of the twinning/anti-twinning asymmetry of the BCC lattice, and this is more pronounced for the edge dislocation. The short range nature of the EAM potential results in a stress computation at the dislocation core only. A more comprehensive approach would be to generate stress components due to dislocation cores at locations removed from the dislocation. This would be invaluable in the study of dislocation interaction with other dislocations, obstacles and grain boundaries. Thus, there is need for the development of a longer range potential, specifically suited to dislocation interaction analysis.

A better resolution of the dislocation core evolution was realized in this application of the EAM model for the study of dislocation cores. The graphical presentation reveals that the complex mechanism of dislocation motion is dependent on atomic movements around the dislocation core. The use of the POLR analysis illustrates the contribution of the {110} planes in dislocation motion by the "peeling" of atoms around the dislocation core. It is noted that a narrow band

catastrophic ultimate stress is only probable for the pure screw dislocation and the 35.26^{o} screw dislocation.

4.1.2. EFFECT OF RECONSTRUCTION DEFECTS - RBM METHOD

4.1.2.1. Motion of Atoms Forming the Dislocation

The stress tensor components about the dislocation core resulting from the formation of reconstruction defects were evaluated and the results are presented in Table 4.2. These stress components reveal that the direction of least resistance is along the σ_{11} tensor component for a $[\bar{1}1\bar{1}]$ dislocation line direction. This observation is similar to that made for the screw dislocation core without reconstruction defects. This suggests that the mechanism for dislocation motion proposed for a screw dislocation core without reconstruction defects remains active. The minimum retained stress component for both reconstructed screw dislocations is in the [100] direction with the symmetric screw dislocation exhibiting a lower minimum stress than the anti-symmetric screw dislocation. It is noted that the stress component along the [100] direction acts outside the slip plane, while the stress component along the [001] direction acts along the slip plane considered. This further supports the assertion that the "peeling of atoms" around the dislocation core (which would have been enhanced by an out-of-plane stress) is the more likely mechanism for stress enabled dislocation core evolution.

Table 4.2: Stress tensor components for screw dislocations with reconstruction defects.

Dislocation Core Type	Stress (GPa)					
	σ_{11}	σ_{12}	σ_{13}	σ_{22}	σ_{23}	σ_{33}
Pure screw	1.48	-6.28	-5.16	4.13	-5.61	3.78
Symmetric screw	0.93	-8.05	-5.41	2.13	-5.53	4.24
Anti-symmetric screw	1.58	-6.16	-5.20	4.86	-5.83	3.54

The formation of reconstruction defects of the non-screw dislocations has not been detected by empirical work or suggested by *ab-inito* work. This may be explained as follows: the formation of reconstruction defects for pure screw dislocation cores involves the core splitting into three {111} zone planes. For the non-screw dislocations where the dislocation line is coincident with the $[\bar{1}1\bar{1}]$ direction, the dislocation Burger's vectors does not lie on an intersection of {111}

zone planes. Consequently, the action of these vectors could not traverse different planes in the {111} family and hence formation of these reconstruction defects is unlikely.

4.1.2.2. Dynamic Dislocation Stress Analysis

The EAM was used to analyze dynamic screw dislocation cores with and without reconstruction defects and the results shown in Figures 4.6 and 4.7.

The variation of induced stress as screw dislocations with reconstruction defects in the Fe lattice, move in the direction of their Burger's vector is illustrated in Figure 4.6. For the symmetric screw dislocation (Figure 4.6a), the direction corresponding to σ_{11} continues to be the POLR with stress values from 0.707 GPa to 2.32 GPa. It is noted that the intersection of stress component curves occurs over a limited range, and it is inferred that the symmetric reconstruction of screw dislocation cores inhibits the "peeling action" of atoms about the dislocation core. For this type of defect, the shear stresses are recorded between -6.0 GPa and -8.0 GPa. This spreading shows that a narrow band catastrophic ultimate stress is unlikely for the lattice configurations incorporating symmetric screw reconstruction.

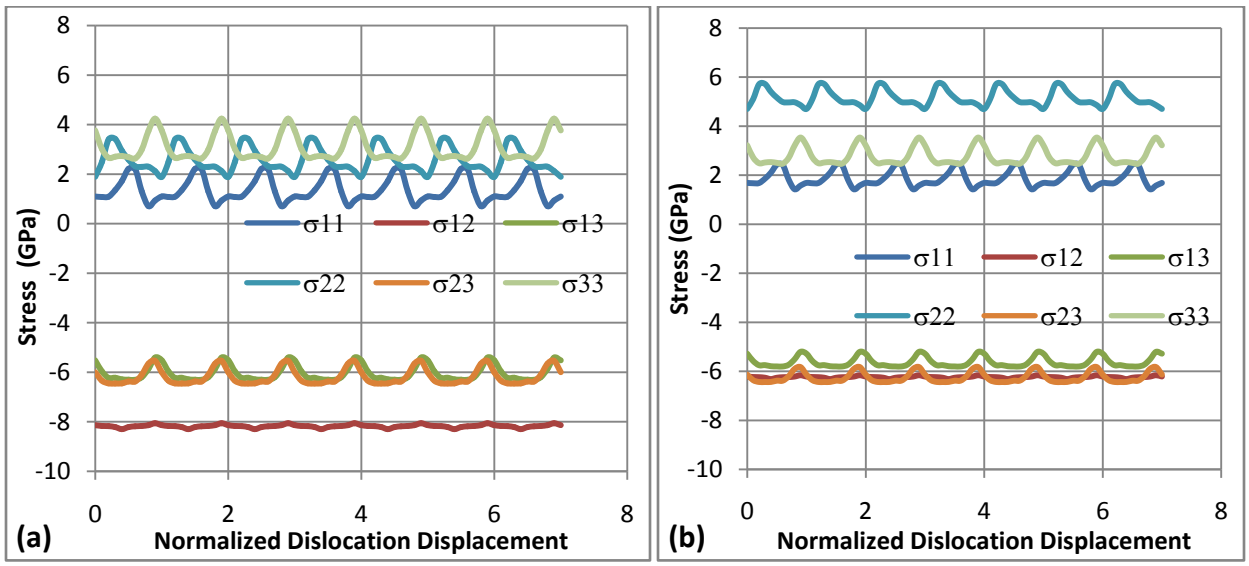

Figure 4.6: Stress variation as pure screw dislocations with (a) symmetric, (b) anti-symmetric, defects in Fe move in the $[1\bar{1}1]$ direction.

The behaviour of the anti-symmetric screw dislocation is given in Figure 4.6b. The σ_{11} path remains the POLR, intersecting marginally with the σ_{33} path and spanning 1.42 GPa to 2.53 GPa. As a result, the anti-symmetric screw dislocation is expected to incur a higher energy cost to surmount the crests of the σ_{11} path, and consequently be harder to move than the symmetric screw dislocation. No spreading of the shear stress is observed and so a narrow band catastrophic ultimate stress may be experienced, corresponding to a shear stress of -6.0 GPa.

Figure 4.7 shows that the anti-symmetric dislocation core requires a higher activation stress for dislocation motion, accompanied by a marginally higher peak stress. These findings reinforce the earlier suggestion that the anti-symmetric dislocation core experiences the greatest resistance to motion. This is consistent with empirical results published separately by Duesbery [95] and Wuthrich [97].

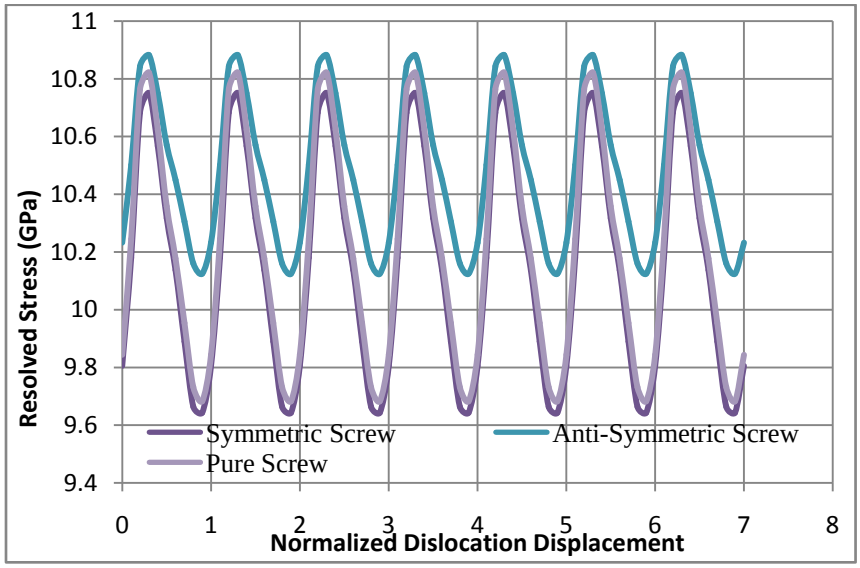

Figure 4.7: Resolved stress variation as screw dislocations with reconstruction defects in Fe move in the direction of their Burger's vector.

4.1.3. EFFECT OF CARBON ON SCREW DISLOCATION CORES - RBM METHOD

4.1.3.1. Static Analysis of the Dislocation Core

Table 4.3 presents retained stress components for the equilibrium lattice configuration for screw dislocations with interstitial carbon. There is a marked increase in retained stresses with the

introduction of carbon into the lattice, which is consistent with empirical observations [193]. As noted in the analysis of the cohesive strength, the symmetric dislocation core has a higher value of retained stress components than the anti-symmetric dislocation core, when compared with results for the lattice without carbon. This reversal in behaviour suggests that the anti-symmetric screw dislocation core is more energetically favoured in Fe-C lattice, and has a greater mobility than the symmetric dislocation core. It is inferred that the distortion introduced by carbon atoms in the neighbourhood of the dislocation core was larger for the symmetric dislocation core.

From simulations of the Fe lattice with and without carbon, and considering the expected random nature of dispersion of carbon within the lattice, it is expected that the formation of both symmetric and anti-symmetric screw dislocation cores would occur, with the symmetric dislocation cores forming in zones with low carbon concentrations, while anti-symmetric dislocation cores forming in zones with higher carbon concentrations (where it is more energetically favoured). It is recommended that the transition point between these two states be considered for further investigation.

Table 4.3: Stress tensor components for screw dislocations with reconstruction defects and octahedral interstitial carbon.

Dislocation Type	Stress (GPa)					
	σ_{11}	σ_{12}	σ_{13}	σ_{22}	σ_{23}	σ_{33}
Pure screw, Fe-C	-24.03	-25.94	-24.57	-24.75	-25.24	-21.89
Symmetric core, Fe-C	-27.98	-28.90	-26.06	-26.77	-25.86	-22.34
Anti-symmetric core, Fe-C	-23.53	-26.16	-24.99	-25.50	-25.97	-22.81

4.1.3.2. Dynamic Dislocation Stress Analysis

The static analysis results illustrate that the EAM formulation possesses the qualitative capacity to detect the consolidated effects of carbon in Fe matrix for materials under direct stresses. A study of its capability in determining dynamical properties of the Fe-C dislocation cores structures containing reconstruction defects was undertaken.

Figure 4.8 shows results for the screw dislocations with reconstruction defects. All the stress components for the screw dislocations with reconstruction defects in Fe-C lattice are negative. This is in contrast to results for the Fe lattice where the direct stresses are positive, while the shear stresses are negative. This suggests that the dislocation core experienced compressive stresses as a result of the lattice distortion. These stresses act to constrict the dislocation core and restrain the motion of the dislocation core atoms, making it more difficult for the dislocation to move through the lattice. The existence of negative stresses further restricts the extension of the length of the dislocation line further minimizing dislocation evolution. Additionally, the maximum stress values increase from -10 to -29 GPa. This is a considerable increase and an indication of the magnitude of lattice strengthening at the nano-scale due to the introduction of interstitial carbon.

The symmetric screw dislocation core generates stress components within the range -22.4 to -29 GPa. The POLR is along the direction corresponding to σ_{33} with a range of -22.4 to -24 GPa. This direction is along the slip plane, but at an angle to the dislocation line, which suggests that the symmetric screw dislocation translates at an angle to its dislocation line.

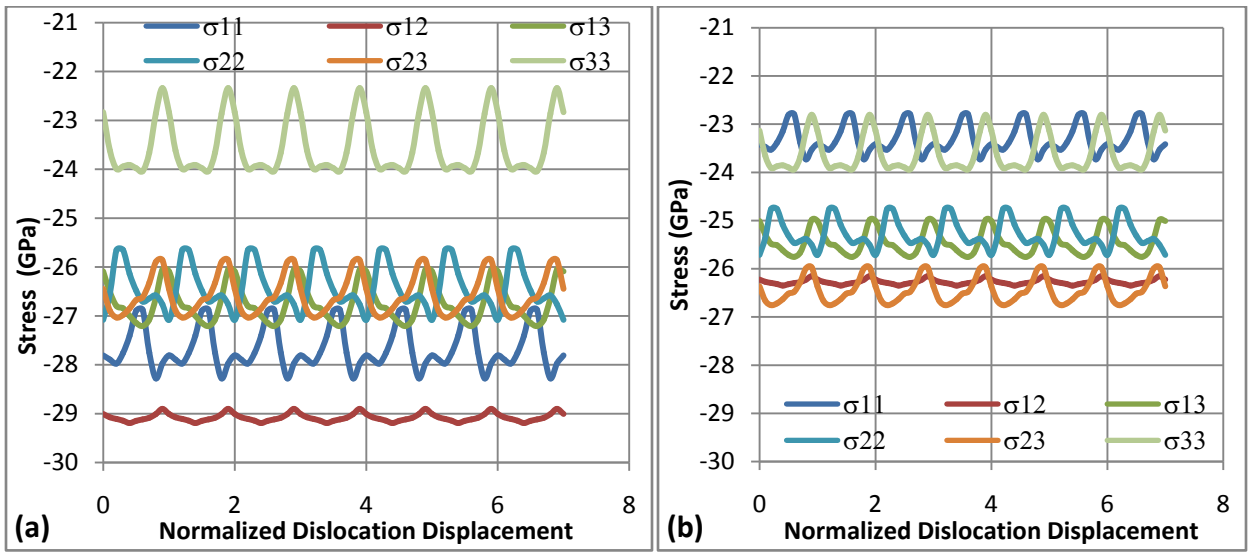

Figure 4.8: Stress variation as pure screw dislocations with (a) symmetric, (b) anti-symmetric, defects in Fe-C move in the $[1\bar{1}1]$ direction.

On the other hand, the anti-symmetric screw dislocation generates stress components within the range -22.7 to -26.8 GPa as shown in Figure 4.8b. The POLR is along the direction corresponding to the stress components σ_{11} and σ_{33} over the range -22.7 to -23.5 GPa. The anti-symmetric dislocation core is therefore expected to acquire greater mobility as inferred from the smaller stress amplitudes and lower peaks than the symmetric screw dislocation in Fe-C lattice.

4.1.4. EFFECT OF CARBON ON NON-SCREW DISLOCATION CORES –RBM METHOD

4.1.4.1. Static Stress Analysis

Table 4.4 shows the results of the static stress components for dislocation types in the Fe-C lattice. The least stress components were σ_{33} for all the dislocation types, similar to the screw dislocations with reconstruction defects in the same lattice. Thus, the introduction of carbon interstitials changed the minimum stress components from σ_{11} to σ_{33} for the equilibrium lattice structure.

Table 4.4: Stress tensor components for dislocations with octahedral interstitial carbon without reconstruction defects.

Dislocation Core Type	Stress (GPa)					
	σ_{11}	σ_{12}	σ_{13}	σ_{22}	σ_{23}	σ_{33}
Pure screw	-24.03	-25.94	-24.57	-24.75	-25.24	-21.89
70.53^{o} screw	-28.62	-27.73	-24.22	-24.34	-25.38	-22.79
35.26^{o} screw	-24.01	-25.84	-24.48	-24.36	-24.90	-21.50
Pure edge	-23.50	-27.21	-24.68	-27.59	-25.19	-21.72

4.1.4.2. Dynamic Dislocation Stress Analysis

Figure 4.9 shows the results of the stresses generated as non-screw dislocations move along the slip plane in the direction of their Burger's vector in Fe-C lattice. All the stress components recorded are negative. This is in contrast to results for the Fe lattice (Figures 4.4 and 4.5) where the direct stresses are positive, while the shear stresses are negative. This means that the dislocation core in the Fe-C lattice experiences compressive stresses as a result of the lattice distortion due to interstitial carbon.

The variation of the stress components for the 70.53° screw dislocation core is shown in Figure 4.9a. The POLR is along σ_{33} with short range paths along σ_{11} and σ_{22}, spanning the range -21.6 to -23.2 GPa. Figure 4.9b shows results for the stress components for the 35.26° screw dislocation core. As in the case of the 70.53° screw dislocation core, the POLR for the 35.26° screw dislocation core is along σ_{33} with short range paths along σ_{11} and σ_{22}, spanning -21.5 to -23.4 GPa. This is evidence that the reduction in screw content of a dislocation core does not appreciably affect the limits of the range of the POLR.

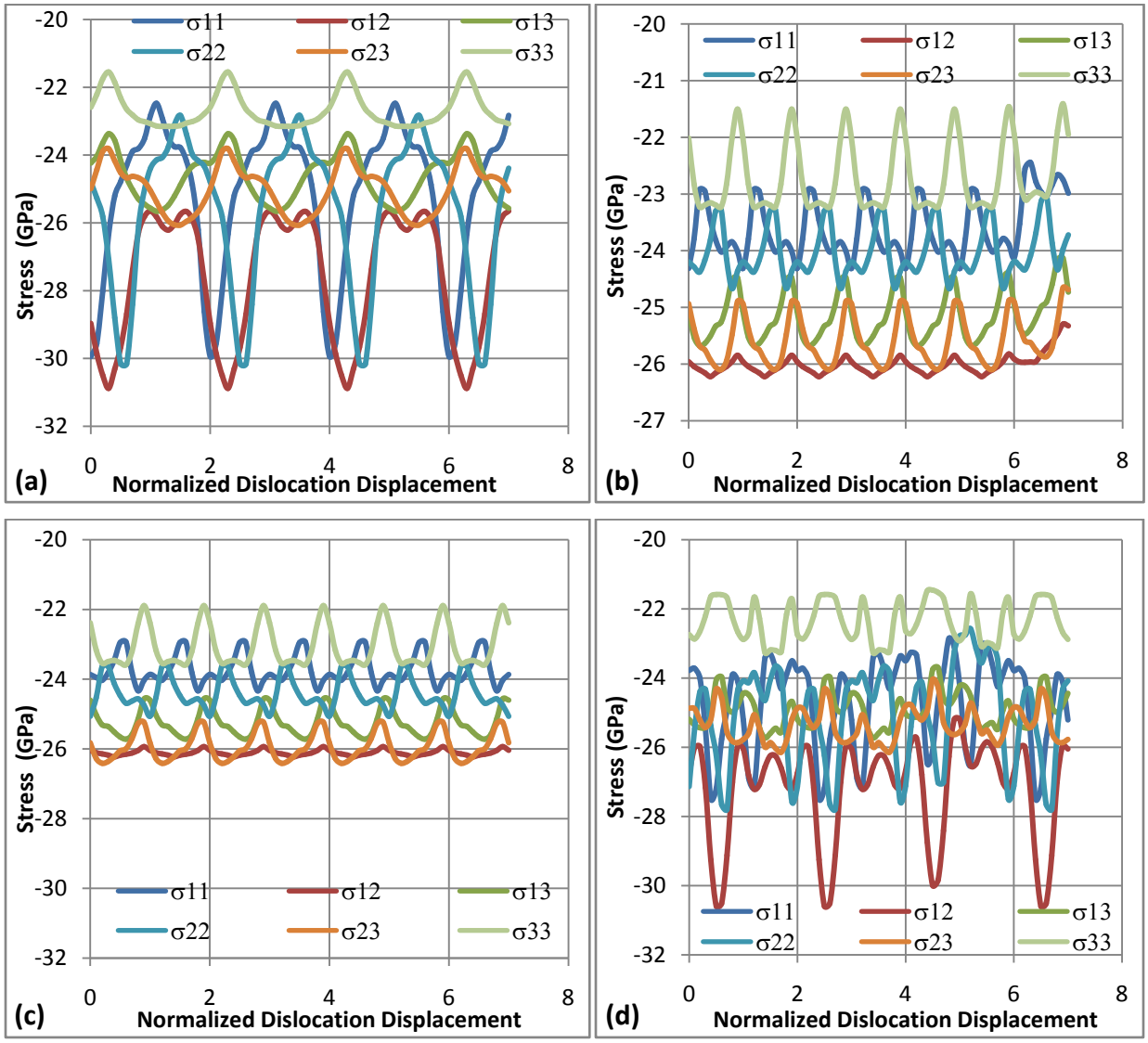

Figure 4.9: Stress variation as (a) 70.53° screw, (b) 35.26° screw, (c) screw, (d) edge, dislocations in Fe-C move in the (a) $[\bar{1}10]$, (b) $[\bar{1}11]$, (c) $[1\bar{1}1]$, (d) $[\bar{1}12]$, directions.

Additionally, the spread of the shear stresses for the pure screw (Figure 4.9c) and the 35.26^o screw (Figure 4.9b) dislocation cores are similar, as are those of the 70.53^o screw dislocation and the pure edge dislocation core.

The screw dislocation core shows a spread of -21.9 to -23.5 GPa (Figure 4.9c) with the POLR in the direction of σ_{33} and σ_{11} stress components. This behaviour compares well with that of the mixed dislocation cores (Figures 4.9a and 4.9b).

A departure from the regular cyclic pattern observed for the pure screw, 35.26^o screw and the 70.53^o screw (Figures 4.9a-4.9c) dislocation cores is noted for the edge dislocation core in the Fe-C lattice (Figure 4.9d). The edge dislocation core stress components exhibit a cyclic variation, each with three crests within two lattice periods. The POLR is in the direction of σ_{33} and σ_{11}, spanning a stress range from -21.7 to -23.2 GPa. This deviation in pattern is similar to that in the carbon-free lattice. However, unlike the curves for the carbon-free lattice, the intersection of stress component curves is limited, implying a reduction in direction changes during the motion of this dislocation. Consequently, edge dislocation motion in the Fe-C lattice is expected to be severely limited, as the "peeling" atom mechanism is not as active. This inference is consistent with the lower ductility of the Fe-C lattice [193].

4.1.5. POLR STRESS RANGE FOR BCC Fe – RBM METHOD

A summary of the active stresses characterizing the POLR for the single element Fe lattice is presented in Table 4.5. The amplitude of the stress ranges compares well with the Peierl's stress.

These results reveal a high Peierl's stress for the 70.53^o screw dislocation (2.91 GPa) consistent with empirical findings [97]. However, these results also suggest that the Peierl's stress of the pure edge dislocation is higher than that of the pure screw dislocation which is contrary to empirical findings. There is an increase in Peierl's stress for the screw dislocation on the introduction of reconstruction defects, with the anti-symmetric screw dislocation having a higher Peierl's stress. Empirical results on the dislocation kink [95], which comprises screw and edge dislocation components, had long straight screw dislocation components joined by edge dislocation components that indicated that the edge dislocation component had a greater

mobility. The current findings are therefore indicative that the screw dislocation components in dislocation kinks may contain appreciable sections of anti-symmetric reconstruction defects, which would result in an overall reduction of the mobility of the screw dislocation component, leaving the edge dislocation with the higher mobility.

Table 4.5: Stress range for the POLR in Fe.

Dislocation Type	Stress Range (GPa)		Stress Amplitude (GPa) - POLR	Peierl's stress (GPa)
	Lower	Upper		
Pure screw	1.26	2.27	1.01	1.2 - 1.8 [181, 194], 1.3 - 1.9 [191], 1.1 [195]
70.53^{o} screw	-2.91	2.54	5.46	-
35.26^{o} screw	1.27	2.42	1.15	-
Pure edge $[\bar{1}12]$	-0.85	2.40	3.30	1.5 [194]
Symmetric screw	0.71	2.59	1.88	-
Anti-symmetric screw	1.42	2.53	1.11	-

4.1.6. POLR STRESS RANGE FOR BCC Fe-C – RBM METHOD

A summary of the active stresses simulated by the POLR for the Fe-C lattice is given in Table 4.6. The highest value of the stress range compares well with the Peierl's stress.

The POLR stress values for the edge and screw dislocations are in the order of magnitude obtained from empirical work [181, 191, 194]. However, the higher value of the edge dislocation POLR stress value suggests that deformation by the mobility of kinks is inhibited. The Peierl's stress derived for the 70.53^{o} screw dislocation is of the same order of magnitude as the other dislocation types, and it is evident that the type of dislocation is not a critical consideration when stress analysis is conducted on the Fe-C lattice.

Table 4.6: Stress range for the POLR in Fe-C.

Dislocation Type	Stress Range (GPa)		Stress Amplitude (GPa) - POLR	Peierl's stress (GPa)
	Lower	Upper		
Symmetric screw	-22.3	-24.0	1.7	-
Anti-symmetric screw	-22.7	-26.8	4.1	-
Pure screw	-21.9	-23.5	1.6	1.2 - 1.8 [181, 194], 1.3 - 1.9 [191], 1.1 [195]
70.53^{o} screw	-21.6	-23.2	1.6	-
35.26^{o} screw	-21.5	-23.4	1.9	-
Pure edge	-21.6	-23.3	1.7	1.5 [194]

4.1.7. MOTION OF DISLOCATION CORES – FMDCA METHOD

Simulations were then carried out to evaluate the dynamic stresses as the dislocation core atoms moved through the lattice under the effect of the stress field. These results were obtained by allowing the movement of dislocation core atoms under load, according to the force acting on each of the atoms. This was referred to as the FMDCA. The objective of these simulations was to corroborate the results generated by the RBM. The RBM results were obtained over a longer length scale (typically 9 lattice vectors) in comparison to those of the FMDCA (which were generated over less than one lattice vector) for the same number of cycles. The RBM results were therefore suited to depicting the evolution of the stress field as rows of atoms moved across the slip plane. On the other hand, the FMDCA results were more suited to depict the "peeling action" of dislocation core atoms as the core translated through the lattice. Figures 4.10 to 4.17 show the stress tensor components for dislocations within the Fe lattice according to the FMDCA.

4.1.7.1. Analysis of Stress Components for the Screw Dislocation

Figure 4.10 shows the stress profile of atoms about the core with no externally applied load. Under such conditions, the atoms move under internal stresses resulting from the core's distortion. The curves show moderate stress values as the atoms move from their initial location at 0 nm. This motion is explained as lattice relaxation under internal stress, and occurs to a

displacement of approximately 40% of a Burger's vector. At about 1.1 nm from the origin, a maximum displacement is achieved and the atoms experience fairly high stress values on the return path. It is therefore inferred that the motion shown in the return path is unlikely.

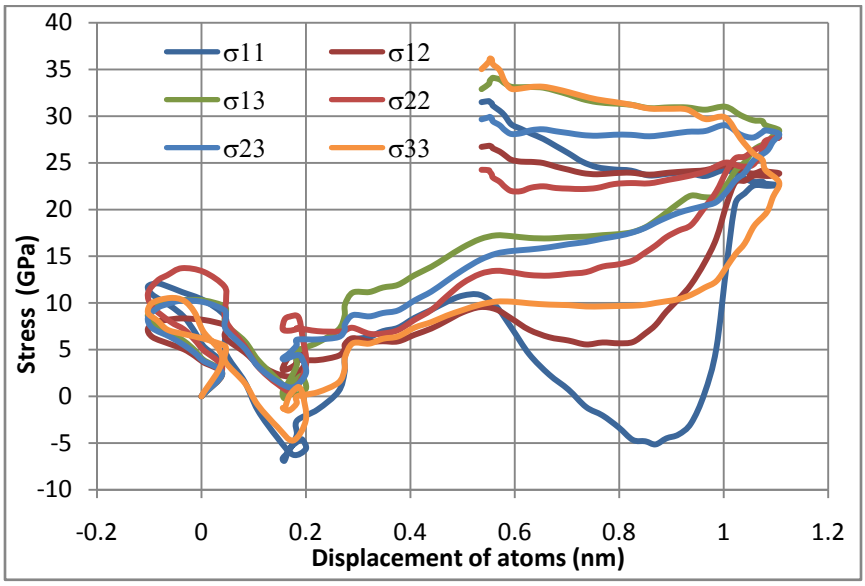

Figure 4.10: Stress variation as atoms around a screw dislocation core in Fe move in the $[11\bar{1}]$ direction – No load.

Figure 4.11a shows the stress profile of atoms about the core with 0.2 kN externally applied load. The atoms move under a combination of external and internal stresses. These curves illustrate that the atoms experience a steady growth in stress attaining a high stress value within a displacement magnitude of the order of a quarter of a Burger's vector. The path traced in Figure 4.11a is in the opposite direction to that illustrated in Figure 4.10.

Figure 4.11b shows the stress profiles of atoms about the core with a 0.4 kN externally applied load. The curves also show a steady growth in stress similar to Figure 4.11a. A comparison with Figures 4.11c and 4.11d reveals that the shape of the stress profiles is maintained. No peak values of the POLR are observed, except for σ_{11} and σ_{33} (Figure 4.11b), and instead there is a steady growth in stress values. A maximum displacement magnitude occurs at about a quarter of the magnitude of the Burger's vector, and this maximum is accompanied by a reversal in stress gradient.

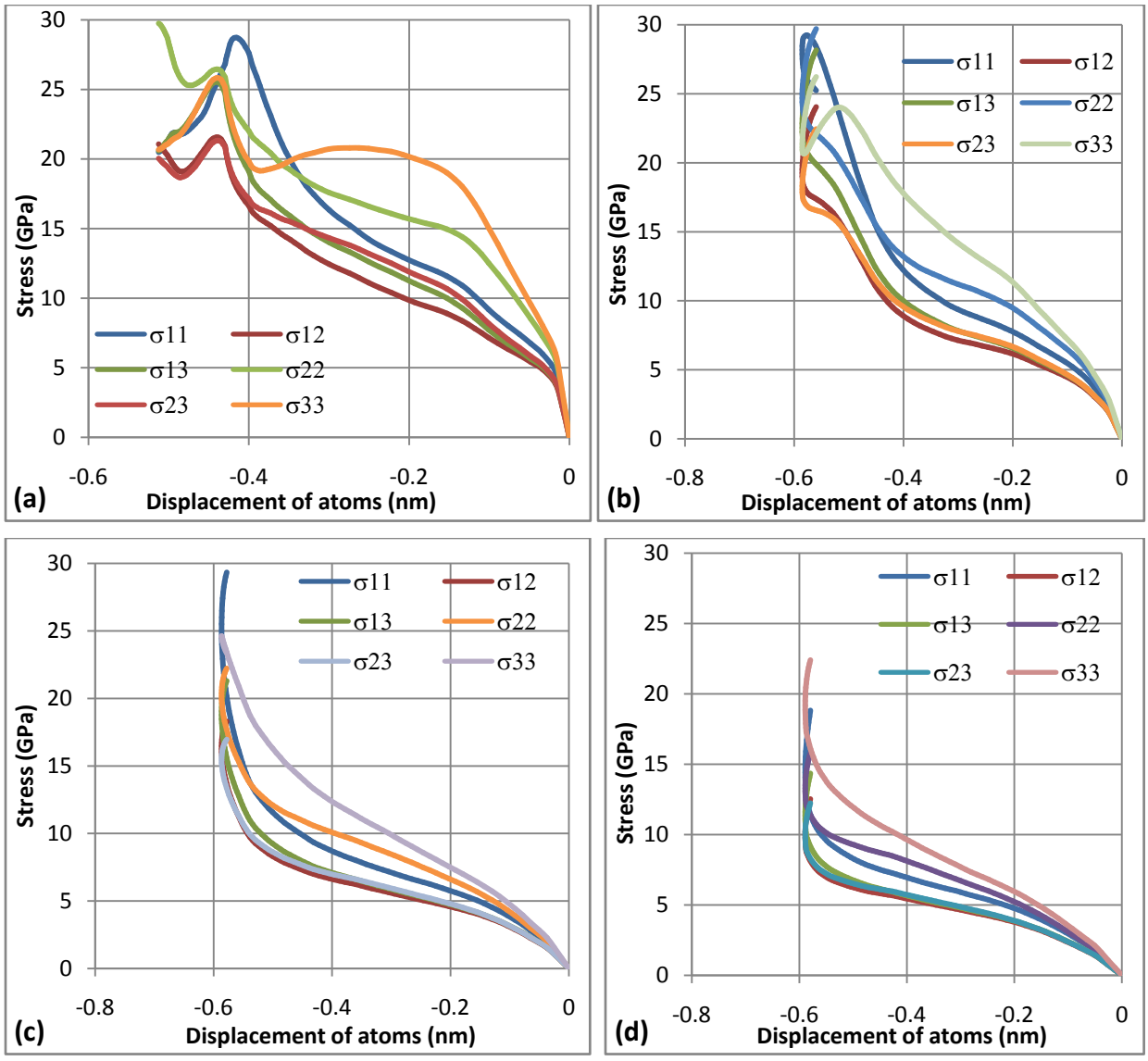

Figure 4.11: Stress variation as screw dislocation core atoms in Fe move in the $[11\bar{1}]$ direction – (a) 0.2 kN, (b) 0.4 kN, (c) 0.6 kN, (d) 0.8 kN, external load.

4.1.7.2. *Analysis of the Screw Dislocation using Resolved Stresses*

Analysis of the resolved stress profiles under FMDCA conditions was carried out to evaluate the overall effect of the stress field on dislocation core atoms for the screw dislocation. Figure 4.12 shows the simulated resolved stress profiles. A steady increase in the stress values with displacement is observed. The 0.2 kN load curve displays a resolved stress peak of 9.57 GPa, while the other curves do not exhibit resolved stress peaks. Additionally, the reversal of the motion of the atoms is observed in the 0.4 kN, 0.6 kN, 0.8 kN load curves. Figure 4.12a also

shows similar stress curves to Figure 4.11. It is therefore deduced that it is sufficient to analyze the motion of atoms using the resolved stress curves in place of the individual component curves. The maximum displacement of atoms takes place at approximately 24.2% of the magnitude of the Burger's vector.

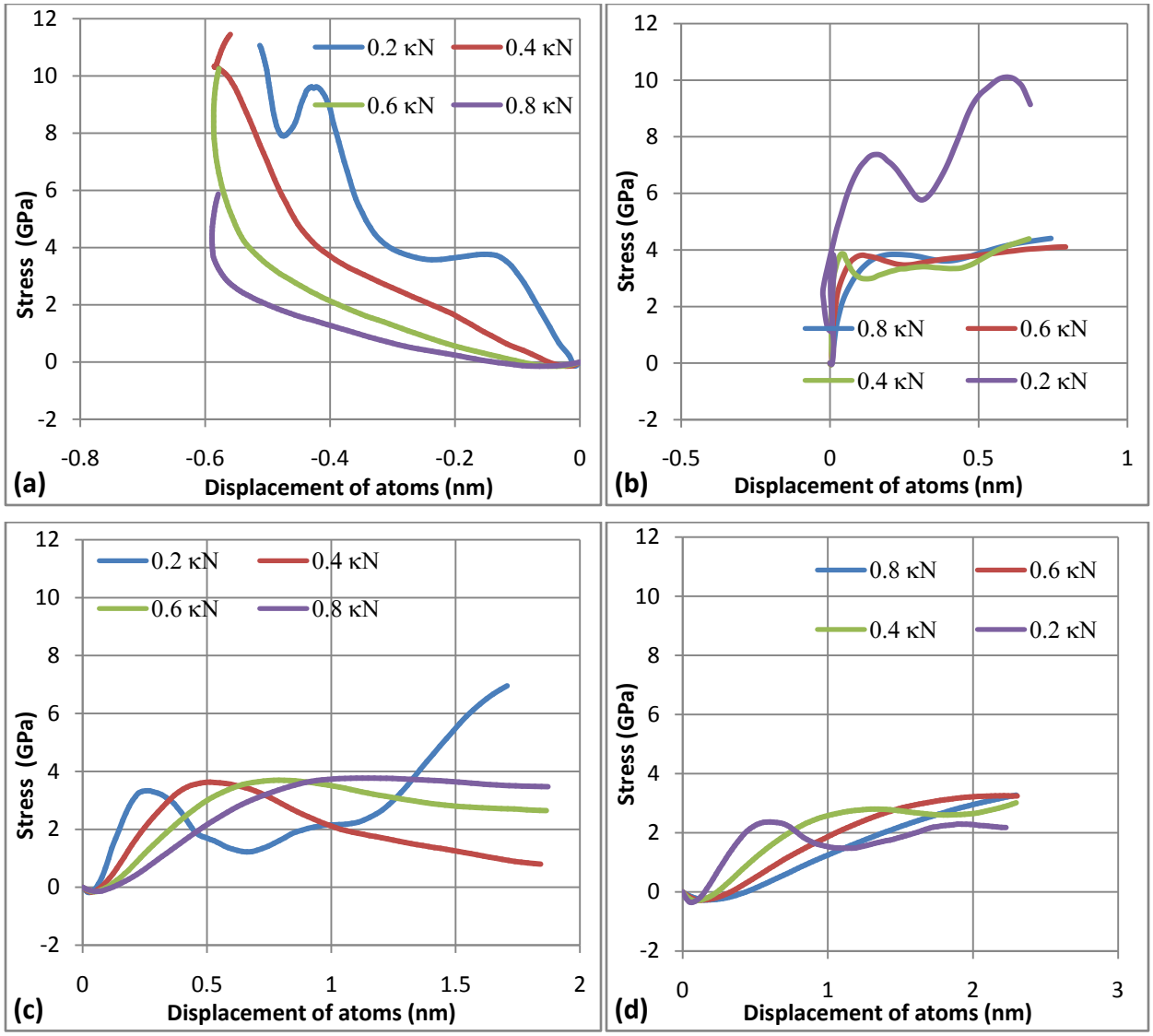

Figure 4.12: Resolved stress variation as screw dislocation core atoms in Fe move under load in the (a) $[11\bar{1}]$, (b) [110], (c) [111], (d) [112], directions.

Additional simulations were carried out on the screw dislocation with the applied loads in directions corresponding to the Burger's vectors of the mixed dislocation types. The results of

the resolved stress profiles are given in Figure 4.12. The resolved stress peaks for the three loading directions analysed are summarized in Table 4.7.

Figure 4.12b shows the resolved stress cycles for screw dislocations loaded in the $[\bar{1}10]$ direction. The increase in applied load results in the attainment of the first resolved stress peak at a larger displacement. However, the first resolved stress peak for all loading conditions applied occurs in the order of 3.8 GPa. These peaks present a maximum resolved stress experienced by the moving atoms and corresponds to the Peierl's stress. The resolved stress peak values occur over a small range under different loading conditions, and this is considered as evidence that this stress is a material property. Additionally, for the 0.2 kN loading condition, secondary peaks are at 7.37 GPa and 10.10 GPa. In the algorithm used in the loading cycle, a higher load results in a lower contribution by the internal stresses to the force driving the dislocation. Consequently, the secondary resolved stress peaks are evidence that motion of atoms is unlikely, unless under the effect of sufficiently large externally applied stress. This therefore leads to the inference that a secondary level of dislocation mobility related to the secondary resolved stress peaks is improbable.

The results from loading the screw dislocation in the [111] direction are given in Figure 4.12c. The peak stress values are higher than those of Chaussidon, Fivel and Rodney [181], and of Ventelon [191], and the results of the RBM technique by a factor of approximately two. This is also noted in the results for loading in the [110] direction. The results show a gradual increase in the peak resolved stress value as the applied load is increased. However, in contrast to results for loading in the [110] direction, the secondary peak resolved stress value for the 0.2 kN load is less than the first peak resolved stress value. The stress values and the profiles simulated lead to the inference that the screw dislocation is likely to move under this type of loading. Again, the stress profile of the 0.2 kN loading scenario is attributed to the greater influence of the internal stresses.

Figure 4.12d shows results of the screw dislocation loaded in the [112] direction. These results are appreciably lower than those under loading in the [111] direction, and the resolved stress peaks occur at a greater displacement. The resolved stress peaks tended towards published values

of 1.2 - 1.8 GPa [181] and 1.3 - 1.9 GPa [191] as the loading direction is changed from the [110] to the [112] direction. This implies that motion in the [112] direction **i**s more probable than motion in the [110] or the [111] directions, as at the same displacement, the loading in the [112] direction occurs at a lower stress level.

Table 4.7: Resolved stress peaks as screw dislocation core atoms in Fe move under load.

Loading direction	Load (kN)	POLR (GPa)		
		1st Peak	2nd Peak	3rd Peak
[110]	0.2	3.83	7.37	10.10
	0.4	3.86	3.38	-
	0.6	3.79	4.06	-
	0.8	3.84	-	-
[111]	0.2	3.31	2.17	-
	0.4	3.62	-	-
	0.6	3.68	-	-
	0.8	3.77	-	-
[112]	0.2	2.36	2.29	-
	0.4	2.80	-	-
	0.6	3.24	-	-
	0.8	3.27	-	-

4.1.7.3. Edge Dislocation

Just as in the case for the screw dislocation, the loading of the edge dislocation in the $[11\bar{1}]$ direction (Figure 4.13a) gave resolved stress curves that had either a high peak (13.69 GPa for the 0.2 kN loading), or no peaks. This type of loading coincides with the dislocation line direction, and again it is inferred that this type of motion is unlikely.

Figure 4.13b comprises stress curves for the edge dislocation loaded in the [110] direction. As in the case for the screw dislocation, the increase in applied load delays the attainment of the peak resolved stress. In addition, the increase in load results in a reduction of the resolved stress peak. This behaviour differs from that of the screw dislocation, and it is expected to greatly aid the

motion of this type of dislocation. The initial peak resolved stress values all compared favourably with published results [194], and they are evidence that edge dislocation's mobility is higher than that of the screw dislocation.

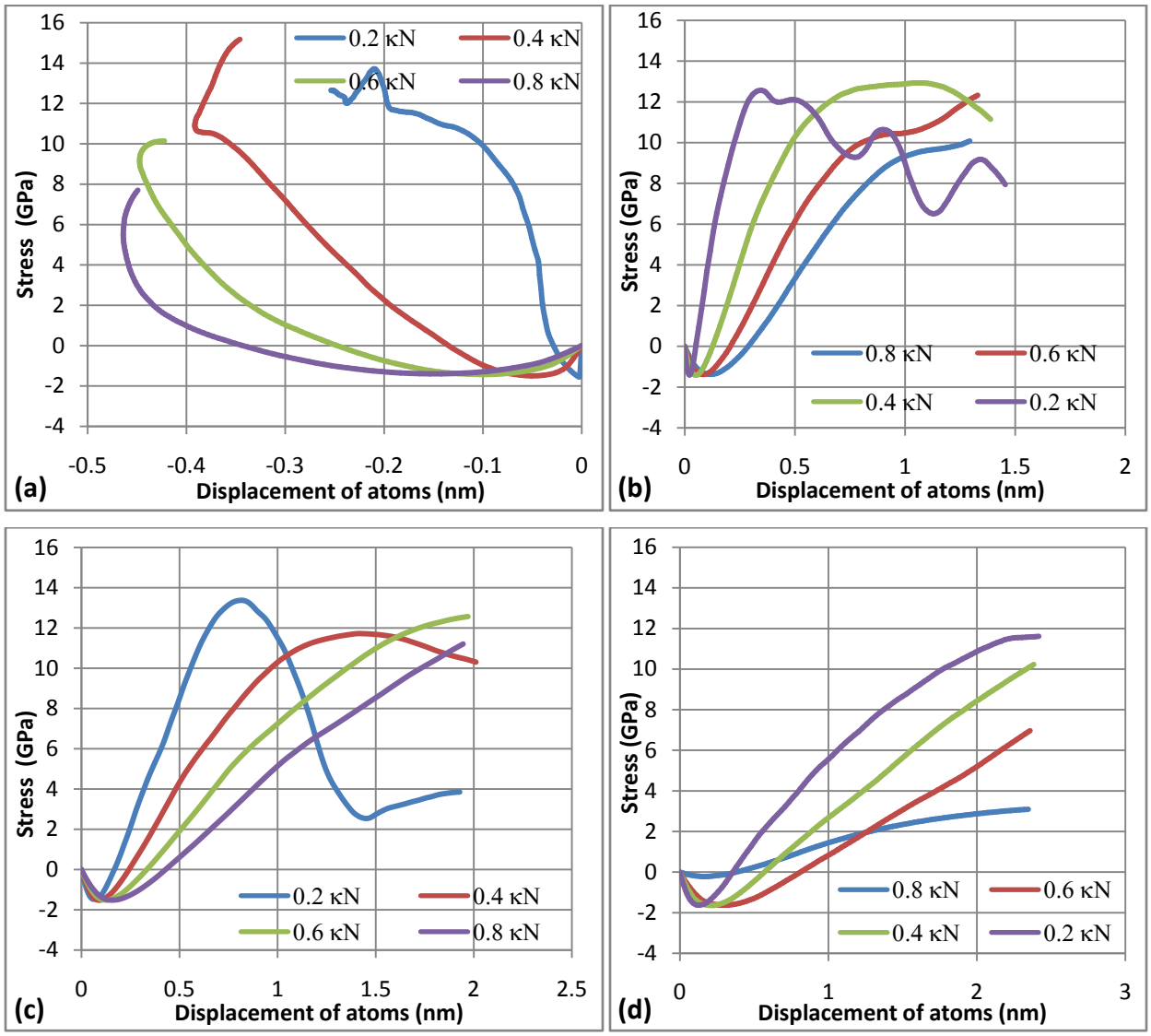

Figure 4.13: Resolved stress variation as edge dislocation core atoms in Fe move under load in the (a) [11$\bar{1}$], (b) [110], (c) [111], (d) [112], directions.

Figure 4.13c shows stress curves for the edge dislocation loaded in the [111] direction. The resulting peaks are comparable with values of 1.2 - 1.8 GPa by Chaussidon, Fivel and Rodney [181], and 1.3 - 1.9 GPa by Ventelon [191], and also values provided by the RBM technique. These results lead to a reconsideration of the earlier assertion that a scaling factor of 0.5 is

necessary to attain the correct stress levels. Additionally, it is inferred that motion of the edge dislocation in the [111] direction is also favourable as in the case of loading in the [110] direction. Secondary resolved stress peaks are also observed in the 0.2 kN and 0.4 kN loading cycles.

Figure 4.13d shows stress curves for the edge dislocation loaded in the [112] direction. As in the case of the screw dislocation, the resolved stress peak values increase marginally when compared to those of loading in the [111] direction for the same dislocation. Additionally, the stress peak values are attained at marginally larger amplitudes, which leads to the inference that motion in the [112] direction is more probable than that of loading in the [111] direction. The peak resolved stress values are summarized in Table 4.8.

Table 4.8: Resolved stress peaks as edge dislocation core atoms in Fe move under load.

Loading direction	Load (kN)	POLR (GPa)			
		1st Peak	2nd Peak	3rd Peak	4th Peak
[110]	0.2	-1.41	12.56	10.64	9.17
	0.4	-1.40	12.93	-	-
	0.6	-1.38	10.43	-	-
	0.8	-1.38	9.70	-	-
[111]	0.2	-1.31	13.37	3.83	-
	0.4	-1.46	11.72	-	-
	0.6	-1.48	-	-	-
	0.8	-1.52	-	-	-
[112]	0.2	-1.62	-	-	-
	0.4	-1.64	-	-	-
	0.6	-1.63	-	-	-
	0.8	-0.22	3.08	-	-

For loading in all three directions, the initial peak values which compare well with published values of 1.2 - 1.8 GPa by Chaussidon, Fivel and Rodney [181], and 1.3 - 1.9 GPa by Ventelon [191]. It is noted that at 0.8 kN loading in the [112] direction, the initial resolved stress peak is

much smaller than that obtained for the other load levels. It is inferred that in this case, the momentum of the dislocation core atoms overshadows the "peeling" effect and a secondary peak whose magnitude is appreciably higher than empirical values [181, 191] is found.

4.1.7.4. 35.26° Screw Dislocation

Figure 4.14 shows results obtained from the loading of the 35.26° screw dislocation. As in the case of the screw and edge dislocations, loading in the $[11\bar{1}]$ direction is considered unlikely as a result of the asymptotic-like increase in stress.

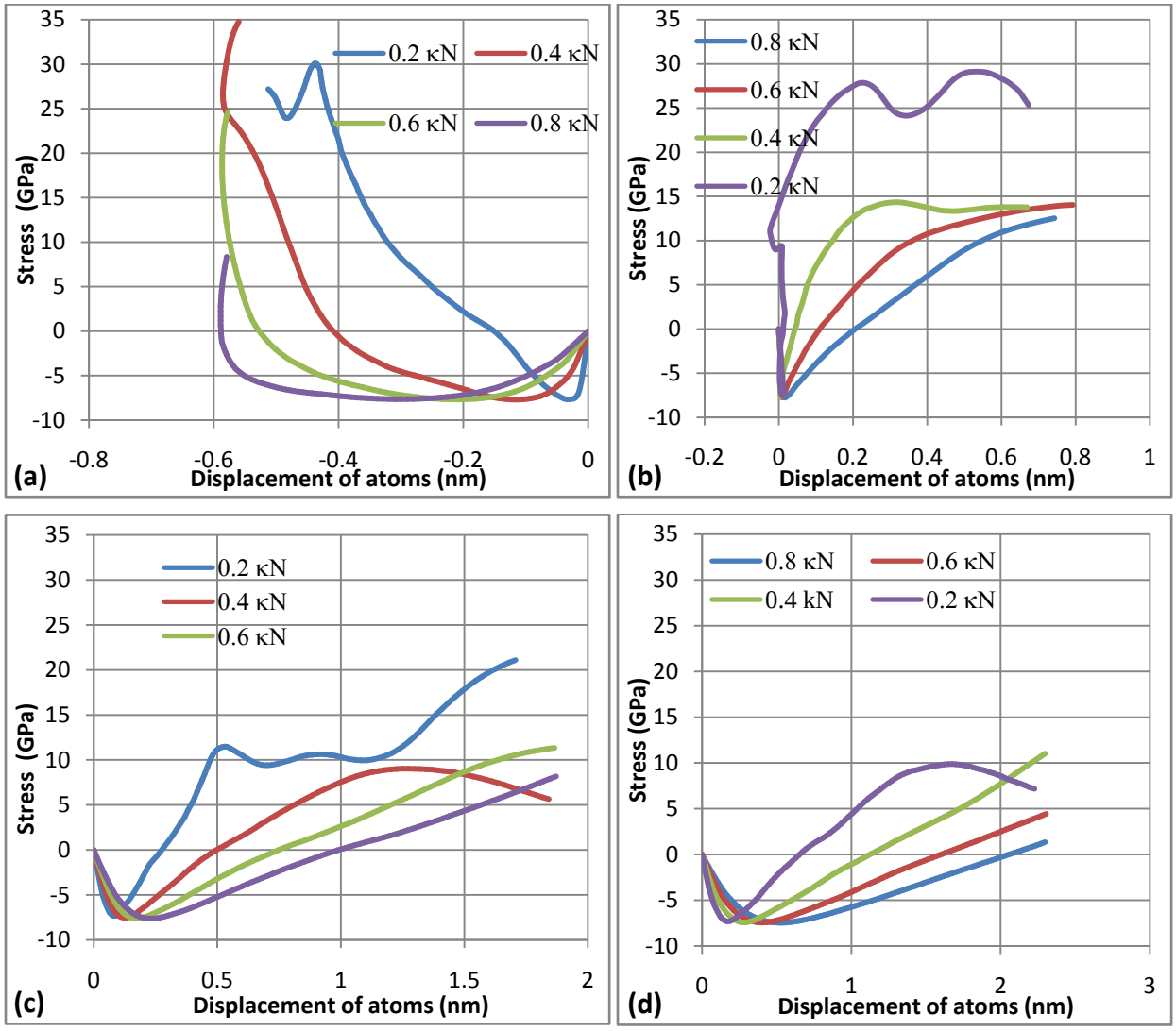

Figure 4.14: Resolved stress variation as 35.26° screw dislocation core atoms in Fe move under load in the (a) $[11\bar{1}]$, (b) [110], (c) [111], (d) [112], directions.

Loading in the [110], [111] and the [112] directions gave initial resolved stress peak values between -7.09 and -7.62 GPa. These values are much higher than published values of 1.1 - 1.9 GPa [181, 191, 194, 195]. As the load is increased, the peak resolved stresses also increase, as in the case of the screw dislocation. Additionally, loading in the [111] direction gives the lowest peak resolved stress values with a marginal increase in the resolved stress generated in the [121] direction (c.f. [111] loading).

The 35.26^{o} screw dislocation gives fairly high initial resolved stress peaks compared to the screw and edge dislocations. These higher resolved stress peaks are an indication that the motion of this dislocation is highly unlikely. This is similar to results obtained from the RBM simulations, although the relative difference is larger in the FMDCA simulations. The resolved stress peaks for the [110], [111] and the [112] directions are summarized in Table 4.9.

Table 4.9: Resolved stress peaks as 35.26^{o} screw dislocation core atoms in Fe move under load.

Loading direction	Load (kN)	POLR (GPa)		
		1st Peak	2nd Peak	3rd Peak
[**110**]	0.2	-7.55	27.86	29.11
	0.4	-7.10	14.29	13.70
	0.6	-7.57	-	-
	0.8	-7.55	-	-
[**111**]	0.2	-7.30	11.39	10.57
	0.4	-7.41	9.01	-
	0.6	-7.51	-	-
	0.8	-7.61	-	-
[**112**]	0.2	-7.16	9.86	-
	0.4	-7.38	-	-
	0.6	-7.44	-	-
	0.8	-7.42	-	-

4.1.7.5. 70.52° Screw Dislocation

Figure 4.15 shows results obtained from the loading of the 70.52° screw dislocation. The resolved peak stresses are summarized in Table 4.10. As in the case of the screw, edge and 35.26° screw dislocations, loading in the $[11\bar{1}]$ direction (Figure 4.15a) is unlikely as a result of the asymptotic-like increase in the simulated stress values.

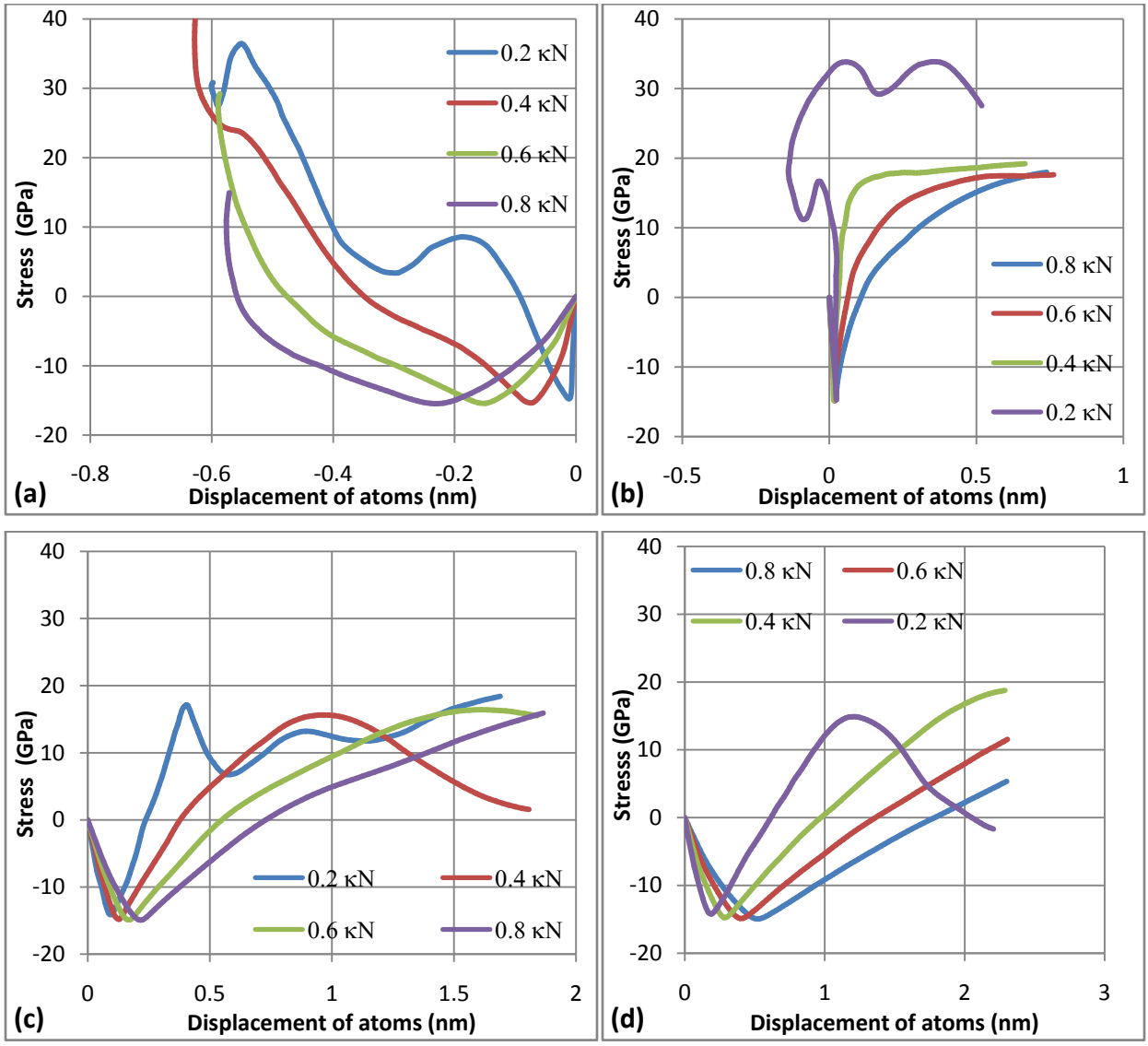

Figure 4.15: Resolved stress variation as 70.52° screw dislocation core atoms in Fe move under load in the (a) $[11\bar{1}]$, (b) [110], (c) [111], (d) [112], directions.

Figure 4.15b provides resolved stress profiles for loading in the [110]. The 0.2 kN curve shows an unusual path with a reversal in direction during the loading cycle at fairly high stresses. This reversal is similar to that in the unloaded conditions for the screw dislocation illustrated in Figure 4.10. This leads to the inference that this type of motion is unlikely.

Loading in the [111] and [112] directions produces resolved stress peak values between -13.9 and 14.9 GPa. Figure 4.13c shows stress curves for the [111] loading direction for the 70.52^{o} screw dislocation. An increase in the first peak resolved stress is accompanied by an increase in the displacement to this peak stress, as the applied load is increased. The 0.2 kN load continues to provide curves that differ in shape, and this is attributed to the effect of the internal stress field. Again, the results are much higher than those obtained for the screw and edge dislocations, and are much higher than published values of 1.1 - 1.9 GPa [181, 191, 194, 195].

Figure 4.13d gives stress curves in the [112] loading direction for the 70.52^{o} screw dislocation. The first peak stress is marginally higher than that for the [110] and [111] directions, and is accompanied by an increase in the displacement to the peak stress. No secondary resolved stress peaks are noted for the 0.4 kN to 0.8 kN loads for the range of displacements simulated.

Table 4.10 shows that the initial peak stress in the [110] direction initially reduces with increased load, with an increase on application of 0.8 kN load. However, for the [111] and [112] loading directions, the initial peak stress increases with increased load. These peak stresses are all of the same order of magnitude with the [110] direction giving the most favourable peak stress values.

Table 4.10: Resolved stress peaks as 70.52^o screw dislocation core atoms in Fe move under load.

Loading direction	Load (kN)	POLR (GPa)		
		1st Peak	2nd Peak	3rd Peak
[**110**]	0.2	-14.69	16.63	33.82
	0.4	-13.98	-17.92	-
	0.6	-13.95	-17.47	-
	0.8	-14.69	-17.98	-
[**111**]	0.2	-13.97	17.03	13.20
	0.4	-14.44	15.61	-
	0.6	-14.80	16.39	-
	0.8	-14.88	-	-
[**112**]	0.2	-14.21	14.86	-
	0.4	-14.65	-	-
	0.6	-14.86	-	-
	0.8	-14.92	-	-

Sections 4.1.7.2 to 4.1.7.5 provide evidence of the existence of a Peierl's-like stress peak for the various dislocations under various loading conditions. The peak stresses are indicative of limits in the cyclic dislocation core evolution process. The values obtained for the screw and edge dislocations are consistent with published values of 1.1 - 1.9 GPa for the BCC Fe lattice [181, 191, 194, 195], but the values for the 35.26^o screw dislocation and the 70.52^o screw dislocation are higher. The use of the resolved stress profiles for FMDCA provides sufficient correlation with the Peierl's stress for the edge and screw dislocations, and provides further evidence that the Peierl's stress is related to stress amplitudes encountered by the moving dislocation core atoms as the dislocation line moves (as noted in the analysis in Sections 4.1.1 to 4.1.4).

4.1.8. EFFECT OF RECONSTRUCTION DEFECTS – FMDCA METHOD

Core reconstruction served to modify the peak resolved stresses for the screw dislocation. However, the cyclic profile was maintained. In the case of the symmetric screw dislocation, the

peak resolved stresses reduced for the [110] loading scenario, and increased for the [112] loading scenario. The opposite was observed for the anti-symmetric screw dislocation.

4.1.8.1. Symmetric Screw Dislocation

Figure 4.16 shows results for simulations on the symmetric screw dislocation. Again, as concluded on all the pure and mixed dislocation types, motion presented for the $[11\bar{1}]$ loading direction (Figure 4.16a) is unlikely, due to the asymptotic-like resolved stress curves.

Figure 4.16b shows results for simulations for loading in the [110] direction, with curves similar to those for the basic dislocation types under [110] loading. The large secondary resolved stress peak for the 0.2 kN loading scenario is evidence of the appreciable contribution by the internal stresses. The obtained stress values are all higher than published values of 1.1 - 1.9 GPa [181, 191, 194, 195] by a factor of about 2. However, the values are comparable with those obtained for the pure screw dislocation.

Figure 4.16c shows results for simulations for loading in the [111] direction, and the curves are similar to those derived for the pure screw dislocation under [111] loading. As in other simulations in the same direction, the 0.2 kN curve indicates that there is a larger peak as the displacement moves past 1.7 nm. The values obtained are also higher than published values of 1.1 - 1.9 GPa [181, 191, 194, 195] for the edge and screw dislocation.

Figure 4.16d shows results for simulations for loading in the [112] direction. The curves are similar to those for the pure screw dislocation under [112] loading. The results obtained are higher than those obtained for loading in the [110] and [111] directions. This is evidence that the symmetric screw dislocation is more likely to move in the [110] and [111] directions.

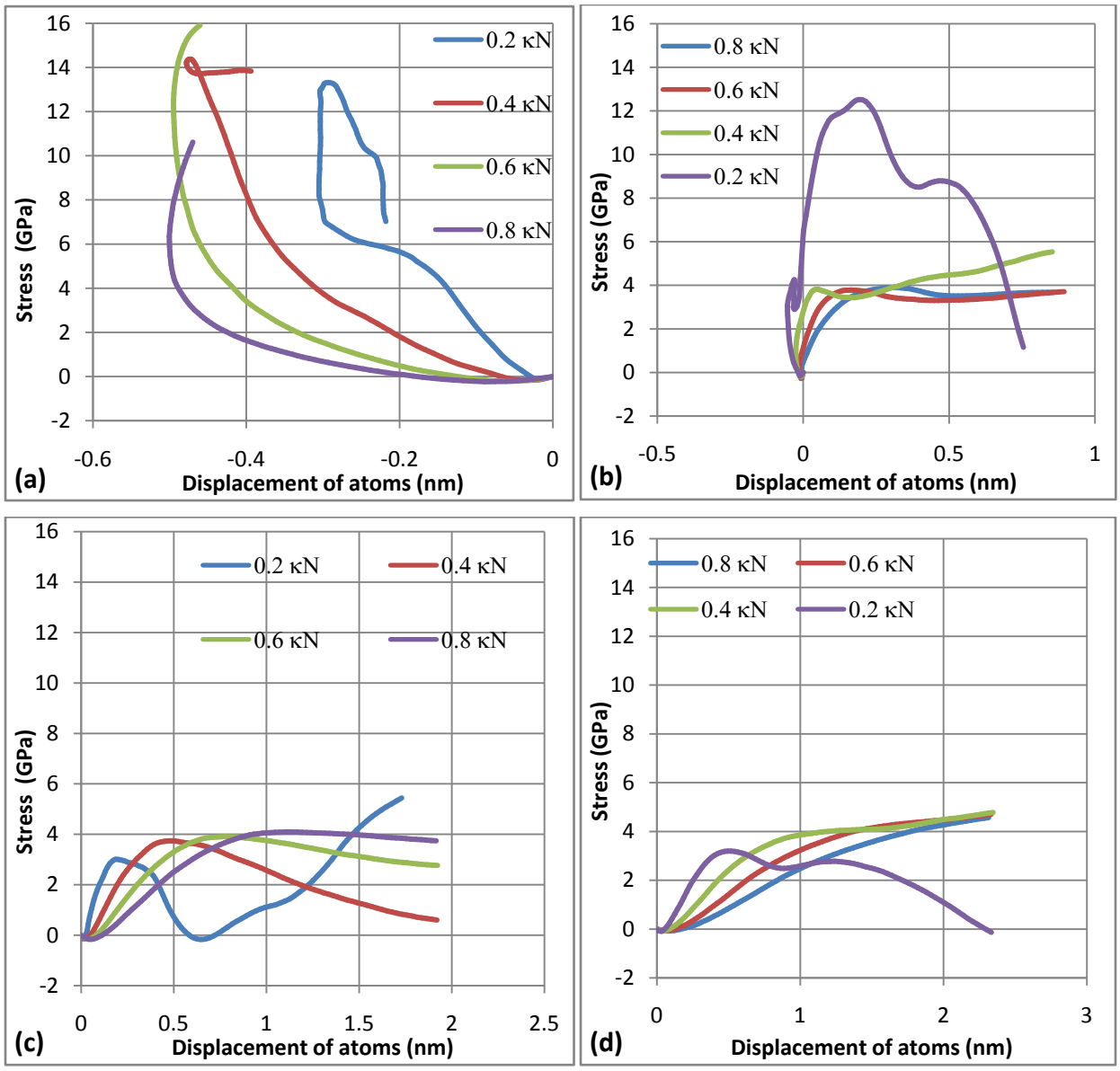

Figure 4.16: Resolved stress variation as symmetric screw dislocation core atoms in Fe move under load in the (a) [$11\bar{1}$], (b) [110], (c) [111], (d) [112], directions.

Table 4.11 summarizes the peak resolved stresses for the [110], [111] and the [112] loading directions. The resolved stress peaks increase with increased load, with loading in the [112] direction having the highest peaks. The resolved stress peaks for the pure screw dislocation are lower than those of the symmetric screw dislocation, and it is inferred that the existence of symmetric core reconstruction is likely to further reduce the mobility of the screw dislocation core.

Table 4.11: Resolved stress peaks as symmetric screw dislocation core atoms in Fe move under load.

Loading direction	Load (kN)	POLR (GPa)		
		1st Peak	2nd Peak	3rd Peak
[110]	0.2	4.05	12.52	8.77
	0.4	3.76	-	-
	0.6	3.77	-	-
	0.8	3.89	-	-
[111]	0.2	2.95	-	-
	0.4	3.74	-	-
	0.6	3.89	-	-
	0.8	4.09	-	-
[112]	0.2	3.20	2.77	-
	0.4	4.78	-	-
	0.6	4.75	-	-
	0.8	4.67	-	-

4.1.8.2. Anti-symmetric Screw Dislocation

Similar results were obtained (compared with symmetric screw and pure screw dislocations) for the anti-symmetric screw dislocation, as illustrated in Figure 4.17. A peak stress for the 0.2 kN loading scenario occurs well before a displacement equal to a quarter of the Burger's vector is attained. This is evidence that dislocation reconstruction does present some obstacle to dislocation motion.

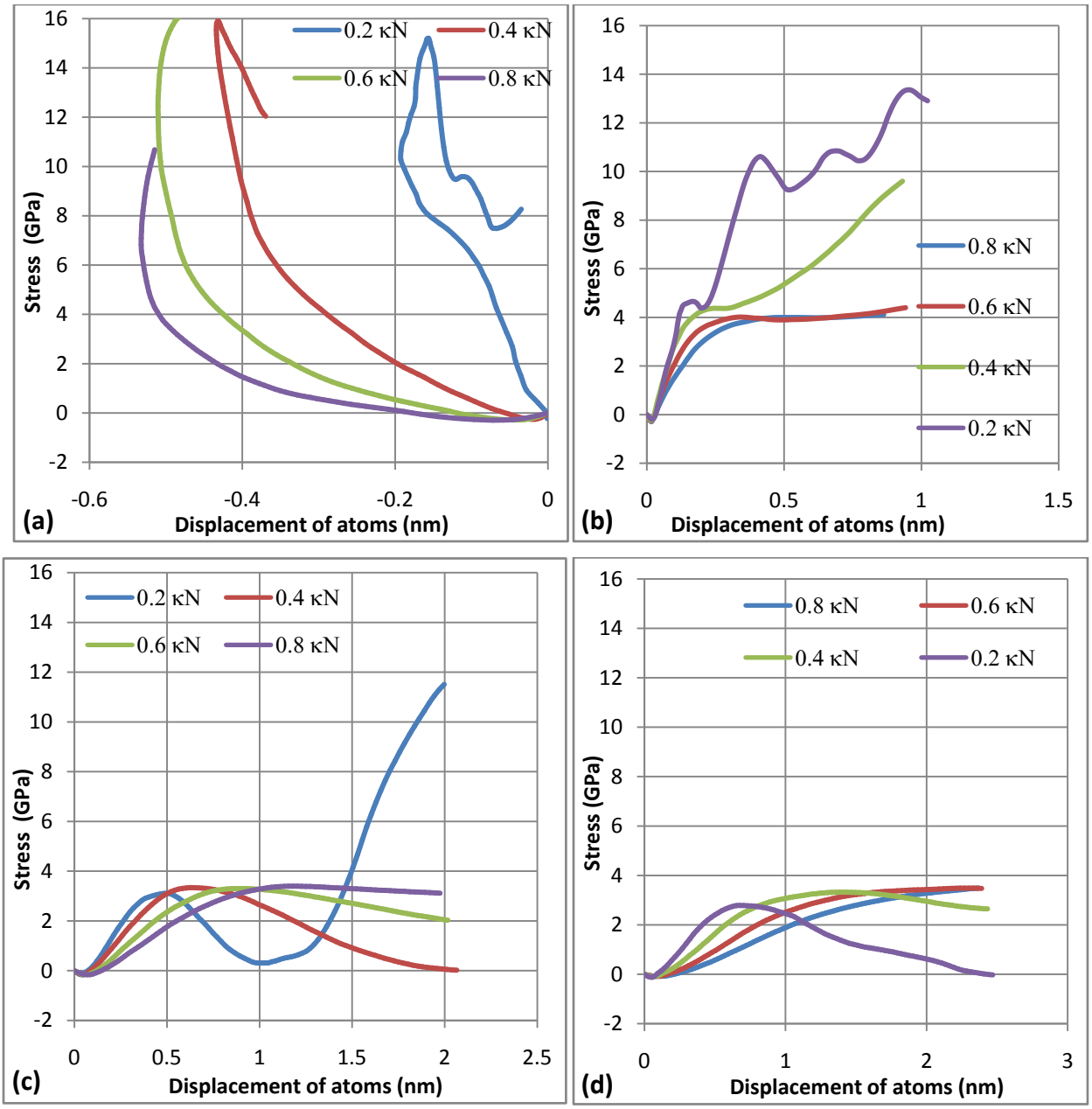

Figure 4.17: Resolved stress variation as anti-symmetric screw dislocation core atoms in Fe move under load in the (a) $[11\bar{1}]$, (b) $[110]$, (c) $[111]$, (d) $[112]$, directions.

Table 4.12 summarizes the results for the anti-symmetric screw dislocation from Figures 4.17b to 4.17d. For the [110] loading, the stress peaks decrease in value with increased load. This behaviour is only replicated by the edge dislocation. Additionally, loading in the [110] direction

produced the highest peak stress values. Secondary peaks were observed for the [110] and [111] loading directions.

Table 4.12: Resolved stress peaks as anti-symmetric screw dislocation core atoms in Fe move under load.

Start	Load (kN)	POLR (GPa)		
		1st Peak	2nd Peak	3rd Peak
[110]	0.2	4.64	10.60	10.80
	0.4	4.34	9.60	-
	0.6	4.01	-	-
	0.8	3.95	-	-
[111]	0.2	3.10	0.31	11.50
	0.4	3.34	-	-
	0.6	3.28	-	-
	0.8	3.39	-	-
[112]	0.2	2.78	-	-
	0.4	3.32	-	-
	0.6	3.48	-	-
	0.8	3.46	-	-

4.1.9. POLR STRESS RANGE FOR BCC DISLOCATRION CORES IN Fe– FMDCA

The curves presented for the FMDCA consistently feature resolved stress peaks that are related to the Peierl's stress. The values obtained for the pure screw dislocation and screw dislocations with reconstruction defects are all higher than published values of 1.1 - 1.9 GPa [181, 191, 194, 195] by a factor of about two. However, for the edge dislocation, the values obtained compared well with published values of 1.2 - 1.9 GPa [181,191]. It is also noted that the peak stresses vary marginally with the applied load, but appreciably with the direction of loading. These resolved stress peaks compare well with results for the RBM simulations. A summary of the peak resolved stresses for the single element Fe lattice is given in Table 4.13.

Loading in the [110] direction gives results in contrast to the other two directions. For the edge dislocation and the anti-symmetric screw dislocation, the peak resolved stresses reduce marginally as the load in the [110] direction is increased. In contrast, all peak resolved stresses increase marginally with increased load for the [111] and the [112] loading directions. While only of marginal significance, motion in the [110] direction is most likely for all dislocation types.

The peak resolved stresses recorded for the edge dislocation are lower than those for the screw dislocation. This agrees with empirical work that places the Peierl's stress for the edge dislocation below that of the screw dislocation [64, 181, 191]. The 70.52^{o} screw dislocation produces the highest resolved stress peak values at the higher applied loads for the [111] and [112] loading directions. The high stresses are consistent with empirical work that places the Peierl's stress for this dislocation core as one of the highest [192].

The symmetric screw core reconstruction favours the [110] loading direction, while the anti-symmetric screw core reconstruction favours the [111] and [112] loading directions. The symmetric screw dislocation loaded in the [110] direction shows resolved stress peaks that are marginally lower than those of the pure screw, while those for the other loading directions are higher. This is considered evidence of a higher mobility of the symmetric screw dislocation in the [110] direction. The anti-symmetric screw dislocation loaded in the [111] direction shows resolved stress peaks that are lower in magnitude than those of the pure screw, while those for the other loading directions are higher. This leads to the inference that the anti-symmetric screw dislocation is likely to possess higher mobility in the [111] direction. The variation in relative mobility of the screw dislocation and its variants suggests that the motion of the screw dislocation may be enhanced by mechanisms to alter the core's structure as the direction of the applied load is varied.

Table 4.13: Peak resolved stresses for dislocation cores in Fe – FMDCA.

Start	Load (kN)	Peak Stress (GPa)		
		[110]	[111]	[112]
Screw	0.2	3.83	3.31	2.36
	0.4	3.86	3.62	2.80
	0.6	3.79	3.68	3.24
	0.8	3.84	3.77	3.27
Edge	0.2	-1.41	-1.31	-1.62
	0.4	-1.40	-1.46	-1.64
	0.6	-1.38	-1.48	-1.63
	0.8	-1.38	-1.52	-0.22
35.26^{o} screw	0.2	-7.55	-7.30	-7.16
	0.4	-7.10	-7.41	-7.38
	0.6	-7.57	-7.51	-7.44
	0.8	-7.55	-7.61	-7.42
70.52^{o} screw	0.2	-14.69	-13.97	-14.21
	0.4	-13.98	-14.44	-14.65
	0.6	-13.95	-14.80	-14.87
	0.8	-14.69	-14.88	-14.92
Symmetric screw	0.2	4.05	2.95	3.20
	0.4	3.76	3.74	4.78
	0.6	3.77	3.89	4.75
	0.8	3.89	4.09	4.67
Anti-symmetric screw	0.2	4.64	3.10	2.78
	0.4	4.34	3.34	3.32
	0.6	4.01	3.28	3.48
	0.8	3.95	3.39	3.46

It is also proposed that the overall lower mobility of screw dislocations with reconstruction defects is evidence of a greater stability of the reconstruction defects observed in empirical work

[95, 97]. In addition, the peak stresses observed for screw dislocations with core reconstructions are still higher than those for the edge dislocation. This is consistent with empirical work as the existence of screw dislocations with reconstruction defects does not alter the relative higher mobility of the edge dislocation [118, 119] within the dislocation kink. It is proposed that up-scaling of the effects of dislocation motion to the dislocation line-length scale, for the Fe lattice, should be concentrated on the [111] and the [112] directions.

4.1.10. EFFECT OF CARBON ON DISLOCATION CORES – FMDCA METHOD

The introduction of interstitial carbon atoms into the Fe lattice was studied and curves for the FMDCA simulations plotted. Figures 4.18 to 4.21 give the results of these simulations.

4.1.10.1. Edge Dislocation

Figure 4.18 shows simulations of the edge dislocation in Fe-C lattice. The curves in Figure 4.18a are results for loading in the $[11\bar{1}]$ direction. As observed for the edge dislocation core in the Fe lattice, loading in the $[11\bar{1}]$ direction for the Fe-C lattice results in a reversal of the displacement with a peak displacement marginally below a quarter of the Burger's vector for all but the 0.2 kN applied load. This behaviour is similar to that observed for the edge dislocation in the Fe lattice other than the stresses in the Fe-C lattice are negative. As a result of the reversed displacement and the stress reversal at the peak displacement, it is inferred that this motion is unlikely.

Figure 4.18b shows curves for loading in the [110] direction. The curves show a rapid reduction in gradient between 5 to 10 GPa, which is followed by a region of gentle gradient with the gradient reducing with higher levels of loading. The profile of the curve for the 0.2 kN load cycle differed, with a stress peak of -28 GPa recorded at 0.3 nm displacement followed by a stress trough of -18.9 GPa. This is considered evidence that at lower loading levels, the internal stress field enabled the "peeling action" of atoms.

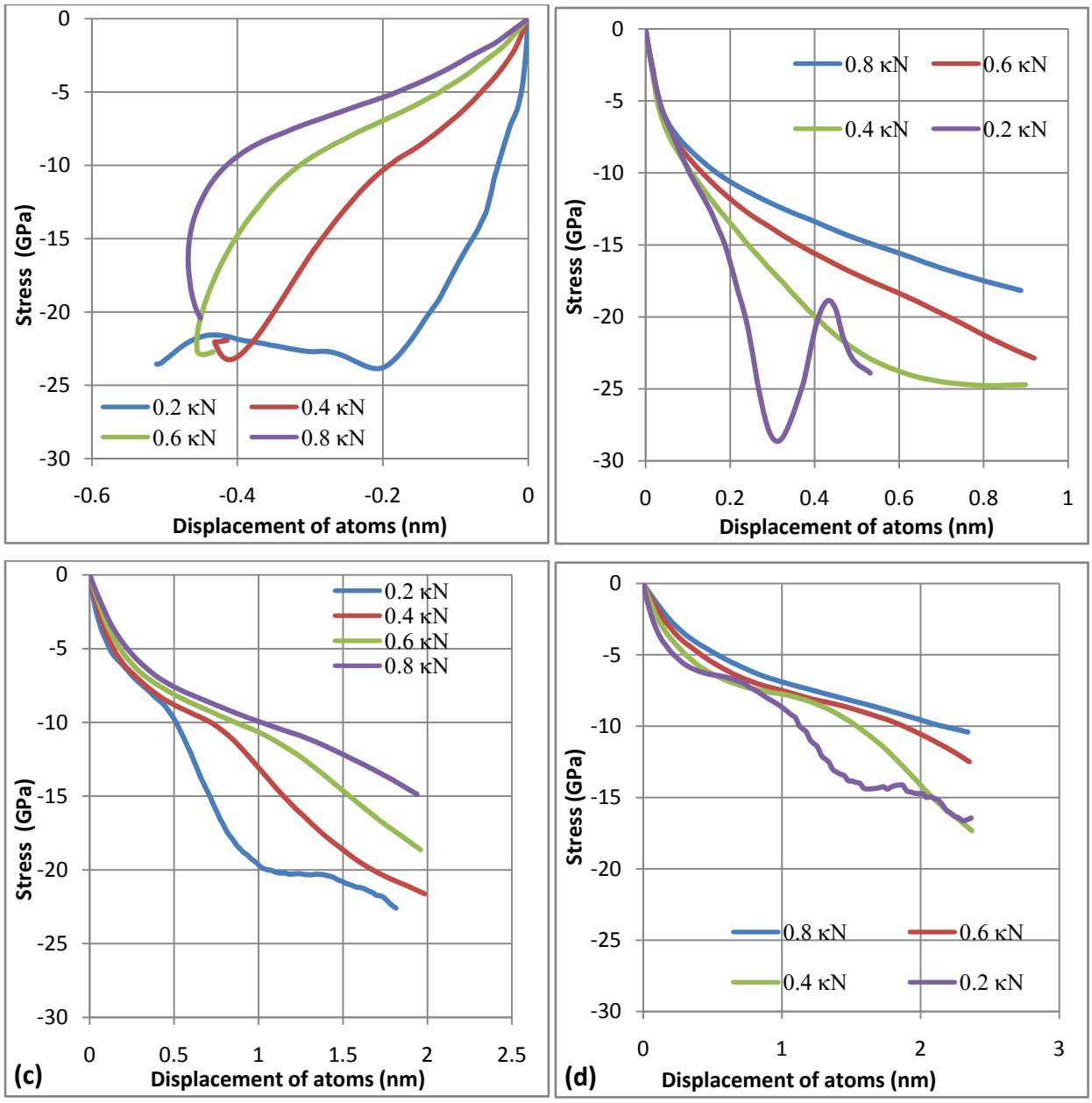

Figure 4.18: Resolved stress variation as edge dislocation core atoms in Fe-C move under load in the (a) [11$\bar{1}$], (b) [110], (c) [111], (d) [112], directions.

Curves for loading in the [111] and [112] directions are shown in Figures 4.18c and 4.18d respectively. The profiles of these curves are similar to those for loading in the [110] direction, with a difference in the shape of the 0.2 kN loading curve, where the stress peak is replaced with an inflection. It is inferred that reduced "peeling action" occurs for the [111] and [112] directions. Additionally, the stress peak/inflection occur at larger displacements as the loading

direction is changed to [111] and subsequently to [112] loading directions. It is observed that the lattice resistance is least in the [112] direction, and hence the dislocation's motion is most probable in this direction. The 0.2 kN loading scenario results in high peak/inflection stresses that are consistent with the strain hardening evident in Fe-C lattices. The lack of a clearly defined peak stress in the 0.4 kN, 0.6 kN and 0.8 kN loading scenarios is an indication that the strain limits for this lattice had not been achieved. The results shown in Figures 4.18b to 4.18d are summarized in Table 4.14.

Table 4.14: Resolved stress trough as edge dislocation core atoms in Fe-C move under load.

Start	Load (kN)	Trough Stress (GPa)			
		$[11\bar{1}]$	[110]	[111]	[112]
0	0.2	-23.86	-28.49	-20.30	-14.40
	0.4	-21.16	-24.73	-	-
	0.6	-22.84	-	-	-
	0.8	-	-	-	-

4.1.10.2. 35.26^o Screw Dislocation

Figure 4.19 shows simulations of the 35.26^o screw dislocation in Fe-C lattice. As observed in all other dislocations and lattice combinations, loading in the $[11\bar{1}]$ direction for the 35.26^o screw dislocation in Fe-C lattice is considered unlikely, due to the reversal of displacement coupled with the steady increase in stress values with displacement and the high stresses simulated.

Figures 4.19b to 4.19d show a steady increase in stress amplitude values with displacement. This increase is observed for the 0.4 kN, 0.6 kN, and the 0.8 kN loading scenarios, and is considered an indication of gradual strain hardening. The 0.2 kN loading led to peak stresses for each loading direction which is followed by a modest recovery. This behaviour is specific to the 0.2 kN loading scenario and reinforced earlier inferences that the internal stresses were significant (with respect to the applied load), and enough to influence the direction of motion of the atoms. The high peak stresses are consistent with the strain hardening evident in Fe-C lattices. It is recognized that the true stress strain curves do not depict a definite yield point, but instead show

an initial near linear profile, followed by a smooth curve with steadily decreasing gradient towards some stress maximum. The curves representing the 0.4 kN, 0.6 kN and the 0.8 kN loading conditions are therefore consistent with this behaviour observed at the macro-scale [196].

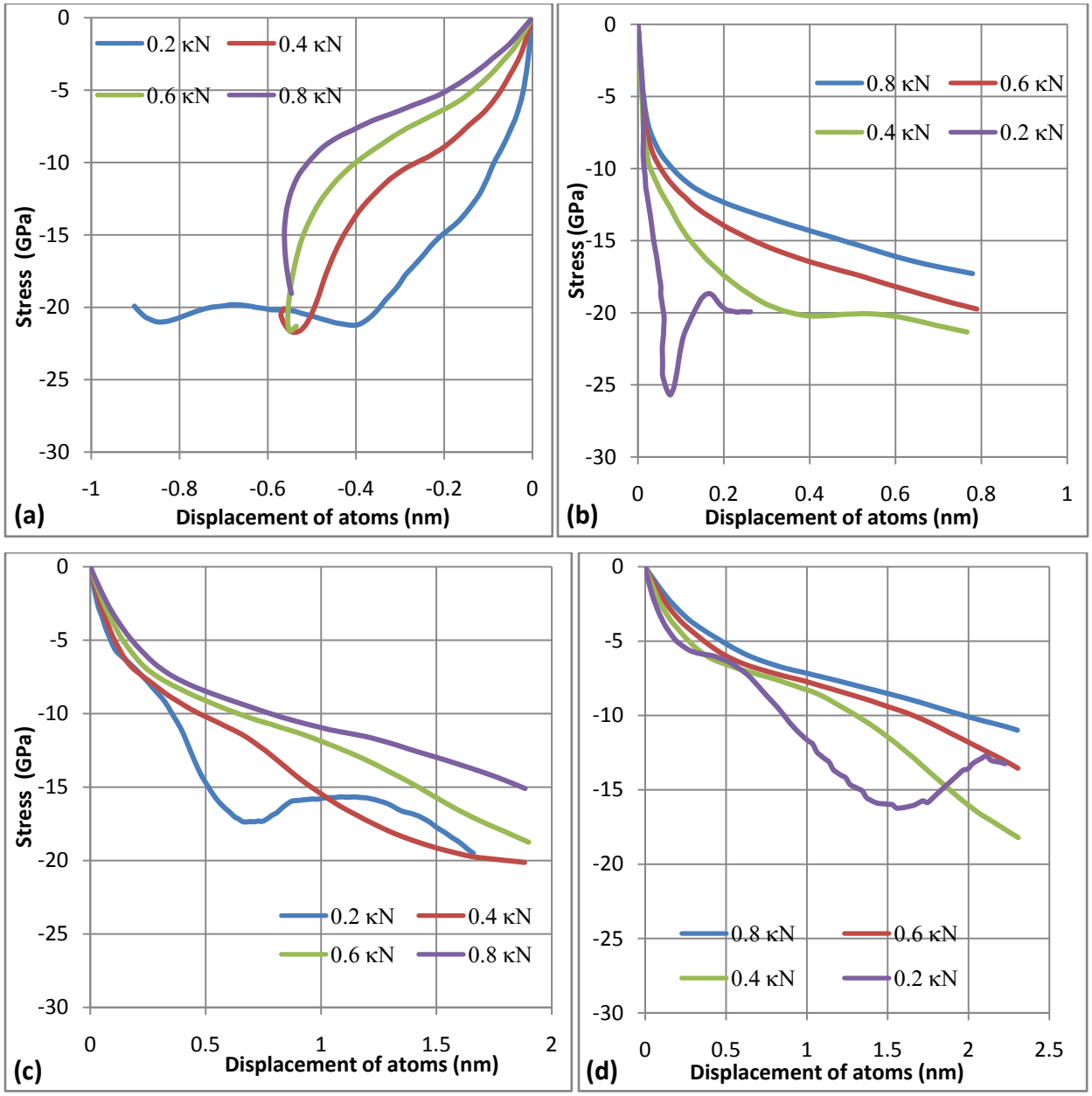

Figure 4.19: Resolved stress variation as 35.26° screw dislocation core atoms in Fe-C move under load in the (a) [11$\bar{1}$], (b) [110], (c) [111], (d) [112], directions.

The resolved stress peaks are summarized in Table 4.15.

Table 4.15: Resolved stress troughs as 35.26^o screw dislocation core atoms in Fe-C move under load.

Start	Load (kN)	Trough Stress (GPa)			
		[11$\bar{1}$]	[110]	[111]	[112]
0	0.2	-21.20	-25.69	-17.34	-16.17
	0.4	-21.69	-20.20	-	-
	0.6	-21.09	-	-	-
	0.8	-	-	-	-

4.1.10.3. 70.52^o Screw Dislocation

Similar comments may be made for the 70.52^o screw dislocation in the Fe-C matrix. Figure 4.20 illustrates the same patterns observed for the edge and 35.26^o screw dislocations. Table 4.16 summarizes the peak stresses for these simulations.

Table 4.16: Resolved stress troughs as 70.52^o screw dislocation core atoms in Fe-C move under load.

Start	Load (kN)	Trough Stress (GPa)			
		[11$\bar{1}$]	[110]	[111]	[112]
0	0.2	-20.80	-24.86	-15.86	-16.94
	0.4	-21.90	-	-	-
	0.6	-	-	-	-
	0.8	-	-	-	-

Applying 0.2 kN in the [110] direction results in appreciable "peeling action" at fairly large stresses and at low displacement as shown on Figure 4.20b. It is inferred that for the 70.52^o screw dislocation, small applied loads aided the "peeling action" of atoms.

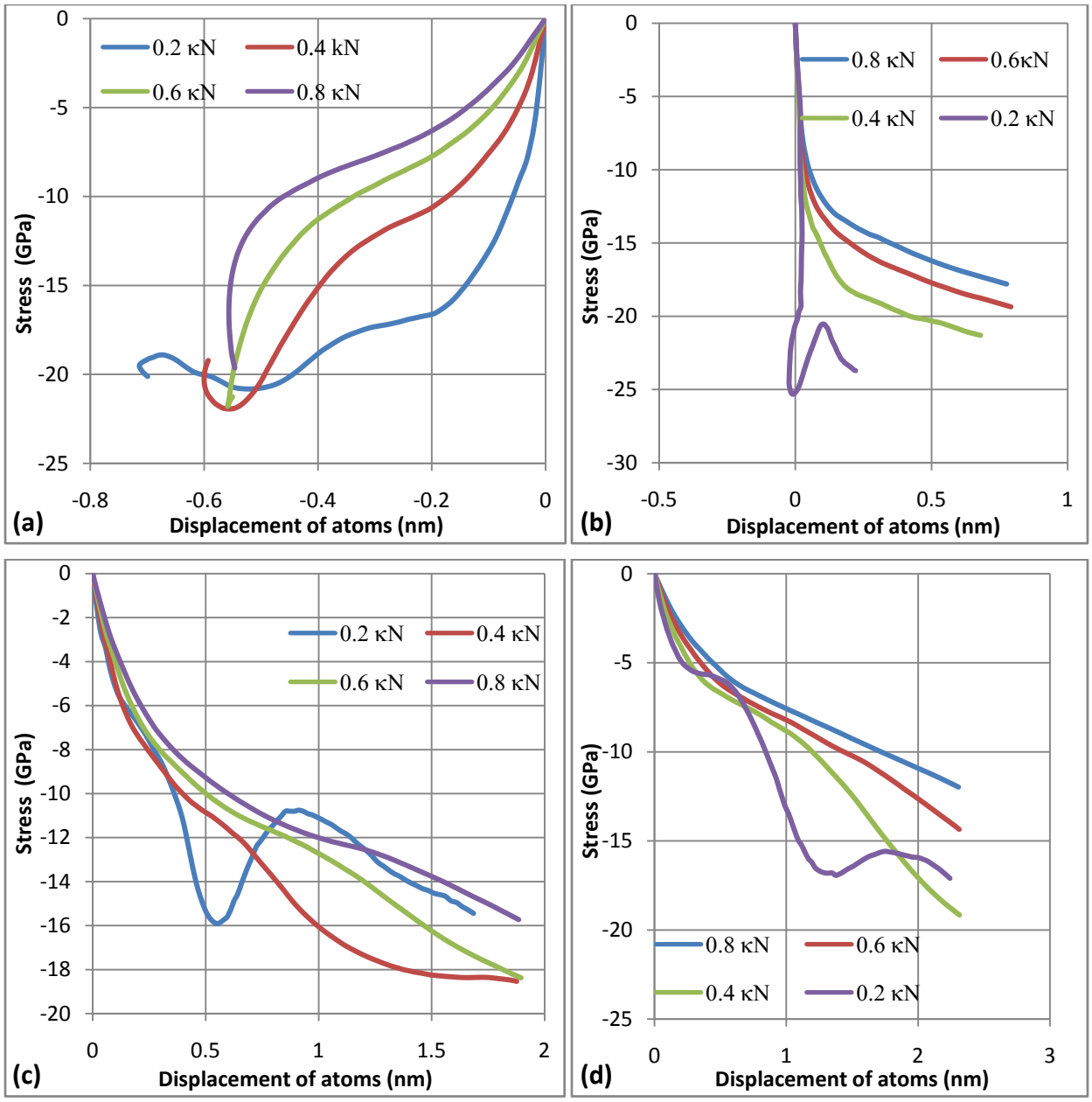

Figure 4.20: Resolved stress variation as 70.52° screw dislocation core atoms in Fe-C move under load in the (a) [11$\bar{1}$], (b) [110], (c) [111], (d) [112], directions.

4.1.10.4. Screw Dislocation

Figure 4.21 shows the stress curves for the screw dislocation in Fe-C lattice. The curves for loading in the [11$\bar{1}$] direction illustrate stress profiles that increase leading to the inference that motion in this direction is unlikely. Figure 4.21b shows stress curves for loading in the [110]

direction. The stress peaks are summarized in Table 4.17, and reduce in value as the load is increased. In addition, the number of peaks increase as the load is increased.

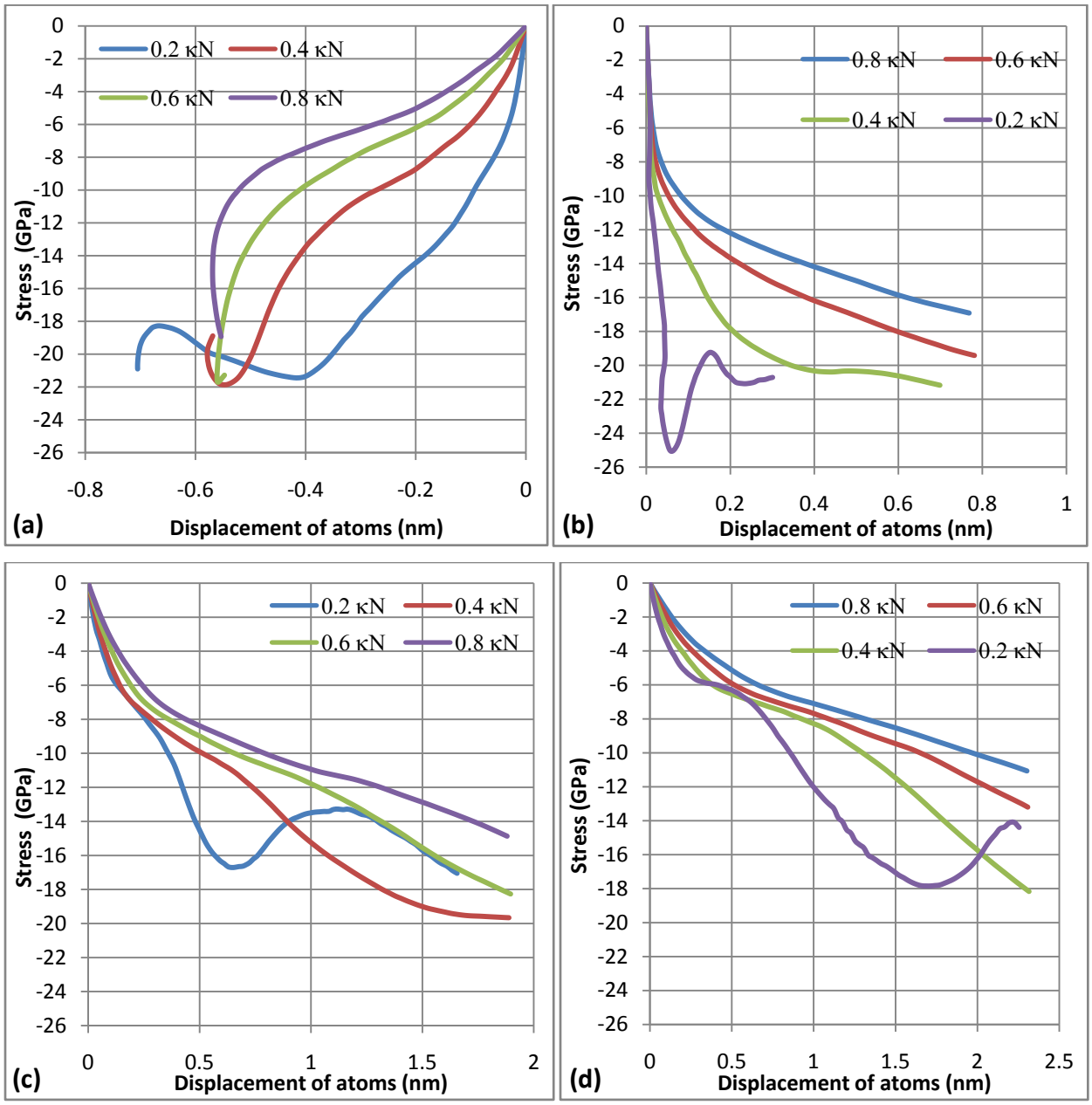

Figure 4.21: Resolved stress variation as screw dislocation core atoms in Fe-C move under load in the (a) $[11\bar{1}]$, (b) $[110]$, (c) $[111]$, (d) $[112]$, directions.

Table 4.17: Resolved stress troughs as screw dislocation core atoms in Fe-C move under load.

Start	Load (kN)	Trough Stress (GPa)			
		$[11\bar{1}]$	[110]	[111]	[112]
0	0.2	-21.43	-25.07	-16.70	-17.85
	0.4	-21.60	-20.33	-	-
	0.6	-21.35	-	-	-
	0.8	-	-	-	-

4.1.11. EFFECT OF CARBON ON RECONSTRUCTION DEFECTS – FMDCA METHOD

The effect of interstitial carbon on reconstruction defects was evaluated using FMDCA simulations and the results are shown in Figures 4.22 and 4.23.

4.1.11.1. Symmetric Screw Dislocation

Figure 4.22 shows the curves for the symmetric screw dislocation in Fe-C lattice loaded in the four directions. Figure 4.22a shows loading in the $[11\bar{1}]$ direction. Like all other simulations in this direction, there is a maximum displacement in the neighbourhood of 0.6 nm from the dislocation start position.

Figure 4.22b shows a unique shape, with an initial negative motion at the start of the cycle, accompanied by a large increase in stress. This is particularly pronounced for 0.2 kN loading. The rear-ward direction of the curves is related to rearward atom motion that is attributed to the need for dislocation core reorganization, to enable the motion of the dislocation core. However, the nature of the reorganization has not been established.

The rear-ward direction of the curve persists for 0.2 kN loading once the loading direction changes to the [111] direction and to a lesser degree, the [112] direction. This behaviour is shown in Figures 4.22c and 4.22d. It is inferred that the greater the contribution of the internal stress to the overall motion of the dislocation core, the greater is the need for dislocation core reorganization.

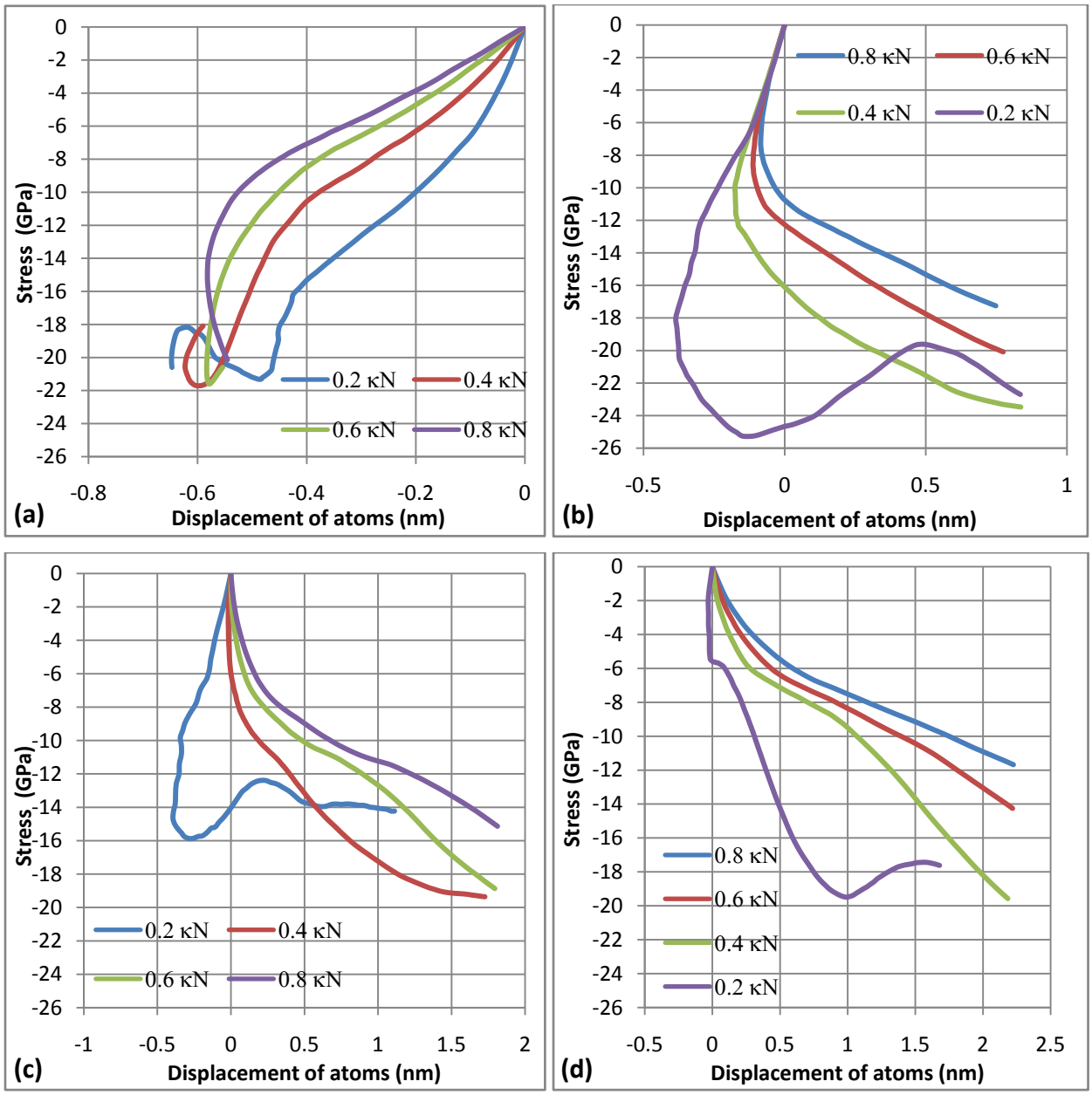

Figure 4.22: Resolved stress variation as symmetric screw dislocation core atoms in Fe-C move under load in the (a) [11$\bar{1}$], (b) [110], (c) [111], (d) [112], directions.

Table 4.18 summarizes the trough stresses for simulations in the four loading directions. The values of the stress troughs were greater than the Peierl's stress by a factor of about 10.

Table 4.18: Resolved stress troughs as symmetric screw dislocation core atoms in Fe-C move under load.

Start	Load (kN)	Trough Stress (GPa)			
		$[11\bar{1}]$	[110]	[111]	[112]
0	0.2	-21.31	-25.27	-15.76	-19.45
	0.4	-21.66	-	-	-
	0.6	-21.33	-	-	-
	0.8	-	-	-	-

4.1.11.2. Anti-Symmetric Screw Dislocation

Figure 4.23 shows the curves for the loading of the anti-symmetric screw dislocation in Fe-C lattice. Table 4.19 summarizes the trough stresses for simulations in the four loading directions. As discussed before, loading in the $[11\bar{1}]$ direction (Figure 4.23a) is improbable due to the reversal in displacement coupled with the steady increase in stress values.

Table 4.19: Resolved stress troughs as anti-symmetric screw dislocation core atoms in Fe-C move under load.

Start	Load (kN)	Trough Stress (GPa)			
		$[11\bar{1}]$	[110]	[111]	[112]
0	0.2	-21.34	-26.25	-16.63	-15.86
	0.4	-21.70	-	-	-
	0.6	-21.27	-	-	-
	0.8	-	-	-	-

Loading 0.2 kN in the [110], [111] and [112] directions produces similar stress profiles. The steady increase in stresses with displacement for the other loading cycles suggests that some maximum does occur at some extended displacement, which implies that peak stresses are not cyclic as presented in the P-N model [55]. This is particularly so for loading in the [112] loading direction, where peak stress values occur at close to one Burger's vector displacement.

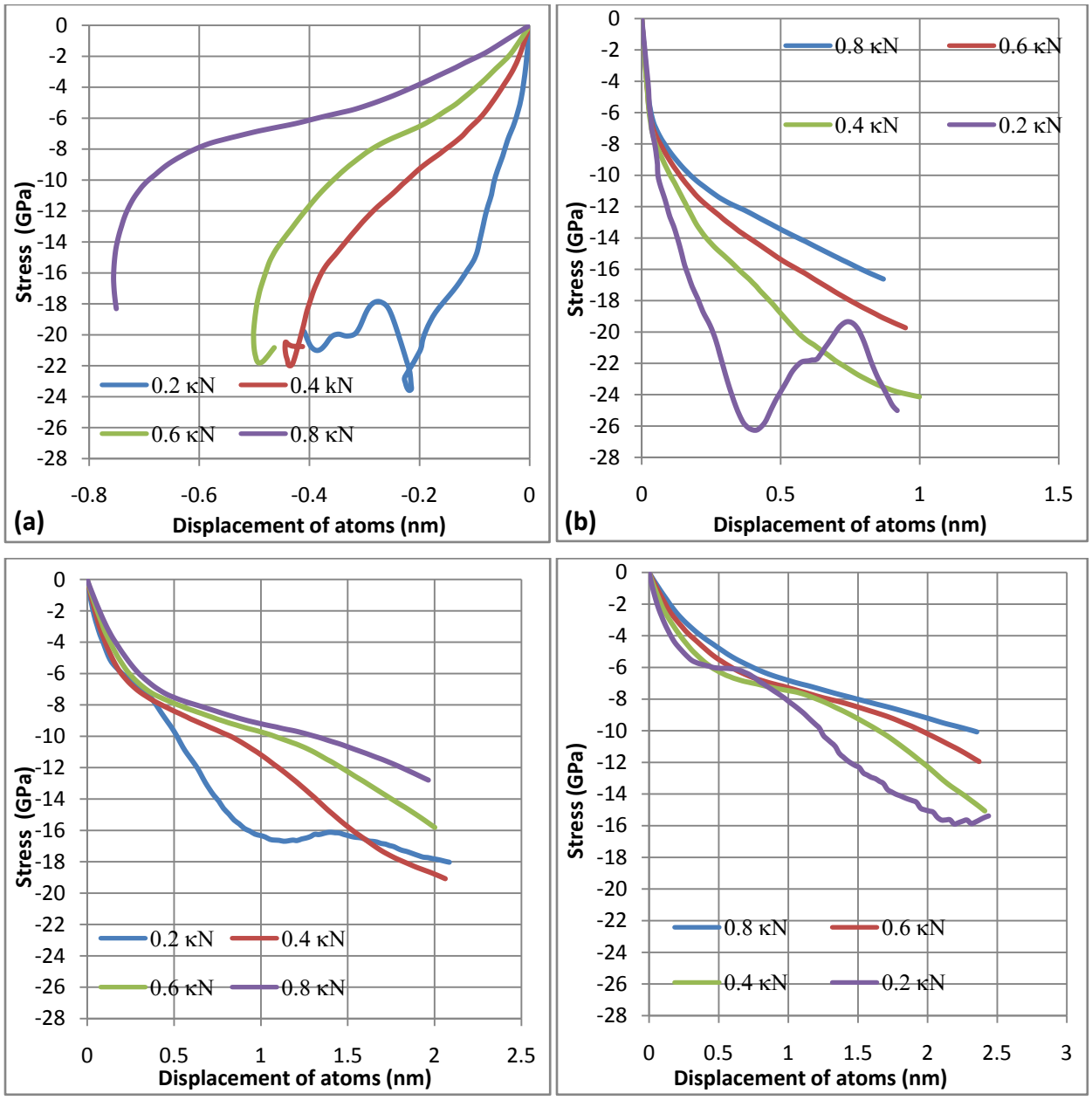

Figure 4.23: Resolved stress variation as anti-symmetric screw dislocation core atoms in Fe-C move under load in the (a) $[11\bar{1}]$, (b) [110], (c) [111], (d) [112], directions.

4.1.12. POLR STRESS RANGE FOR BCC Fe-C– FMDCA METHOD

The curves produced by the FMDCA consistently featured stress peaks that were much larger than the Peierl's stress of 1.1 - 1.9 GPa [181, 191, 194, 195]. This is expected, as published values are for Fe lattices. However, using the results for the pure Fe lattice as a benchmark, it is

noted that results for the Fe-C lattice are larger than those of the Fe lattice by a factor in the order of 10. The simulations were carried out near the interstitial carbon atom sites, and hence the stresses were sampled in regions with high concentration of carbon. In practice, pockets of carbon-rich regions exist within a matrix with low concentrations of carbon. The resulting stress field would be the ensemble average of the carbon-free and carbon bearing material matrix. A summary of the trough stresses for the Fe-C lattice is given in Table 4.20.

Table 4.20: Trough stresses for dislocation cores in Fe-C – FMDCA.

Dislocation Type	Load (kN)	Trough Stress (GPa)			
		$[11\bar{1}]$	[110]	[111]	[112]
Screw	0.2	-21.43	-25.07	-16.70	-17.85
	0.4	-21.60	-20.33	-	-
	0.6	-21.35	-	-	-
	0.8	-	-	-	-
Edge	0.2	-23.86	-28.49	-20.30	-14.40
	0.4	-21.16	-24.73	-	-
	0.6	-22.84	-	-	-
	0.8	-	-	-	-
35.26^o screw	0.2	-21.20	-25.69	-17.34	-16.17
	0.4	-21.69	-20.20	-	-
	0.6	-21.09	-	-	-
	0.8	-	-	-	-
70.52^o screw	0.2	-20.80	-24.86	-15.86	-16.94
	0.4	-21.90	-	-	-
	0.6	-21.40	-	-	-
	0.8	-	-	-	-
Symmetric screw	0.2	-21.31	-25.27	-15.76	-19.45
	0.4	-21.66	-	-	-
	0.6	-21.33	-	-	-
	0.8	-	-	-	-
Anti-symmetric screw	0.2	-21.34	-26.25	-16.63	-15.86
	0.4	-21.70	-	-	-
	0.6	-21.27	-	-	-
	0.8	-	-	-	-

4.1.13. POLR MODEL

The POLR was defined as that path traced by an atom moving in the direction of the lowest stress component, with the direct stress components coincident with the edges of the Bravis unit forming the lattice.

The movement of the dislocation through the lattice generated a variable stress profile about a non-zero mean value. The analysis sought to determine whether the Peierl's stress was related to the initial or the maximum value of the resolved stress cycle, the amplitude of the resolved stress cycle, the initial or the maximum stress value of the POLR, or the amplitude of the POLR. The resolved stress cycle incorporated the total energy gradient, including that due to the material cohesion and the formation of the dislocation core, which was represented by the stress value before dislocation motion began.

The concept of metallic bonding is founded on attraction and repulsive forces arising from the charge distribution between valence electrons removed from atomic energy levels into crystal energy levels known as bands, and the atoms that provide the valence electrons [182]. The displacement of a dislocation retains the dislocation core intact and does not require the breaking of bonds. Instead, this motion requires a relative translation of the atoms. Consequently, the energy to coalesce the atoms and the energy to form the dislocation core do not feature in the movement of the dislocation line. Rather, it is the incremental energy that is required to move the atoms that contributes to the energy gradient encountered in dislocation motion. Consequently, any formulation explaining the Peierl's stress should relate to the incremental energy required to move the atoms, and not the total energy of the system as represented by the resolved stress cycle. The amplitude of the resolved stress cycle excludes the energy gradient due to material cohesion and dislocation formation, and is a possible basis for a formulation explaining the Peierl's energy.

The initial values for both the resolved stress cycles and the component stress cycles were unlikely to present values of the Peierl's stress as they were in themselves snap shots of a dynamic system, in this case the start of the cycle located at some arbitrary point in the cycle by

the set up of the simulation code. The remaining values to be considered were the peak values and the amplitudes, of the resolved stress cycles and the component stress cycles.

The graphs presented were formed by a series of snapshots during the movement of a dislocation, comprising predetermined atom displacements that retained an overall BCC spatial lattice arrangement. What was lacking was the individual atom motion that cumulatively generated the dislocation motion. The movement of the atom was expected to follow the lowest energy gradient profile. Therefore, instead of displacement of atoms along the prescribed dislocation motion vector, the atoms were expected to move in the direction represented by the lowest stress profile. The notion that directional movement of atom is the prime mechanism for dislocation motion is embodied in the definition of the POLR. The POLR was related to the stress components, and it was presumed that the total energy gradient, including that due to the material cohesion and the formation of the dislocation core, was in specific directions. However, it was necessary to exclude the effects of material cohesion and dislocation formation, and hence the amplitude of the POLR was considered as the value that would most closely relate to the Peierl's stress. The amplitude of the POLR presumed that the energy gradients due to material cohesion and dislocation formation did not contribute to the resistance to dislocation motion, and that the active energy gradients occurred in specific directions.

4.1.14. FITTING OF COEFFICIENTS OF THE POLR EQUATION

The stress components in the [100], [010] and [001] directions at the first peak of the resolved stress profile were used to compare with the stress components from the RBM and the FMDCA simulations. These components are presented in Table 4.21.

The resolved stresses for the screw dislocation are the highest values, while the values for the edge dislocation have the narrowest range. However, despite the large value in the [111] direction, the 35.26^{o} screw has the lowest resolved stresses. This further reinforces the earlier assertion that the 35.26^{o} screw moving in the direction of the edge dislocation's Burger's vector is a probable mechanism contributing to plastic deformation. The stress component values are used as reference values in the fitting of the coefficients of the polynomial function that characterized the stress profile.

Table 4.21: Direct stress components at the first peak for the different dislocation types.

Dislocation type	Direct stress components (GPa)			Resolved stress (GPa)
	[100]	[010]	[001]	
Screw [**11$\bar{1}$**]	2.67	0.57	-9.58	9.96
Screw [**110**]	-2.92	-5.56	-12.45	13.95
Screw [**111**]	-7.44	-9.65	-10.76	16.26
Screw [**112**]	-8.84	-10.44	-8.02	15.86
35.26^o [**11$\bar{1}$**]	3.14	-0.26	3.14	4.45
35.26^o [**110**]	6.10	2.26	-4.83	8.10
35.26^o [**111**]	6.82	3.95	-11.03	13.55
35.26^o [**112**]	0.92	-1.67	7.23	7.48
70.52^o [**11$\bar{1}$**]	1.36	-1.52	-9.77	9.98
70.52^o [**110**]	5.268	-1.52	-9.77	11.20
70.52^o [**111**]	-3.05	-5.06	-5.50	8.07
70.52^o [**112**]	-5.09	-6.28	-2.14	8.36
Edge [**11$\bar{1}$**]	7.54	2.52	8.62	11.73
Edge [**110**]	10.19	5.67	0.77	11.69
Edge [**111**]	9.49	4.10	6.41	12.17
Edge [**112**]	7.16	5.17	-5.15	10.22

The amplitudes at the first displacement peak are used as input into the misfit potential, which is then used to determine the stress field due to the dislocation core over the slip plane. Using the peak displacements, linking of the core model to the misfit potential is achieved. The maximum displacements are given in Table 4.22.

Table 4.22: Displacement amplitude at the first peak for the different dislocation types.

Dislocation type	Principal displacement components (nm)			Displacement amplitude (nm)
	[100]	[010]	[001]	
Screw - [**11$\bar{1}$**]	0.56	-1.94	0.81	2.17
Screw [**110**]	0.16	-1.92	1.10	2.22
Screw [**111**]	0.29	-1.82	0.94	2.07
Screw [**112**]	0.32	-1.62	0.97	1.91
35.26^o [**11$\bar{1}$**]	2.02	-0.34	1.82	2.74
35.26^o [**110**]	1.57	-0.51	1.51	2.23
35.26^o [**111**]	1.52	-0.68	1.41	2.18
35.26^o [**112**]	1.47	-0.60	1.35	2.08
70.52^o [**11$\bar{1}$**]	0.35	-1.35	1.16	1.82
70.52^o [**110**]	0.63	-0.91	1.13	1.58
70.52^o [**111**]	0.60	-0.88	1.15	1.57
70.52^o [**112**]	0.61	-0.87	1.17	1.58
Edge [**11$\bar{1}$**]	1.39	-0.15	1.92	2.37
Edge [**110**]	1.34	-0.21	2.03	2.44
Edge [**111**]	1.52	-0.27	1.94	2.47
Edge [**112**]	1.49	-0.15	1.85	2.37

4.2. MISFIT POTENTIAL

Section 4.2 gives results from the application of the misfit potential in the analysis of the stress fields due to dislocation cores within slip planes in BCC Fe lattice. Within each sub-section, the resulting distortion profiles in the [100], [010] and [001] directions are analysed, followed by an analysis of the corresponding stress amplitude profiles with and without the contribution of the misfit potential.

4.2.1. MISFIT DUE TO A STRAIGHT EDGE DISLOCATION LINE

The distortion profile was plotted for three planes intersecting the dislocation line. The first direction was along the centre of the block of atoms and the other two were at the front and rear

planes of the block. This is illustrated on Figure 4.24a. Figure 4.25 shows results of the amplitude of the distortion along the Cartesian coordinate axes.

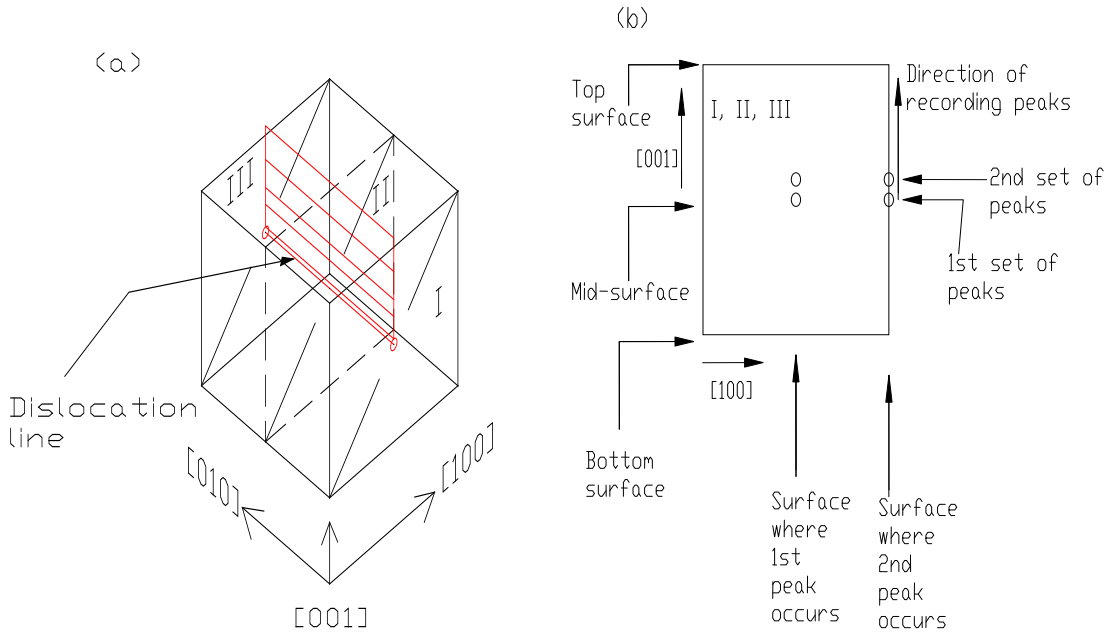

Figure 4.24: Block of atoms containing dislocation core and slipped surface, and showing front (I) middle (II), rear (III) surfaces; (a) 3D illustration (b)2D illustration.

The simulations produced a series of peaks that occurred in pairs representing planes of atoms parallel to the slip plane. For every pair of peaks, the first peak pair represented the lattice point adjacent to the slip plane and the second peak represented the lattice point at the edge of the simulation block, on the same plane of atoms. The first pair of peaks represented the plane of atoms adjacent to the slip plane, while the second pair of peaks represented the plane of atoms adjacent to the first plane on the same side of the slip plane. The other peaks represented planes of atoms similarly located. This is illustrated on Figure 4.24b.

Three curves are presented on each chart. The curve labelled “x-313 to 625” represents lattice sites on the front surface of the block of atoms (surface I), with site number 313 adjacent to the dislocation core. The curve labelled “x-7813 to 8125” represents lattice sites on the mid-surface of the block of atoms (surface II), with site number 7813 adjacent to the dislocation core. The curve labelled “x-15313 to 15625” represents lattice sites on the rear surface of the block of

atoms (surface III), with site number 15313 adjacent to the dislocation core. This notation is applied in all the distortion curves in section 4.2. The distortion peaks of interest are the first peak in every pair as these gave data related to the distortion in the neighbourhood of the dislocation core.

Figure 4.25 shows distortion results for the edge dislocation. It is noted that for the edge dislocation, these three curves overlap in each direction considered, and this is evidence that the distortion is not influenced by the free surfaces of the block. The distortion peak amplitude increases as the distance from the slip plane increases over the first four rows of atoms, and then decreases over the next two rows of atoms. A further increase in distortion occurs on the seventh row of atoms before a considerable drop on the eighth row. The peak then gradually increases from the ninth to the 13^{th} rows. This behaviour is observed along all three directions considered. The peak distortion occurs at the fourth row of atoms from the slip plane. This is considered significant as it suggests that the study of the dislocation core behaviour should include the behaviour of the first four rows of atoms. It is inferred that dislocation aggregation such as in grain boundaries is likely to consist of dislocations with a minimum spacing of four Burger's vectors.

Secondary peaks at the seventh and the 13^{th} row of atoms reveal that the dislocation core has a sinusoidal distortion effect on the lattice. This means that, depending on the location of a lattice feature with respect to the dislocation core, the lattice feature experiences different distortional influences due to the core. This cyclic behaviour, occurring over a number of lattice points, differs from the Peierl's Nabarro (P-N) model [98, 99], where the cycles occur between lattice points. This feature has not been found in other studies.

The distortion maximum amplitude occurs over a very small region, as evidenced by the sharp peaks. These localized peaks suggest that the dislocation core effects occur in narrow bands and the determination of the spread and distances to this band would aid the modelling of the interaction of the dislocations.

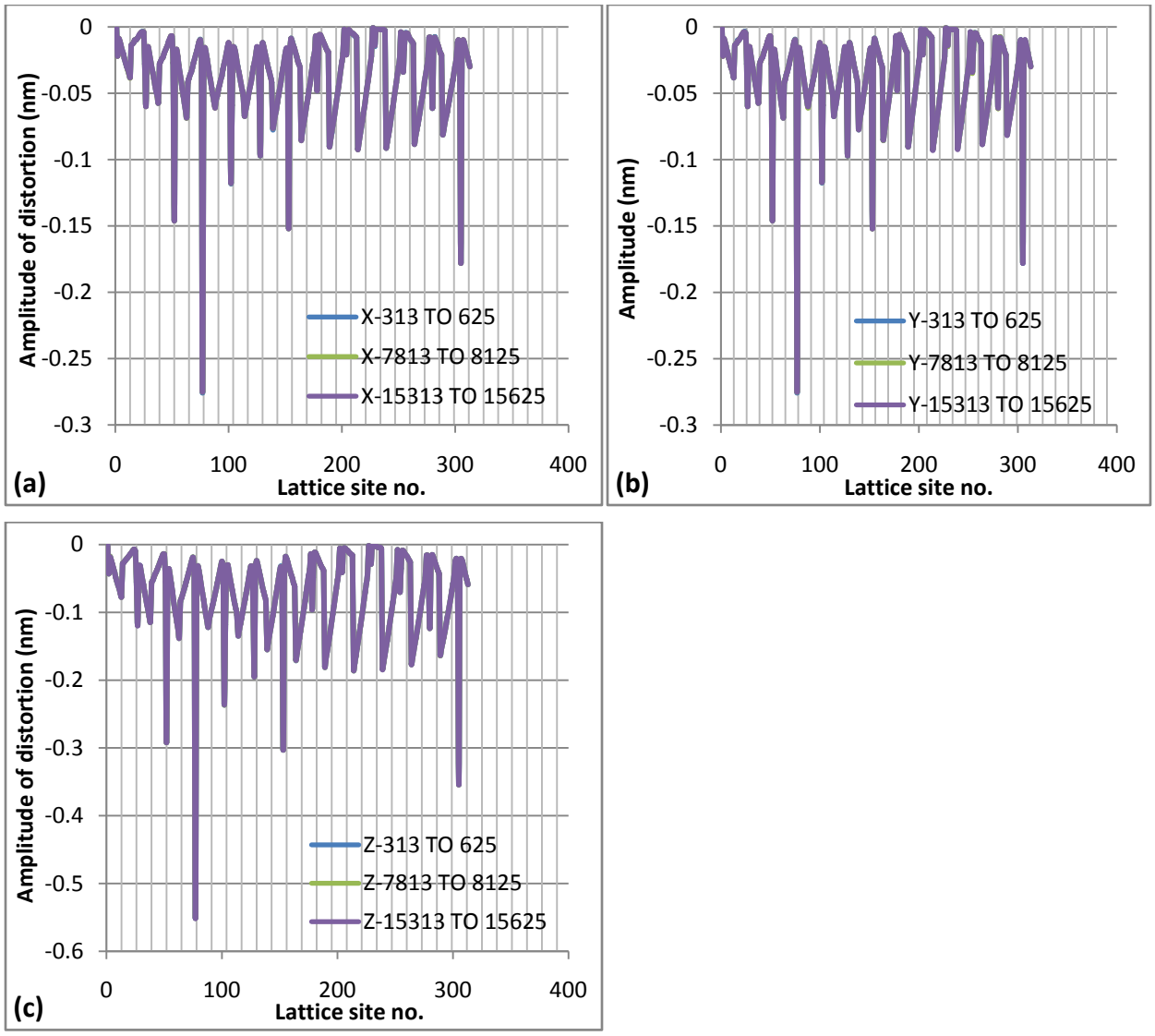

Figure 4.25: Lattice distortion along the (a) [100] , (b) [010], (c) [001] directions for an edge dislocation with misfit effect.

The distortion in the *z* direction is nearly twice that in the other two directions. This is attributed to the fact that the Burger's vector of the edge dislocation has twice the amplitude in the *z* direction in comparison with the other two directions. This behaviour is mirrored in the stress amplitude profile shown in Figure 4.27b.

Figures 4.26 and 4.27 show the stress amplitude profiles at lattice points about the dislocation core. The stress is constant, with and without the misfit effects, along the dislocation line as

shown in Figure 4.26. This is consistent with the expectations since the dislocation line was modelled as a series of identical cores. The variation observed on the left side of the curve is attributed to the effects of the free surface.

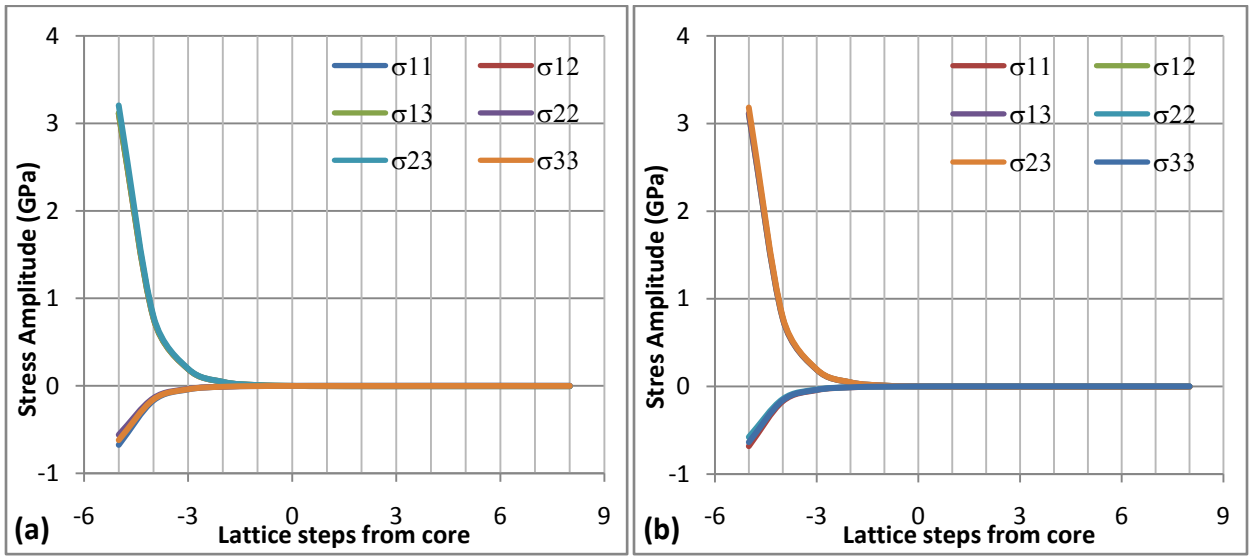

Figure 4.26: Stress amplitude variation for an edge dislocation at lattice sites along the dislocation line – (a) without the misfit effect, (b) with misfit effect.

However, normal to the dislocation line, a stress plateau is observed within the slipped region in the absence of the misfit effects as shown in Figure 4.27a. This stress increase is expected as the dislocation core is observed to generate an increase in lattice stress over the slipped region, as shown in Table 4.1.

The application of the misfit results in the spreading of the stress values coupled by a cyclic stress amplitude profile are shown in Figure 4.27b. The spreading of the stress components is consistent with the "peeling action", as it provides the mechanism for which motion of atoms across the slip plane could occur to support slip plane motion. On the other hand, the cyclic behaviour differs with that presented in the P-N model, [98, 99] as it occurs over several Burger's vectors. The peaks of these stress component curves increase marginally further away from the dislocation core. This indicates that the dislocation core induces a lattice strengthening phenomena at specific distances from the dislocation core. The effect of this phenomenon is that the dislocations are likely to experience low resistance to motion as long as they are located

within these stress valleys. It is proposed that the pattern of the stress peaks be studied later in greater detail.

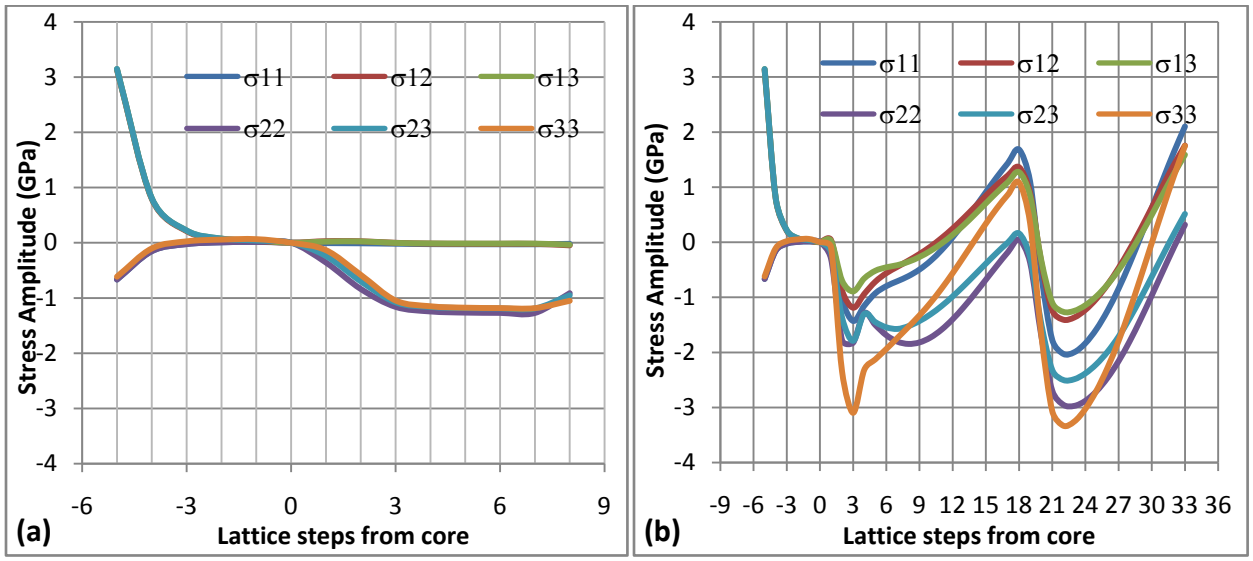

Figure 4.27: Stress amplitude variation for an edge dislocation at lattice sites normal to the dislocation line – (a) without the misfit effect, (b) with misfit effect.

POLR values of 1.185 and 1.429 GPa are obtained from Figure 4.27a and 4.27b along σ_{33} and σ_{11} respectively. These compare well with values of the Peierl's stress of 1.2 - 1.8 GPa by Chaussidon et al. [181], 1.3 - 1.9 GPa by Ventelon [191], 1.5 GPa by Terentyev et al. [194] and 1.1 GPa by Shimizu et al. [195] for the BCC Fe lattice. It is noted that the misfit effect is to concentrate the POLR peak stress value about the 3rd lattice position and to amplify its magnitude.

4.2.2. MISFIT DUE TO A STRAIGHT SCREW DISLOCATION LINE

Figures 4.28 to 4.30 show the distortion amplitude curves for the screw dislocation along the same paths as used in the edge dislocation simulations. These curves show amplitudes of the distortion for the screw dislocation that are markedly smaller than for the edge dislocation, after the initial large distortion at the dislocation core. This initial distortion at the core is larger than that of the edge dislocation, and it is consistent with large core stresses for the screw dislocations [181, 194]. It is noted that the curves at the front, middle and rear surfaces of the block of atoms do not overlap as for the edge dislocation.

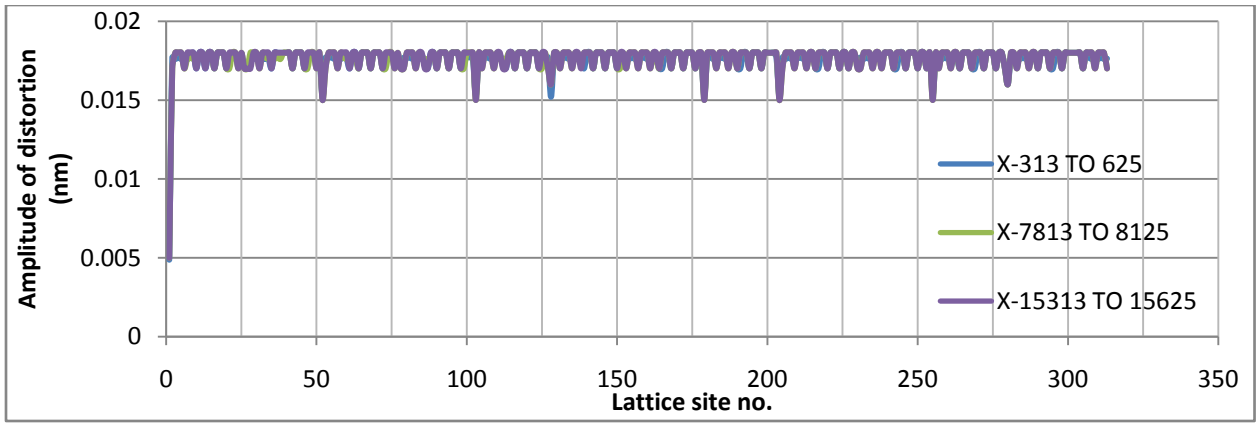

Figure 4.28: Lattice distortion along the [100] direction for a screw dislocation with misfit effect.

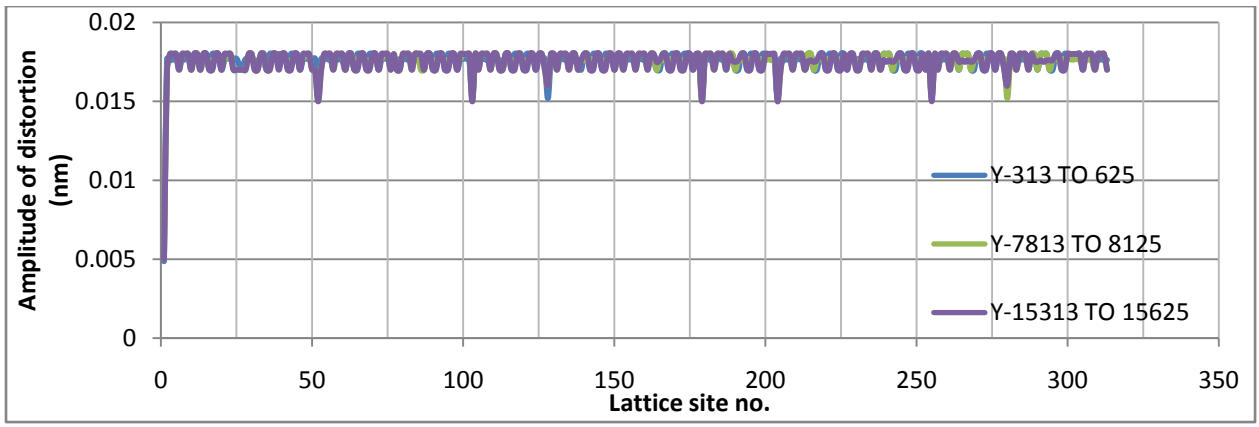

Figure 4.29: Lattice distortion along the [010] direction for a screw dislocation with misfit effect.

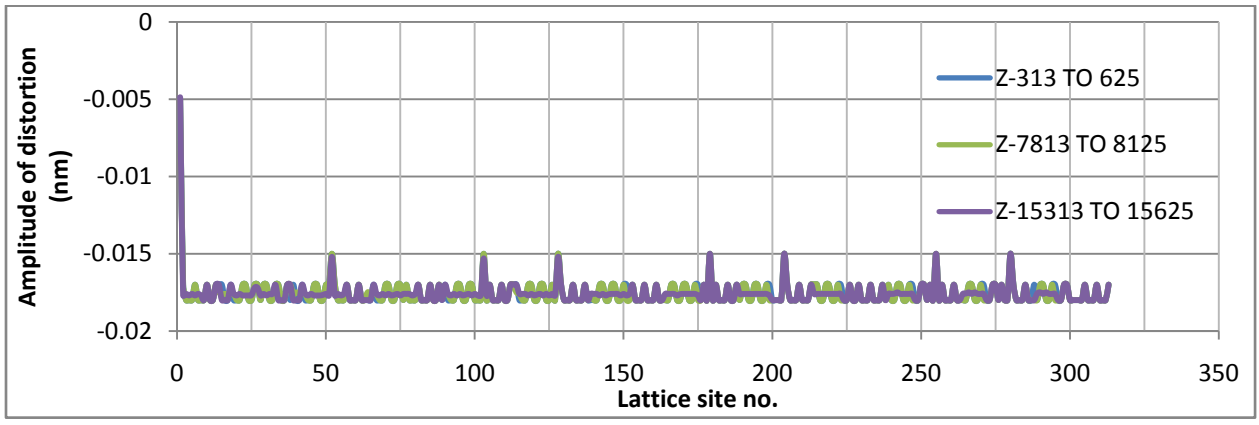

Figure 4.30: Lattice distortion along the [001] direction for a screw dislocation with misfit effect.

The distortion peaks recorded are two per atomic plane (compared with those for the edge dislocation). Additionally, in contrast to the findings for the edge dislocation, the peaks for the screw dislocation are approximately of the same magnitude. The increase in the number of distortion peaks, coupled by a near constant value of peak distortion, is an indication that the lattice would provide a near constant stress amplitude profile over the slipped region. This is consistent with the stress curves in Figure 4.31b. The amplitude of the distortion in the three directions considered is of the same order of magnitude, which is different from the findings for the edge dislocation.

The distortions in the [100], [010] and [001] directions along the middle of the block of atoms (x-7813 to 8125) differ from those obtained from the surface of the block of atoms. It is therefore inferred that surface effects do affect the screw dislocation along the three directions considered, unlike for the other dislocation types. This does not appear to contribute to the variation of the stress amplitude profiles obtained, largely due to the size of the block of atoms. However, it is expected that it may contribute to the stress amplitude profile of an assembly of dislocations.

Figures 4.31 and 4.32 show stress amplitudes for the screw dislocation in the Fe lattice. Figure 4.31a shows results without the contribution of the misfit potential, and demonstrates that the dislocation core did introduce stress increases in the lattice. This is consistent with the concept of the P-N model [98, 99]. On the other hand, the misfit effect shown in Figure 4.31b shows a marginal increase in the POLR (along σ_{11}) stress peak from 1.732 GPa (Figure 4.31a) to 2.070 GPa, followed by a near constant stress. This is an indication that the screw dislocation does not provide stress valleys which could aid dislocation motion. This is a major difference in behaviour from that of the edge dislocation, and is believed to contribute to the higher mobility of edge dislocations [118]. The effect of the misfit is to increase the POLR stress for the screw dislocation to 2.070 GPa, which compares well with published values of 1.1 - 1.9 GPa [181, 191, 194, 195], but more importantly, is higher than values recorded for the edge dislocation. This is consistent with expectations, as empirical work [118] showed that the edge dislocations process a higher mobility than the screw dislocations. Figure 4.32 shows the stress amplitude profile along the dislocation line. As expected, there is no variation in the stress component values, apart from that due to the surface of the block of atoms.

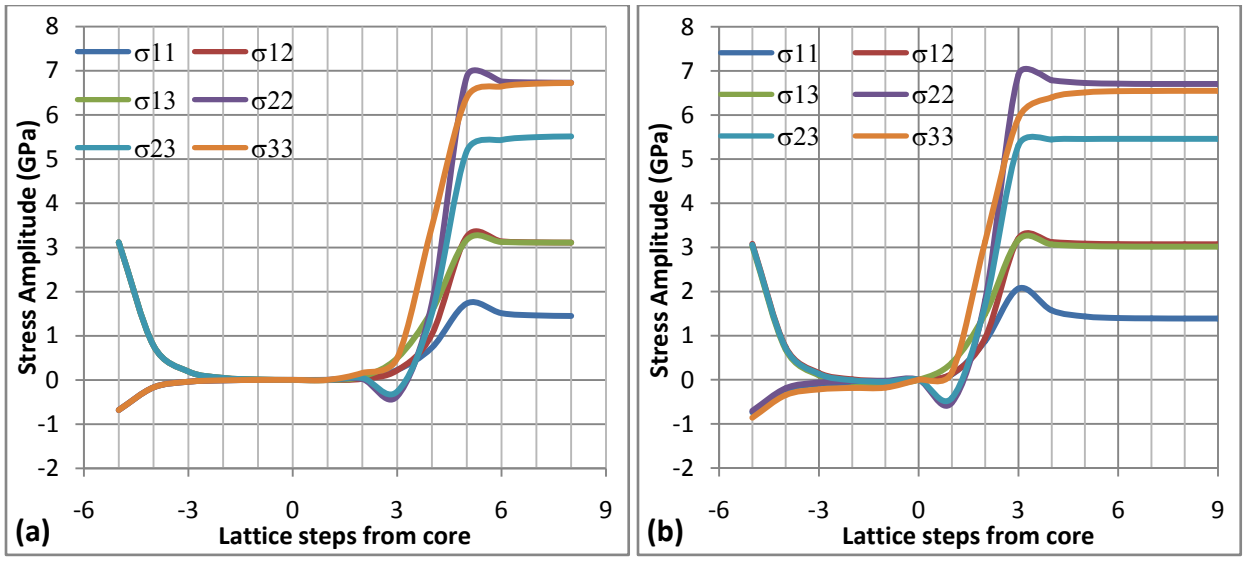

Figure 4.31: Stress amplitude variation for a screw dislocation at lattice sites normal to the dislocation line – (a) without the misfit effect, (b) with misfit effect.

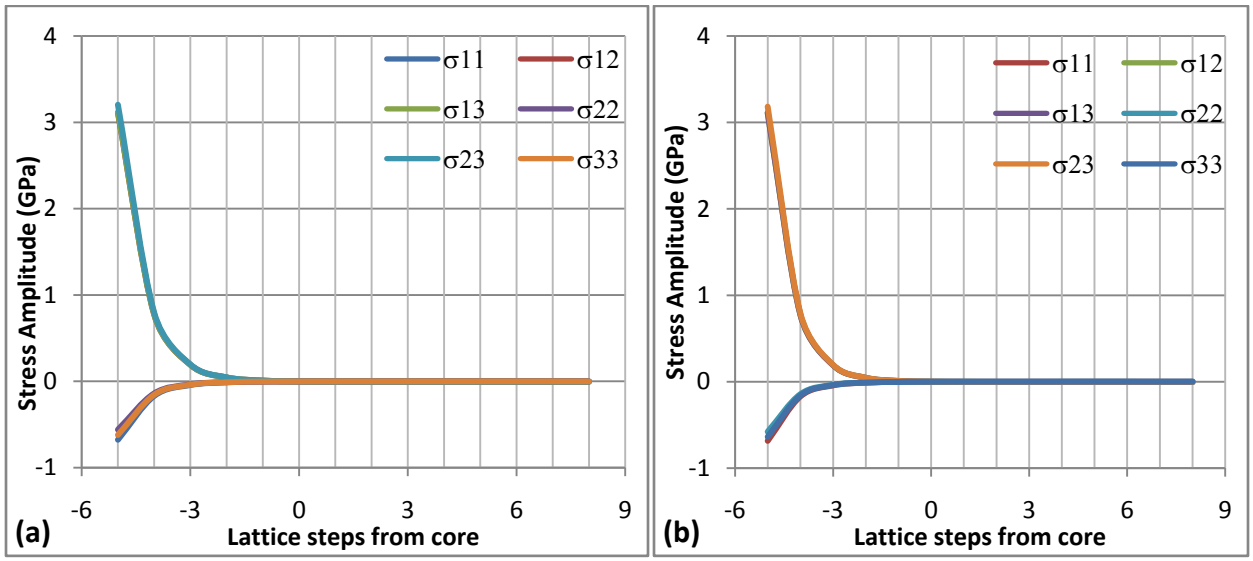

Figure 4.32: Stress amplitude variation for a screw dislocation at lattice sites along the dislocation line – (a) without the misfit effect, (b) with misfit effect.

4.2.3. MISFIT DUE TO A STRAIGHT 35.26° SCREW DISLOCATION LINE

Figure 4.33 shows the distortion amplitudes for the 35.26° screw. The notation used on these figures is the same as that used on the Figures 4.25, 4.28-4.30 for the edge and screw dislocations. The maximum peak amplitude occurred along the 3rd plane of atoms from the slip

plane, normal to the edge of the dislocation core (site no. 50), as for the other dislocation types. The height of the peaks decreased after the third row, and then increased towards the surface of the block of atoms. It is noted that the magnitude of the distortion at the centre of the block of atoms is the same as that of the free surfaces of the block of the atoms, and as in the case for the edge dislocation, the three curves overlapped.

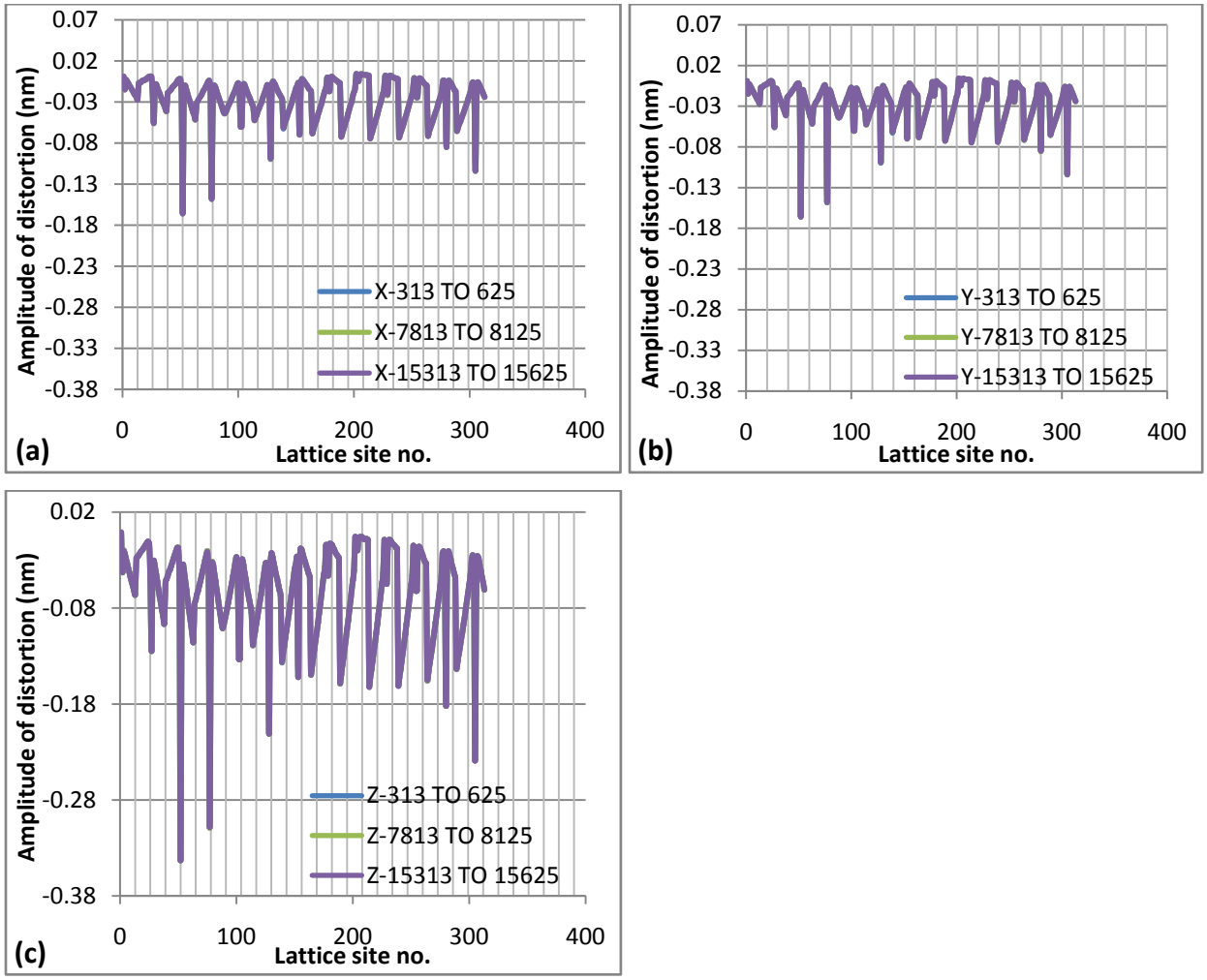

Figure 4.33: Lattice distortion along the (a) [100], (b) [010], (c) [001] directions for a 35.26° screw dislocation with misfit effect.

Figures 4.34 and 4.35 show stress amplitude results for the 35.26° screw dislocation. Figure 4.34a reveals that the dislocation introduces a marginal increase in lattice stress over the slip plane. Figure 4.34b reveals that the misfit potential introduces a larger increase in lattice stress that is cyclic in nature. A POLR peak stress value of 0.998 GPa (along σ_{22}) is obtained from

Figure 4.34b, and it compares well with Peierl's stress values form other work [181, 191, 194, 195]. Figure 4.35 gives results that confirm that the misfit potential does not alter the behaviour along the dislocation core.

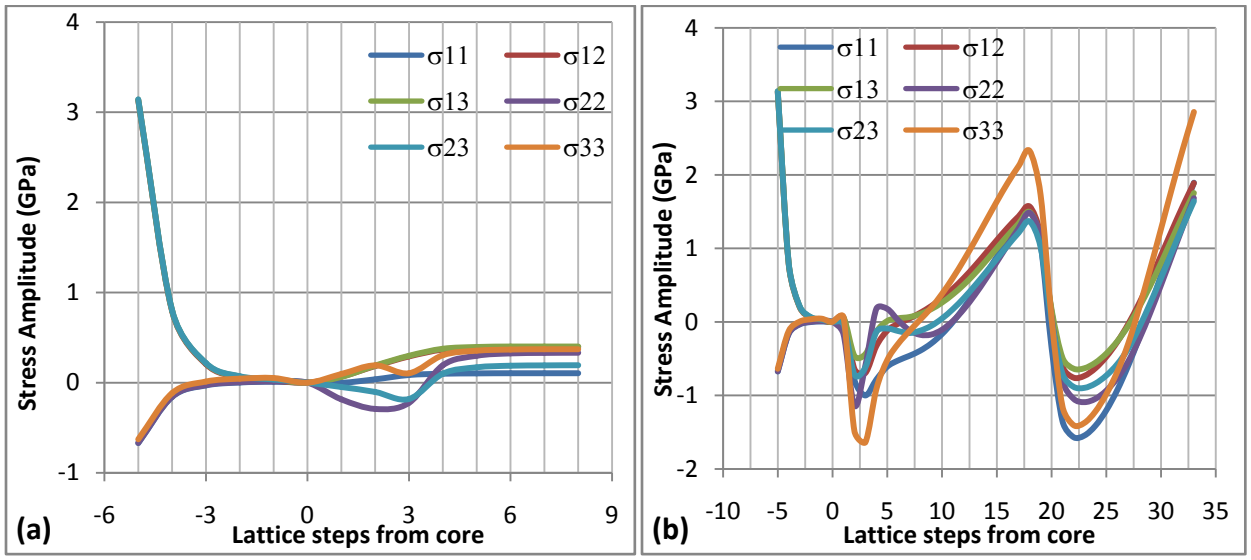

Figure 4.34: Stress amplitude variation for a 35.26° screw dislocation at lattice sites normal to the dislocation line – (a) without the misfit effect, (b) with misfit effect.

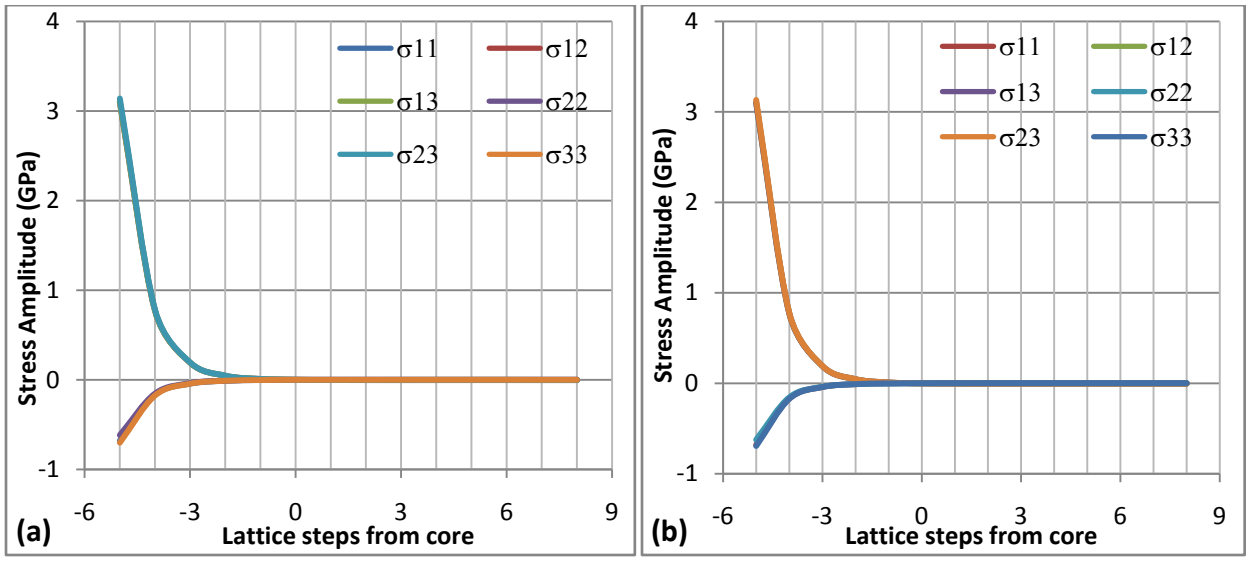

Figure 4.35: Stress amplitude variation for a 35.26° screw dislocation at lattice sites along the dislocation line – (a) without the misfit effect, (b) with misfit effect.

4.2.4. MISFIT DUE TO A STRAIGHT 70.52° SCREW DISLOCATION LINE

Figure 4.36 shows results of the distortion of the 70.52° screw dislocation in the [100], [010] and [001] directions. The notation used on these graphs is the same as that used on the distortion curves for the other dislocation types. As in the case for the edge and 35.26° screw dislocations, the three curves are identical.

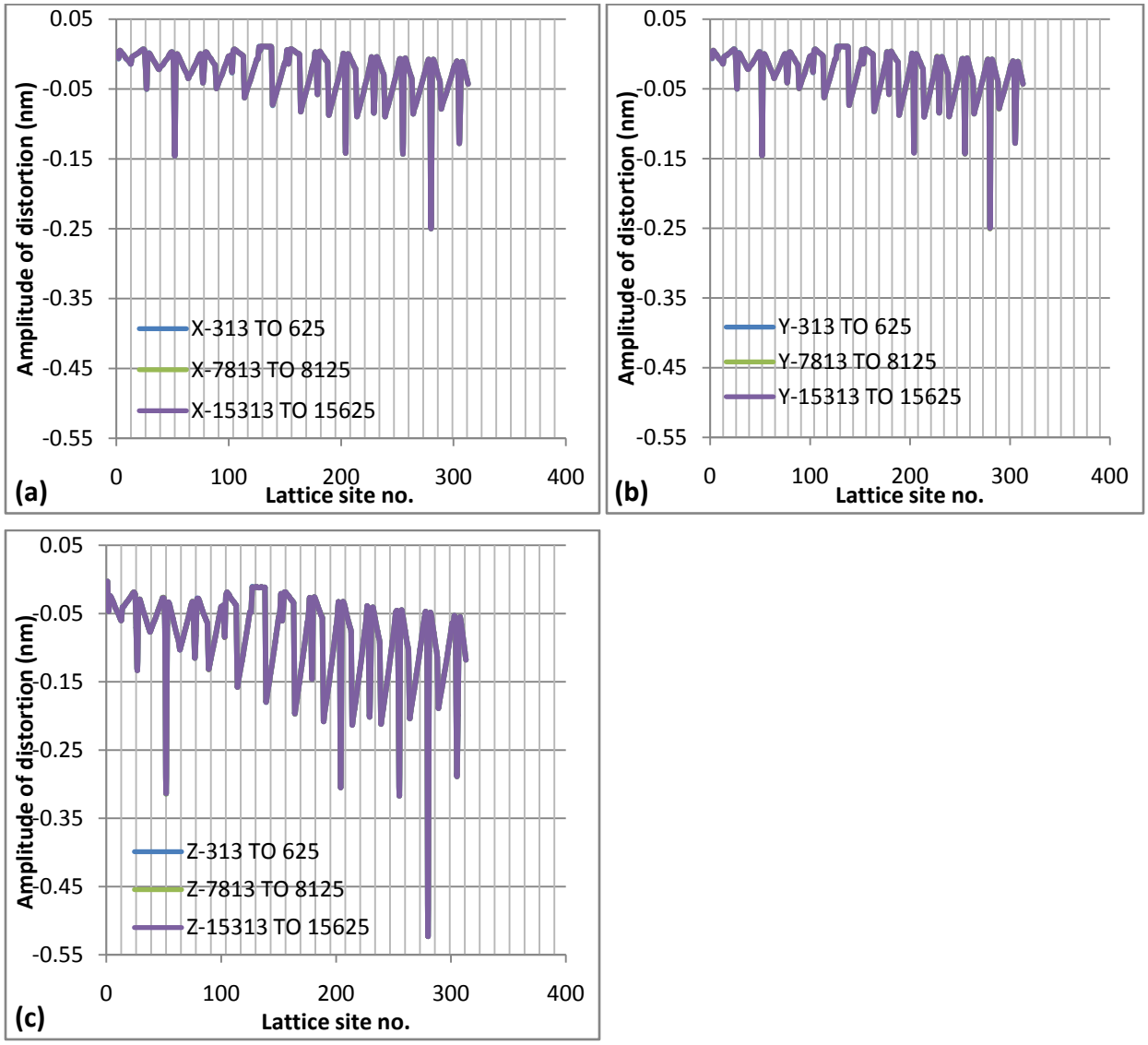

Figure 4.36: Lattice distortion along the (a) [100], (b) [010], (c) [001] directions for a 70.52° screw dislocation with misfit effect.

It is found that the distortion increases away from the slip plane, peaking as the surface of the block of atoms is approached. However, the underlying pattern of the distortion is steady far from the dislocation core, and therefore the induced behaviour is expected to tend towards that of the pure screw dislocation. The growth in peak distortion towards the surface of the block of atoms is an indication of a possible source of lattice strengthening associated with the 70.52^o screw dislocation core [192]. The curves for the centre and the surfaces of the block of atoms overlap and this is evidence that the distortion is not affected by the free surfaces normal to the dislocation line.

Figure 4.37 shows the stress amplitude profiles for the 70.52^o screw dislocation core. A comparison of Figures 4.37a and 4.37b reveals that the use of the misfit potential results in increased stress components around the dislocation core. The POLR increased from 0.87 GPa (along σ_{11} on Figure 4.37a) to 1.398 GPa (along σ_{22} on Figure 4.37b), with the latter value comparing well with empirical Peierl's stresses [181, 191, 194, 195]. Figure 4.38 shows similar curves to those for other dislocation types for simulations along the dislocation line.

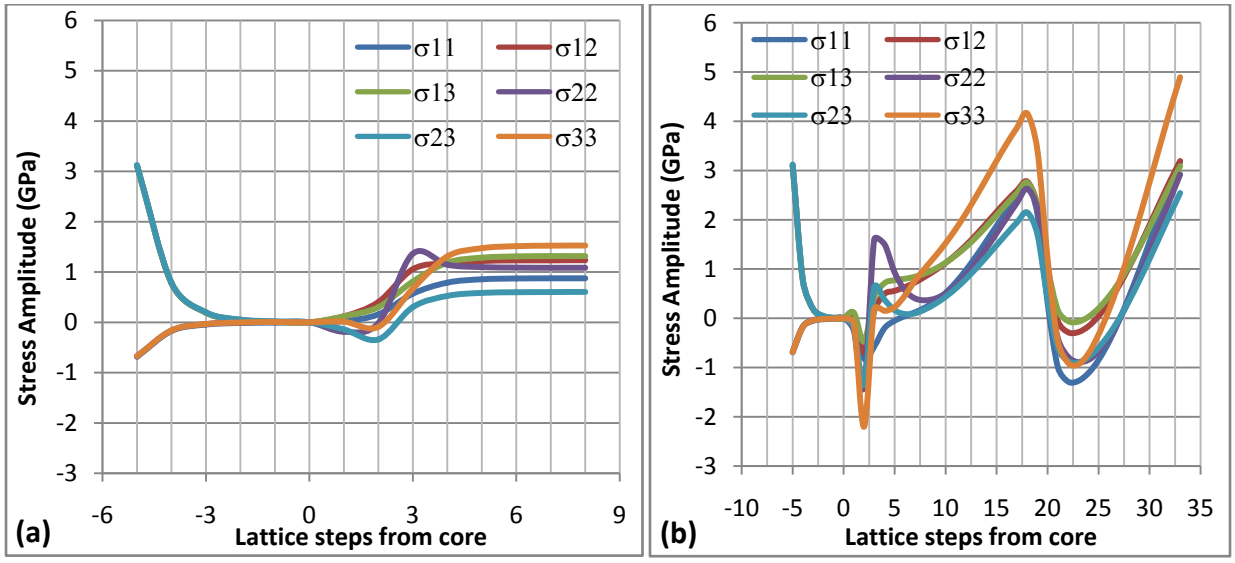

Figure 4.37: Stress amplitude variation for a 70.52^o screw dislocation at lattice sites normal to the dislocation line – (a) without the misfit effect, (b) with misfit effect.

It is inferred that while secondary peaking of the stress amplitude would result in lattice hardening and stress amplitude valleys would aid movement of dislocations, the interplay of the two would determine the true mobility of dislocations.

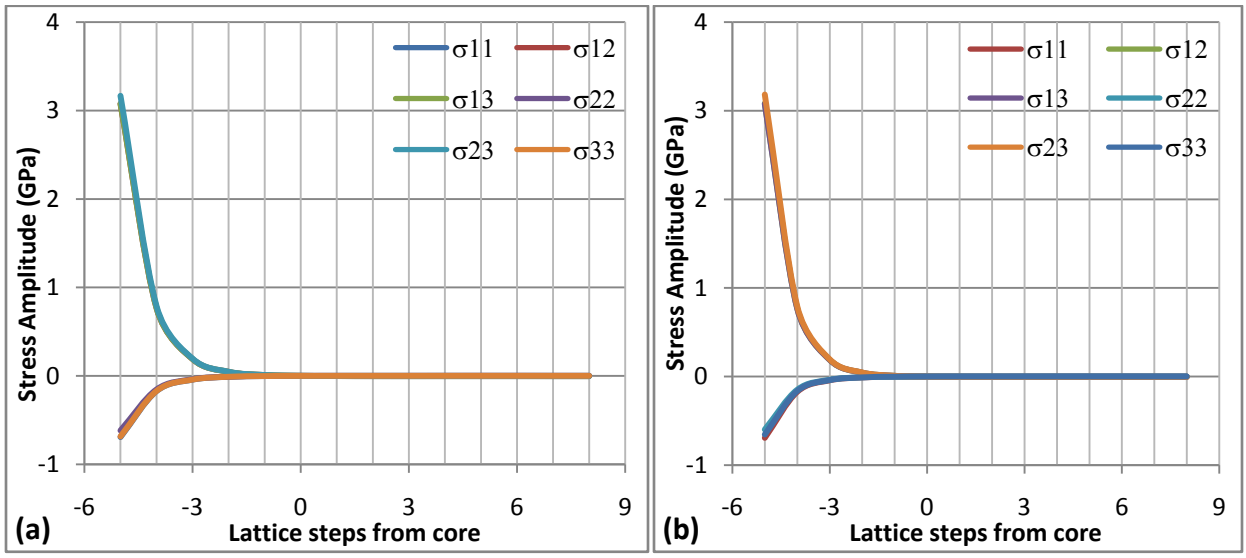

Figure 4.38: Stress amplitude variation for a 70.52° screw dislocation at lattice sites along the dislocation line – (a) without the misfit effect, (b) with misfit effect.

4.3. PLANE STRUCTURE FACTOR

Section 4.3 gives results for analysis of dislocation structures within slip planes in BCC Fe lattice. Sub-sections 4.3.1, 4.3.3, 4.3.5 and 4.3.7 give results of the stress amplitude profiles, while sub-sections 4.3.2, 4.3.4, 4.3.6 and 4.3.8 give results of the plane structure factors.

4.3.1. STRESS AMPLITUDE PROFILE FOR AN EDGE DISLOCATION DIPOLE

Figures 4.39 and 4.40 show simulation results for edge dislocation dipoles at different separation. It is noted that in all scenarios, the stress "hump" occurs across five lattice steps. This result reveals that the dislocation line creates a stress peak along a line normal to the slip plane. The difference between these scenarios is the height of the stress "hump" and the stress levels in the slipped zone. Consequently, these elements were used to characterize the dislocation set in the plane structure factor.

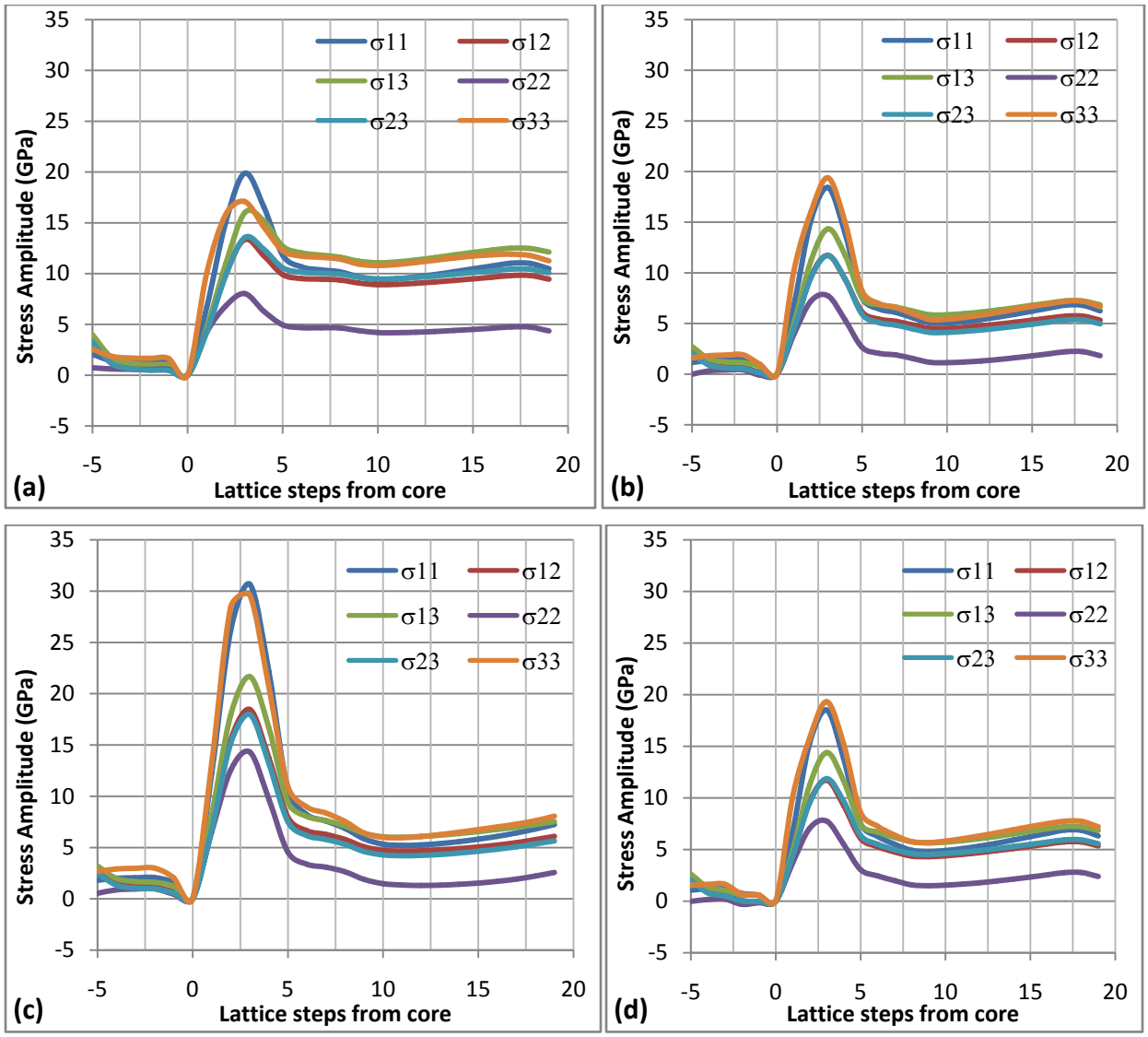

Figure 4.39: Stress amplitude variation of an edge dislocation dipole at (a) 1 and 2, (b) 1 and 3, (c) 2 and 3, (d) 1 and 4, lattice steps from the sampling line in Fe.

As the distance to the nearest dislocation was increased, the stress components over the slipped surface (section beyond the stress peak) reduced. This reduction in stresses is expected as the distortion intensity along the sampling line reduces as the nearest dislocation moves further away. This is evident from the comparison of Figures 4.39a and 4.39b, comparison of Figures 4.39b and 4.39c, and Figures 4.39d and 4.40b. Where the nearest dislocation is equal or greater than three lattice steps from the sampling line, the stress components over the slipped surface are about zero. In cases where the dislocation closest to the sampling point is at one lattice step, the "hump stress" is approximately equal to 20 GPa, while where it is further away, the "hump

stress" is in the order of 30 GPa. This is evidence that the stress transition zone extended beyond the first lattice step from the dislocation line.

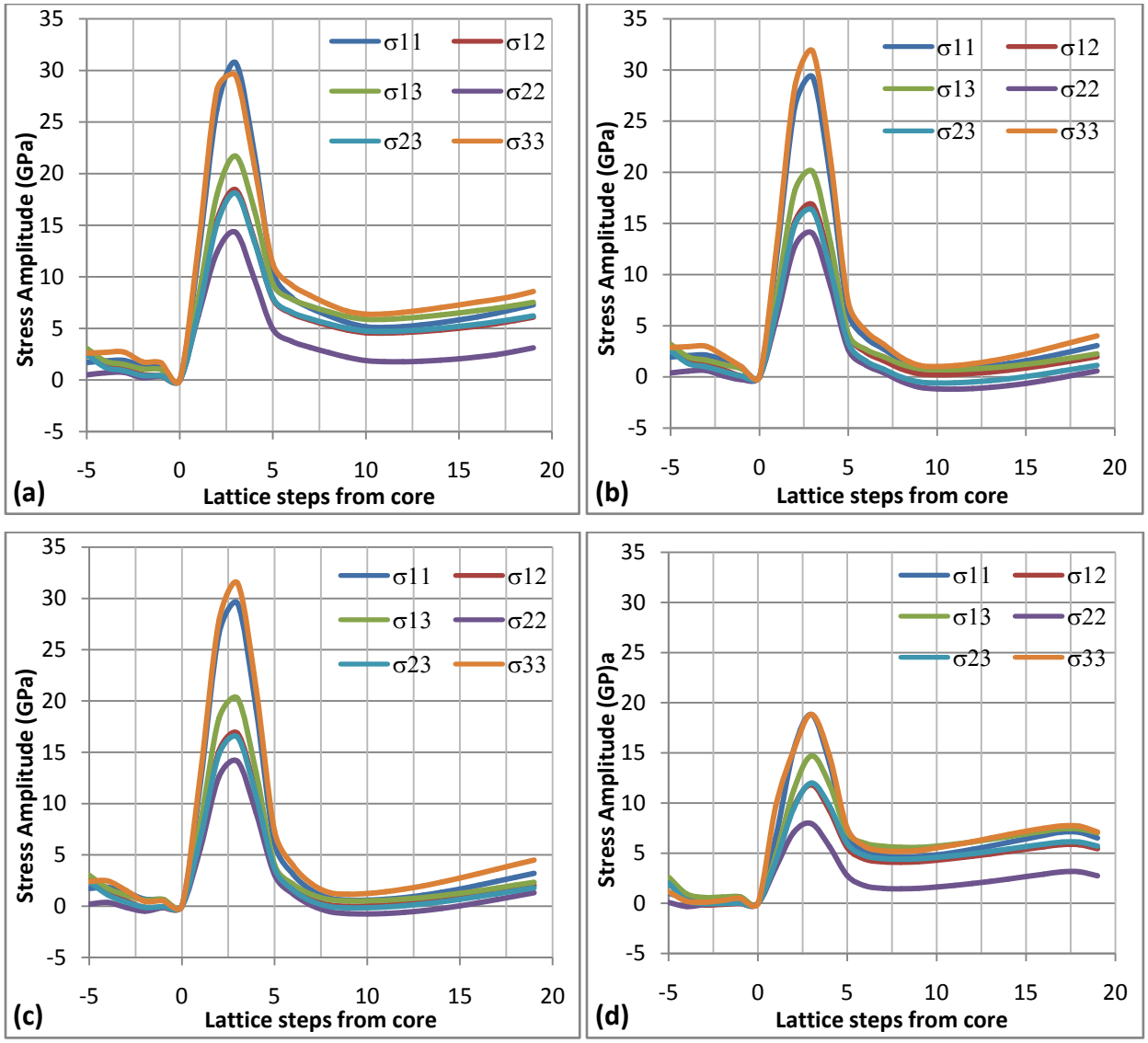

Figure 4.40: Stress amplitude variation of an edge dislocation dipole at (a) 2 and 4, (b) 3 and 4, (c) 4 and 5, (d) 1 and 6, lattice steps from the sampling line in Fe.

4.3.2. PSF FOR EDGE DISLOCATION DIPOLES

The peak stress (also referred to as the hump stress) and the lowest stress over the slipped region (also referred to as trough stress) were extracted from Figures 4.39 and 4.40 and are given in Table 4.23. In all cases, the hump stress is given by σ_{22}. These stress values were used to fit the

test function φ in Equation 3.100, and the factor ε was established. The plane structure factor components $[\mathcal{F}:\mathcal{F}_{\mu}]$ obtained for the edge-edge dislocation dipole are also given in Table 4.23.

Table 4.23: Characteristic stress and PSF data for edge dislocation dipole combinations.

Dislocation locations		Hump stress (GPa)	Trough stress (GPa)	Fitting factor ε	$\langle \mathcal{F}', \psi \rangle$	$\langle \mathcal{F}'_{\mu}, \varphi \rangle$	$\hat{\varrho}\ (m^{-1})$
2	1	8.03	4.17	0.0341	5.991E-26	1.422E-25	4.06E+08
3	1	7.73	1.13	0.0081	1.198E-25	3.791E-25	2.03E+08
3	2	14.30	1.30	0.0050	5.991E-26	2.369E-25	4.06E+08
4	1	7.74	1.49	0.0109	1.797E-25	7.108E-25	1.35E+08
4	2	14.30	1.88	0.0073	1.198E-25	5.687E-25	2.03E+08
4	3	14.00	-1.17	-0.0042	5.991E-26	3.317E-25	4.06E+08
5	4	14.10	-0.76	-0.0028	5.991E-26	4.265E-25	4.06E+08
6	1	7.93	1.44	0.0103	2.996E-25	1.659E-24	8.11E+07

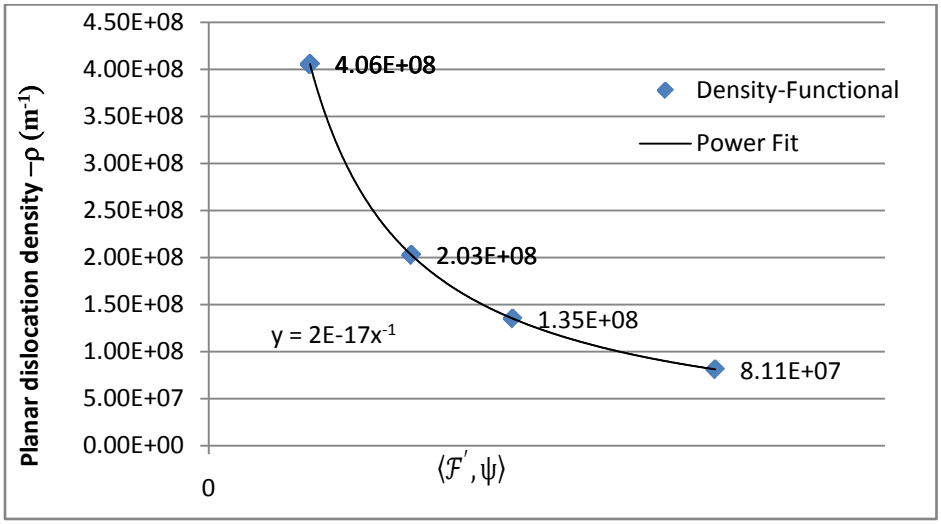

Figure 4.41: Planar dislocation density fit to $\langle \mathcal{F}', \psi \rangle$ functional for edge dislocation dipoles in Fe.

A plot of the calculated planar dislocation density $\hat{\varrho}$ versus the functional $\langle \mathcal{F}', \psi \rangle$ is given in Figure 4.41, and a fit of the form given in Equation 3.106 was obtained. It is significant that this

relationship is replicated for all the dislocation types. The functional $\langle \mathcal{F}'_{\mu}, \varphi \rangle$ was retained for use at the next higher length scale to convey the nature of the dislocation dipole's character.

4.3.3. STRESS AMPLITUDE PROFILE FOR A SCREW DISLOCATION DIPOLE

Figures 4.42 and 4.43 show results from simulations for screw dislocation dipoles. Initial simulations with the nearest dislocation below three lattice steps from the sampling line produced very high stresses (in the order of 250 to 300 GPa). A typical stress amplitude profile is shown in Figure 4.42a. It is inferred that dislocation line spacing for the screw dislocation extends to at least three lattice steps, and that the distortion is sufficiently high to occur beyond the limits of capability of the EAM potential utilized.

Figures 4.42b-4.42d and 4.43 show the stress amplitude profiles for nearest dislocations greater than two lattice steps from the sampling line. Each set of curves is within ± 10 GPa. The "hump" stresses for the screw dislocation dipoles were selected as the stress peak values in a manner consistent with the POLR concept. These hump stresses are much lower than those of the edge dislocation dipoles. However, no direct comparison could be made, as these stresses were measured at different sampling points. For cases where the nearest dislocation is further than three lattice steps from the sampling line, the stress humps are approximately symmetrical about the peak point, and the stress amplitude over the slipped region is approximately zero. This suggests that the principle effect of the dislocation dipole is concentrated over a narrow region spanning six atomic planes, with one end of this profile at the slip plane. However, this does not imply that the dislocation line effects are insignificant on the side of the "zero-slipped" side of the slip plane, as the stresses on that side were used as the reference stresses for computation of the amplitude. The stress amplitude is dependant on the reference point, and in absolute terms, and it is expected that the stress hump should straddle the slip plane. The stress hump straddles five lattice steps as in the case of the edge dislocation dipoles.

The trough stresses were selected as the values at the stress trough from the same curve as that giving the hump stresses. Stress trough values about the dislocation line are not known to have been published previously.

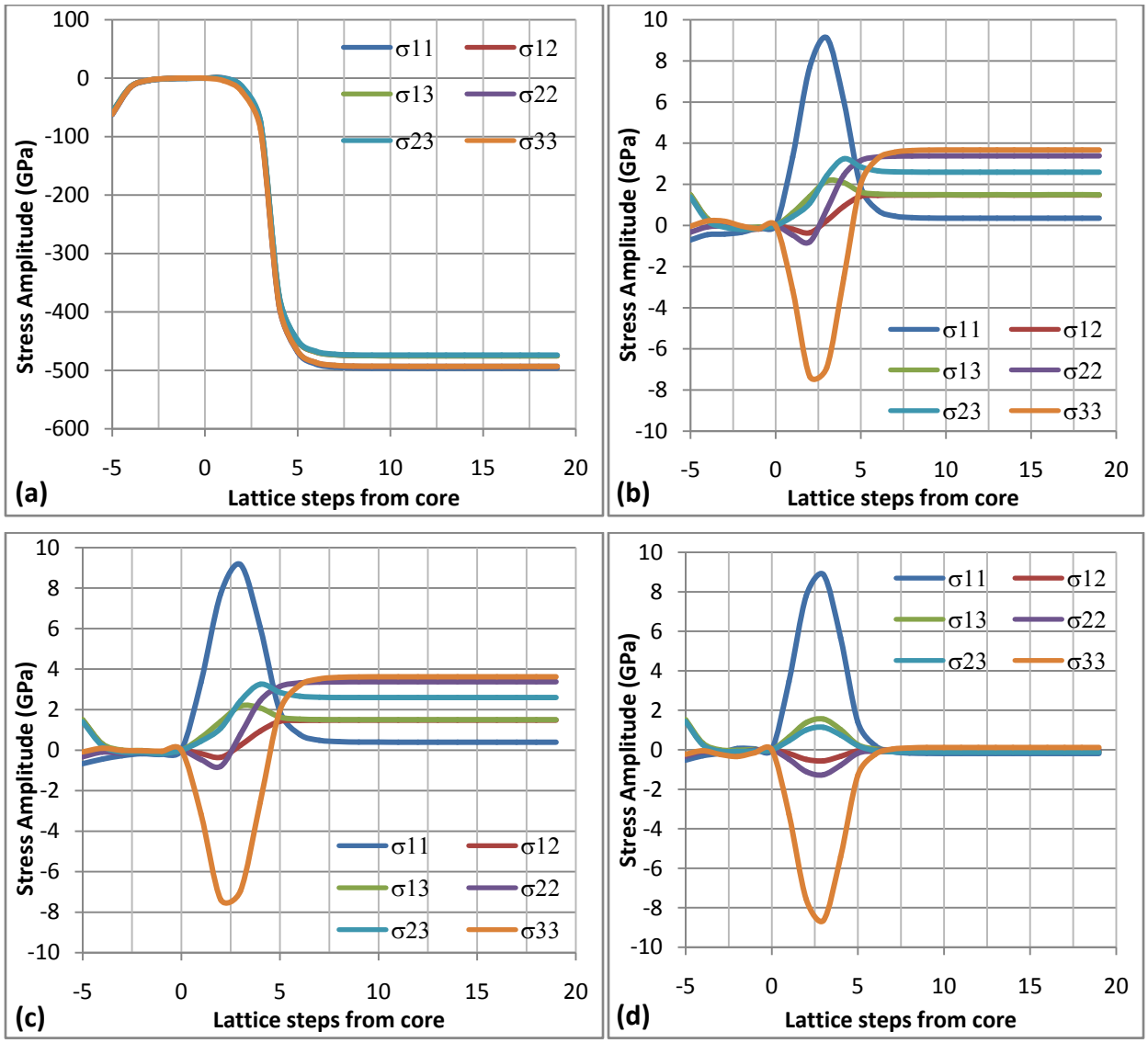

Figure 4.42: Stress amplitude variation of a screw dislocation dipole at (a) 1 and 2, (b) 3 and 4, (c) 5 and 3, (d) 4 and 5, lattice steps from the sampling line in Fe.

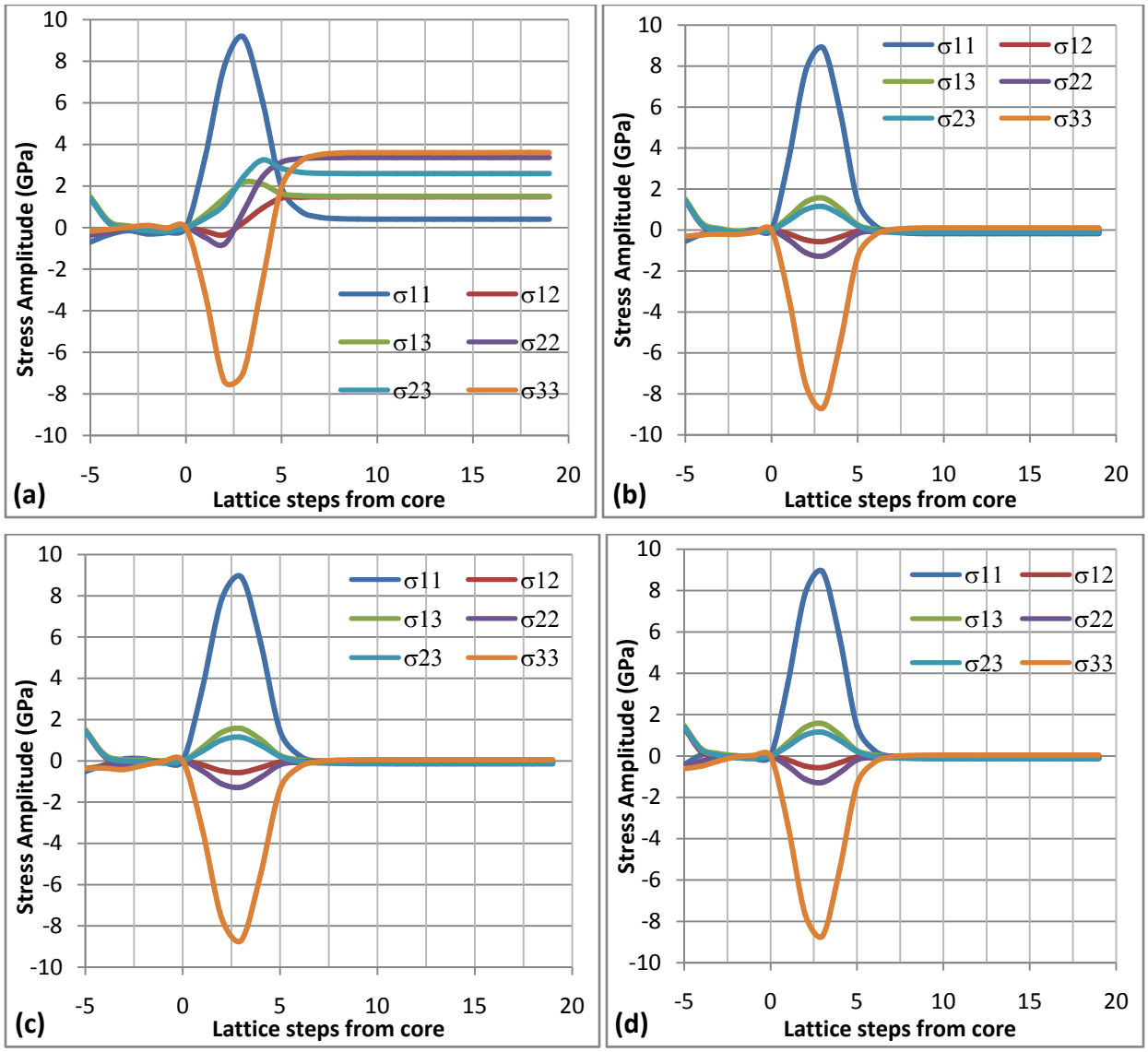

Figure 4.43: Stress amplitude variation of a screw dislocation dipole at (a) 6 and 3, (b) 6 and 4, (c) 6 and 5, (d) 7 and 6, lattice steps from the sampling line in Fe.

4.3.4. PSF FOR SCREW DISLOCATION DIPOLES

Table 4.24 shows characteristic stresses for the screw dislocation dipoles. The stress hump value is extremely high when the dislocation line was close to the sampling line. As a result, the computation for this condition was excluded from the analysis.

The plane structure factor components $[\mathcal{F}:\mathcal{F}_{\mu}]$ obtained for the screw dislocation dipole are given in Table 4.24. A plot of the calculated planar dislocation density $\hat{\varrho}$ versus the functional

$\langle \mathcal{F}', \psi \rangle$ similar to Figure 4.42a was used and the fitting function given in Equation 3.106 obtained. It is noted that the plane structure factor values are identical with those obtained for the edge dislocation dipoles for the same simulation conditions.

Table 4.24: Characteristic stress and PSF data for screw dislocation dipole combinations.

Dislocation locations		Hump stress (GPa)	Trough stress (GPa)	Fitting factor ε	$\langle \mathcal{F}', \psi \rangle$	$\langle \mathcal{F}'_{\mu}, \varphi \rangle$	$\hat{\varrho}\ (m^{-1})$
2	1	-472	-	-	5.991E-26	-	4.06E+08
4	3	-0.79	3.38	-0.0042	5.991E-26	3.317E-25	4.06E+08
5	3	-0.80	3.37	-0.3465	1.198E-25	7.582E-25	2.03E+08
5	4	-1.27	-0.12	-0.0028	5.991E-26	4.265E-25	4.06E+08
6	3	-0.80	3.61	0.0073	1.797E-25	1.280E-24	1.35E+08
6	4	-1.27	0.11	0.0081	1.198E-25	9.478E-25	2.03E+08
6	5	-1.28	0.06	0.0109	5.991E-26	5.213E-25	4.06E+08
7	6	-1.29	0.04	0.0103	5.991E-26	6.161E-25	4.06E+08

4.3.5. STRESS AMPLITUDE PROFILE FOR A 70.52^{o} SCREW DISLOCATION DIPOLE

Figures 4.44 and 4.45 show results obtained for the 70.52^{o} screw dislocation dipoles. As in the case of the screw dislocation dipoles, stress amplitude profiles for dislocation lines within two lattice steps from the sampling line are extraordinarily high, and it is inferred that the nature of the distortion occurs outside the range where the EAM computation provides reasonable results. Figure 4.44a shows these stress amplitude profiles.

Figures 4.44b to 4.45d show stress humps that straddle five lattice steps as in the case for the edge dislocation dipoles. In addition, the shape of the stress amplitude profiles does not vary much as the location of the dislocation lines is changed, and this differs from the behaviour of the edge and screw dislocation dipoles. In all instances, the hump stress components are bunched between 5 and 10GPa with a single stress component peaking at about 25GPa. The stresses over the slipped region are bunched together dipping to about 0GPa and then gradually increasing. It

is therefore inferred that the spatial dislocation positioning does not appreciably alter the effects of the 70.52° screw dislocation dipole on the slip plane.

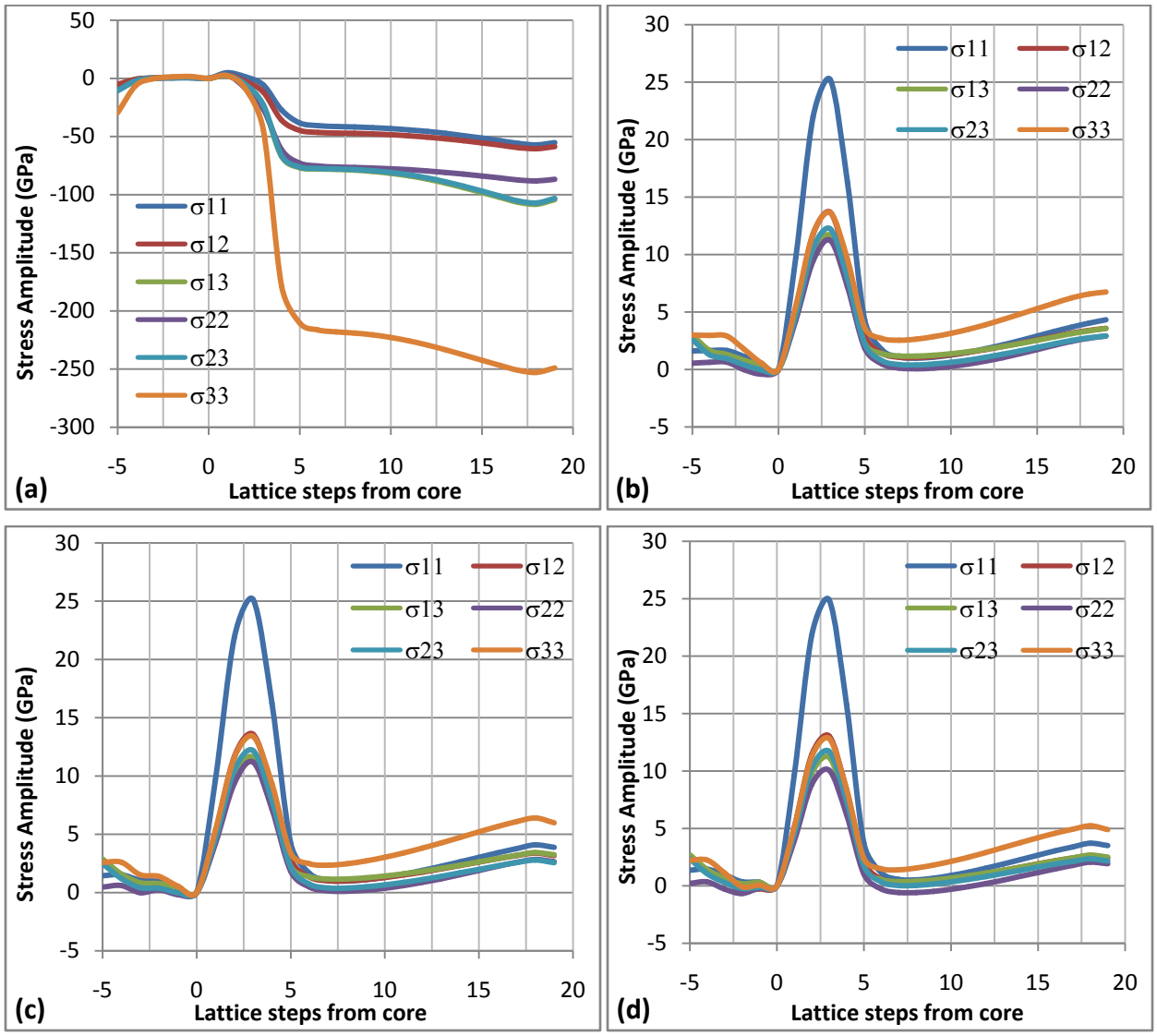

Figure 4.44: Stress amplitude variation of a 70.52° screw dislocation dipole at (a) 1 and 2, (b) 3 and 4, (c) 5 and 3, (d) 4 and 5, lattice steps from the sampling line in Fe.

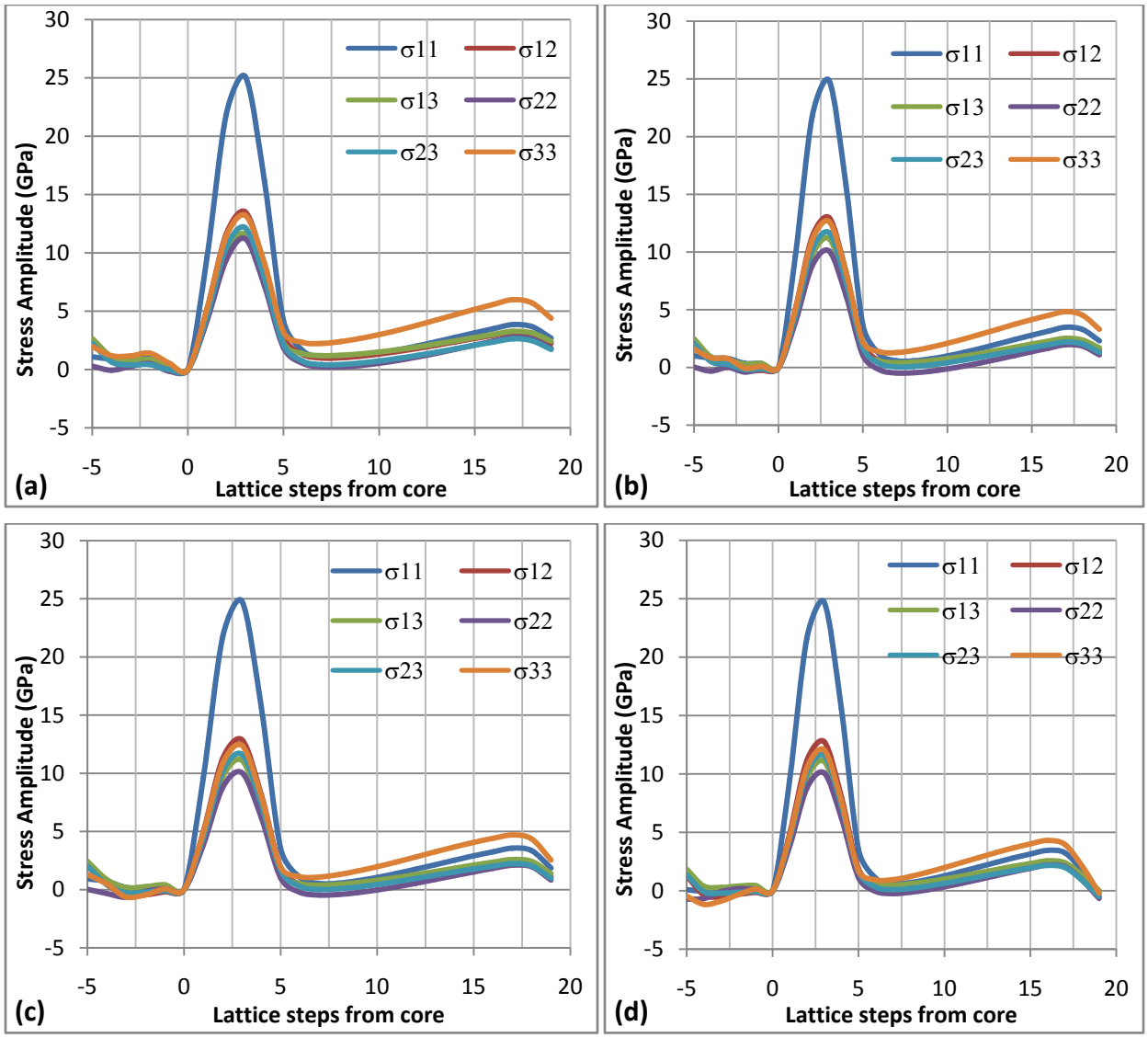

Figure 4.45: Stress amplitude variation of a 70.52° screw dislocation dipole at (a) 6 and 3, (b) 6 and 4, (c) 6 and 5, (d) 7 and 6, lattice steps from the sampling line in Fe.

4.3.6. PSF FOR 70.52° SCREW DISLOCATION DIPOLES

Table 4.25 shows characteristic stresses and resulting plane structure factor and plane dislocation densities. The hump stresses are much higher than those for the screw dislocation dipoles. This is consistent with other work where the 70.52° screw dislocation has a high Peierl's stress [118]. The plane structure factor components $[\mathcal{F}:\mathcal{F}_{\mu}]$ obtained are also given in Table 4.25.

A fit of the dislocation density to the functional $\langle \mathcal{F}', \psi \rangle$ was carried out on a plot similar to Figure 4.42a, and the relation given in Equation 3.106 verified. The plane structure factor values compared with those obtained for the edge dislocation dipoles.

Table 4.25: Characteristic stress and PSF data for 70.52^o screw dislocation dipole combinations.

Dislocation locations		Hump stress (GPa)	Trough stress (GPa)	Fitting factor ε	$\langle \mathcal{F}', \psi \rangle$	$\langle \mathcal{F}'_{\mu}, \varphi \rangle$	$\hat{\varrho}\ (m^{-1})$
2	1	-57	-	-	5.991E-26	-	4.06E+08
4	3	11.23	0.13	0.0025	5.991E-26	3.3173E-25	4.06E+08
5	3	11.19	0.14	0.0005	1.198E-25	7.5823E-25	2.03E+08
5	4	10.07	-0.57	-0.0024	5.991E-26	4.265E-25	4.06E+08
6	3	9.38	0.24	0.0013	1.797E-25	1.2795E-24	1.35E+08
6	4	10.09	-0.47	-0.0030	1.198E-25	9.4779E-25	2.03E+08
6	5	10.05	-0.46	0.0007	5.991E-26	5.2128E-25	4.06E+08
7	6	10.09	0.10	0.0006	5.991E-26	6.1606E-25	4.06E+08

4.3.7. STRESS AMPLITUDE PROFILE FOR THE 35.26^o SCREW DIPOLE

Figures 4.46 and 4.47 show results for the 35.26^o screw dislocation dipoles. For this dislocation dipole, the stress amplitude profiles are of acceptable magnitudes when the dislocation lines are close to the sampling line (as in the case of the edge dislocation dipoles). Where the nearest dislocation is at one lattice step from the sampling line, the peak stress amplitude values decrease as the second dislocation moves away from the sampling line. This is demonstrated by Figures 4.46a, 4.46b and 4.47d, and is an indication that the peak stress values are related to the dislocation dipole spacing. It is inferred that dislocation motion is aided by an increase in dislocation dipole spacing.

As the nearest dislocation line is moved away from the sampling line, the stress components on the slipped side decrease and bunch together, even as the highest hump stress attained increases.

This behaviour is seen on comparison of Figures 4.46b and 4.46c. This variation in stress components is affected more by the movement of the nearest dislocation line.

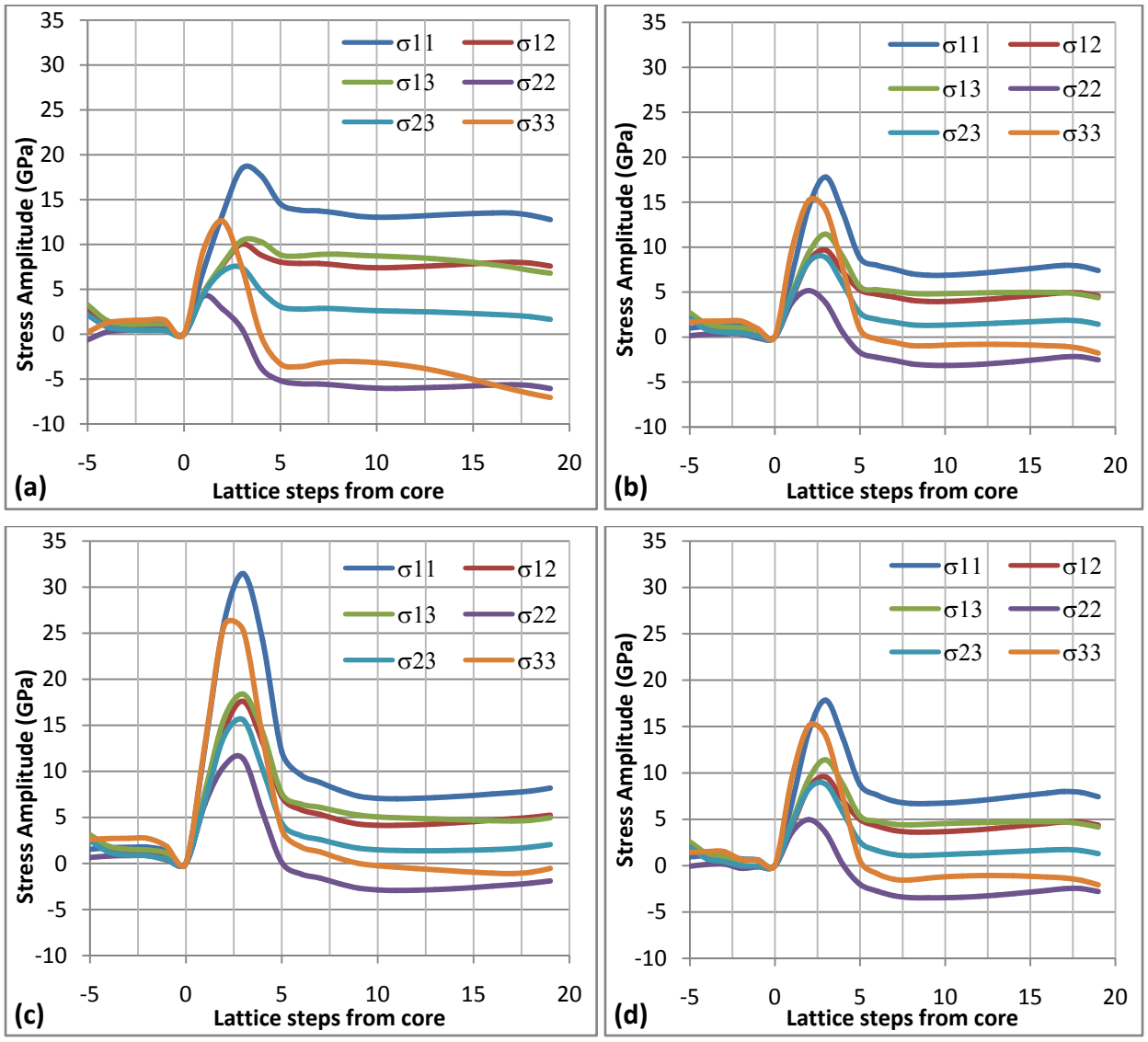

Figure 4.46: Stress amplitude variation of a 35.26^{o} screw dislocation dipole at (a) 1 and 2, (b) 1 and 3, (c) 2 and 3, (d) 1 and 4, lattice steps from the sampling line in Fe.

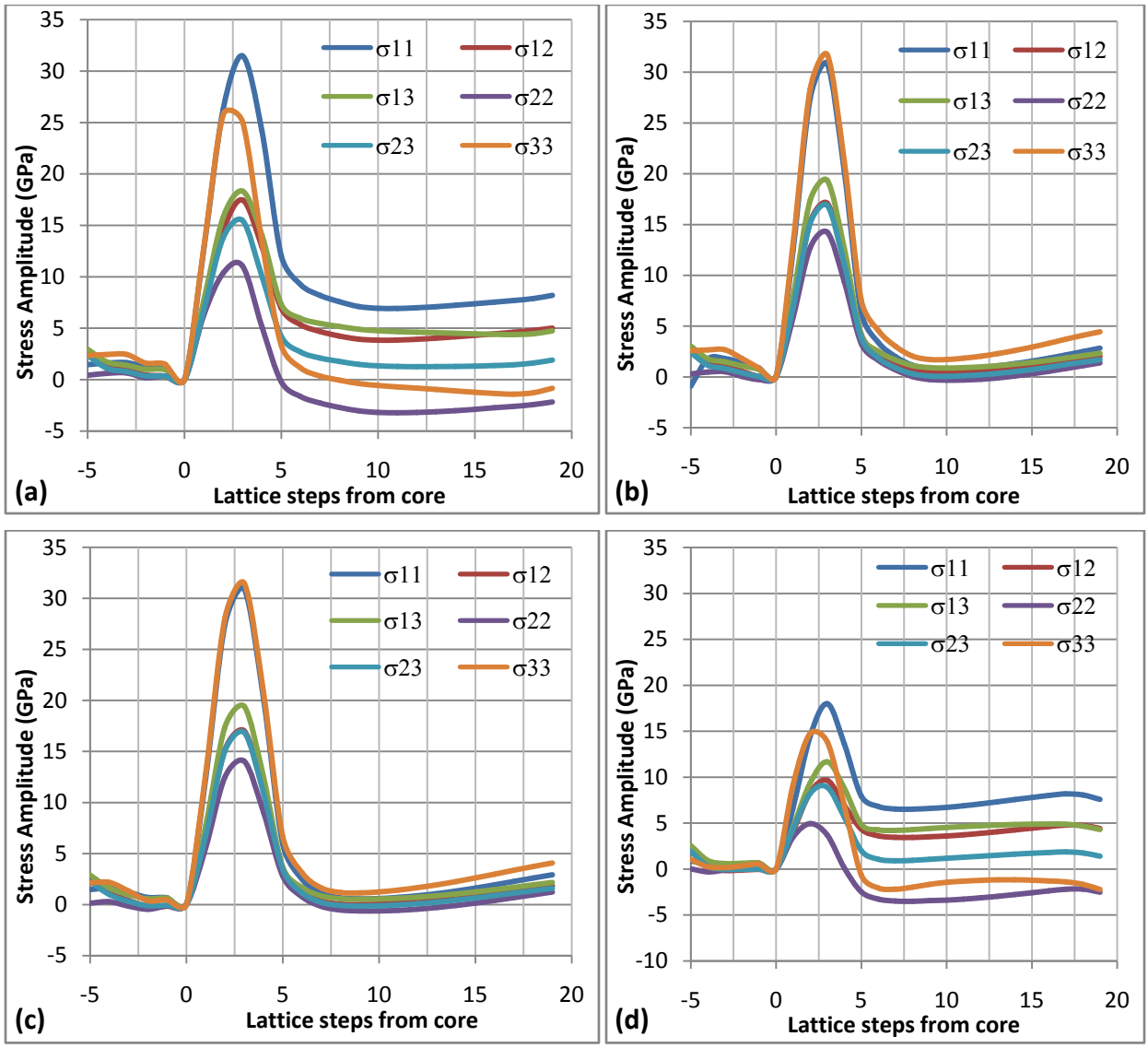

Figure 4.47: Stress amplitude variation of a 35.26° screw dislocation dipole at (a) 2 and 4, (b) 3 and 4, (c) 4 and 5, (d) 1 and 6, lattice steps from the sampling line in Fe.

4.3.8. PSF FOR 35.26° SCREW DIPOLES

Table 4.26 shows results for the 35.26° screw dislocation dipoles. A wider variation of the hump stress with changes in dislocation spacing is observed (compared with that for the edge dislocation dipole), although the highest values recorded for these two dipole types are of the same order of magnitude. However, the trough stresses are appreciably lower. The plane structure factors were determined and compared to those of the edge dislocation dipoles.

Table 4.26: Characteristic stress and PSF data for 35.26^{o} screw dislocation dipole combinations.

Dislocation locations		Hump stress (GPa)	Trough stress (GPa)	Stress hump fitting factor ε	$\langle \mathcal{F}', \psi \rangle$	$\langle \mathcal{F}'_{\mu}, \varphi \rangle$	$\hat{\varrho}\ (m^{-1})$
2	1	4.23	-6.00	0.1658	5.991E-26	1.422E-25	4.06E+08
3	1	5.17	-3.15	0.0418	1.198E-25	3.791E-25	2.03E+08
3	2	11.33	-2.91	0.0150	5.991E-26	2.369E-25	4.06E+08
4	1	4.96	-3.47	0.0485	1.797E-25	7.108E-25	1.35E+08
4	2	10.36	-3.22	0.0185	1.198E-25	5.687E-25	2.03E+08
4	3	14.25	0.11	0.0004	5.991E-26	3.317E-25	4.06E+08
5	4	14.04	-0.62	-0.0023	5.991E-26	4.265E-25	4.06E+08
6	1	4.95	-3.50	0.0511	2.996E-25	1.659E-24	8.11E+07

4.4. NETWORK STRUCTURE FACTOR

Section 4.4 gives results for stress amplitude profiles and resulting structure factors across parrallel slip planes in BCC Fe lattice. The stress amplitude profiles along a line joining slip planes containing dislocations were plotted in Figures 4.48 to 4.59. This line was placed to join the coordinate origin in each plane and the separation of the planes was recorded. The displacement of the dislocation measured from the plane origin was also recorded.

These figures show results of stress fields formed by parallel planes containing opposite sense, parallel dislocation dipoles, at identical positions with reference to the origin in each plane. The six independent stress components of the stress amplitude profile were recorded from five lattice steps before the first slip plane was encountered, running through 24 lattice steps. The Cartesian coordinate system aligned to the edges of the BCC Bravis unit cell was adopted for all the simulation cycles.

4.4.1. STRESS AMPLITUDE PROFILE FOR SLIP PLANES CONTAINING EDGE DIPOLES

The stress amplitude profiles of parallel edge dislocation dipoles aligned in the $[11\bar{1}]$ direction, contained in the (112) slip planes, are presented in Figures 4.48 to 4.50. The displacement of the edge dislocation dipoles from the origin, and the spacing between the slip planes were recorded and the resulting stress amplitude profiles analyzed.

Figure 4.48a shows the case where the spacing between the slip planes was three lattice steps. The stress amplitude peaks resulting from the two slip planes are close enough for the initial peak to be absorbed into the second peak. It is noted that the second peak dominates the stress amplitude cycle. Additionally, the wake of the stress amplitude peak has negative stress amplitudes for all the components, with a severe stress amplitude decrease at six lattice steps from the slip plane.

Figure 4.48b shows the case where the spacing between the slip planes was five lattice steps. The stress amplitude peaks for the two slip planes are in this case clearly distinct. Again, the second stress amplitude peak dominates. The stress amplitudes are all positive except at about 13 lattice steps from the slip plane, where a severe decrease in the stress amplitude components occurs. The peak values for these stress amplitude profiles are larger than those for the slip planes with a separation of three lattice steps, which indicates that the stress intensification due to interacting slip planes increases as the separation between the slip planes increases.

Figure 4.48c shows the case where the spacing between the slip planes was seven lattice steps. Again, the stress amplitude peaks are well defined, and in this case, a small stress decrease occurs between the two peaks. Again, the second stress amplitude peak dominates, as is the case in the two previous simulations. The stress amplitudes are all positive, except at about 16 lattice steps from the core, where a severe dip in the stress amplitude components occurs. It is also noted that the peak values for these stress amplitude profiles are larger than those for the slip planes with a separation of three and five lattice steps.

A general pattern is noted from these simulations. The first is that as the spacing between the slip planes increases, the stress amplitude humps become more distinct and the peak values increase. In addition, the position of the stress dip is further displaced away from the first slip plane, although a definite pattern is not evident. In all these simulations, the width of the stress hump is approximately five lattice steps.

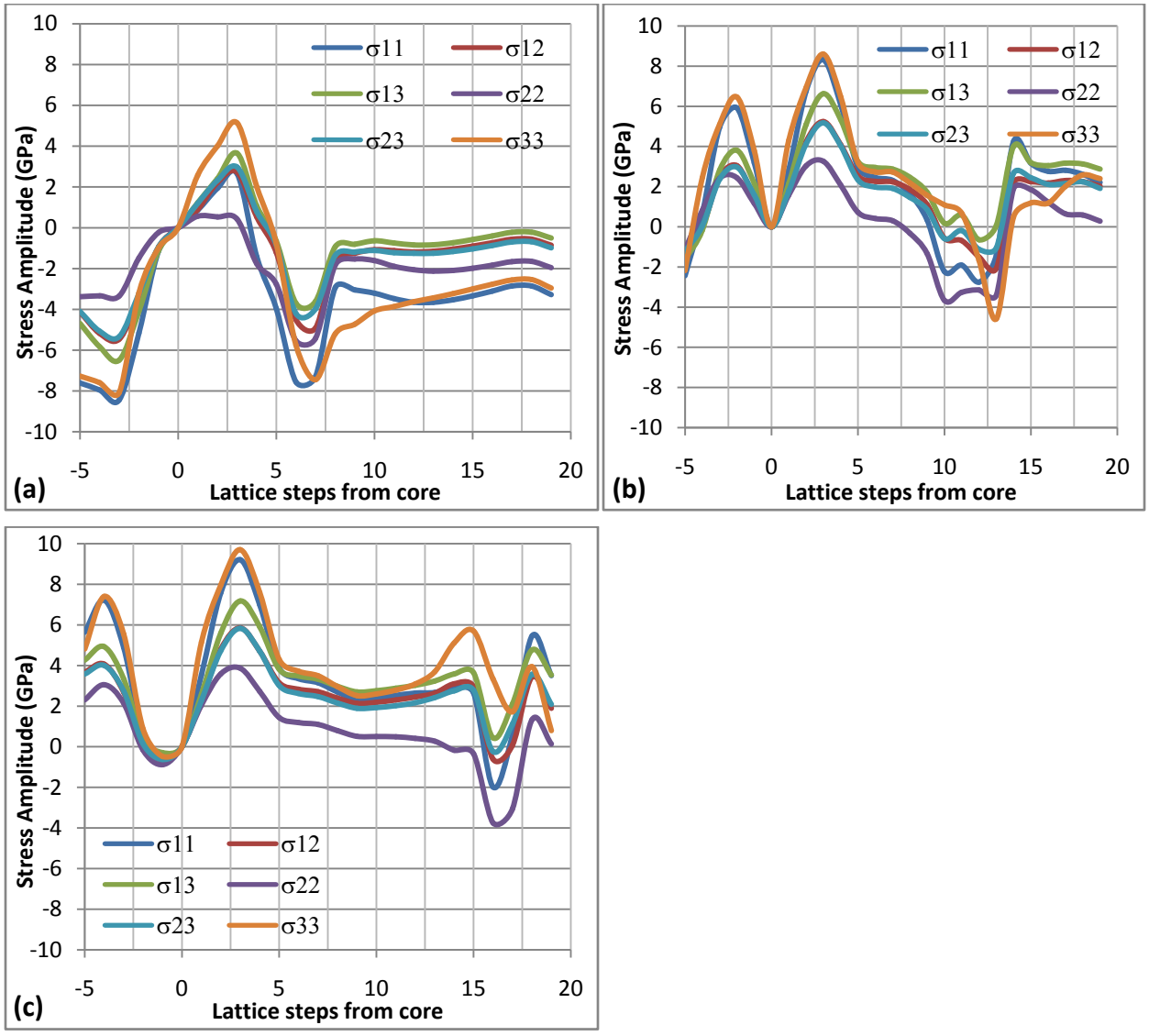

Figure 4.48: Stress amplitude variation along the normal to two slip planes separated by (a) three, (b) five, (c) seven, lattice steps each containing edge dislocation dipoles at one and three lattice steps from sampling point in Fe.

Figure 4.49 gives results for simulations where the dislocation lines were at three and five lattice steps from the line of analysis. In Figure 4.49a, the spacing between the slip planes is three lattice steps. A similar stress amplitude profile is obtained as for the same spacing between slip planes in Figure 4.48a. However, in Figure 4.49a, the severe stress amplitude decrease after the second stress peak is replaced by a gentle stress amplitude trough. Again, the stress amplitude components in Figure 4.49a are all negative, except for the second stress amplitude peak, as in Figure 4.48a.

Figure 4.49b shows results for stress amplitude peaks for slip planes with a separation of five lattice steps. Again, the stress amplitude peaks are distinct, as in Figure 4.48b, where the spacing between the slip planes is similar. As in Figure 4.49a, a stress amplitude trough is present after the second stress amplitude peak, with its lowest point at 11 lattice steps from the sampling line.

Figure 4.49c shows results for simulations with a seven lattice step spacing between the slip planes. Again, the stress amplitude humps are more distinct and a small trough exists between the two humps. This hump is also observed in Figures 4.48b, 4.48c and 4.49b. The trough in the wake of the slip plane is not as distinct as in the case where the slip plane were closer together (Figure 4.48c).

It is observed that as the spacing between the slip planes increases, the stress amplitude humps become more distinct and the peak values increase. In addition, the severe trough in the wake of the second slip plane is replaced by a gentle trough on increasing the displacement of the two dislocations from the line of observation. This change is accompanied by an overall increase in the peak value of the stress amplitude as the change from dislocation dipole location of 1:3 to 3:5 occurs.

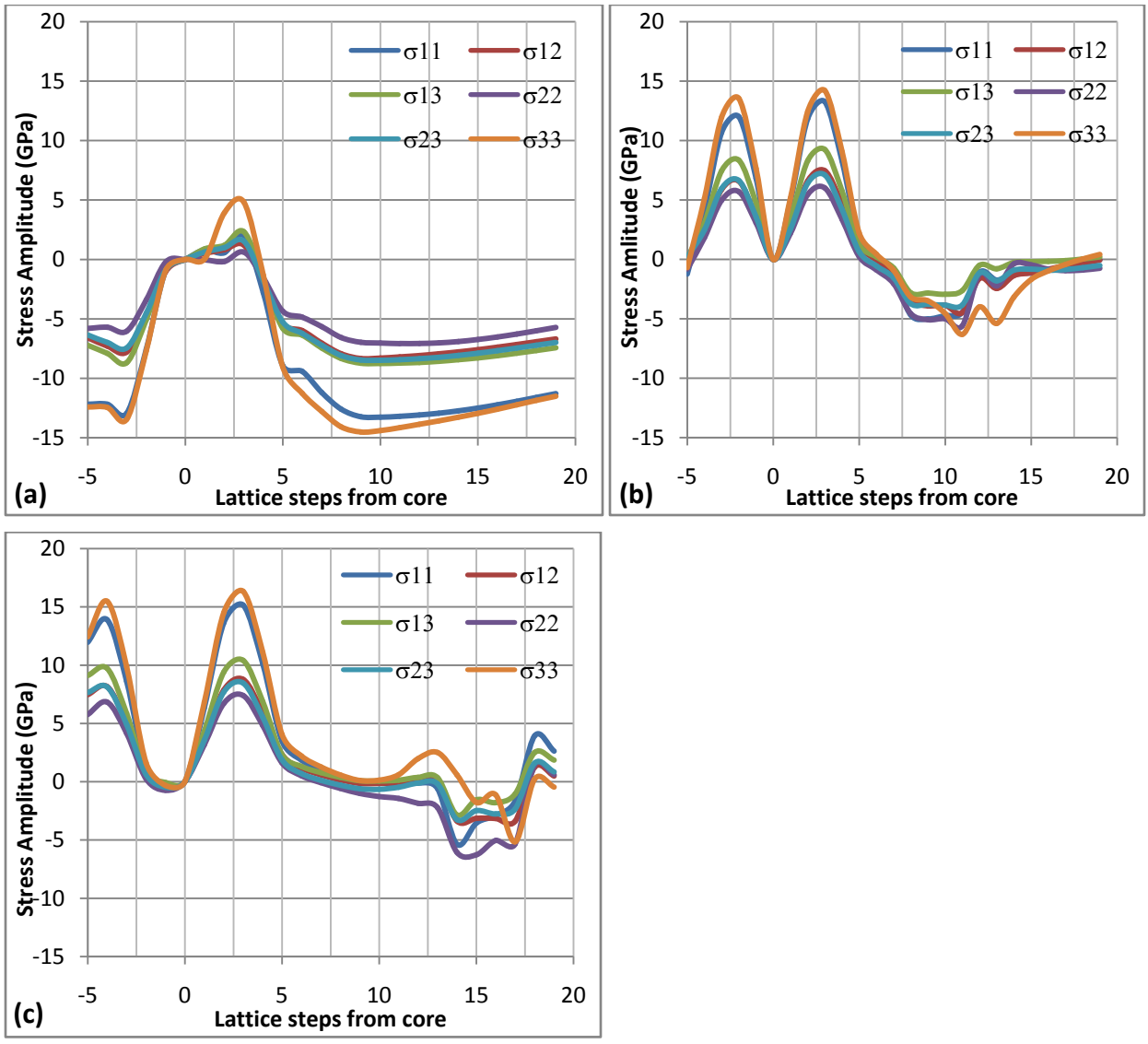

Figure 4.49: Stress amplitude variation along the normal to two slip planes separated by (a) three, (b) five, (c) seven, lattice steps, each containing edge dislocation dipoles at three and five lattice steps from the sampling point, in Fe.

Figure 4.50a shows results for three lattice step spacing between slip planes for dislocations at four and seven steps from the sampling line. As has been observed previously, at this spacing between slip planes, the stress amplitude peaks interfered with each other, with the second stress amplitude hump being larger. Also, as noticed earlier, as the spacing between the dislocation lines increases, the depth of the stress trough in the wake of the slip planes reduces. In addition, the stress amplitude humps separate and the peak amplitudes increase, as shown in from Figure 4.50. However, the width of the stress humps remains at approximately five lattice steps.

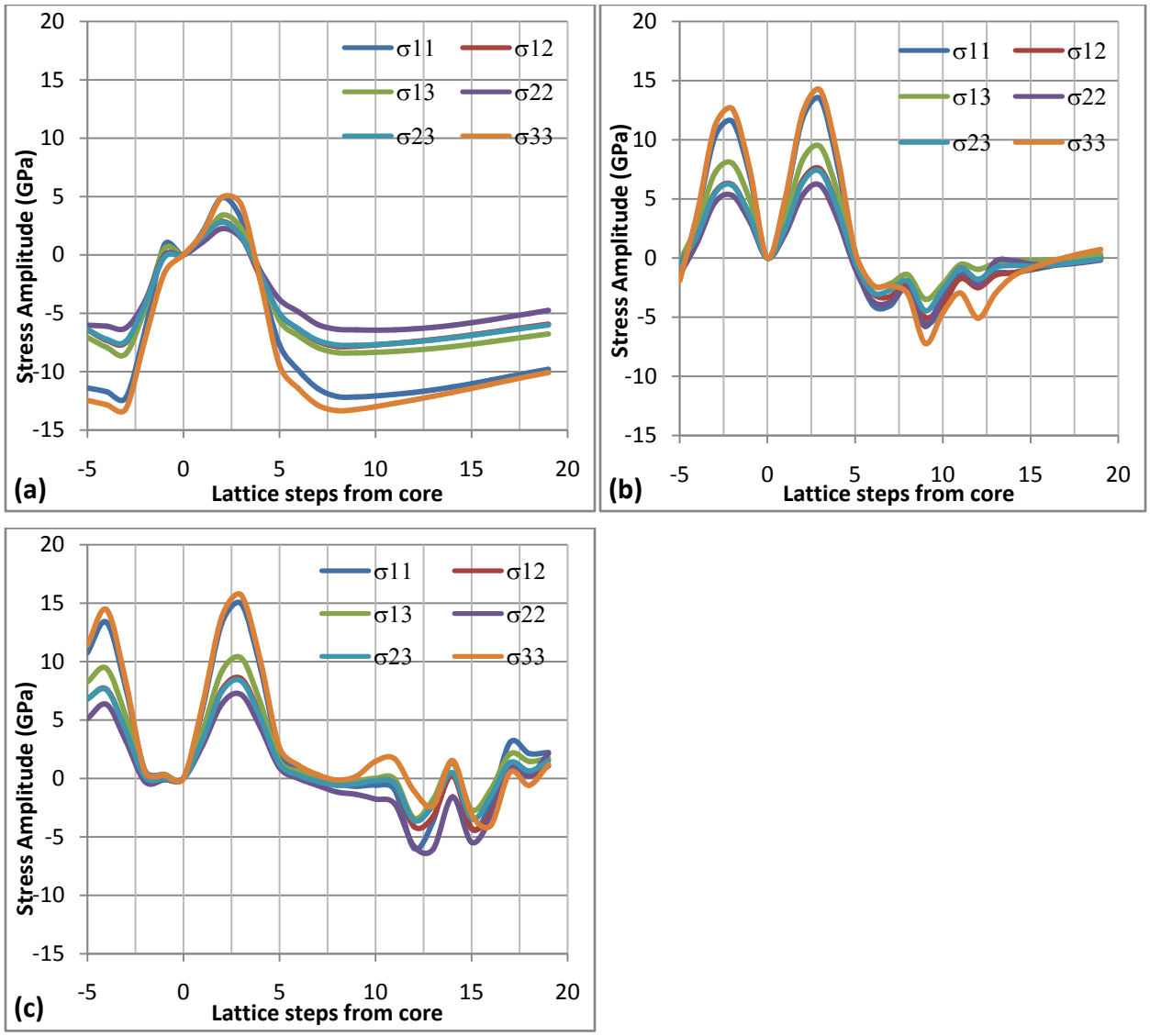

Figure 4.50: Stress amplitude variation along the normal to two slip planes separated by (a) three, (b) five, (c) seven, lattice steps, each containing edge dislocation dipoles at seven and four lattice steps from the sampling point, in Fe.

The significance of this dip/trough/ripple is that the slip planes give rise to a stress peaks at some displacement from the second slip plane, which would provide a measure of resistance to the motion of other dislocations. It is thought that this feature is related to the stress amplitude inflection observed in Figure 4.27b that gave results for a single screw dislocation. However, no similar effects were observed from the simulations for screw dislocation dipoles in a single slip plane.

4.4.2. NSF FOR SLIP PLANES CONTAINING EDGE DISLOCATION DIPOLES

From the curves shown in Figures 4.48 to 4.50, the peak stress and the lowest stress over the slipped region were extracted and are given in Table 4.27. These stresses were used to fit the test function χ in Equation 3.134 and the factors ε_i were established. Finally, the network structure factor components $\langle \mathcal{M}, \chi \rangle$ were obtained, the dislocation network density, $\emptyset_d$, calculated and compared with the directly computed network density (as illustrated in section 3.5.4). The fitting factors are also presented in Table 4.27.

Table 4.27: Characteristic stress and NSF data for parallel slip planes each containing parallel edge dislocation dipoles.

Dislocation locations		Plane separation	Hump stress 1 (GPa)	Hump stress 2 (GPa)	Pre-trough stress (GPa)	Post trough stress (GPa)	ε_1	ε_2	NSF $\langle \mathcal{M}, \chi \rangle$
3	1	3	0.23	0.42	-3.35	-2.76	-0.151	-0.114	7.395E-09
3	1	5	2.41	3.26	-1.13	0.72	-0.021	0.013	1.233E-08
3	1	7	3.06	3.87	2.31	1.44	0.059	0.023	1.726E-08
5	3	3	-0.21	0.62	-5.70	-4.35	-0.374	-0.118	7.395E-09
5	3	5	4.97	6.02	-0.69	0.25	-0.007	0.002	1.233E-08
5	3	7	6.83	7.40	5.76	1.61	0.07	0.013	1.726E-08
7	4	3	0.21	2.25	-6.26	-3.81	-0.181	-0.056	7.395E-09
7	4	5	4.69	6.15	-1.91	-0.32	-0.018	-0.003	1.233E-08
7	4	7	6.33	7.17	0.51	1.28	0.004	0.010	1.726E-08

It is noted that all the stress amplitude peaks are positive, and that they increase with the spacing between the slip planes. This is accompanied by a change from negative to positive trough stress values. The value of the network structure factor is proportional to the spacing between the slip planes. This result is not trivial, but instead is evidence that the method is able to capture the remaining parameter required to define the 3-D dislocation density (the other parameters are

contained in the plane structure factor). The value of this result is revealed when the orientation of the slip planes is changed and when the curvature of the slip planes is considered.

4.4.3. STRESS AMPLITUDE PROFILE FOR SLIP PLANES CONTAINING SCREW DISLOCATION DIPOLES

The stress amplitude profiles for opposite sense parallel screw dislocation dipoles aligned in the $[11\bar{1}]$ direction, contained in (112) slip planes, are presented in Figures 4.51 to 4.53. The displacement of the dislocation dipoles from the origin, and the spacing between the slip planes were recorded, and the resulting stress amplitude profiles analyzed.

Figure 4.51a shows results for slip planes separated by five lattice steps, each containing a screw dislocation dipole at three and seven lattice steps from the sampling line. The stress amplitude profile exhibits symmetry about the origin with a slight rotation in the region where the humps occur. In addition, a combination of positive and negative stress humps is noted. This differs from results for the interacting slip planes containing edge dislocation dipoles, where the stress amplitude components are all positive. As in the case of the edge dislocation dipole set, the second hump tends to rise above the first hump. Additionally, the wake of the stress amplitude profile consists of straight lines in the neighbourhood of the zero stress value, hence the intensification of the stress field for the slip planes containing screw dislocation dipoles are concentrated in the neighbourhood of these planes.

Figure 4.51b shows results for slip planes separated by five lattice steps, each containing a screw dislocation dipole at five and seven lattice steps from the sampling line. The stress amplitude profiles are symmetrically placed about the origin and this (the elimination of the rotation of the stress amplitude profile) is attributed to the increase in distance of the first screw dislocation from the sampling point. In this case, the two stress amplitude humps are almost identical. Additionally, the wake of the stress field consists of straight lines, hence the stress intensification is concentrated in the neighbourhood of the slip planes.

Figure 4.51c shows results for slip planes separated by five lattice steps, each containing a screw dislocation dipole at six and seven lattice steps from the sampling line. The symmetry of the

stress amplitude profile of Figure 4.51b is still present, and it is inferred that a critical distance of the order of five lattice steps from the sampling line is required for this symmetry to be fully defined. From Figure 4.51, it is noted that the maximum amplitude is about 4 GPa and these values are attained from the direct stress components. Additionally, these peak values are considerably lower than those of the slip planes containing the edge dislocations dipoles.

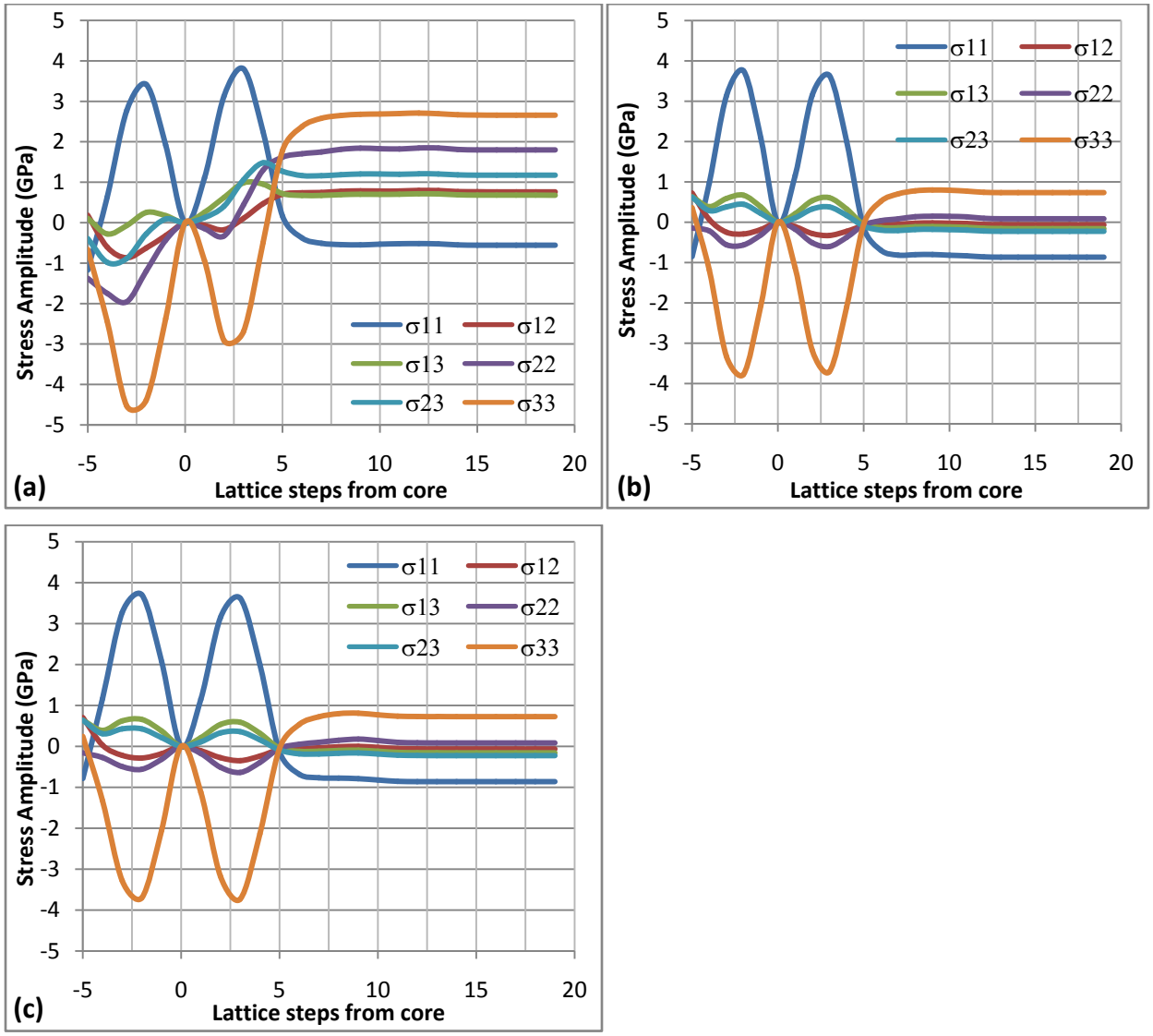

Figure 4.51: Stress amplitude variation along the normal to two slip planes separated by five lattice steps, each containing screw dislocation dipoles at (a) three and seven, (b) five and seven, (c) six and seven, lattice steps from the sampling point, in Fe.

It is inferred that the distortion arising from the slip planes containing screw dislocation dipoles is consistent beyond the immediate region of the slip plane, and as a result, the long range influence of the interacting slip planes is independent of the distance from the interacting slip planes.

Figure 4.52a shows results for slip planes separated by three lattice steps, each containing a screw dislocation dipole at three and five lattice steps from the sampling line. The stress amplitude profile exhibits symmetry about the origin, with a slight rotation in the region where the humps occur. However, in this case, the interaction of the dislocations in the region between them provides near zero amplitude stress components. This is interpreted as being a region of near zero distortion resulting from the relative positions of the slip plane. The stress components in the wake of the dislocation dipole again present near constant stress amplitude values. However, the values are much larger and it is inferred that the close proximity of the dislocation dipole to the sampling line generates a region possessing high induced stresses in the lattice, which is related to the screw dislocation's relative immobility.

Figure 4.52b shows results of a similar scenario to Figure 4.52a, with the difference being the increased separation of the two slip planes. At a spacing of five lattice steps, the humps are more clearly defined and the peak stress amplitude reduces from 7.0 to 4.0 GPa. It is inferred that the spacing of slip planes is most likely to stabilize at five lattice steps or more. In addition, the stress amplitudes in the wake of the dislocation dipole are much lower and the POLR value is of the order of 1.87 GPa. The rotation of the stress amplitude profile about the slip planes is also observed.

Figure 4.52c shows results for slip planes separated at seven lattice steps, each containing a screw dislocation dipole at three and five lattice steps from the sampling line. Some spreading of the dislocation humps is noted, as well as the rotation of the stress amplitude profile about the zero stress line. In the region of the wake of the slip planes, the stress amplitude components are nearly linear, although the rotation of the humps results in increasing the values of these components such that the symmetry about the zero stress line was lost.

Figure 4.52 provides evidence that the separation of planes is not the cause of the slight rotation of the stress amplitude profile about the zero stress line. Instead, the proximity to the sampling line is the cause of this rotation. Figures 4.51 and 4.52 show that the rotation of the stress component profiles is due to the location of the dislocation line closest to the sampling line, and the critical distance to eliminate this rotation is five lattice steps.

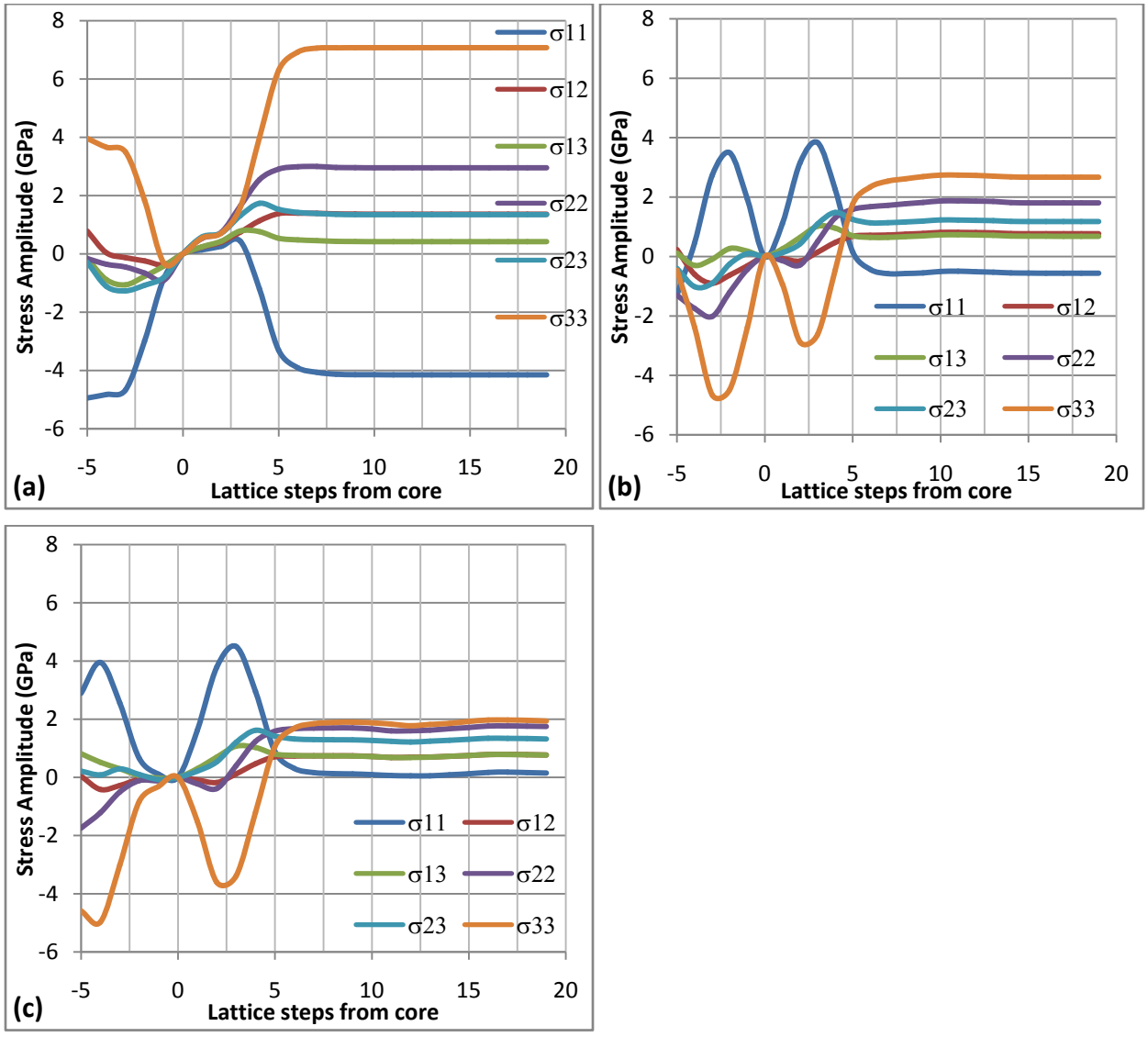

Figure 4.52: Stress amplitude variation along the normal to two slip planes separated by (a) three, (b) five, (c) seven, lattice steps, each containing screw dislocation dipoles at three and five lattice steps from the sampling point, in Fe.

Figure 4.53a shows results for slip planes at a separation of three lattice steps, each containing a screw dislocation dipole at four and seven lattice steps from the sampling line. It is noted that minimal rotation of the stress amplitude peaks occurs, despite the smaller separation of slip planes. However, the large peak stress amplitudes are consistent with other results where the separation was small. The near constant stress amplitude values are again consistent with earlier simulations for the screw dislocation dipoles.

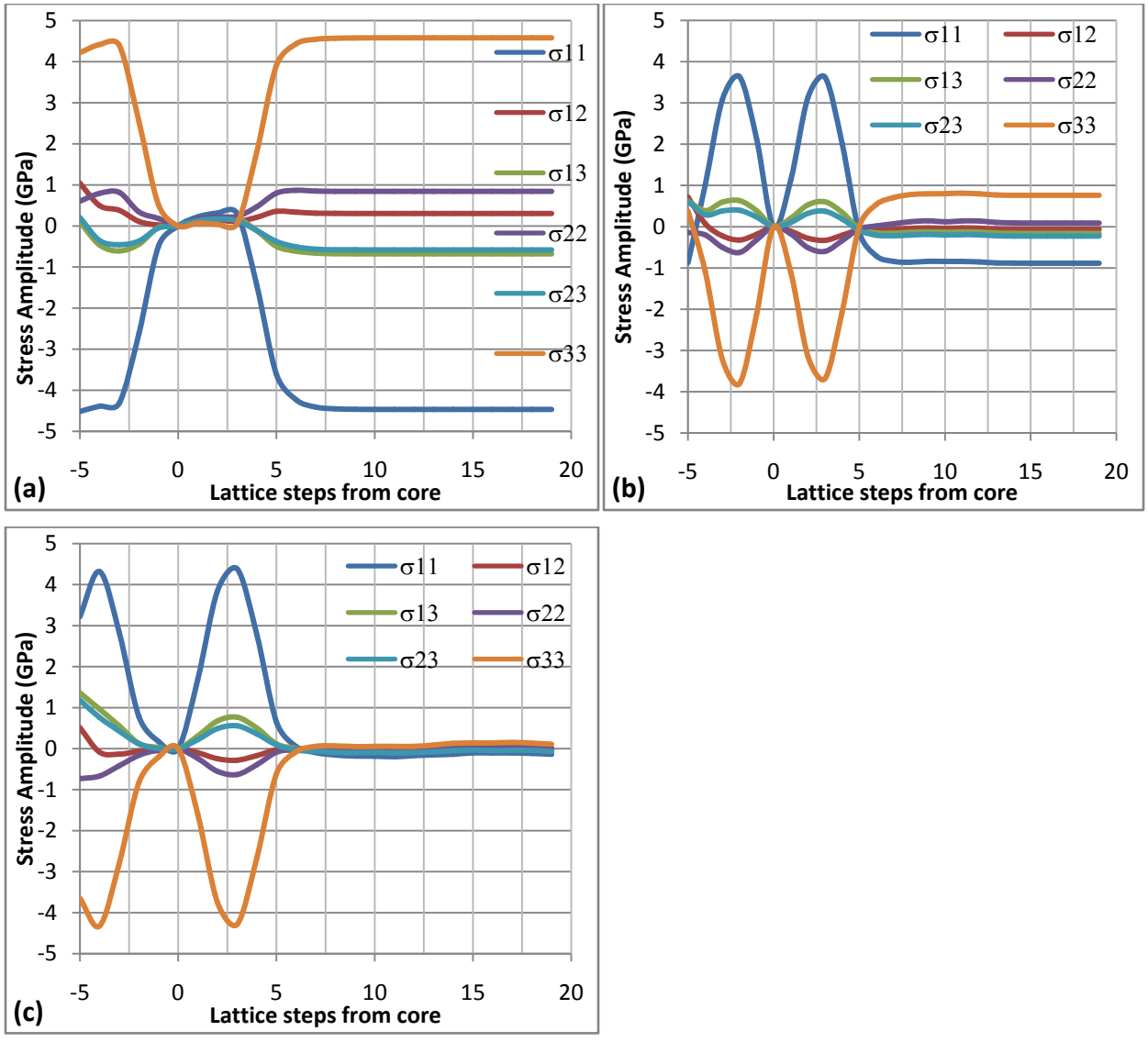

Figure 4.53: Stress amplitude variation along the normal to two slip planes separated by (a) three, (b) five, (c) seven, lattice steps, each containing screw dislocation dipoles at seven and four lattice steps from the sampling point, in Fe.

Figures 4.53b and 4.53c show simulation results for the same dislocation dipole configuration as for Figure 4.53a, with the difference being the separation of the slip planes. The trend observed over these simulations is that as the separation increases, a spreading of the stress humps occurs, accompanied by a reduction in the values of the stress components in the wake of the slip planes. The minimum peak value of the stress humps occurs at a lattice spacing of five lattice steps.

4.4.4. NSF FOR SLIP PLANES CONTAINING SCREW DISLOCATION DIPOLES

From the curves shown in Figures 4.51 to 4.53, the peak stress and the lowest stress over the slipped region were extracted (Table 4.28), together with the fitting factors. It is noted that the stress amplitude humps are largely similar except in the instances where the profile is marginally rotated.

Table 4.28: Characteristic stress and NSF data for parallel slip planes each containing parallel screw dislocation dipoles.

Dislocation locations		Plane separation	Hump stress 1 (GPa)	Hump stress 2 (GPa)	Pre-trough stress (GPa)	Post trough stress (GPa)	ε_1	ε_2	NSF $\langle \mathcal{M}, \chi \rangle$
7	3	5	-1.98	-0.33	-1.37	1.62	0.052	-0.102	7.395E-09
7	5	5	-0.56	-0.60	-0.14	-0.07	0.015	0.007	1.233E-08
7	6	5	-0.56	-0.64	-0.16	-0.05	0.016	0.004	1.479E-08
5	3	3	-0.66	0.53	-0.16	2.91	0.014	-0.394	7.395E-09
5	3	5	-2.02	-0.29	-1.30	1.59	0.046	-0.107	1.233E-08
5	3	7	-0.11	-0.39	-1.74	1.59	-0.260	-0.093	1.726E-08
7	4	3	0.79	0.22	0.61	0.80	0.060	-1.480	7.395E-09
7	4	5	-0.63	-0.60	-0.14	-0.05	0.013	0.005	1.233E-08
7	4	7	-0.73	-0.63	-0.73	-0.09	0.097	0.008	1.726E-08

The stress amplitudes given in Table 4.28 correspond to the POLR. The variation does not present any pattern and the values do not compare with any Peierl's stresses [181, 191]. It is

noted that the stress peaks are smaller than those for slip planes containing edge dislocations. This is similar to results obtained for edge dislocation dipoles and it is inferred that the POLR concept does not apply across slip planes. The results consist of network structure factor data that are proportional to the separation of slips, and this is similar to results for the slip planes containing edge dislocation dipoles.

4.4.5. STRESS AMPLITUDE PROFILE FOR SLIP PLANES CONTAINING 35.26^{o} SCREW DISLOCATION DIPOLES

The stress amplitude profiles of parallel 35.26^{o} screw dislocation dipoles aligned in the $[11\bar{1}]$ direction, contained in (112) slip planes, are shown in Figures 4.54 to 4.56. The displacement of the dislocation dipoles from the origin, and the spacing between the slip planes were recorded and the resulting stress amplitude profiles analyzed.

The curves in Figure 4.54a show two stress amplitude humps representing the effects of the interacting slip planes. As in the case of the edge and screw dislocations, the second hump is larger. A clearly defined trough is formed immediately after the second hump. This dip in the stress amplitude is considered an indication that the atoms around the slip plane would have tended to move away from the slip plane towards the region of lower stress amplitude. This is consistent with the “peeling action” mechanism suggested in the POLR model in this thesis.

The curves in Figure 4.54b also show two stress humps, which are distinct. This is similar to findings made for the edge and screw dislocations. As the distance of the sampling line from the slip planes increases, the stress amplitude humps become more distinct and a region of low stress amplitude is formed between them. It is inferred that the atoms around the slip plane would have tended to “peel” into this area of low stress amplitude, aiding the motion of the dislocation within the slip plane. Additionally, it is noticed that as the distance of the sampling line from the slip planes increases, the location of the stress trough in the wake of the second slip plane moves further away from this slip plane. As inferred earlier in this work, the stress amplitude trough would have aided the “peeling” of atoms about the slip plane. Consequently, an increase in separation between slip planes diminishes the contribution of the “peeling” mechanism. It is noticed that the peak value of the stress amplitude hump increases with the separation between

the slip planes. However, the POLR value remains within the ±4 GPa range. This trend is also seen in the stress amplitude profile in Figure 4.54c.

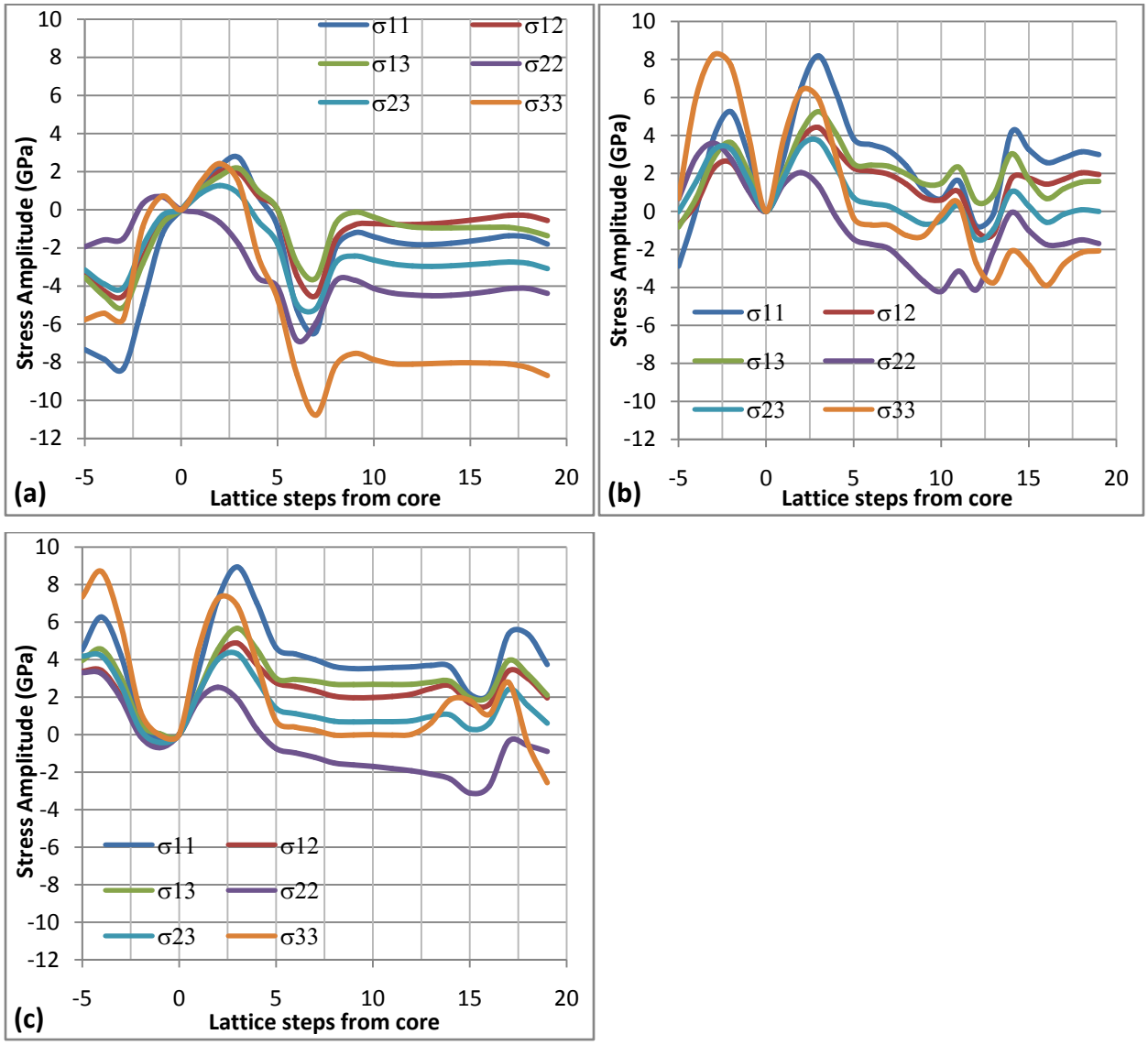

Figure 4.54: Stress amplitude variation along the normal to two slip planes separated by (a) three, (b) five, (c) seven, lattice steps, each containing 35.26° screw dislocation dipoles at one and three lattice steps from the sampling point, in Fe.

Figure 4.55a shows results for the slip planes separated by three lattice steps, with dislocation dipoles at three and five lattice steps from the sampling line. The stress amplitude profile shows

an overlap of the stress amplitude humps, again with a larger second hump. The wake of the stress amplitude humps comprises of large negative stress component values, indicating that stress reversal occurs in this region. In addition, the stress amplitudes in this region do not vary much.

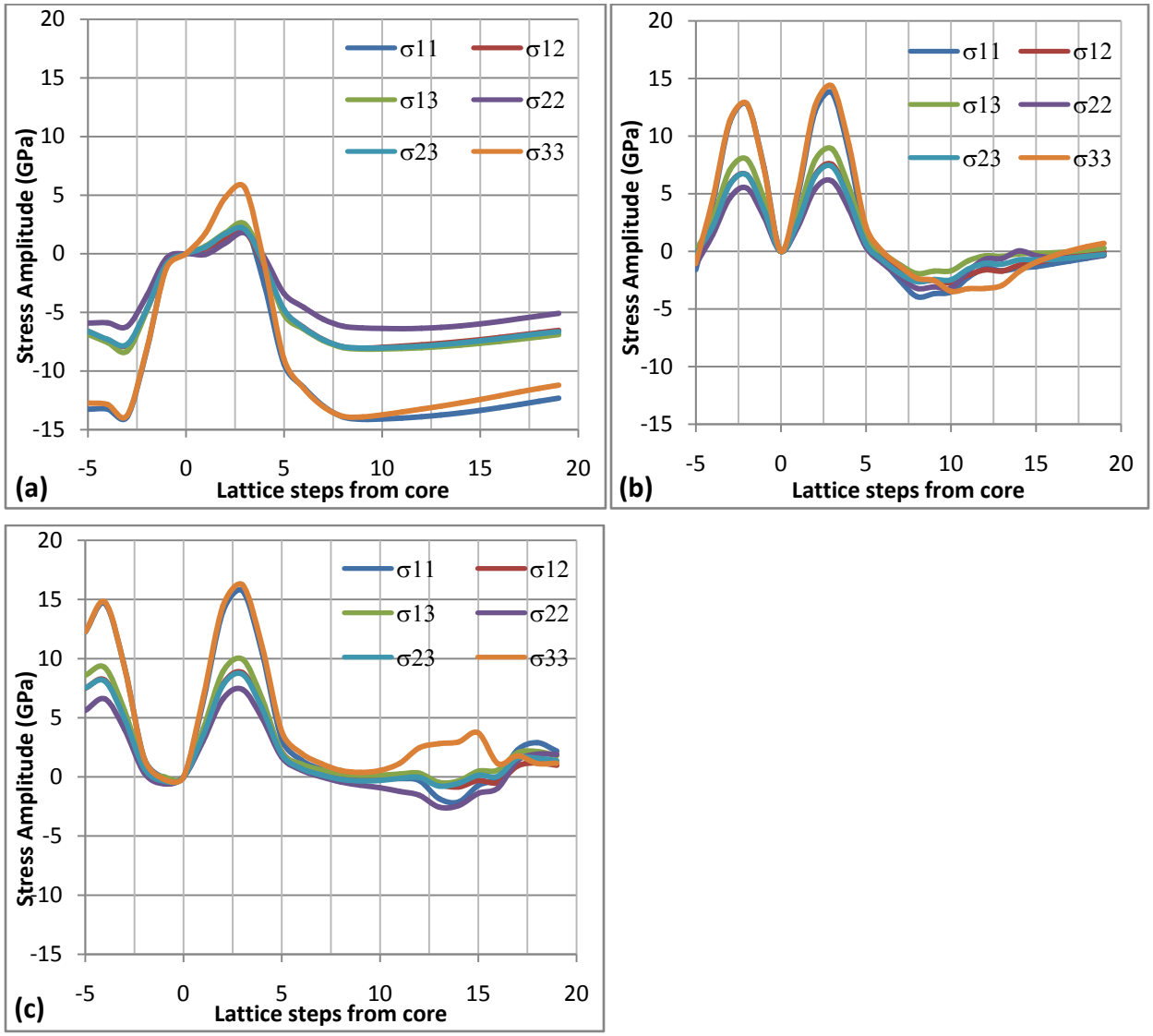

Figure 4.55: Stress amplitude variation along the normal to two slip planes separated by (a) three, (b) five, (c) seven, lattice steps, each containing 35.26° screw edge dislocation dipoles at three and five lattice steps from the sampling point, in Fe.

Figures 4.55b and 4.55c show the stress amplitude profiles for cases where the separation of slip planes is increased. As observed earlier, as the separation increases, the stress amplitude humps are more distinct, the stress trough in the wake of the profile moves further away from the slip planes, and the peak value of the humps increases. However, the POLR stress amplitude peak does not vary much. It is inferred that the "peeling" mechanism would be aided by a reduction in the separation of the slip planes.

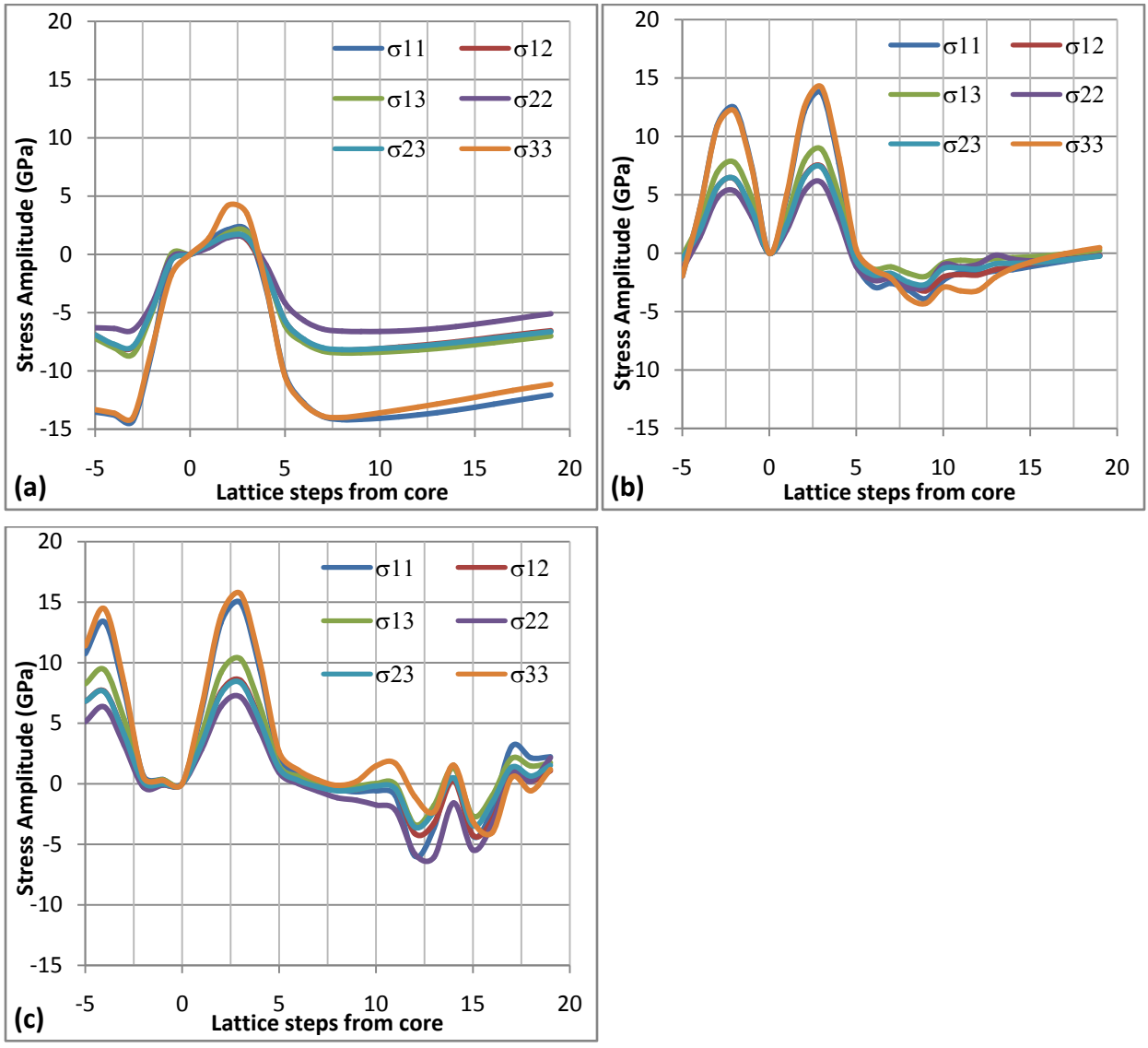

Figure 4.56: Stress amplitude profile along the normal to two slip planes separated by (a) three, (b) five, (c) seven, lattice steps, each containing 35.26° screw dislocation dipoles at seven and four lattice steps from the sampling point, in Fe.

Figure 4.56 shows results for slip planes containing dislocation dipoles formed by screw dislocations at four and seven lattice steps from the sampling line. The stress amplitude profiles are similar to those in Figure 4.55. However, the trough in Figure 4.56c is larger than that of Figure 4.55c, suggesting that the increased spacing between the dislocations forming the dipole had a greater contribution if the slip planes were further apart. The POLR stress amplitude peak increases marginally with increase in separation between the slip planes.

4.4.6. NSF FOR SLIP PLANES CONTAINING 35.26° SCREW DISLOCATION DIPOLES

From the curves shown in Figures 4.54 to 4.56, the peak stresses and the lowest stresses over the slipped region were extracted (Table 4.29) as are the fitting factors. The stress amplitudes are also given in Table 4.29 and they corresponded to the POLR.

Table 4.29: Characteristic stress and NSF data for parallel slip planes each containing parallel 35.26° screw dislocation dipoles.

Dislocation locations		Plane separation	Hump stress 1 (GPa)	Hump stress 2 (GPa)	Pre-trough stress (GPa)	Post trough stress (GPa)	ε_1	ε_2	NSF $\langle \mathcal{M}, \chi \rangle$
3	1	3	0.31	-0.16	-1.51	-4.06	-0.100	-0.225	1.233E-08
3	1	5	2.27	2.04	-0.82	-1.46	-0.017	-0.030	1.233E-08
3	1	7	3.31	2.52	3.31	-0.74	0.097	-0.014	1.233E-08
5	3	3	-0.38	1.78	-6.19	3.39	-0.156	-0.060	7.395E-09
5	3	5	4.62	6.10	-1.46	0.37	-0.015	0.003	1.233E-08
5	3	7	6.59	7.40	5.62	1.65	0.071	0.013	1.726E-08
7	4	3	-0.29	1.44	-6.49	-4.15	-0.169	-0.077	7.395E-09
7	4	5	4.72	6.05	3.78	-1.13	0.064	-0.009	1.233E-08
7	4	7	6.33	7.17	-5.12	0.92	-0.033	0.007	1.726E-08

In all cases, the value of the hump stress increases with the separation of the slip planes. However, these values do not compare well with values of Peierl's stress reported elsewhere

[181, 191]. This is similar to the results derived for slip planes containing edge dislocation dipoles and it is inferred that the POLR concept does not apply across slip planes. The resulting network structure factor data are proportional to the separation of the slip planes and this is consistent with results for the slip planes containing edge dislocation dipoles.

4.4.7. STRESS AMPLITUDE PROFILE FOR SLIP PLANES CONTAINING 70.52^{o} SCREW DISLOCATION DIPOLES

The stress amplitude profiles of parallel 70.52^{o} screw dislocation dipoles aligned in the $[11\bar{1}]$ direction, contained in (112) slip planes, are presented in Figures 4.57 to 4.59. The displacement of the dislocation dipoles from the origin, and the spacing between the slip planes were recorded and the resulting stress amplitude profiles analyzed.

Figure 4.57 shows a set of curves for slip planes separated by five lattice steps, and with a varying location of the dislocation dipole, with respect to the sampling line. The magnitudes of the stress amplitude humps do not vary much, although the shape of the trough beyond the second hump changes. As the dislocation dipole is moved away from the sampling line, the depth of the trough increases at the start of the trough and reduces at the end of the trough. This is interpreted to be an indicator that the “peeling” mechanism would have had a greater effect with the dislocation dipole closer to the sampling line, which is consistent with deductions made for the other dislocation types.

Figure 4.58 shows results for dislocation dipole at three and five lattice steps from the sampling line, with the separation of the slip planes varied. At a separation of three lattice steps, the stress amplitude humps overlap, as observed for the other dislocation types. As the separation is increased, the humps are more clearly defined, and with sufficient separation, a region of very low stress amplitudes is found between the humps. This region would have aided the “peeling” mechanism and dislocation motion. Additionally, a trough forms in the wake of the second hump. As the separation between the slip planes increases, the trough moves away from the sampling line. It is deduced that the stress hump would have aided the “peeling action” and hence the increase in spacing between the slip planes diminishes its effect. A similar pattern is

observed on Figure 4.59, with the main change being in the reduction in the value of the peak values of the stress amplitude hump.

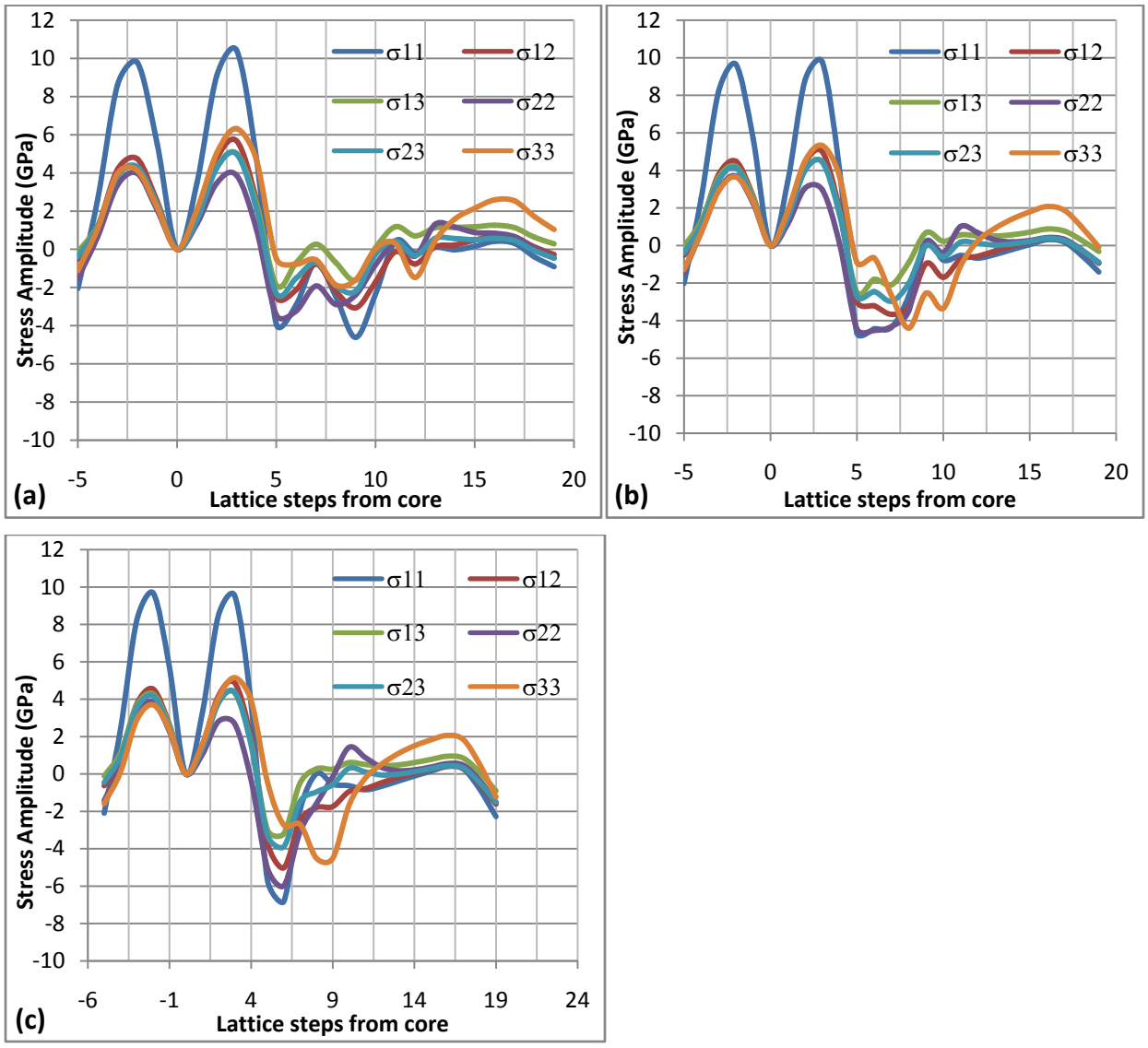

Figure 4.57: Stress amplitude variation along the normal to two slip planes separated by five lattice steps, each containing 70.52° screw dislocation dipoles at (a) three and seven, (b) five and seven, (c) six and seven, lattice steps from the sampling point, in Fe.

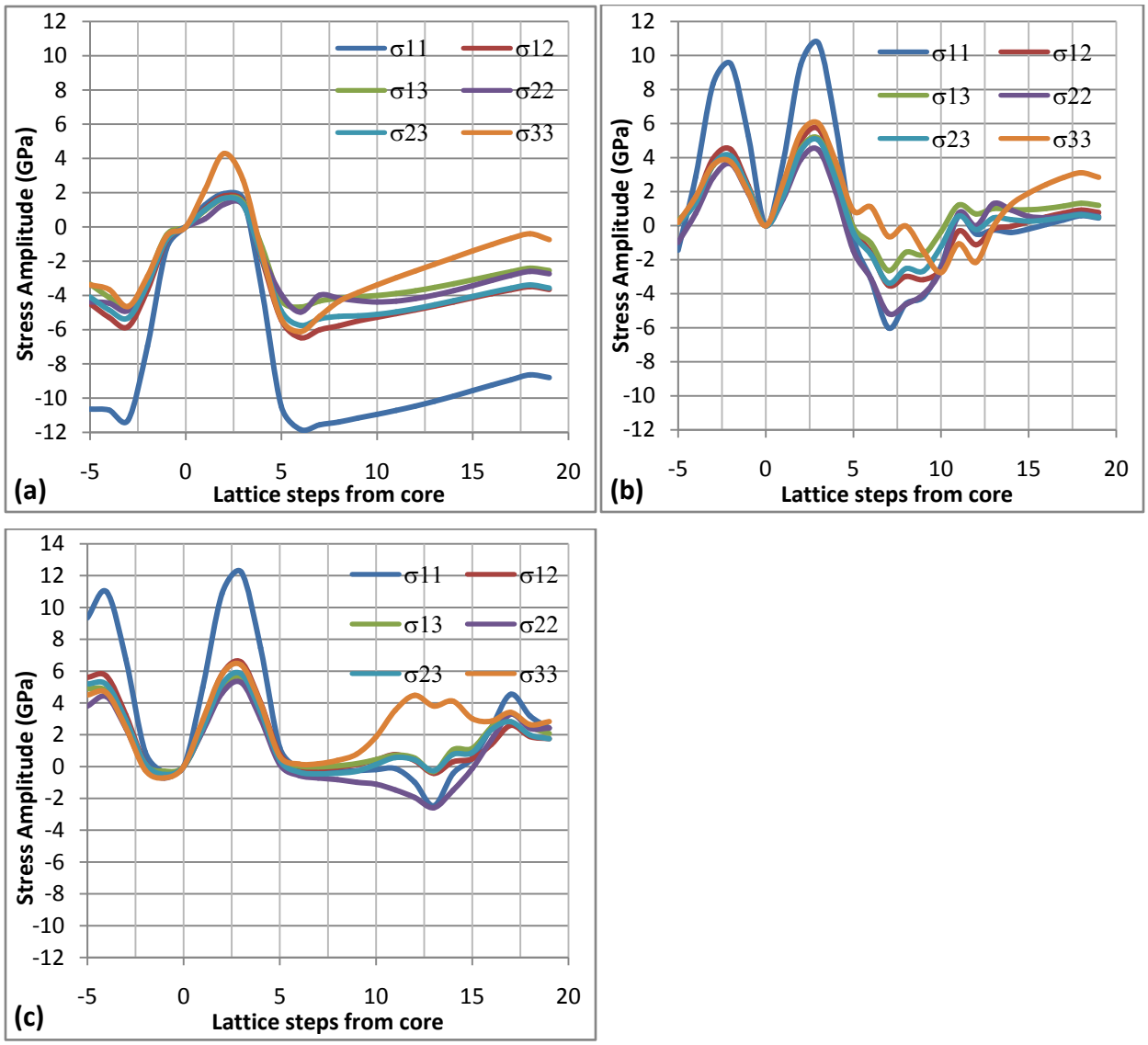

Figure 4.58: Stress amplitude variation along the normal to two slip planes separated by (a) three, (b) five, (c) seven, lattice steps, each containing 70.52° screw edge dislocation dipoles at three and five lattice steps from the sampling point, in Fe.

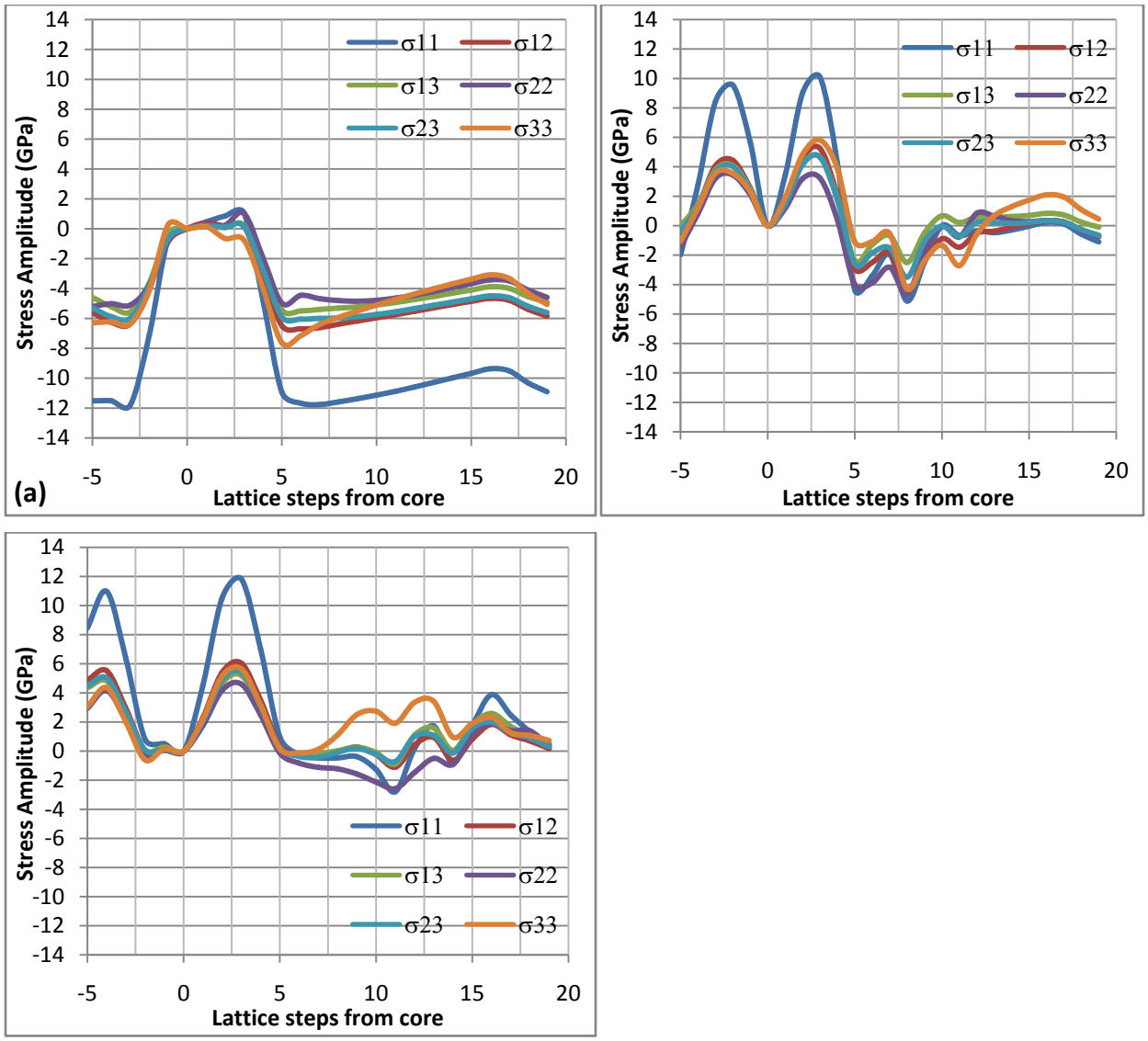

Figure 4.59: Stress amplitude variation along the normal to two slip planes separated by (a) three, (b) five, (c) seven, lattice steps, each containing 70.52° screw dislocation dipoles at seven and four lattice steps from the sampling point, in Fe.

4.4.8. NSF FOR SLIP PLANES CONTAINING 70.52° SCREW DISLOCATION DIPOLES

From the curves shown in Figures 4.57 to 4.59, the peak stress and the lowest stress over the slipped region were extracted and are presented in Table 4.30. The fitting factors are also given in Table 4.30. The stress amplitudes given in Table 4.30 represent the POLR. In all cases, the

value of the hump increases with the separation between the slip planes. However, the increase in values is much smaller than for the slip planes containing edge or 35.26^o screw dislocation dipoles. The stress peak values do not compare well with any published values of 1.1 - 1.8 GPa [181, 191] of the Peierl's stress. This is similar to results obtained for the edge dislocation dipoles and it is inferred that the POLR concept does not apply across slip planes. The results reveal that network structure factor data are proportional to the separation of slip, which is consistent with results for the slip planes containing edge dislocation dipoles.

The values of the fitting factors ε_1 and ε_2 were used to set the profile of the test function χ. This was done to ensure the test function mimicked the stress amplitude profile obtained from simulations. In consequence, the integration of the network structure factor over the integration limits would therefore yield the requisite structure factor and the dislocation density resulting from these structures. This approach was adopted for all the dislocation types.

Table 4.30: Characteristic stress and NSF data for parallel slip planes each containing parallel 70.52^o screw dislocation dipoles.

Dislocation locations		Plane separation	Hump stress 1 (GPa)	Hump stress 2 (GPa)	Pre-trough stress (GPa)	Post trough stress (GPa)	ε_1	ε_2	NSF $\langle \mathcal{M}, \chi \rangle$
7	3	5	3.36	3.46	-1.12	-3.44	-0.0155	-0.0383	1.233E-08
7	5	5	3.76	3.05	-1.42	-4.44	-0.0173	-0.0505	1.233E-08
7	6	5	3.86	2.81	0.48	-5.04	0.00679	-0.0581	1.233E-08
5	3	3	-1.26	1.32	-4.88	-3.95	-0.0901	-0.0783	7.395E-09
5	3	5	2.83	4.45	-0.98	-1.48	-0.0161	-0.0154	1.233E-08
5	3	7	4.39	4.61	3.80	0.39	0.0658	0.00455	1.726E-08
7	4	3	0.26	1.03	-5.11	-4.99	-0.1638	-0.1008	7.395E-09
7	4	5	3.21	3.24	-1.41	-4.00	-0.0197	-0.045	1.233E-08
7	4	7	4.17	4.17	2.94	-0.14	0.05279	-0.0017	1.726E-08

4.5. MESO-SCALE

A gauge length of 1 mm long, 0.6 mm wide and 0.6 mm high specimen was selected. The selection of these dimensions was arbitrary, but enabled meaningful discretization (to match required meso scale elements) without inordinate degrees of freedom. The applied load was axial at all times.

4.5.1. MESH GENERATION

The sample was divided into 5 x 3 x 3 steps along the length, width and height respectively. Plastic behaviour was limited to the middle of the specimen as viewed along the specimen's length. The macro-scale finite elements forming the "two mid-planes" (planes 2 and 3 in Figure 4.60) were discretized further into meso-scale finite elements. A total of 18 macro-scale elements were therefore discretized.

The specimen was anchored at four corners on one face forming a 0.6 mm x 0.6 mm cross-section, and loaded at the corners on the opposite face with (0.05,0,0) kN load at each node. The resulting applied load was (0.2,0,0) kN.

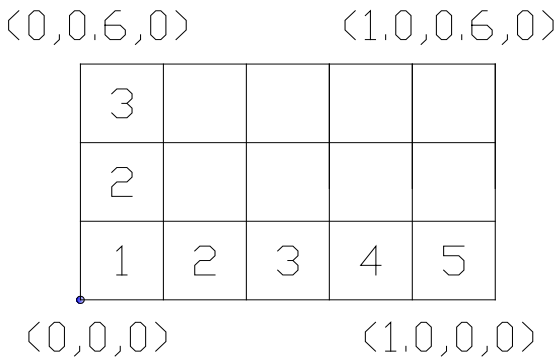

Figure 4.60: 2-D macro-scale discretization of the sample.

The selection of the meso-scale finite element size is outlined in Equations 4.1 to 4.3. This finite element size was selected within the characteristic grain size range where the Hall-Petch effect was evident. For Fe this range has been reported as 4 μm to 200 μm [167]. Due to the limitations in simulation capacity, variations in the meso-scale element size were achieved by varying the specimen size instead of varying the degree of discretization.

An average ASTM grain size number of 11.632 ± 0.1002 [188] was obtained from a grain size and distribution test on a Universal Microscope (Optika B-353 MET) at 256X magnification, with microstructural analysis carried out using "Microstructural Characterizer 3.0" software. A test report is found in Figure 4.61. An estimate of the grain size was obtained using the relation [188]:

$$N_{AE} = 15.5 * 2^{G-1} \quad (4.1)$$

where:

N_{AE} is the number of grains per square inch at a magnification of 100X

G is the ASTM grain size number

15.5 is the multiplication factor to obtain number of grains per square millimetre at 1X magnification [188].

The number of grains in a square mm was obtained as:

$$15.5 * 2^{11.632-1} = 24{,}597.03 \quad (4.2)$$

The typical dimension of the grain was obtained as:

$$\sqrt{1x10^{-3}/24{,}597.03} = 1.26x10^{-4} \quad (4.3)$$

From this data, a typical meso-scale element was determined as 202 μm x 202 μm x 202 μm for a fully annealed material. From this result, the meso-scale full scale discretization was determined as 10 x 3 x 3 finite elements along the length, width and height respectively for each macro-scale finite element. A 2-D representation of the meso-scale discretization and the numbering of the elements is shown in Figure 4.62. Additionally, the node numbers for this discretization are shown on Figure 4.63.

UNIVERSITY OF NAIROBI

DEPARTMENT OF MECHANICAL ENGINEERING

Telegrams: 'Varsity' Nairobi, Fax: +254(020)2245566, P.O. Box 30197 – 00100, Nairobi.
Telephone: +254 (02) 318262 Ext: 28383, Email: dept-mmengineering@uonbi.ac.ke

TEST REPORT

Report No: Date: 2/19/2013

To,

GRAIN SIZE ESTIMATE AND DISTRIBUTION

Test Method : ASTM E-112

Sample Received Date	:	
Reference	:	
Party's Reference	:	

SAMPLE ID: Parent Metal

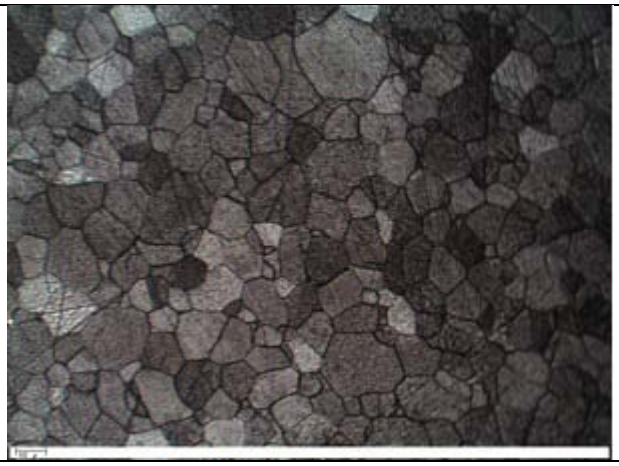

Sample Photograph

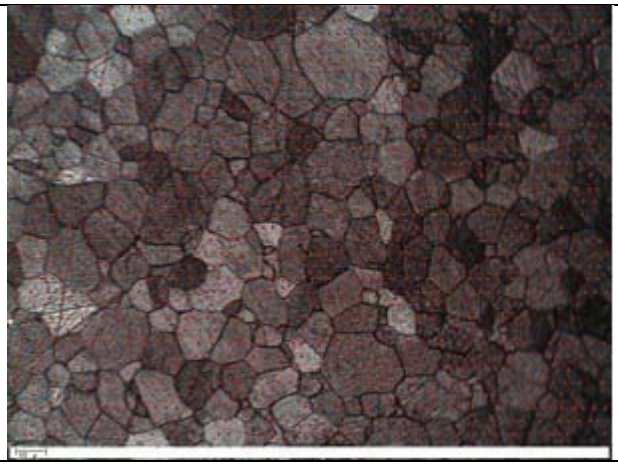

Magnification :265 x

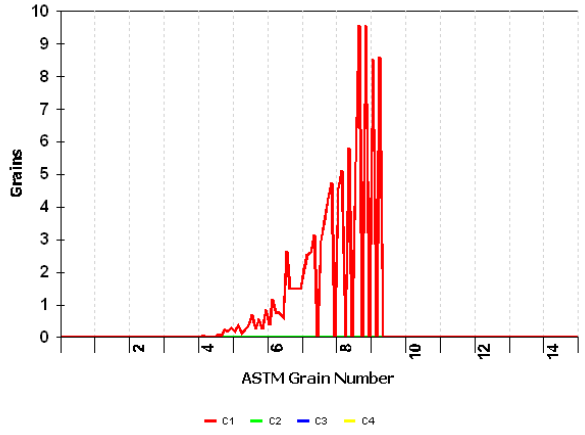

AVERAGE ASTM
GRAIN SIZE NUMBER

11.632
±
0.1002

Figure 4.61: Grain size estimate and distribution of the Fe sample.

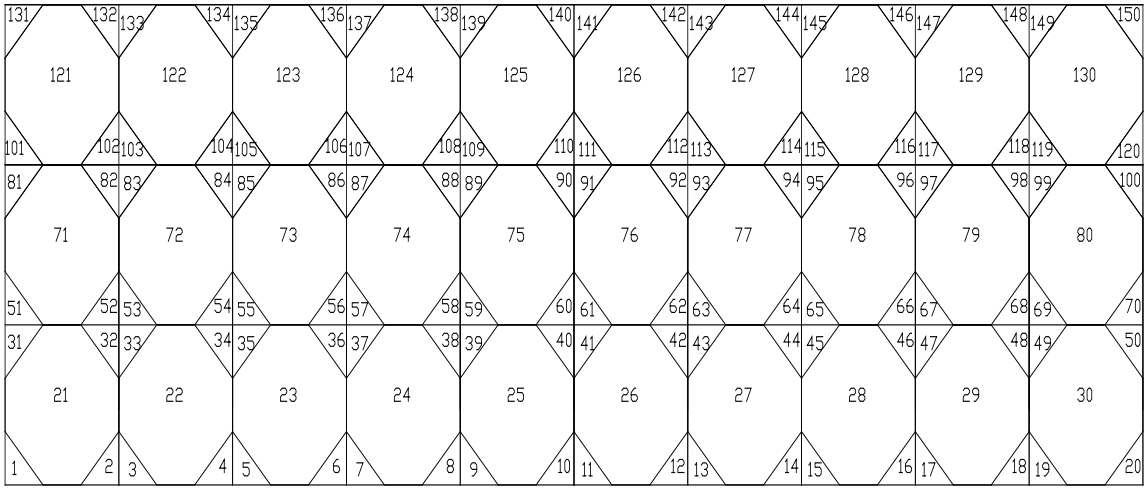

Figure 4.62: 2-D meso-scale discretization of a macro-scale finite element.

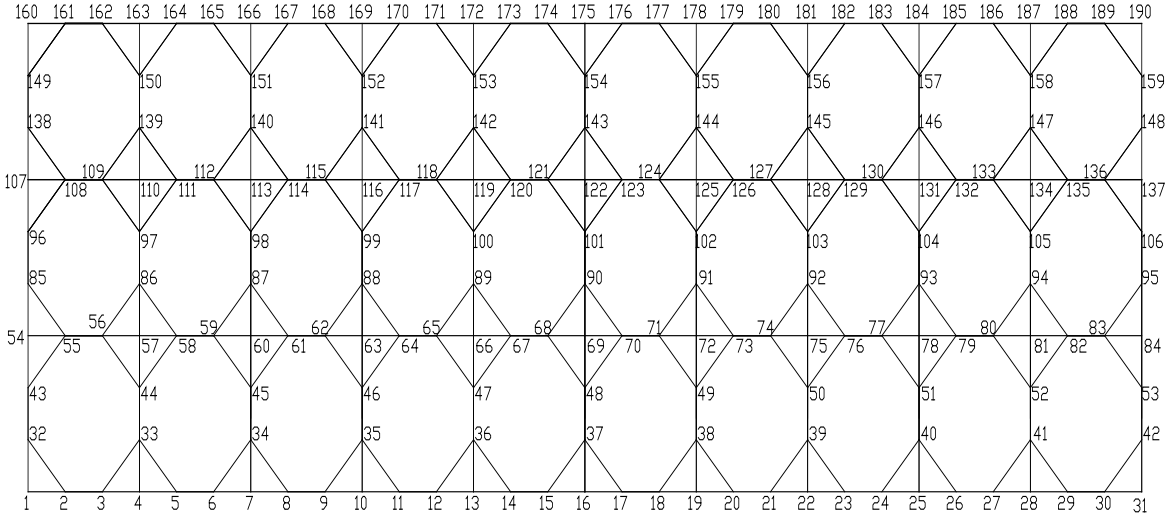

Figure 4.63: Node numbering of the 2-D meso-scale mesh.

The discretization process enabled the simulation to replicate a typical meso-scale structure. The meso-scale discretization was replicated in all macro-scale finite elements considered for plastic deformation. This generalization is considered reasonable as the 3D dislocation structure was that obtained from the material matrix considered to most susceptible to plastic flow. By enabling plastic flow at the mid-section of the specimen, no generality is lost as the specific

location of plastic flow in a prism loaded along its axis of symmetry is not a critical determinant of the overall material's deformation.

4.5.2. NSF RELATIONS FOR THE MOBILE DISLOCATIONS

The plots of the square root of the dislocation density versus the network structure factor for each type of grain boundary structure, for the various dipole configurations are shown in Figure 4.64. The equations for the lines of best fit (see Equation 3.236) are given in Table 4.31.

Table 4.31: Equations for the lines of best fit between the square root of the dislocation density and the NSF.

Dislocation Type (in Fe lattice)	$\sqrt{\rho_m}\ (m^{-1})$
Edge	$1.8825 * 10^4 * NSF^{-0.5}$
Screw	$1.0 * 10^6 * NSF^{-0.27}$
36.26^o screw	$1.5292 * 10^4 * NSF^{-0.5}$
70.52^o screw	$1.5292 * 10^4 * NSF^{-0.5}$

Figures 4.64a and 4.64b show fitting curves for the edge and the screw dislocation networks respectively. A higher gradient is obtained for the grain boundary structure formed from edge dislocation networks which indicates that this network's dislocation density exhibits a greater sensitivity to variations in the NSF. It is also noted that the curves for the grain boundary structures formed from 35.26^o screw and the 70.52^o screw dislocation networks have identical profiles, while the gradient of the grain boundary structure formed from the edge dislocation network is similar with a 51.5% increase in gradient over that of the mixed dislocations. The larger increase in gradient for the edge dislocation grain boundary indicates that this network experiences a larger change in dislocation density with change in NSF, than the mixed dislocation networks. It is also noted that the dislocation density for the non-screw grain boundary scales to the inverse of the fourth root of the network structure factor while that of the screw grain boundary scales to the inverse of the square root of the NSF. This indicates that the screw grain boundary experiences an even larger reduction in the change in NSF, than the mixed grain boundary.

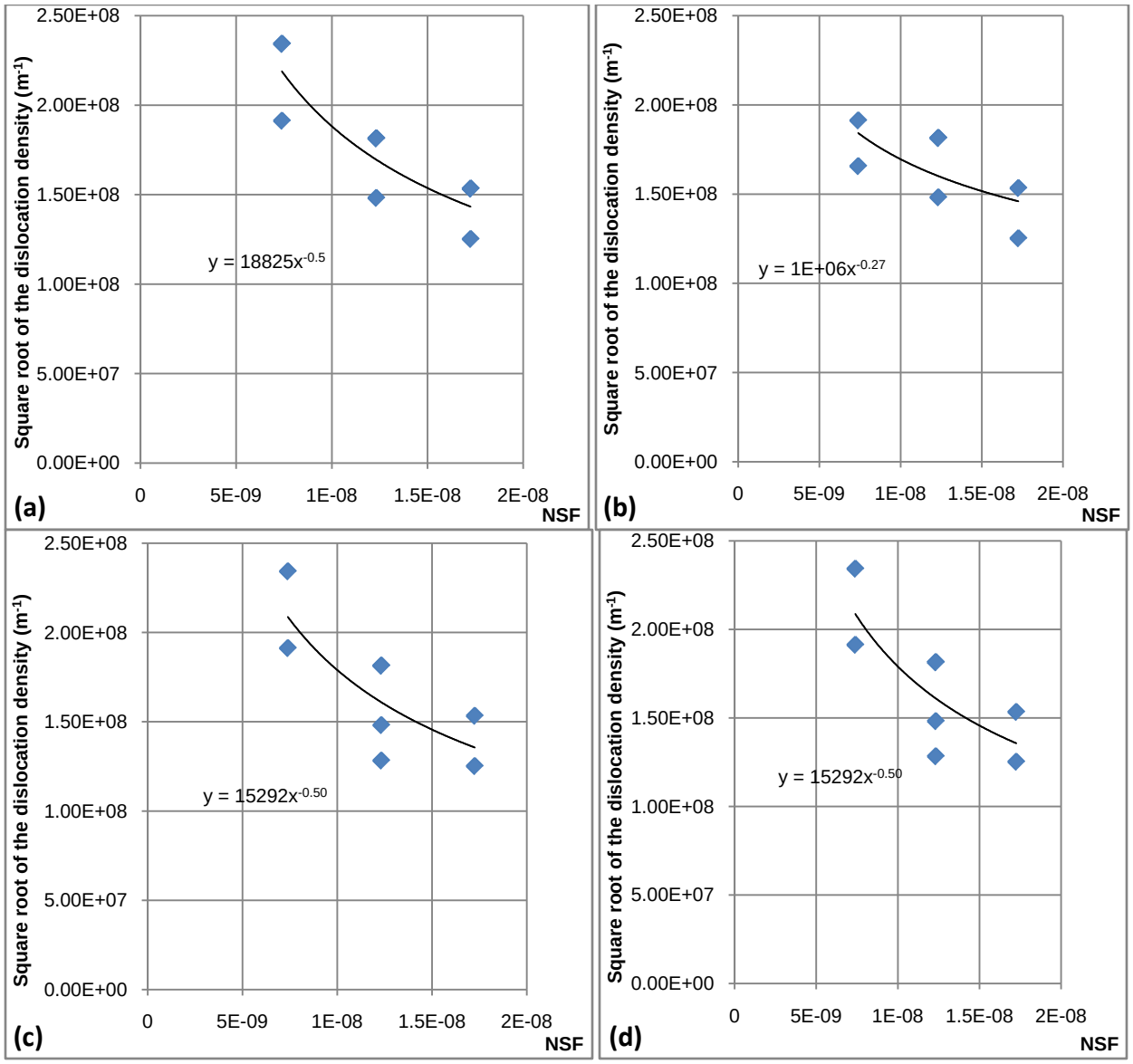

Figure 4.64: Square root of the dislocation density versus the NSF for (a) edge, (b) screw, (c) 35.26° screw, (d) 70.52° screw, dislocation networks.

4.5.3. NSF RELATIONS FOR THE GRAIN BOUNDARY DISLOCATIONS

The plots of the inverse of the dislocation density versus the network structure factor for each grain boundary type, for the various dipole configurations are shown in Figure 4.65. The equations for the lines of best fit (see Equation 3.240) are given in Table 4.32.

These plots were prepared to enable the direct generation of relationships for the variation of the inverse of the dislocation density in the grain boundary with the NSF. This was used as an input into Equation 3.241 to compute the POLR peak stress. It is noteworthy that the plots for the edge, the 35.26^{o} screw and the 70.52^{o} screw grain boundary are straight lines, consistent with the plots in Figures 4.64a to 4.64c. Additionally, the values of the inverse of the dislocation density at the sampling points are indicated.

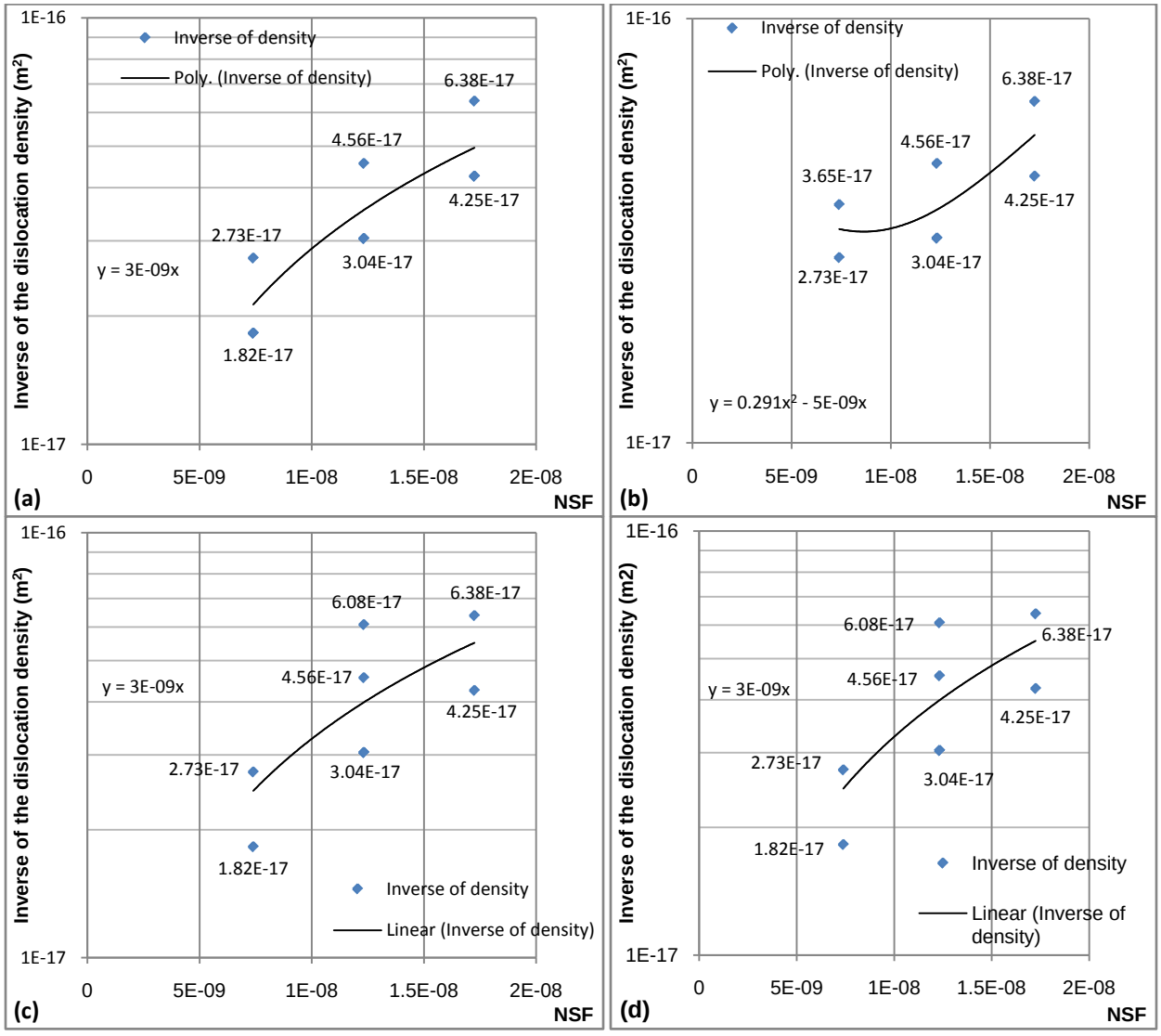

Figure 4.65: Dislocation density versus the NSF for (a) edge, (b) screw, (c) 35.26^{o}, (d) 70.52^{o}, dislocation networks.

Table 4.32: Equations for the lines of best fit between the dislocation density and the NSF.

Dislocation Type (in Fe lattice)	$\rho_b\ (m^{-2})$
Edge	$3.0 * 10^{-9} * NSF$
Screw	$0.291 * NSF^2 - 5.0 * 10^{-9} * NSF$
36.26^o screw	$3.0 * 10^{-9} * NSF$
70.52^o screw	$3.0 * 10^{-9} * NSF$

The plots of the first POLR peak stress versus the corresponding NSF, for the various dipole configurations are shown in Figure 4.66. The equations for the lines of best fit (see Equation 3.241) are given in Table 4.33.

A linear variation of the POLR stress with the network structure factor is observed for all the grain boundary types. It is noted that these relations are very close for the edge, 35.26^o screw and 70.52^o screw grain boundary. This is consistent with the variation observed for the dislocation density. The gradient for the screw grain boundary is the least indicating that the POLR stress for this structure is the least affected by variations in the network structure factor.

Table 4.33: Equations for the lines of best fit between the first peak POLR stress and the NSF.

Dislocation Type (in Fe lattice)	σ (GPa)
Edge	$5.0x10^8 * NSF - 3.494$
Screw	$1.0 * 10^7 * NSF - 0.887$
36.26^o screw	$7.0x10^8 * NSF - 5.441$
70.52^o screw	$5.0x10^8 * NSF - 3.238$

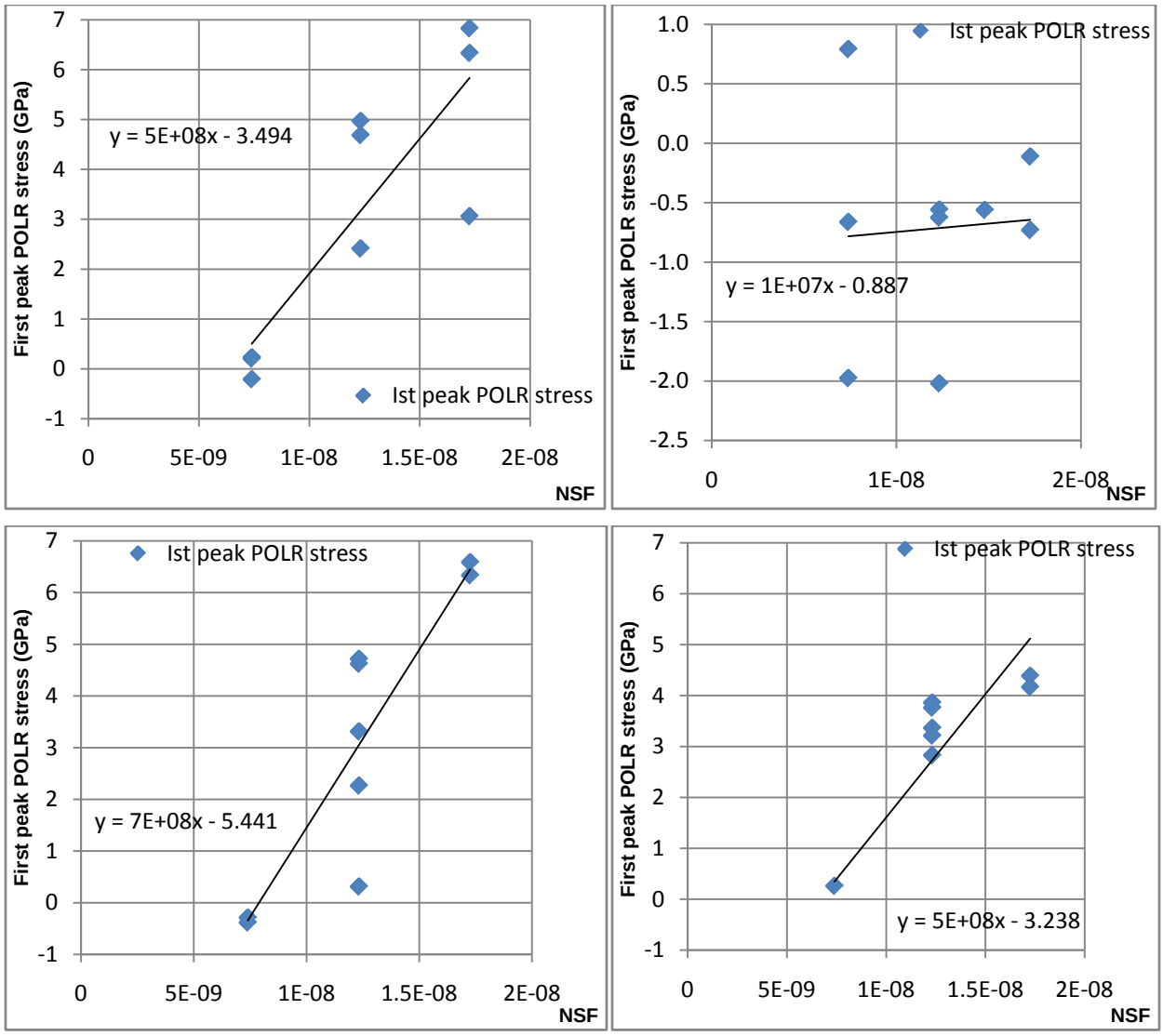

Figure 4.66: First peak POLR stress versus the NSF for (a) edge, (b) screw, (c) 35.26°, (d) 70.52°, dislocations.

4.5.4. VARIATION OF THE NETWORK STRUCTURE FACTOR

Simulations with constant network structure factor resulted in a linear stress-strain profile with the exception in the edge grain boundary as shown in Figure 4.67. The network structure factor values used were $1.726 * 10^{-8}$ and $1.726 * 10^{-16}$ for the grain boundary and the bulk material respectively. These corresponded to dislocation density values of $1.931 * 10^{16}$ and $1.433 * 10^{12}$, with the former value in the order of $10^{16}\ m^{-2}$ as proposed by Nakashima et al. [197], and the latter value consistent with results from Kocks [198] where SND were of the order of $10^{12}\ m^{-2}$. These curves provide evidence that yielding is largely dependent on the variation

of the dislocation density within a material. The change in slope observed for the edge grain boundary is related to lattice strengthening associated with grain elongation coupled with refinement of the grain cross-section. It is noted that the 70.52° screw grain boundary shows the lowest gradient alongside that of the edge grain boundary. This is inconsistent with reports of high stresses required to move this dislocation [192].

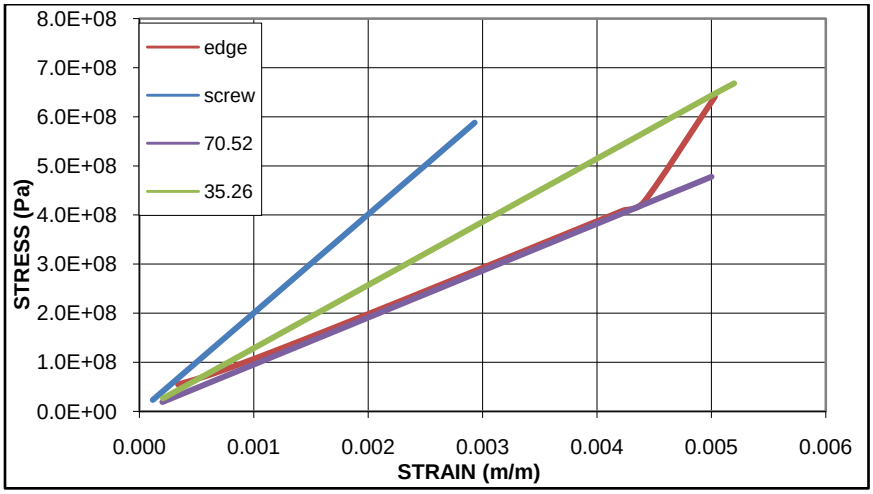

Figure 4.67: Stress-strain profile for constant NSF in the Fe lattice.

The application of trial functions for the variation of the network structure factor in the grain boundary and within the bulk material revealed that a linear dependence occurs within the grain boundary while a geometric series occurs in the bulk of the material. The relations are presented in Equations 4.4 and 4.5 respectively.

$$NSF = NSF_1 + (NSF_2 - NSF_1) * (n_z.\alpha_r)^1 \ldots\ldots\ldots\ldots\ldots\ldots\ldots\ldots\ldots\ldots\ldots\ldots (4.4)$$

$$NSF = NSF_1 * 10^{-\cos(n_z.\alpha_1)^t} \ldots\ldots\ldots\ldots\ldots\ldots\ldots\ldots\ldots\ldots\ldots\ldots (4.5)$$

where:

NSF_1	is the reference NSF
NSF_2	is the final NSF
n_z	is the factor used to increase load from 0 to 100% of target maximum load
α_r	is the cycle amplitude factor

4.5.5. GENERATED STRESS AMPLITUDE PROFILE

Simulations were carried out to determine the stress-strain profile of a strip of Fe loaded in tension in the axial direction. The strip was incrementally loaded from 0.2 kN to 5 kN in 25 equal steps.

Figure 4.68 shows results for simulations for the different grain boundary types. These simulations were carried out for a 12 μm grain size. The curves all reveal that the material yielded at about 0.2% strain, except for the 70.52^o screw grain boundary. The lack of a clear yield point for the 70.52^o screw grain boundary was not explained and it is recommended that this behaviour be studied in future work. The gradient for the curves for all grain boundary (except for the screw grain boundary) at the initial stages is similar. This is consistent with the existence of a single Young's modulus for the material.

It is noted that the curve for the screw grain boundary forms an "S" curve with a gradient greater than the edge and 70.52^o screw grain boundary structures. The higher gradient is indicative of the need for larger applied loads for deformation to occur driven by this grain boundary type, which is consistent with the lower mobility of the screw dislocation with respect to the edge dislocation as reported by Imura et al. [118].

The 35.26^o screw grain boundary also forms an "S" curve, with an initial yield stress greater than that of the edge and 70.52^o screw grain boundary. This is in contrast to expectations as the POLR stress for the 70.52^o screw dislocation is consistently higher than that of the 35.26^o screw dislocation. This behaviour is attributed to the higher values of the stress components at the point where the peak stress POLR value is obtained. It implies that the material lattice containing critical stage 35.26^o screw grain boundary requires a larger applied stress for yielding to occur. In addition, the 35.26^o screw grain boundary demonstrates some strain reversal during yielding. This is not expected as in the limit, strain increases at constant stress. The explanation for this observation is that the grain experiences negative internal strain as dislocations are nucleated within an existing grain boundary. It is recommended that the nature of this rearrangement be studied in future work.

The edge grain boundary yields at extended strain levels in comparison to the pure screw and 35.26^{o} screw grain boundary. This implies that extensive movement within the edge G.B may occur without material yielding. This is consistent with the evidence of the high mobility of edge dislocations as reported by Imura et al. [118].

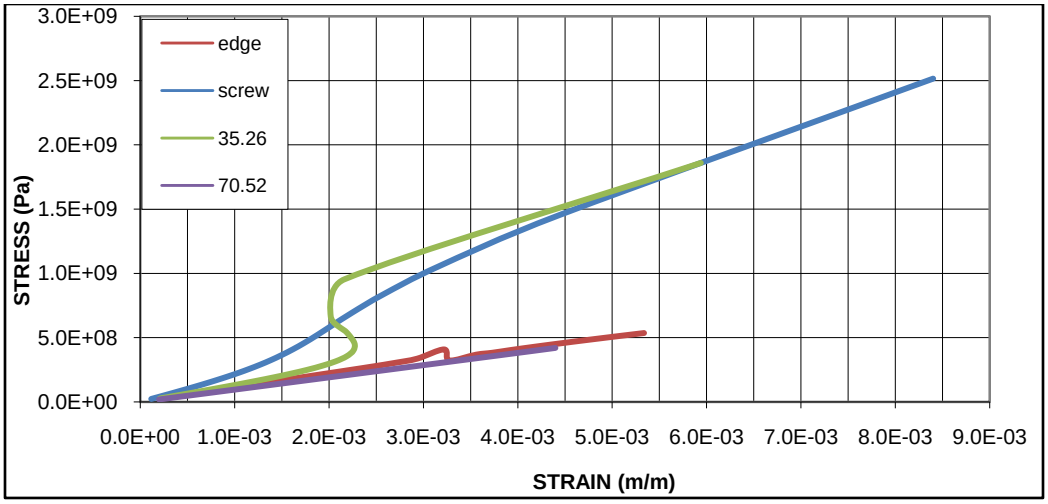

Figure 4.68: Stress-strain profile for variable dislocation density in the Fe lattice: α=0.8 (Ref. NSF =1.726E-8 m^{-2}).

Table 4.34: Yield stress for the various Grain boundary types.

Dislocation Type (in Fe lattice)	Limit of elasticity (MPa)	$\sigma_{y-upper}$ (MPa)	$\sigma_{y-lower}$ (MPa)
Edge	170	409	323
Screw	–	–	–
36.26^{o} screw	80.6	–	–
70.52^{o} screw	167	–	–

The yield stresses are presented in Table 4.34. The limit of elasticity represents the critical network structure factor beyond which the changes caused appreciable changes to the strength of the lattice. No limit of elasticity was recorded for the screw grain boundary, and the continuously changing gradient was an indication that this structure varied continuously as load was increased.

These simulations were repeated for an initial network structure factor of $1.726*10^{-10}$ for the grain boundary and $1.726*10^{-16}$ for the bulk material. The results are shown in Figure 4.69 and reveal that a change in the reference network structure factor up to an order of magnitude of 10^{-6} did not appreciably alter the behaviour of the material.

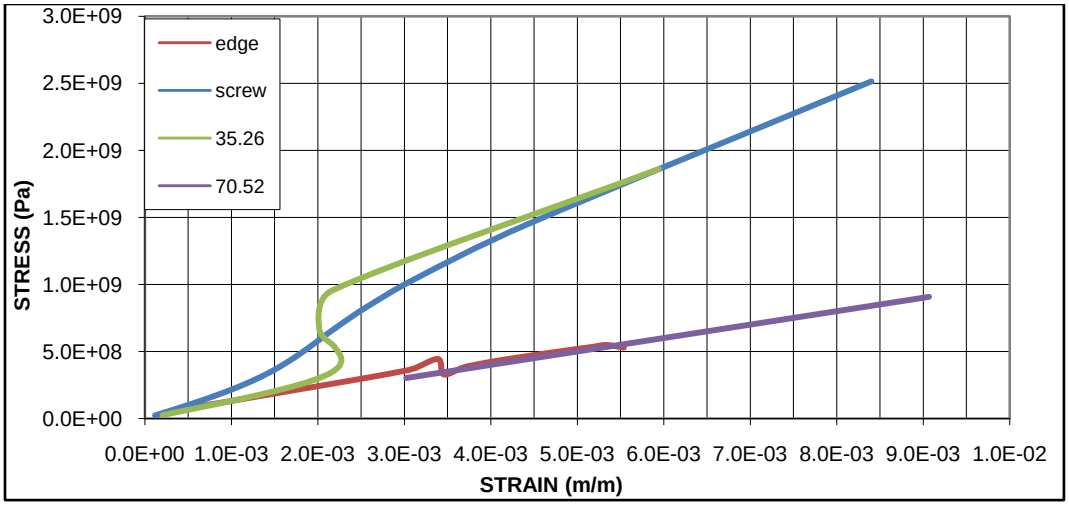

Figure 4.69: Stress-strain profile for variable dislocation density in the Fe lattice: α=0.8 (Ref. NSF =1.726E-10 m^{-2}).

The simulations were then repeated for a value of $a = 0.9$. The resulting curves are shown in Figures 4.70 and 4.71, and reveal that the mixed dislocation type grain boundaries do not exhibit any yielding for the range analysed. For the 35.26^{o} screw grain boundary, this is significantly different from results presented for $a = 0.8$. This difference is attributed to distortion errors from the shape of the 24 node serendipity finite element and it is inferred that the $\alpha = 0.9$ form should not be used for further analysis.

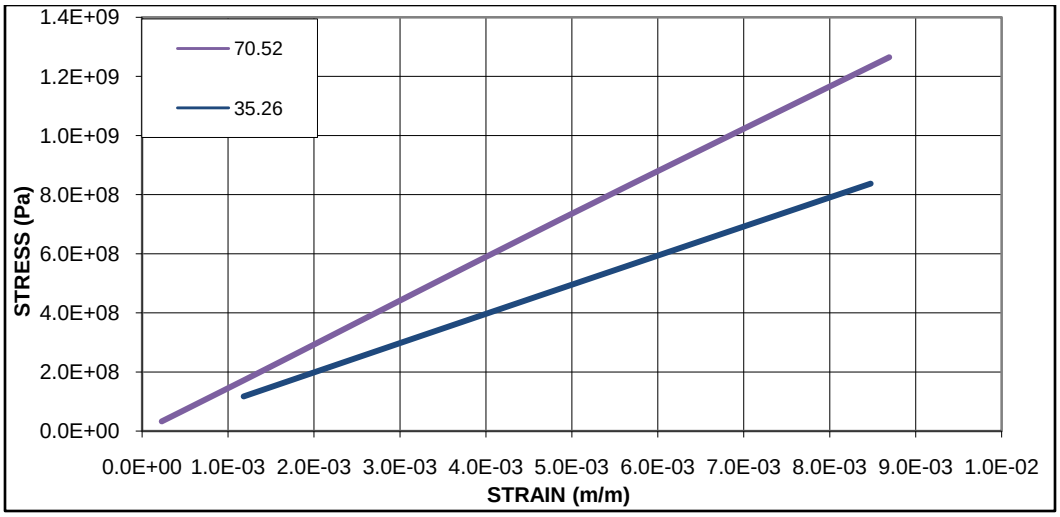

Figure 4.70: Stress-strain profile for variable dislocation density in the Fe lattice: 35.26^{o} & 70.52^{o} screw dislocations: α=0.9 (Ref. NSF =1.726E-8 m^{-2}).

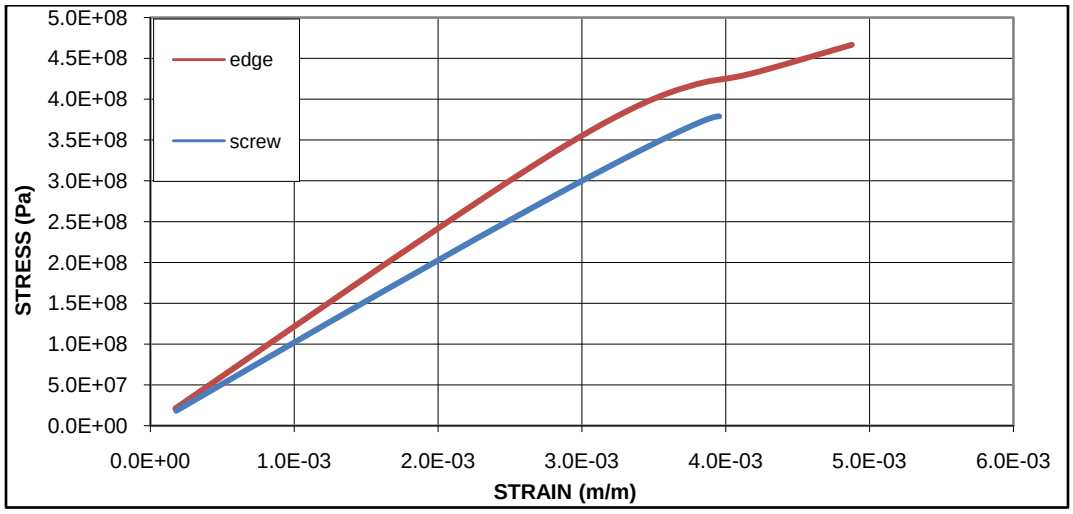

Figure 4.71: Stress-strain profile for variable dislocation density in the Fe lattice: edge & screw dislocations: α=0.9 (Ref. NSF =1.726E-8 m^{-2}).

The curves for the edge and screw grain boundary shown on Figure 4.71 each possess a limit of proportionality though this is more pronounced for the edge grain boundary. The curves for the edge grain boundary however possess a higher gradient that implies that the modification of this structure at critical stress levels would require a higher applied stress. This is in contrast with earlier results that show that the individual edge dislocation requires lower stresses for motion.

4.6. VALIDATION OF THE MODELS

4.6.1. MESO-SCALE MODEL

The meso-scale model characterized the behaviour of the lattice as a result of the evolution of grains. The model was used to predict the yield stress of the material at various grain sizes. The variation of the yield stress with grain size was plotted and the resulting curves compared with empirical results by other researchers [170].

Figure 4.72 shows results of the variation of the yield stress with the inverse of the square root of the characteristic grain size for edge grain boundary. The yield stress from the meso-scale simulations compares reasonably with the work by Fu, Benson and Meyers [170] and Hall and Petch [165, 166] for the range analyzed. The curve of best fit from data generated in this work is a linear fit given by the relation $\tau_y = ({D_g}^{-0.5} - 4*)10^9$ which slightly understates the yield stress at larger grain sizes.

where:

τ_y Yield stress (Pa)

D_g Diameter of grain (m)

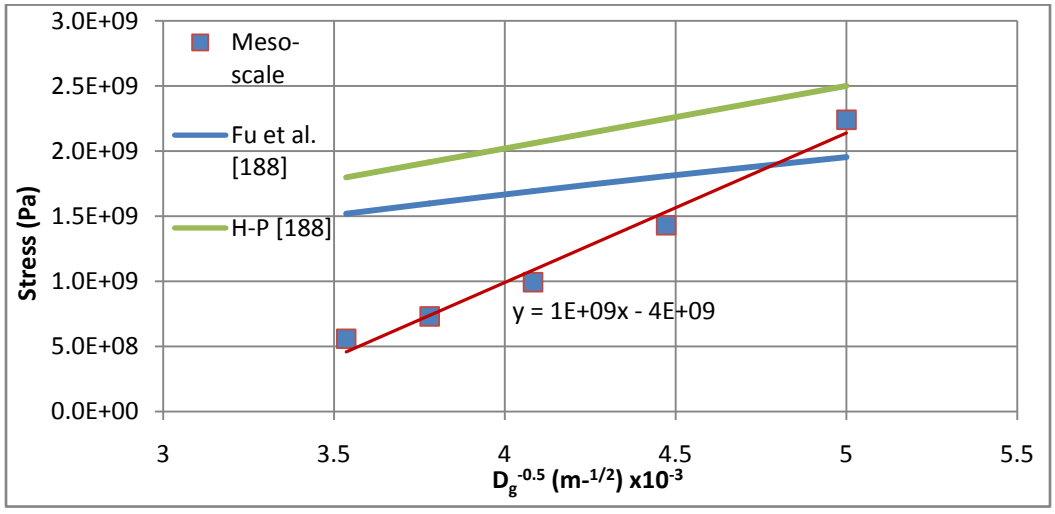

Figure 4.72: Yield stress v/s $D_g^{-0.5}$ curve for Grain boundary formed from edge dislocation structures, and α=0.8, in Fe.

Figure 4.73 shows results of the variation of the yield stress with the inverse of the square root of the characteristic grain size for screw grain boundary. Again, the yield stress from the meso-scale simulations compares reasonably with the work by Fu, Benson and Meyers [170] and Hall and Petch [165, 166] for the range analyzed. The curve of best fit from data generated in this work is a linear fit given by the relation $\tau_y = (D_g - 5) * 10^9$ which has the same gradient as that of the edge grain boundary.

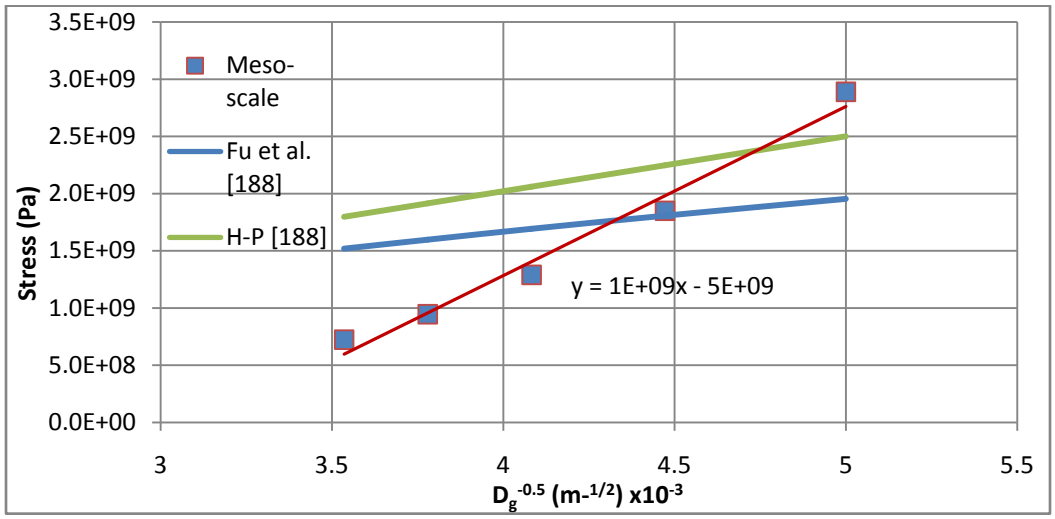

Figure 4.73: Yield stress v/s $D_g^{-0.5}$ curve for Grain boundary formed from screw dislocation structures, and α=0.8, in Fe.

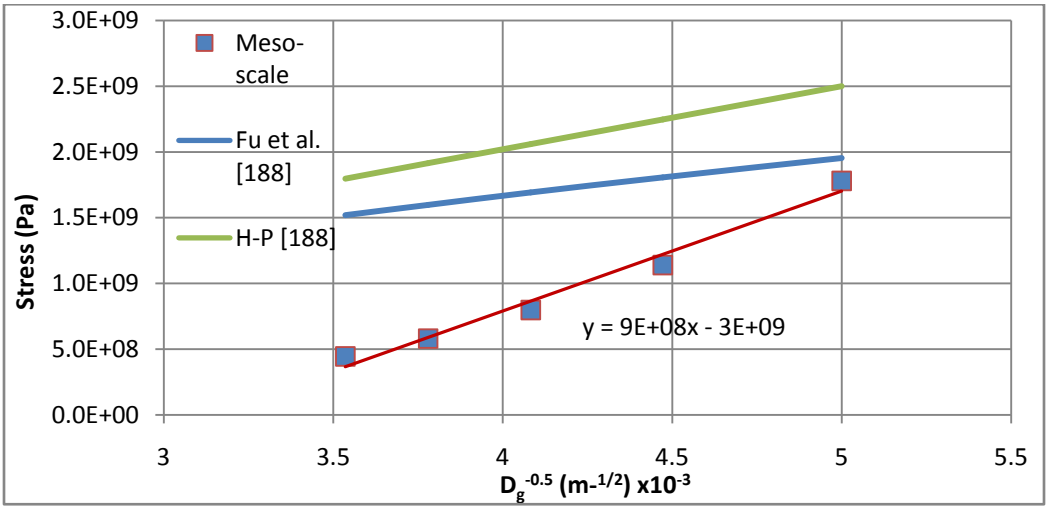

Figure 4.74: Yield stress v/s $D_g^{-0.5}$ curve for Grain boundary formed from 35.26^o screw dislocation structures, and α=0.8, in Fe.

The results for grain boundaries formed from 35.26° screw and the 70.52° screw dislocation structures are shown in Figures 4.74 and 4.75 respectively. Both results compare reasonably with the work by Fu, Benson and Meyers [170] and Hall and Petch [165, 166] for the range analyzed. The curves of best fit from data generated in this work are linear fits given by the relations $\tau_y = (0.9 * D_g - 3) * 10^9$ and $\tau_y = (2 * D_g - 6) * 10^9$ respectively. The gradient of the curve for the 35.26° screw grain boundary is the lowest suggesting this structure is the least affected by refinement of grain size.

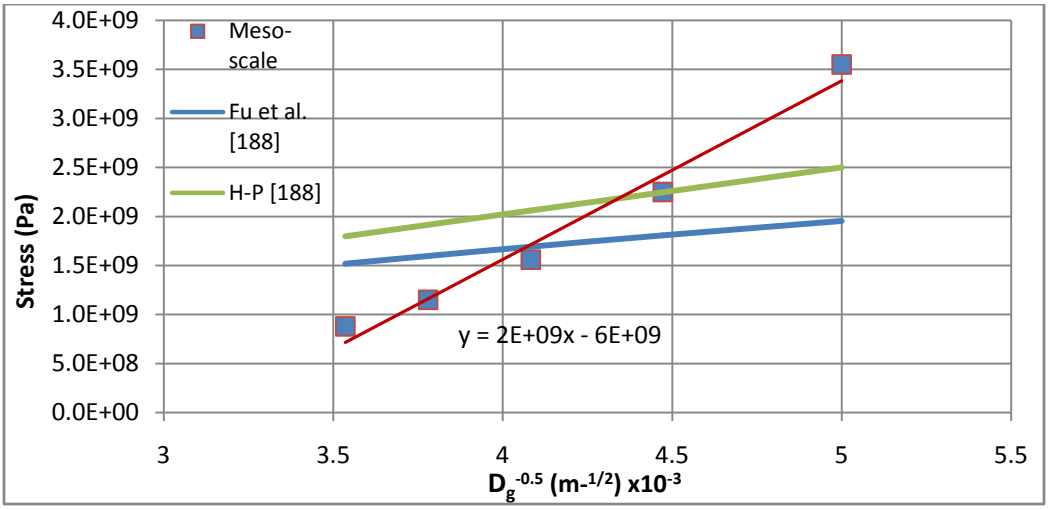

Figure 4.75: Yield stress v/s $D_g^{-0.5}$ curve for Grain boundary formed from 70.52° screw dislocation structures, and α=0.8, in Fe.

The Hall-Petch [199] relationship has been explained as due to dislocation pile-up formed at grain boundary. The alternative explanation is that pile-ups activated sources in neighbouring grains. In this work, variation of the dislocation density (and hence dislocation sources) has been allowed. Additionally, this model serves to intensify the contribution of stresses along the grain boundary, consistent with work by Meyers and Ashworth [167] that demonstrated that stress intensification occurred in the vicinity of the grain boundary. It is also noteworthy that the Hall-Petch relationship has been demonstrated for yield stresses values in order of 1 GPa to 3 GPa [170], and the stresses published in this work are in the same order of magnitude. It is concluded that the meso-scale model is consistent in its implementation and in the results generated, with empirical work [167, 170].

4.6.2. USE OF DIRECT STRESS AMPLITUDES IN LINKING THE POLR TO THE PEIERL'S STRESS

It is understood that the Peierl's stress is a shear stress [101]. However, in this work, the direct stresses that describe the POLR are related to the Peierl's stress based on the following rational. The stresses considered are those that act on an atom located at a given lattice point. At this level of resolution, the direct stresses are responsible for the displacement of the atom away from this site. However, the shear stresses cannot be considered to shear the atom at this site as this model retains the atom as an indivisible particle. Instead, shear stresses would give rise to rotational torques on the atom at the lattice site. The movement of a dislocation line is concerned with the displacement of atoms forming the dislocation core, and as a result the linking of the Peierl's stress to the direct stresses is consistent with the physics of the problem.

Comparisons were made with shear stress-strain profiles based on Tresca's and von Mises yield criteria [200]. These profiles are shown in Figures 4.74 and 4.75 for the edge and screw dislocations respectively. In these figures τ_1, τ_2 and τ_3 are derived from Tresca's yield criterion while τ_4 is derived from von Mises yield criteria. The yield stresses are obtained from the Equations 4.6 and 4.7 for these criteria respectively [200]:

$$\tau_y = \frac{1}{2}(\sigma_{m1} - \sigma_{m3}) \dots\dots\dots\dots\dots\dots\dots\dots\dots\dots\dots\dots\dots\dots\dots\dots\dots\dots\dots\dots\dots\dots\dots\dots\dots\dots\dots\dots\dots\dots\dots\dots\dots\dots\dots\dots\dots\dots. (4.6)$$

where:

τ_y	is the yield stress
σ_{m1}	is the maximum principle stress in the lattice
σ_{m2}	is the intermediate value principle stress in the lattice
σ_{m3}	is the minimum principle stress in the lattice

$$\tau_y = 0.471 * [0.5 * \{({\sigma_{m1}}^2 - {\sigma_{m2}}^2) + ({\sigma_{m2}}^2 - {\sigma_{m3}}^2) + ({\sigma_{m1}}^2 - {\sigma_{m3}}^2)\}]^{1/2} \dots\dots\dots. (4.7)$$

From Tresca's and von Mises yield criteria, yielding is related to the maximum shear stress in the material as obtained from the separate equations. From Figure 4.74 and 4.75, the yield stress

(based on the various yield criteria) from the simulations are all above 10 GPa which does not compare well with published values of Peierl's stress of 1.2 GPa - 1.8 GPa by Chaussidon et al. [181] and 1.3 GPa - 1.9 GPa by Ventelon [191] for BCC Fe. Additionally, at the onset of this study, it was noted that the stress amplitude and not the actual stress was correlated with the Peierl's stress through the POLR. Consequently, it is concluded that Tresca's and von Mises yield criteria do not hold at the degree of resolution corresponding to the dislocation line length scale, and the use of direct stresses in the definition of the criterion for dislocation core atom motion is reasonable.

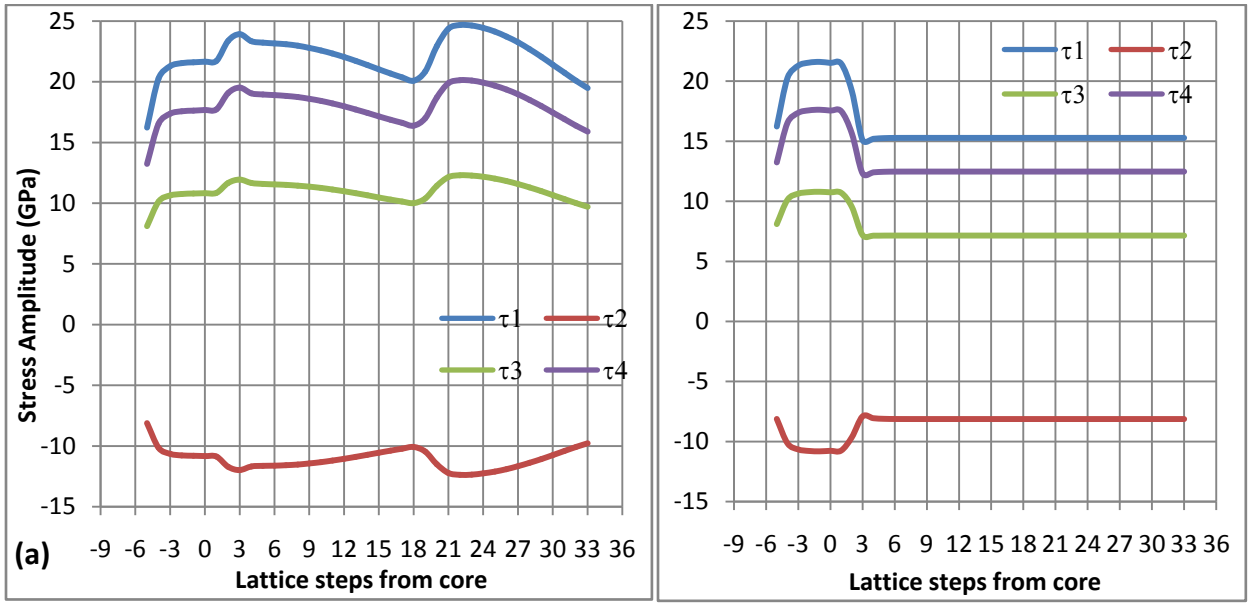

Figure 4.76: Yield stress amplitude profile for the (a) edge, (b) screw, dislocations with misfit in Fe, based on Tresca's and von Mises criteria.
(τ_1, τ_2 and τ_3 : Tresca's criterion; τ_4 : Mises criteria)

CHAPTER 5: CONCLUSIONS AND RECOMMENDATIONS

5.1. CONCLUSIONS

This research set out to develop a multi-scale method that incorporates dislocation evolution to predict meso-scale plasticity. The hierarchy of models developed captured the contributions of various processes at the appropriate length scales, resulting in a dislocation based multi-scale material formulation with a more sound physical foundation. The development, application and the linking of the models has been demonstrated. The following conclusions are made from this study:

i. Dislocation motion occurs by the "peeling" of atoms around the core by contributions of $\langle 100 \rangle$ motion of atoms, for all dislocation types, with the dislocation line in the $[\bar{1}1\bar{1}]$ direction.

ii. Combinations of direct stress tensor components could be used to explain dislocation core evolution.

iii. The dislocation core model gave rise to the "path of least resistance" (POLR) concept. The characteristic POLR stress is related to the Peierl's stress.

iv. The Peierl's stress is related to the contribution of dislocation core stress components where "rigid body motion" (RBM) is implemented and to the dislocation core resultant stress where "free motion of dislocation core atoms" (FMDCA) is implemented.

v. The characteristic peak POLR stresses could be used to transfer dislocation core length-scale data to the dislocation line length-scale.

vi. The dislocation line model gave rise to the misfit potential (MP). The MP could be used to account for the long range stress profile (at displacements outside the capability of the embedded atom method (EAM)) arising from the dislocation core.

vii. The long range dislocation stress profiles arising from the use of the MP could be used in the characterization of long range interaction between dislocations.

viii. The dislocation core induces a cyclic stress field with a wavelength of several Burger's vectors along a line normal to the dislocation line and within the slip plane. The cyclic nature is absent along the dislocation line.

ix. The two dimensional dislocation structure model gave rise to the plane structure factor (PSF). The PSF suitably characterizes the extended stress amplitude profile (obtained using the MP) around interacting dislocation lines and their spatial locations.

x. The PSF is related to the planar dislocation density. A characterising function has been presented.

xi. Interacting dislocation dipoles produce a stress amplitude hump with a base width of five lattice vectors over the slipped surface, with one end of the hump at the reference dislocation core.

xii. The three dimensional dislocation structure model gave rise to the network structure factor (NSF). The NSF suitably characterises the PSF data and the spatial locations of slip planes.

xiii. The NSF is related to the network dislocation density. A characterising function has been presented.

xiv. Stress intensification due to interacting slip planes containing dislocations is in the neighbourhood of these slip planes.

xv. Five lattice steps is the critical spacing (between interacting slip planes) at which stress amplitude peak values are stabilized, and stress amplitude hump symmetry is established.

xvi. The peeling mechanism is aided by the reduction in separation between slip planes containing dislocation dipoles.

xvii. The POLR concept does not apply across slip planes.

xviii. The NSF could be used to transfer mechanistic information to the meso-scale.

xix. A linear and power law dislocation density variation exists for the grain boundary and the bulk of the grain respectively.

xx. The meso-scale model is consistent in its implementation and in the results generated, with empirical work. Specifically, its capability to predict the yield stress of the material at different grain sizes compares well with empirical work.

xxi. Tresca's and Von Mises yield criteria do not hold at the degree of resolution corresponding to the dislocation line length scale.

5.2. RECOMMENDATIONS

The following recommendations are made from this study:

i. A database of Peierl's stress data for different types of dislocations in different lattice configurations (in this case a variation of the carbon content), under different loading conditions should be developed. This would aid the validation of the POLR model. The use of well-tested molecular dynamics code to generate this database would overcome the limitations encountered in undertaking experimental work (cost, availability of equipment, control of microstructure).

ii. The effect of carbon on screw dislocation reconstruction defects in Fe should be investigated further. This would establish concentrations of carbon at which the relative stability of reconstruction defects is reversed.

iii. Future research work should be carried out to empirically establish the distortion of the lattice in the extended neighbourhood of the dislocation core. This would aid the correlation of the MP.

iv. An EAM potential with a greater sensitivity to distortions should be developed to enhance the capability of the MP.

v. The wavelength of the cyclic stress field in the lattice due to the dislocation core should be studied further. This would aid the correlation of the MP.

vi. Future work should be carried out to compare the resultant stress field as determined by the PSF and NSF models, and that obtained by the super-positioning of stress fields determined empirically. This would provide additional collaboration of these models.

vii. A greater variety of dislocation combinations should be studied using the PSF model including structures containing dislocation quadruples, dislocation kinks and dislocation junctions. This would yield a larger database of PSF data for 2-D dislocation structures which would be used in modelling complex 3-D dislocation structures.

viii. Further studies on slip planes containing edge dislocation dipoles should be carried out to establish the spacing at which stress peak values stabilize as it was noted that the increase in spacing between these slip planes resulted in an increase in stress peaks.

ix. The yield behaviour of the 70.52^{o} screw grain boundary should be investigated further as it was noted that this dislocation structure does not yield at 0.2% strain, in contrast to the other dislocation structure types.

x. Strain reversal during yielding of the 35.26^{o} screw grain boundary should be studied in future work as it was noted that this grain structure experienced negative internal strain as dislocations were nucleated within an existing grain boundary..

xi. Empirical work should be carried out using micro-indentation tests to generate deformation stress data, coupled with X-ray line profile measurement of the resulting dislocation content, to enable further correlation of the NSF with dislocation density.

REFERENCES

1. D.L. McDowell, C.N. Paden Jr. Future Research Trends In Metal Plasticity For Simulation of Metals Processing and Life Cycle Analysis. Georgia Institute of Technology, USA. 2004.
2. D. Walgraef, E. C. Aifantis. On the Formation and Stability of Dislocation Patterns. III. Three Dimensional Considerations. International Journal of Engineering Science. 1985, Vol. 23, pp. 1365-1372.
3. L.P. Kubin, G. Canova. Modelling of Dislocation Patterns. Scripta Metallurgica et Materialia. 1992, Vol. 27, pp. 957-962.
4. E.C. Aifantis. Pattern Formation in Plasticity. International Journal of Engineering Science. 1995, Vol. 33, pp. 2161-2178.
5. M. Glazov, L.M. Glanes, C. Liard. Self Organised Dislocation Structures (SODS) in Fatigue of Metals. Physical Status Solida A. 1999, Vol. 149, pp. 297-321.
6. M. Zaiser, E.C. Aifantis. Material Instabilities and Deformation Patterning in Plasticity. Recent Research Developments in Metallurgical & Materials Sciences. 1999, Vol. 3, pp. 79-103.
7. L. Bortoloni, P. Cermelli. Statistically Stored Dislocations in Rate-Independent Plasticity. Rend Sem Mathematica. 2000, Vol. 58, pp. 25-36.
8. M. Zaiser, M.C. Miguel, I. Groma. Statistical Dynamics of Dislocation Systems: The Influence of Dislocation-Dislocation Correlations. Physical Review B. 2001, Vol. 64, pp. 4102-4110.
9. Van der Gissen, A. Needleman. Discrete Dislocation Plasticity: A Simple Planar Model. Model Simulation Material Science Engineering. 1995, Vol. 3, pp. 689-735.
10. V.V. Bulatov, W. Cai. Nodal Effects on Dislocation Mobility. Physical Review Letters. 2002, Vol. 89, pp. 5501-5504.
11. M.S. Daw, M.I. Baskes. Embedded Atom Method: Derivation and Applications to Impurities, Surfaces, and Other Defects in Metals. Physical Review B. 1984, Vol. 29, pp. 6443-6453.
12. P. Gumsch. An Atomistic Study of Brittle Fracture: Towards Explicit Failure Criteria From Atomistic Modelling. Journal of Materials Research. 1995, Vol. 10, pp. 2897-2907.

13. J.P. Hirth, M. Rees, H. Zbib. Modeling of Deformation by a 3D Simulation of Multiple Curved Dislocations. Journal of Computer Aided Materials Design. 1996, Vol. 3, pp. 164-166.
14. F.F. Abraham, J.Q. Broughton, N. Bernstein, E. Kaxiras. Spanning the Length Scales in Dynamic Simulation. Computers in Physics. 1998, Vol. 12, pp. 538-546.
15. V. Shenoy, R. Miller, E.B. Tadmor, D. Rodney, R. Philips, M. Oritz. An Adaptive Methodology for Atomic Scale Mechanics - The Quasi Continuum Method. Journal of Mechanical Physical Solutions. 1999, Vol. 47, pp. 611-642.
16. F.F. Abraham, J.Q. Broughton, N. Bernstein, D. Hess. Dynamic Fracture of Silicon: Concurrent Simulation of Quantum Electrons, Classical Atoms and the Continuum Solid. MRS Bulletin. 2000, Vol. 25, pp. 27-32.
17. V. Kouznetsova, M.G.D. Geers, W.A.M. Brekelmans. Multi-Scale Modelling of Heterogenous Materials with a Gradient Enhanced Computational Homogenization Scheme. International Journal for Numerical Methods in Engineering. 2002, Vol. 54, pp. 1235-1260.
18. F. Feyel, J.L. Chaboche. F.E. Multi-scale Approach for Modelling the Elasto-Viscoplastic Behaviour of Long Fibre SiC/Ti Composite Materials. Computer Methods in Applied Mechanics and Engineering. 2000, Vol. 183, pp. 417-455.
19. J. Fish, K. Sheck, M. Pandheeradi, M.S. Shepard. Computational Plasticity for Composite Structures Based on Mathematical Homogenization: Theory and Practice. Computational Methods in Applied Mechanics and Engineering. 1997, Vol. 148, pp. 53-73.
20. J.T. Oden, K. Vemaganti, N. Mos. Hierarchal Modeling of Heterogenous Solids. Computer Methods in Applied Mechanics and Engineering. 1999, Vol. 172, pp. 2-25.
21. R.J.M. Smit, W.A.M. Bekelmans, H.E.H. Meijer. Prediction of Mechanical Behavior of Non-linear Heterogenous Systems by Multi-level Finite Element Modeling. Computer Methods in Applied Mechanics and Engineering. 1998, Vol. 155, pp. 181-192.
22. T.I. Zohdi, J.T. Oden, G.J. Rodin. Hierarchial Modeling of Heterogenous Bodies. Computer Methods in Applied Mechanics and Engineering. 1996, Vol. 138, pp. 273-298.
23. H. Ben Dhia. Multi-scale Mechanical Problems: The Arlequin Method. C.R. Academy of Science. 1998, pp. 899-904.

24. E. Van der Gissen, A. Needleman. Discrete Dislocation Plasticity: A Simple Planar Model. Model Simulation Material Science Engineering. 1995, Vol. 3, pp. 689-735.
25. M.P. O'Day, W.A. Curtin. A Superposition Technique for Discrete Dislocation Plasticity. Journal of Applied Mechanics. 2005, Vol. 71, pp. 805-815.
26. H.M. Zbib, M. Shehadeh, S.M.A. Khan, G. Karami. Multi-scale Dislocation Dynamics Plasticity. International Journal for Multiscale Computational Engineering. 2002, Vol. 1, pp. 74-90.
27. J.Q. Broughton, F.F. Abraham, N. Bernstein, E. Kaxiras. Concurrent Coupling of Length Scales: Methodology and Applications. Physical Review B. 1999, Vol. 60, pp. 2391-2403.
28. H.S. Park, E.G. Karpov, W.K. Lui, P.A. Klein. The Bridging Scale Method for Two-dimensional Atomistic/Continuum Coupling. Philosophical Magazine. 2005, Vol. 85, pp. 79-113.
29. S. Hao, W.K. Lui, B. Moran, F. Vernerey, G.B. Olson. Multi-scale Constitutive Model and Computational Framework for the Design of Ultra-High Strength, High Toughness Steels. Computational Methods in Applied Mechanical Engineering. 2004, Vol. 193, pp. 1865-1908.
30. D.E. Spearot, K.I. Jacob, D.L. McDowell. Nucleation of Dislocations from [001] Bicrystal Interfaces in Aluminum. Acta Materialia. 2005, Vol. 53, pp. 3579-3589.
31. K.D. Njoroge. An Intrinsic Discrete Dislocation - Finite Element Formulation of Metal Plasticity. Department of Mechanical and Manufacturing Engineering, M.Sc. Thesis, University of Nairobi. 2008.
32. D. Gomez-Garcia, B. Devincre, L. Kubin. Dislocation Dynamics in Confined Geometry. Journal of Computer-Aided Materials Design. 1992, Vol. 6, pp. 157-164.
33. R. Madec, B. Devincre, L. Kubin. On the Use of Periodic Boundary Conditions in Dislocation Dynamics Simulations. DPTA Commissariat a l'Energie Atomique. 2002. pp. 1-10.
34. J.P. Hirth, J. Lothe. Theory of Dislocations. 2nd Ed: John Wiley & Sons, 1982.
35. M.S. Duesbery, V. Vitek. Plastic Anisotrophy in BCC Transition Metals. Acta Matallurgica. 1998, Vol. 46, pp. 1481-1492.
36. K. Ito, V. Vitek. Atomistic Study of Non-Schmid Effects in the Plastic Yielding of BCC Metals. Philosophical Magazine A. 2001, Vol. 81, pp. 1387-1407.

37. W. Xu, J. Moriarty. Accurate Atomistic Simulations of the Peierl's Barrier and Kink-Pair Formation Energy for <111> Screw Dislocations in BCC Mo. Computational Material Science. 1989, Vol. 9, pp. 348-356.
38. D.R. Mason, W.M.C. Foulkes, A.P. Sutton. A Simple Model for Large-scale Simulations of FCC Metals with Explicit Treatment of Electrons. Philosophical Magazine Letters. 2010, Vol. 90, pp. 51-60.
39. L. Malerba, G.J. Ackland, C.S. Becquart, G. Bonny, C. Domain, S.L. Dudarev, C.C. Fu, D. Hepburn, M.C. Marinica, P. Olsson, R.C. Pasianot, J.M. Raulot, F. Soisson, D. Terentyev, E. Vincent, F. Willaim. Ab initio Calculations and Interatomic Potentials for Iron and Iron Alloys: Achievements within the Perfect Project. Journal of Nuclear Materials. 2010, Vol. 406, pp. 7-18.
40. D.P. Landau, K. Binder. A Guide to Monte Carlo Simulations in Statistical Physics. Cambridge : Cambridge University Press, 2000.
41. D. Frenkel, B. Smit. Understanding Molecular Simulation: From Algorithms to Applications. San Diego : Academic Press, 2002.
42. M.W. Finnis, J.E. Sinclair. A Simple Empirical N-body Potential for Transition Metals. Philosophical Magazine A. 1984, Vol. 50, pp. 45-55.
43. J.K. Norskov. Covalent Effects in the Effective Medium Theory of Chemical Binding: Hydrogen Heats of Solution in 3D Metals. Physical Review B. 1982, Vol. 26, pp. 2875-2885.
44. D.G. Pettifor. Bonding and Structure of Molecules and Solids. Oxford : Clarendon Press, 1995.
45. F. Ercolessi, M. Parrinello, E. Tosatti. Simulation of Gold In The Glue Model. Philosophical Magazine A. 1988, Vol. 58, pp. 213-226.
46. M.I. Mendelev, S. Han, D.J. Srolovitz, G.J. Ackland, D.Y. Sun, M. Asta. Development of Interatomic Potentials Appropriate for Crystalline and Liquid Iron. Philosophical Magazine. 2003, Vol. 83, pp. 3977-3994.
47. M.J. Scott, E. Zaremba. Quasiatoms: An Approach to Atoms in Non-uniform Electronic Systems. Physical Review B. 1980, Vol. 22, pp. 1564.
48. G. Wu, G. Lu, C.J.G. Cervera, E. Weinan. Density-Gradient Corrected Embedded Atom Method. Physical Review B. 2009, Vol. 79, pp. 1-8.

49. M.J. Puska, R.M. Nieminen, M. Manninen. Atom Embedding in an Electron Gas: Immersion Energies. Physical Review B. 1981, Vol. 24, pp. 3037-3047.
50. G. Bonny, R.C. Pasianot, L. Malerba,. Fitting Interatomic Potentials Consistent with Thermodynamics: Fe, Cu, Ni and their Alloys. Philosophical Magazine. 2009, Vol. 89, pp. 3451-3464.
51. M.P. Puls. Proceedings of "The Structure and Properties of Crystal Defects". Liblice, 1983. Proceedings of the Symposium on the Structure and Property of Crystal Defects.
52. W. Skrotzki, P. Hassen. Hardening Mechanisms of Ionic Crystals on {110} and {100} Slip Planes. Journal Physical Science. 1981, Vol. 42, pp. 119-148.
53. D.J. Bacon. The Structure and Property of Crystal Defects. Liblice, 1983. Proceedings of the Symposium on the Structure and Property of Crystal Defects.
54. T. Bretheau, J. Castaing, J. Rabier, P. Veyssiere. Dislocation Motion and High Temperature Plasticity of Binary and Ternary Oxides. Advances in Physics. 1979, Vol. 28, pp. 835-1014.
55. F.R.N. Nabarro. Dislocations in Simple Cubic Lattice. Proceedings of the Physical Society. 1947, Vol. 59, pp. 256-272.
56. R. Bullough, V.K. Tewary. Dislocations in Solids. [ed.] . F.R. Nabarro. Amsterdam : Elsever Science B. V., 1979. Vol. 2. pp. 1.
57. M.P. Puls. Dislocation Modeling of Physical Systems. [ed.] R. Bullough, G.S. Hartley, J.P. Hirth, M.F. Ashby. New York : Pergamon Press, 1981. pp. 249.
58. A.H. Cottrell, B.A. Bilby. A Mechanism for the Growth of Deformation Twins in Crystals. Philosophical Magazine Series 7. 1951, Vol. 42, pp. 573-581.
59. J.B. Cohen, R. Hinton, K. Lay, S. Sass. Partial Dislocations on the {110} Planes in the BCC Lattice. Acta Metallurgica. 1962, Vol. 10, pp. 894-895.
60. C. Woodward, S.I. Rao,. Flexible Ab Initio Boundary Conditions: Simulating Isolated Dislocations in BCC Mo & Ta. Physical Review Letters. 2002, Vol. 88, pp. 6402-6405.
61. M.S. Daw, S.M. Foiles, M.I. Baskes. The Embedded-Atom Method: A Review of Theory and Applications. Materials Science Reports. 1993, Vol. 9, pp. 251-310.
62. G.J. Ackland, M.I. Mendelev, D.J. Srolovitz, S. Han, A.V. Barashev. Developement of Interatomic Potential for Phosphorous Impurities in alpha-Iron. Journal of Physics: Condensed Matter. 2004, Vol. 16, pp. S2629.

63. K. Masuda, A. Sato. Electronic Theory of Screw Dislocation Motion in Dilute BCC Transition Metal Alloys. Philosophical Magazine A. 1981, Vol. 44, pp. 799-814.
64. E. Clementi, C. Roetti. Atomic Data and Nuclear Data Tables. New York : Academic Press, 1974. Vol. 14.
65. V. Sahni. Quantal Density Functional Theory. Springer-Verlag, 2004. pp. 86.
66. S.M. Foiles, M.I. Baskes, M.S. Daw. Embedded Atom Method Functions for the FCC Metals Cu, Ag, Au, Ni, Pd, Pt and their Alloys. Physical Review B. 1986, Vol. 33, pp. 7983-7991.
67. R.A. Johnson, D.J. Oh. Analytic Embedded Atom Method for BCC Metals. Journal of Material Research. 1989, Vol. 4, pp. 1195-1201.
68. R. Pasainot, D. Farkas, E.J. Savino. Empirical Many-body Interatomic Potential for BCC Transition Metals. Physical Review B. 1991, Vol. 43, pp. 6952-6961.
69. E.H. Lieb. Thomas-Fermi and Related Theories of Atoms and MolecuLes. Reviews of Modern Physics. 1981, Vol. 53, pp. 603-641.
70. M.I. Baskes. Modified Embedded-Atom Potentials for Cubic Materials and Impurities. Physical Review B. 1992, Vol. 46, pp. 2727-2742.
71. M.I. Baskes, J.S. Nelson, A.F. Wright. Semi-empirical Modified Embedded Atom Potentials for Silicon and Germanium. Physical Review B. 1989, Vol. 40, pp. 6085-6100.
72. A. Banerjea, J.R. Smith. Origins of the Universal Binding-Energy relation. Physical Review B. 1988, Vol. 37, pp. 6632-6645.
73. G.J. Ackland, D.J. Bacon, A.F. Calder, T. Harry. Computer Simulation of Point Defect Properties in Dilute Fe-Cu Alloy using a Many-body Interatomic Potential. Philosophical Magazine A. 1997, Vol. 75, pp. 713-732.
74. J.P. Biersack, J.F. Ziegler. Refined Universal Potentials in Atomic Collisions. Nuclear Instrument and Methods in Physics Research. 1982, Vol. 141, pp. 93-100.
75. A. Caro, D.A. Crowson, M. Caro. Classical Many-Body Potential for Concentrated Alloys and the Inversion of Order in Chromium Alloys. Physical Review Letters. 2005, Vol. 95, pp. 1-4.
76. J. Wallenius, P. Olsson, C. Lagerstedt, N. Sandberg, R. Chakarova, V. Pontikis. Modelling of Chromium Precipitation in Fe-Cr Alloys. Physical Review B. 2004, Vol. 69, pp. 094103.

77. D.J. Hepburn, G.J. Ackland. Metallic Covalent Interatomic Potential for Carbon in Iron. Physical Review B. 2008, Vol. 78, pp. 1-6.
78. S. Erkoc. Empirical Many-Body Potential Energy Functions used in Computer Simulations of Condensed Matter Properties. Physics Reports. 1997, Vol. 278, pp. 79-105.
79. H.E. Schaefer, K. Maier, M. Weller, D. Herlach, A. Seeger, J. Diehl. Vacancy Formation in Iron Investigated by Positron Annihilation in Thermal Equilibrium. Scripta Mettalurgica. 1977, Vol. 11, pp. 803-809.
80. A. Vehanen, P. Hautojarvi, J. Johansson, J. Yli-Kauppila, P. Moser. Vacancies and Carbon Impurities in Alpha Iron: Electron Irradiation. Physical Review B. 1982, Vol. 25, pp. 762-780.
81. C.J. Forst, J. Slyeke, K.J.V. Vliet, S. Yip. Point Defect Concentrations in Metastable Fe-C Alloys. Physical Review Letters. 2006, Vol. 96, pp. 1-4.
82. T.T. Lau, C.J. Forst, X. Lin, J.D. Gale, S. Yip, K.J.V. Vliet. Many-Body Potential for Point Defects Clusters in Fe-C Alloys. Physical Review Letters. 2007, Vol. 21, pp. 1-4.
83. C.S. Becquart, J.M. Raulot, G. Bencteux, C. Domain, M. Perez, S. Garruchet, H. Nguyen. Atomistic Modeling of an Fe System with a Small Concentration of C. Computational Materials Science. 2007, Vol. 40, pp. 119-129.
84. C. Domain, C.S. Becquart. Ab Initio Calculations of Defects in Fe and Dilute Fe-Cu Alloys. Physical Review B. 2001, Vol. 65, pp. 1-14.
85. C. Domain, C.S. Becquart, J. Foet. Ab-initio Study of Foriegn Interstitial Atom (C, N) Interactions with Intrinsic Point Defects in Alpha Fe. Physical Review B. 2004, Vol. 69, pp. 144112.
86. H. Chamati, N.I. Papanicolaou, Y. Mishin, D.A. Papaconstantopoulos. Embedded-atom Potential for Fe and its Application to Self-diffusion on Fe (100). Surface Science. 2006, Vol. 600, pp. 1793-1803.
87. M. Yan, M. Sob, G.J. Ackland, D.E. Luzzi, V. Vitek, M. Methfessel, C.O. Rodriguez. Interatomic Forces and Atomic Structure of Grain Boundaries in Copper-Bismuth Alloys. Physical Review B. 1993, Vol. 47, pp. 5571-5583.
88. R. Besson, A. Fraczkiewicz, M. Biscondi. An Empirical Many-body Potential for B2 Fe Al. Journal De Physique IV. 1996, Vol. 6, pp. 47-52.

89. W. Zang, Q. Xie, X. Ge. Interatomic Potentials Between Distinct Atoms from First Principles Calculation and Lattice Inversion Method. Journal of Applied Physics. 1997, Vol. 82, pp. 578-582.
90. R.C. Pasianot, L. Malerba. Interatomic Potentials Consistent with Thermodynamics: The Fe-Cu System. Journal of Nuclear Materials. 2007, Vol. 360, pp. 118-127.
91. G. Bonny, R.C. Pasianot, N. Castin, L. Malerba. Ternary Fe-Cu-Ni Many-body Potential to Model Reactor Pressure Vessel Steels: First Validation by Simulated Annealing. Philosophical Magazine. 2009, Vol. 89, pp. 3531-3546.
92. G. Bonny, R.C. Pasianot, L. Malerba. Fe-Ni Many-body Potential for Metallurgical Applications. Modelling and Simulation in Materials Science and Engineering. 2009, Vol. 17, pp. 1-13.
93. A. Ramasubramaniam, M. Itakura, E.A. Cater. Interatomic Potentials for Hydrogen in Alpha-Iron Based on Density Functional Theory. Physical Review B. 2009, Vol. 79, pp. 1-13.
94. F.C. Frank, J.F. Nicholas. Stable Dislocations in the Common Crystal Lattice. Philosophical Magazine Series 7. 1953, Vol. 44, pp. 1213-1235.
95. M.S. Duesbery. On Kinked Screw Dislocations in the BCC Lattice I: The Structure and Peierl's Stress of Isolated Kinks. Acta Metallurgica. 1983, Vol. 31, pp. 1747-1750.
96. M.S. Duesbery, G.Y. Richardson. The Dislocation Core in Crystalline Materials. CRC Critical Reviews in Solid State and Material Sciences. 1991, Vol. 17, pp. 1-46.
97. C. Wuthrich. The Structure of Kinks and Constrictions of Screw and 71deg Dislocations in BCC Metals. Philosophical Magazine. 1977, Vol. 35, pp. 325-335.
98. R. Peierls. The Size of the Dislocation. Proceedings of the Physical Society. 1940, Vol. 52, pp. 34-37.
99. B. Joos, J. Zhou. The Peierls-Nabarro Model and the Mobility of the Dislocation Line. Philosophical Magazine A. 2001, Vol. 81, pp. 1329-1340.
100. G. Lu, N. Kioussis. The Peierl's-Nabarro Model Revisited. Philosophical Magazine Letters. 2000, Vol. 80, pp. 675-682.
101. F.R.N. Nabarro. Fifty-year study of the Peierl's-Nabarro stress. Materials Science and Engineering. 1997, Vol. A234, pp. 67-76.

102. A.J.E. Foreman, M.A. Jaswon, J.K. Wood. Factors Controlling Dislocation Widths. Proceedings of the Physical Society. A. 1951, Vol. 64, pp. 156.

103. H.B. Huntington. Modification of the Peierl's-Nabarro Model for Edge Dislocation Core. Proceedings of the Physical Society. Section B. 1955, Vol. 68, pp. 1043.

104. D. Kuhlmann-Wilsdorf. Frictional Stress Acting on a Moving Dislocation in an Otherwise Perfect Crystal. Physical Review B. 1960, Vol. 120, pp. 773-781.

105. P. Haasen. On Plasticity of Germanium and Iodine Antimonide. Acta Metallurgica. 1957, Vol. 5, pp. 598-599.

106. H. Wei, Y. Xiang, P. Ming. A Generalized Peierl's-Nabarro Model for Curved Dislocations using Discrete Fourier Transform. Communications in Computational Physics. 2008, Vol. 4, pp. 275-293.

107. V.V. Bulatov, E. Kaxiras. Semidiscrete Variational Peierl's Framework for Dislocation Core Properties. Physical Review Letters. 1997, Vol. 78, pp. 4221-4224.

108. G. Lu, N. Kioussis, V.V. Bulatov, E. Kaxiras. Generalized Stacking Fault Energy Surface and Dislocation Properties of Aluminum. Physical Review B. 2000, Vol. 62, pp. 3099-3108.

109. C.R. Weinberger, B.L. Boyce, C.C. Battaile. Slip Planes in BCC Transition Metals. International Materials Reviews. 2013, Vol. 58, pp. 296-314.

110. D. Calliard. Kinetics of Dislocations in Pure Fe. Part I. In situ Straining Experiments at Room Temperature. Acta Materialia. 2010, Vol. 58, pp. 3493-3503.

111. D. Calliard. Kinetics of Dislocations in Pure Fe. Part II. In situ Straining Experiments at Room Temperature. Acta Materialia. 2010, Vol. 58, pp. 3504-3515.

112. A. Seeger. Why Anomalous Slip in Body Centered Cubic Metals? Material Science and Engineering. 2001, Vols. A319-321, pp. 254-260.

113. P.D. Neumann. The Interactions between Dislocations and Dislocation Dipoles. Acta Metallurgica. 1971, Vol. 19, pp. 1233-1241.

114. M.F. Ashby, R.W. Messler, R. Asthana, E.P. Furlani, R.E. Smallman, A.H.W. Ngan, R.J. Crawford, N. Mills. Engineering Materials and Processes Desk Reference. Butterworth-Heinemann, 2009. pp. 189.

115. F. Kroupa. Dislocation Dipoles and Dislocation Loops. Journal de Physique. 1966, Vol. C3, pp. C3-154 – C3-167.

116. B. Joos, M.S. Duesbery. Dislocation Kink Migration Energies and the Frenkel-Kontorowa Model. Physical Review B. 1997, Vol. 55, pp. 11161-11166.
117. W.T. Sanders, Dislocation Kink in a Crystal Model. Journal of Applied Physics. 1965, Vol. 36, pp. 2822.
118. T. Imura, K. Noda, H. Matsui, H. Saka, H. Kimura. Dislocations in Solids. University of Tokyo Press, 1985. pp. 287.
119. J. Chang, W. Cai, V.V. Butalov, S. Yip. Dislocation Motion in BCC Metals by Molecular Dynamics. Material Science and Engineering A. 2001, Vol. 309, pp. 160-163.
120. K. Edagawa, T. Suzuki, S. Takeuchi. Motion of a Screw Dislocation in a 2 Dimensional Peierl's Potential. Physical Review B. 1997, Vol. 55, pp. 6180-6189.
121. W. Cai, V.V. Butalov, S. Yip, A.S. Argon. Kinetic Monte Carlo Modeling of Dislocation Motion in BCC Metals. Materials Science Engineering A. 2001, Vol. 309, pp. 270.
122. F. Louchet, B. Viguier. Ordinary Dislocations in gamma-TiAl: Cusp Unzipping, Jog Dragging and Stress Anomally. Philosophical Magazine A. 2000, Vol. 80, p. 765.
123. R. Phillips, D. Rodney, V. Shenoy, E. Tadmor, M. Oritz. Hierarchical Models of Plasticity: Dislocation Nucleation and Interaction. Modelling and Simulation in Material Science and Engineering. 1999, Vol. 7, pp. 769-780.
124. L.K. Wickham, K. Schwarz, J.S. Stolken. Dislocation Forest Interactions: Simulation and Prediction. Material Research Society Symposium. 2000, Vol. 578, pp. 125-133.
125. P. Veyssiere, H. Wang, D.S. Xu, Y.L. Chiu. Local Dislocation Reactions, Self Organization and Hardening in Single Slip. Materials Science and Engineering. 2009, Vol. 3, pp. 1-10.
126. W. Puschl. Reactions betweeen Glide Dislocations and Forest Dislocations in Anisotropic BCC Metals. Physica Status Solidi A. 1985, Vol. 90, pp. 181-189.
127. R. Madec, B. Devincre, L.P. Kubin. Simulation of Dislocation Patterns in Multi-Slip. Scripta Materialia. 2002, Vol. 47, pp. 689-695.
128. G. Schoeck, R. Frydman. The Contribution of the Dislocation Forest to Flow Stress. Physical Status Solidi B. 1972, Vol. 53, pp. 661-673.
129. V.V. Bulatov, F.F. Abraham, L.P. Kubin, B. Devincre, S. Yip. Connecting Atomistic and Mesoscale Simulations of Crystal Plasticity. International Weekly Journal of Science. 12 Feb 1998, Vol. 391, pp. 669.

130. D. Rodney, R. Philips. Structure and Strength of Dislocation Junctions: An Atomic Level Analysis. Physical Review Letters. 1999, Vol. 82, pp. 1704-1707.

131. L.K. Wickham, K. Schwarz, J.S. Stolken. Rules for Forest Interactions Between Dislocations. Phsical Review Letters. 1999, Vol. 83, pp. 4574-4577.

132. V.B. Shenoy, R.V. Kukta, R. Phillips. Mesoscopic Analysis of Structure and Strength of Dislocation Junctions in FCC Metals. Physical Review Letters. 2000, Vol. 84, pp. 1491-1494.

133. H. Matsui, H. Kimura. Anomalous {110} Slip and the Role of Coplanar Double Slip in BCC Metals. Scripta Metall. 1975, Vol. 9, pp. 971-978.

134. A.J. Garratt-Reed, G. Taylor. Optical and Electron Microscopy of Nobium Crystals Deformed Below Room Temperature. Philosophical Magazine A. 1979, Vol. 39, pp. 597-646.

135. P.A. Gordon, T. Neeraj, Y. Li, J. Li. Screw Dislocation Mobility in B.C.C. Metals: The Role of the Compact Core on Double-Kink Nucleation. Modelling and Simulation in Materials Science and Engineering. 2010, Vol. 18, pp. 1-13.

136. J.J. Duistermaat, J.A.C. Kolk. Distributions - Theory and Applications. Birkhauser, 2010. pp. 33, 321.

137. A. Gsponer. A Concise Introduction to Colombeau Generalized Functions and their Applications in Clasical Electrodynamics. European Journal of Physics. 2009, Vol. 30, pp. 109-126.

138. V. Vinogradov, J.R. Willis. The Pair Distribution Function for an Array of Screw Dislocations. International Journal of Solids and Structures. 2008, Vol. 45, pp. 3726-3738.

139. J. Deng, A. El-Azab. Mathematical and Computational Modelling of Correlations in Dislocation Dynamics. Modelling and Simulation in Materials Science and Engineering. 2009, Vol. 17, pp. 1-31.

140. L.P. Kubin, B. Devincre. From Dislocation Mechanism to Dislocation Microstructures and Strain Hardening. Roskilde : Risoe Natl. Lab., 1999. pp. 66-83.

141. R.J. Amedo, N.M. Ghoniem. Dislocation Dynamics II: Applications to the Formation of Persistent Slip Bands, Planar Arrays, and Dislocation Cells. Physical Review B. 1990, Vol. 41, pp. 6968-6976.

142. D. Kuhlmann-Wilsdorf. Technological High Strain Deformations of Wavy Glide Metals and LEDS. Physical Status Solidi A. 1995, Vol. 149, pp. 225-241.

143. B. Svendsen. Continuum Thermodynamic Models for Crystal Plasticity including Size Effects of Geometrically Necessary Dislocations. Journal of Mechanics and Physics of Solids. 2002, Vol. 50, pp. 1297-1329.

144. N.A. Fleck, M.F. Ashby, J.W. Hutchinson. The Role of Geometrically Necessary Dislocations in Giving Material Strengthening. Scripta Materialia. 2003, Vol. 48, pp. 179-183.

145. C. Zhou, S.B. Biner, R. LeSar. Discrete Dislocation Dynamics Simulations of Plasticity at Small Scales. Acta Materialia. 2010, Vol. 58, pp. 1565-1577.

146. G. Dhanaraj, K. Byrappa, V. Prasad, M.l. Dudley. Springer Handbook of Crystal Growth. Springer-Verlag Berlin Heidelberg, 2010. pp. 1356.

147. N.F. Mott. Slip at Grain Boundaries and Grain Growth in Metals. Proceedings of the Physical Society. 1948, Vol. 60, pp. 391-394.

148. S.E. Babcock, R.W. Balluffi. Grain Boundary Kinetics II. In situ Observations of Coupled Grain Boundary Dislocation Motion in High Angle Boundary Migration. Acta Metallurgica. 1989, Vol. 37, pp. 2367-2376.

149. R. Jhan, P.D. Bristowe. A Molecular Dynamics Study of Grain Boundary Migration without the Precipitation of Secondary Grain Boundary Dislocations. Scripta Metallurgica et Materialia. 1990, Vol. 24, pp. 1313-1318.

150. B. Schonfelder, G. Gottestein, L. S. Shvidlerman. Collective Study of Grain Boundary Migration and Grain Boundary Self Diffusion of [001] Twist Grain Boundaries in Copper by Atomistic Simulations. Acta Meterialia. 2005, Vol. 53, pp. 1595-1866.

151. H. Zhang, D.J. Srolovitz. Simulation and Analysis of the Migration Mechanism of Σ5 Tilt Grain Boundaries in an FCC Metal. Acta Materialia. 2006, Vol. 54, pp. 623-633.

152. W.T. Read, W. Shockley. Dislocation Models of Crystal Grain Boundaries. Physical Review. 1950, Vol. 78, pp. 275-289.

153. L. Zhou, N. Zhou, G. Song. Collective Motion of Atoms in Grain Boundary Migration of a BCC Metal. Philosophical Magazine. 2006, Vol. 86, pp. 5885-5895.

154. A. Morris. A Practical Guide to Reliable Finite Element Modelling. John Wiley & Sons, 2008. pp. 175, 176.

155. K. Ho-Le. Finite Element Mesh Generation Methods: A Review and Classification. Computer-Aided Design. 1988, Vol. 20, pp. 27-38.

156. S.H. Lo. Finite Element Mesh Generation and Adaptive Meshing. Progressive Structural Engineering Materials. 2002, Vol. 4, pp. 381-399.

157. J.C. Cavendish, D.A. Field, W.H. Frey. An Approach to Automatic Three Dimensional Finite Element Mesh Generation. International Journal of Numerical Methods in Engineering. 1985, Vol. 21, pp. 329-347.

158. S.T. Owen. A Survey of Unstructured Mesh Generation Technology. 1998. Proceedings, 7th International Meshing Roundtable, Scandia National Lab. pp. 239-267.

159. An Approach to Combined Laplacian and Optimization-based Smoothing for Triangular, Quadilateral, and Quad-Dominant Meshes. S.A. Canann, J.R. Tristano, M.L. Staten. 1998. 7th International Meshing Roundtable, Scandia National Lab. pp. 479-494.

160. Local Optimization-Based Untangling Algorithms for Quadilateral Meshes. L.A. Freitag, . 2001. 10th International Meshing Roundtable, Scandia National Lab. pp. 397-406.

161. D. Field. Laplacian Smoothing and Delaunay Triangulations. Communications in Numerical Methods in Engineering. 1988, Vol. 4, pp. 709-712.

162. L.A. Freitag. On Combining Laplacian and Optimization-based Smoothing Techniques. Trends in Unstructured Mesh Generation. 1997, Vol. 220, pp. 37-44.

163. D.N. Arnold, G. Awanou. The Serendipity Family of Finite Elements. Foundations of Computational Mathematics. 2011, Vol. 11, pp. 337-344.

164. V. Jagota, A.P.S. Sethi. Analysis of Distortion Parameters of Eight Node Serendipity Element on the Elements Performance. International Journal of Mechanical and Industrial Engineering. 2012, Vol. 2, pp. 110-117.

165. E.O. Hall. The Deformation and Aging of Mild Steel: III Discussion of Results. Proceedings of the Physical Society. 1951, Vol. 643, pp. 747-753.

166. N.J. Petch. The Cleavage Strength of Polycrystals. Journal of Iron Steel Institute. 1953, Vol. 173, pp. 25-28.

167. M.A. Meyers, E. Ashworth. A Model for the Effect of Grain Size on the Yield Stress of Metals. Philosophical Magazine A. 1982, Vol. 46, pp. 737-759.

168. R.A. Masumura, P.M. Hazzledine, C.S. Pande. Yield Stress of Fine Grained Materials. Acta Metallurgica. 1998, Vol. 46, pp. 4527-4534.

169. H.A. Chokshi, A. Rosen, J. Karach, H. Gleiter. On the Validity of the Hall-Petch Relationship in Nanocrystalline Materials. Scripta Metallurgca. 1989, Vol. 23, pp. 1679-1683.

170. H.H. Fu, D.J. Benson, M.A. Meyers. Analytical and Computational Description of Effect of Grain Size on Yield Stress of Metals. Acta Materialia. 2001, Vol. 49, pp. 2567-2582.

171. T.R. Mallow, C.C. Koch. Grain Growth in Nan0crystalline Iron Prepared by Mechanical Attrition. Acta Materialia. 1997, Vol. 45, pp. 2177-2186.

172. E.P. Abrahamson II. Surfaces and Interfaces. Syracuse University Press, 1986. pp. 262.

173. L. Ventelon, F. Willaime. Core Structure and Peierl's Potential of Screw Dislocations in alpha-Fe from First Principles: Cluster versus Dipole Approaches. Journal of Computer Aided Material Design. 2007, Vol. 14, pp. 85-94.

174. J. Li, C.Z. Wang, J.P. Chang, W. Cai, V.V. Bulatov, K.M. Ho, S. Yip. Core Energy and Peierl's Stress of a Screw Dislocation in bcc Molybdenum: A Periodic-cell Tight-Binding Study. Physical Review B. 2004, Vol. 70, pp. 1-8.

175. A.T. Lim, M. Haataja, W. Cai, D.J. Srolovitz. Stress-driven Migration of Simple Low-angle Mixed Grain Boundaries. Acta Materilia. 2012, Vol. 60, pp. 1395-1407.

176. L.P. Evers, D.M. Parks, W.A.M. Brekelmans, M.G.D. Geers. Crystal Plasticity Model with Enhanced Hardening by Geometrically Necessary Dislocation Accumulation. Journal of the Mechanics and Physics of Solids. 2002, Vol. 50, pp. 2403-2424.

177. D.M. Norfleet, D.M. Dimiduk, S.J. Polasik, M.D. Uchic, M.J. Mills. Dislocation Structures and their Relationship to Strength in Deformed Nickel Microcrystals. Acta Materialia. 2008, Vol. 56, pp. 2988-3001.

178. P. Gay, P.B. Hirsh, A. Kelly. The Estimation of Dislocation Densites in Metals From X-ray Data. Acta Metallurgica. 1953, Vol. 1, pp. 315-319.

179. M.J. Hordon, B.L. Averbach. X-ray Measurements of Dislocation Density in Deformed Copper and Aluminum Single Crystals. Acta Metallurgica. 1961, Vol. 9, pp. 237-246.

180. G. Wang, A. Strachan, T. Cagin, W.A. Goddard III. Calculating the Peierl's Energy and Peierl's Stress from Atomistic Simulations of Screw Dislocation Dynamics: Application to BCC Tantalum. Modelling and Simulation in Materials Science and Engineering. 2004, Vol. 12, pp. S371-S389.

181. J. Chaussidon, M. Fivel, D. Rodney. The Glide of Screw Dislocations in BCC Fe: Atomistic Static and Dynamic Simulations. Acta Materialia. 2006, Vol. 54, pp. 3407-3416.

182. G.S. Rohrer. Structure and Bonding in Crystalline Materials. Cambridge: Cambridge University Press, 2001. pp. 326.

183. Y. Mishin. Interatomic Potentials for Metals. Handbook of Materials Modeling. Springer, 2005.

184. J. Stewart. Caculus: Concepts and Contexts. Richard Stratton, 2009. pp. 594.

185. W.T. Thomson. Theory of Vibrations with Applications. CBS Publishers & Distributorrs, 1990. pp. 427-428.

186. A. Arsenlis, D.M. Parks. Crystallographic Aspects of Geometrically-Necessary and Statistically-Stored Dislocation Density. Acta Materialia. 1999, Vol. 47, pp. 1597–1611.

187. A.S. Argon. Constitutive Equations in Plasticity. The MIT Press, 1975.

188. ASTM Committee E04. Standard Test Methods for Determining Average Grain Size. ASTM International, 2012. Engineering Standard. E112-10.

189. Y.S. Yang, S.H. Hsieh. Iterative Mesh Partitioning Optimization for Parallel Nonlinear Dynamic Finite Element Analysis with Direct Substructuring. Computational Mechanics. 2002, Vol. 28, pp. 456-468.

190. W. Carrington, K.F. Hale, D. McLean. Arrangement of Dislocations in Iron. Proceedings of the Royal Society of London, Series A, Mathematical and Physical Sciences. 1960, Vol. 259, pp. 203-227.

191. L. Ventelon. Core Structure of Screw Dislocations in Fe from First-Principles. Department of Materials for Nuclear Energy at the Nuclear Energy Division, Commissariat à l'énergie Atomique et aux Energies Alternatives. 2008. PhD Thesis.

192. V. Vitek, M. Yamaguchi. Core Structure of Non-screw 1/2[111] Dislocations on (110) Planes in B.C.C. Crystals, II. Peierl's Stress and the Effect on an External Shear Stress on the Cores. Journal of Physical F. Metal Phys. 1973, Vol. 3, pp. 537-542.

193. L.E. Samuels. Light Microscopy of Carbon Steels. ASM International, 1999. pp. 82.

194. D.A. Terentyev, Y.N. Osetsky, D.J. Bacon. Effects of Temperature on Structure and Mobility of the <100> Edge Dislocation in Body Centered Cubic Iron. Acta Materialia. 2010, Vol. 58, pp. 2477-2482.

195. F. Shimizu, S. Ogata, M Yamaguchi, T. Kano, H. Kimizuka, M. Itakura, H. Kaburaki. First Principles Calculation on Core Structures and Peierl's Stress of a Screw Dislocation in BCC Iron. Japan Atomic Energy Agency. Epoch Making Simulation, 2007. Chp. 3.

196. J.R. Davis. Tensile Testing. ASM International, 2004. pp. 130.

197. K. Nakashima, M. Suzuki, Y. Futamura, T. Tsuchiyama, S. Takaki. Limit of Dislocation Density and Dislocation Strengthening in Iron. Materials Science Forum. 2006, Vols. 503-504, pp. 627-632.

198. U.F. Kocks. Laws of Work Hardening and Low Temperature Creep. Journal of Engineering Materials Technology. 1976, pp. 76-85.

199. D. Askeland, P. Phulc'. The Science of Engineering of Materials. Thomson Canada Ltd, 2005. pp. 125.

200. S. Singh. Theory of Plasticity. Khanna Publishers, 1980. pp. 61-62.

APPENDICES

A.1 LIST OF PUBLICATIONS

1. K. D. Njoroge, G. O. Rading, J. M. Kihiu, M. J. Witcomb and L. A. Cornish. Dynamic Analysis of Dislocation Cores in a-Fe Lattice Using the Embedded Atom Method. International Journal of Computational Engineering Research. 2012, Vol. 2, pp. 851-859. ISSN: 2250–3005
2. K. D. Njoroge, G. O. Rading, J. M. Kihiu, M. J. Witcomb, L. A. Cornish, The Impact of Interstitial Carbon on Dislocation Motion in the alpha-Fe Lattice, International Journal of Computational Engineering Research. 2014, Vol. 4, pp. 5-9. ISSN: 2250–3005
3. K. D. Njoroge, G. O. Rading, J. M. Kihiu, M. J. Witcomb, L. A. Cornish, The Dislocation Core Misfit Potential, Computational Materials Science, Elsevier, 2015, Vol. 100, part B – Special Issue on Advanced Simulation Methods, pp. 195-202. ISSN: 0927-0256

A.2 DISLOCATION TYPES

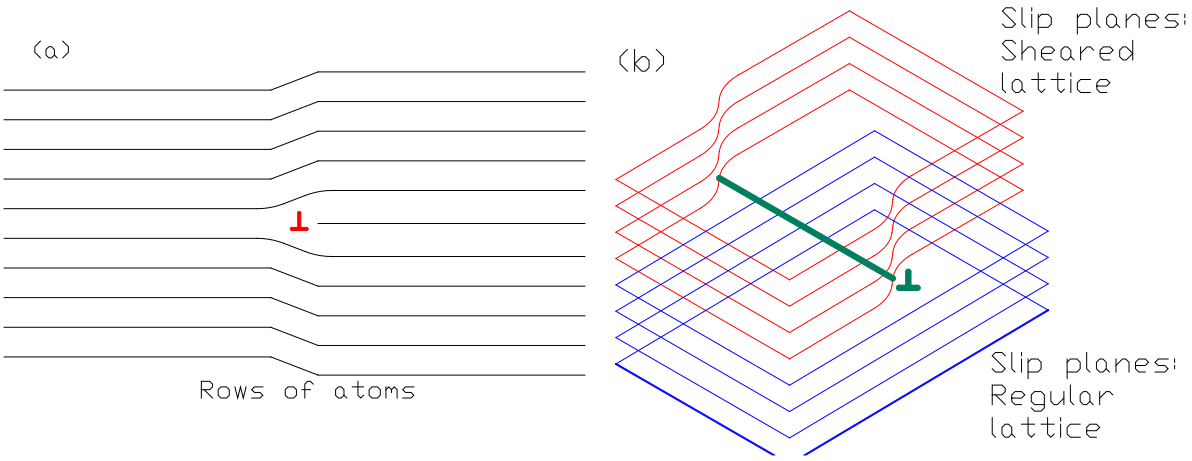

Figure A2.1: Dislocation types (a) Edge, (b) Screw.

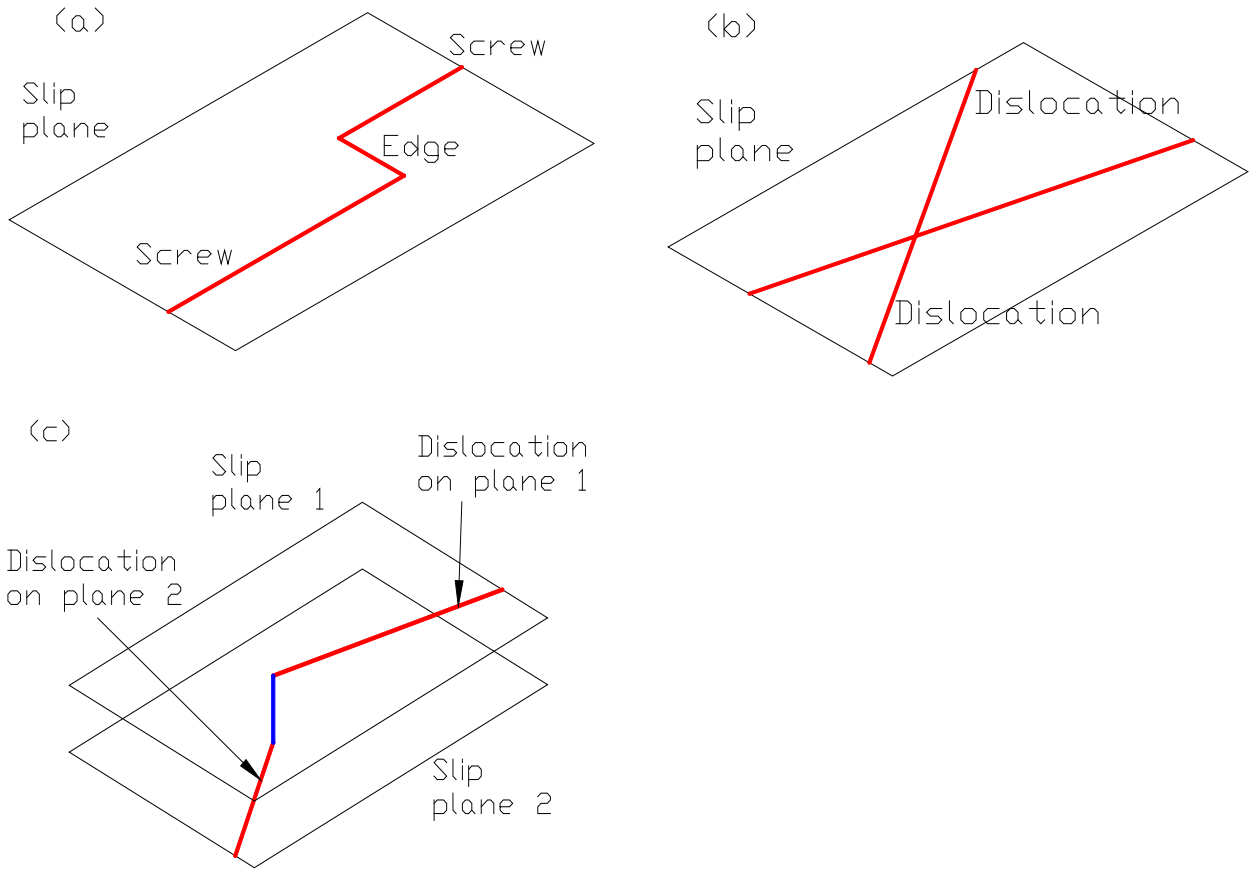

Figure A2.2: 2-D Dislocation structure types (a) Kink, (b) Junction, (c) Jog.